Novel optical fibres for on-chip optical tweezing and bio-applications

Georgia Anastasiadi

A dissertation submitted for the degree of Doctor of Philosophy

School of Engineering and Physical Sciences

Heriot-Watt University

September 2022

Abstract

Optical trapping of a single cell is a technique widely used in many scientific sectors due to the benefits of isolating and examining a single cell in isolation. Studies that use a conventional microscope-based tweezing system demonstrate optical trapping based on strongly focused laser light delivered through a high Numerical Aperture objective. However, this approach poses restrictions to the range of the applications of the tweezing system due to the use of the imaging optics for tweezing beam delivery. To overcome these restrictions, optical fibre-based systems to optically trap a single cell have been studied. In this thesis, an optical tweezing system based on machined four-core optical fibres has been developed and applied to a variety of cells.

Mirrors, with an angle slightly higher than the critical angle for the fibre to medium interface, have been fabricated on the end of a four-core fibre, to alter the propagation of the laser beam exiting the four cores. The four beams are directed to overlap, and the optical fibre trap acts in a manner similar to a conventional optical tweezer. The multicore fibre (MCF) trap is composed of four diverging beams which overlap to form a trapping volume, as opposed to the trapping volume of an optical tweezer which is formed by tightly focusing a single beam via a high numerical aperture objective lens. It is shown that micron-scale particles can be optically trapped in this overlap region of the MCF trap.

Optical trapping of yeast cells, and also a wider range of cells such as red blood cells, U87 cells and mouse embryonic stem cells is reported in this thesis. The optical trapping system has been used also below a Raman microscope. This demonstrates the ability to trap cells under an analytical microscope without modifying the microscope optics, and to capture the Raman spectra from single trapped cells.

The work presented in the thesis demonstrates a flexible system of small dimension, to trap cells for use under a wide range of microscopes, circumventing the need to focus a trapping beam through a high numerical aperture objective lens. The trap has been characterised by measuring the maximum trapping velocities and trap strengths, which are comparable to conventional optical tweezers.

The trapping system has also been used to investigate alternative optical manipulation of 'special' particles, such as hollow glass spheres, that cannot be optically trapped with a conventional optical tweezers system due to their low refractive index. The machined

multicore fibre uses the region between the beam overlap area and the fibre end face, to hold these low refractive index particles in place.

The primary objectives of the work described in this thesis were to optimise the FIB fabrication of the mirrors on the MCF trap, build a robust, portable system capable of cell trapping and manipulation under different analytical microscopes, characterise the beam propagation characteristics, demonstrate stable trapping of some exemplar cell types, and compare the trap strength with conventional optical tweezers.

To my family

Acknowledgements

First of all, I would like to truly thank my supervisors Dr William N. MacPherson and Dr Lynn Paterson for their great support and guidance throughout my PhD, as their encouragement was motivating for me.

I would also like to thank Mr Mark Leonard for his collaboration with the FIB fabrication process and Dr Anusha Keloth for helping me with the conventional tweezers set up as well as with the HF etching process. Additionally, I would like to give my sincere thanks to the whole AOP research group for their support and especially to Dr Jonathan Morton and Dr Richard Carter for their important help in the lab.

I am thankful to all my friends, Niki, Dimitris, Merlinda and Naya for their friendship and encouragement that held me strong. Special thanks to Armen and Giovanna that were there always for me for the good and the bad moments and they never let me down.

Last but not least, my most important thanks to my parents, my grand-parents and my brother back home, for their true love, support and faith in me for all this time.

Research Thesis Submission

Please note this form should be bound into the submitted thesis.

Name:	Georgia Anastasiadi		
School:	EPS		
Version: *(i.e. First, Resubmission, Final)*	Final	Degree Sought:	PhD

Declaration

In accordance with the appropriate regulations I hereby submit my thesis and I declare that:

1. The thesis embodies the results of my own work and has been composed by myself
2. Where appropriate, I have made acknowledgement of the work of others
3. The thesis is the correct version for submission and is the same version as any electronic versions submitted*.
4. My thesis for the award referred to, deposited in the Heriot-Watt University Library, should be made available for loan or photocopying and be available via the Institutional Repository, subject to such conditions as the Librarian may require
5. I understand that as a student of the University I am required to abide by the Regulations of the University and to conform to its discipline.
6. I confirm that the thesis has been verified against plagiarism via an approved plagiarism detection application e.g. Turnitin.

ONLY for submissions including published works

Please note you are only required to complete the Inclusion of Published Works Form (page 2) if your thesis contains published works)

7. Where the thesis contains published outputs under Regulation 6 (9.1.2) or Regulation 43 (9) these are accompanied by a critical review which accurately describes my contribution to the research and, for multi-author outputs, a signed declaration indicating the contribution of each author (complete)
8. Inclusion of published outputs under Regulation 6 (9.1.2) or Regulation 43 (9) shall not constitute plagiarism.

*   *Please note that it is the responsibility of the candidate to ensure that the correct version of the thesis is submitted.*

Signature of Candidate:		Date:	21/9/2022

Submission

Submitted By *(name in capitals):*	GEORGIA ANASTASIADI
Signature of Individual Submitting:	
Date Submitted:	21/9/2022

For Completion in the Student Service Centre (SSC)

Limited Access	Requested	Yes		No		Approved	Yes		No	
E-thesis Submitted (mandatory for final theses)										
Received in the SSC by *(name in capitals):*						Date:				

Inclusion of Published Works

<u>Declaration</u>

This thesis contains one or more multi-author published works. In accordance with Regulation 6 (9.1.2) I hereby declare that the contributions of each author to these publications is as follows:

Citation details	e. g. Author 1 and Author 2, Title of paper, Title of Journal, X, XX-XX (20XX)
Author 1	Contribution….
Author 2	Contribution….
Signature:	
Date:	

Citation details	e. g. Author 1 and Author 2, Title of paper, Title of Journal, X, XX-XX (20XX)
Author 1	Contribution….
Author 2	Contribution….
Signature:	
Date:	

Citation details	e. g. Author 1 and Author 2, Title of paper, Title of Journal, X, XX-XX (20XX)
Author 1	Contribution….
Author 2	Contribution….
Signature:	
Date:	

Publications

Journal articles by the author

G. Anastasiadi, M. Leonard, L. Paterson and W. N. MacPherson, "Fabrication and characterisation of machined multi-core fibre tweezers for single cell manipulation," Optics Express **26** (3), 3557-3567 (2018).

G. Anastasiadi, M. Leonard, L. Paterson and W. N. MacPherson, "Fabrication and characterization of machined multi-core fiber tweezers for single cell manipulation: erratum," Optics Express **28** (12), 17898-17899 (2020).

Proceedings papers by the author

G. Anastasiadi, M. Leonard, L. Paterson and W. N. MacPherson, "Machined multicore optical fibres for on-chip optical manipulation," Proceedings of SPIE The International Society for Optical Engineering, 1034702 (2017).

G. Anastasiadi, F. M. Shaw, A. B. Matheson, T. Mendonca, W. N. MacPherson, A. J. Wright, P. A. Dalgarno, M. Tassieri, and L. Paterson, "Machined Multicore Fibre Tweezers for Single Cell Manipulation," in Biophotonics Congress 2021, OSA Technical Digest (Optical Society of America, 2021), paper ATh1D.1.

Conference oral presentations by the author

- **Georgia Anastasiadi**, Lynn Paterson and William N. MacPherson, "Machined optical fibres for on-chip optical tweezing," Biophotonics North, University of St. Andrews, November 2016, Oral presentation.

- **Georgia Anastasiadi**, Mark Leonard, Lynn Paterson and William N. MacPherson, "Machined multicore optical fibres for on-chip optical manipulation," Optical trapping and optical manipulation XIV, San Diego Convention Centre, August 2017, Oral presentation.

Conference poster presentations by the author

- **Georgia Anastasiadi**, Lynn Paterson and William N. MacPherson, "Novel multicore optical fibres for on-chip optical manipulation," Photonex Scotland, Strathclyde, June 2017, Poster presentation.
- **Georgia Anastasiadi**, Lynn Paterson and William N. MacPherson, "Machined optical fibres for on-chip optical trapping," SU2P, Heriot-Watt University, April 2017, Poster presentation.
- **Georgia Anastasiadi**, Lynn Paterson and William N. MacPherson, "Novel multicore optical fibres for on-chip optical manipulation," IPaQS symposium, Heriot-Watt, May 2017, Poster presentation.
- **Georgia Anastasiadi**, Lynn Paterson and William N. MacPherson, "Novel multicore optical fibres for on-chip optical manipulation," National Day of women in engineering, Heriot-Watt University, June 2016, Poster presentation. *"Best poster presentation" prize winner.*

- **Georgia Anastasiadi**, Lynn Paterson and William N. MacPherson, "Machined optical fibres for on-chip optical tweezing," Marine Microbiome – Discovery & Innovation, Berlin, June 2016, Poster presentation.
- **Georgia Anastasiadi**, Lynn Paterson and William N. MacPherson,"Machined optical fibres for on-chip optical tweezing," Photonex Scotland, June 2016, Poster presentation.
- **Georgia Anastasiadi**, Lynn Paterson and William N. MacPherson,"Machined optical fibres for on-chip optical trapping," Transmed EPSRC conference, University of Edinburgh, June 2016, Poster presentation.

Contents

List of figures

List of Abbreviations

OT	Optical Tweezers
GFP	Green Fluorescent Protein
ES	Embryonic Stem cells
Epi	Epiblast cells
NA	Numerical Aperture
TIRF	Total Internal Reflection Fluorescence
FIB	Focused Ion Beam
TIR	Total Internal Reflection
MACS	Magnetic Activated Cell Sorting
DEP	Dielectrophoresis
IDS	Isodielectric separation
CTC	Circulating Tumor Cell
PCA	Principal Component Analysis
SLM	Spatial Light Modulator
CW	Continuous Wave
Nd:YLF	Neodymium-doped Yttrium Lithium Fluoride
Nd:YAG	Neodymium-doped Yttrium Aluminum Garnet
MCF	Multicore fibre
PA	Polyamide
PE	Polyethylene
PP	Polypropylene
PVC	Polyvinyl Chloride
PVDF	Polyvinylidene Floride
PBT	Polybutylene terephthalate
PEEK	Polyether Ether Ketone
FBG	Fibre Bragg Gratings
SEM	Scanning Electron Microscope
HF	Hydrofluoric (acid)

Chapter 1: Aims and Objectives

Optical trapping of a single cell refers to the ability to physically hold an individual particle using forces due to the transfer of momentum of light. This technique is increasingly used in scientific studies due to its 'non-contact' ability to hold, manipulate and examine a single cell in isolation [1-6]. Cell trapping was first reported by Ashkin *et al.* in 1987 [7], who demonstrated trapping of single cells of different types, such as *E. coli* bacteria, yeast, red blood cells, plant cells and even plant viruses. This study came shortly after the invention of Optical Tweezers, also by Ashkin *et al.*, in 1986 [8] that defined Optical Tweezing (OT) as the ability to trap and manipulate a particle in three dimensions using a single, tightly focussed laser beam.

Initial studies demonstrated optical trapping using conventional microscopes that were modified to include tweezing systems. These modified, bespoke microscopes demonstrate the technique of optical tweezers, but require significant modifications to the optical system. Therefore, this approach is not suitable in some circumstances, for example when optical tweezing is required in a microscope system that may be in use as part of a shared imaging facility, where modification of the microscope optical system would disrupt the research of other users. To enhance flexibility, it is desirable to have a generic, portable tweezing tool that could be used in a range of different microscopes. Recent studies that use optical fibre-based systems to demonstrate optical trapping of a single cell have been reported, but these have limitations due to the deployment geometry involving multiple fibre access points [9]. In this thesis, an optical trapping system based on a *single* fibre, a fibre with four machined cores, is developed, characterised and demonstrated in a range of cell trapping and manipulation experiments.

1.1 Motivation

Optical trapping and manipulation of single cells in single and multiple traps [6-7,10-12] is increasingly important in life- and biomedical-sciences to measure cellular forces [13-15], control cell-to-cell interactions [16-18], pattern cells to build micro-tissues or micro-consortia [19], to sort [3,20-23] or isolate [2, 24] cells and to assist in the interrogation of cells by microscopy or micro-spectroscopy [4-5, 25].

Cell isolation is the process of separating a group of cells (or an individual cell) of interest from a heterogeneous mixture of cells and this is of high importance for many applications in the biomedical and life sciences.

More specifically, cell isolation has several definitions according to the main process and application of the technique; i) the isolation of only one cell from a population (single cell isolation) [26-27], ii) the process of breaking up solid tissue into individual cells that can then be analysed by imaging or electrophysiology [28], and iii) the separation of one specific population of cells from a heterogenous mixture of cells (also known as cell sorting or cell separation) [29]. In the context of this thesis, 'cell isolation' refers to the isolation of a single cell from a population.

Cell isolation is important for several areas of the life sciences. Examples include:

- Creating a pure culture from one single progenitor cell, important in microbiology and creating cell lines for biomedical sciences [30].
- Analysing single cells away from other 'interfering' cells which may affect the dynamics of the cell of interest [31]. This is a requirement for studies in which making a measurement on an ensemble of cells could mask the processes under study. Differences (heterogeneities) between individual cells cannot be detected if a readout is an average from many cells. Studying the dynamics (the biochemical or physical properties) of a single cell instead of the entire sample (the bulk) allows resolution at a single cell level, however biochemical cues from nearby cells may influence these dynamics. As such, interrogating the cell in isolation, without interference from other cells is required in some cases.
- Creating a microconsortium, a small group of different cell types, to understand how cell types interact to alter their dynamics. This is increasingly important in many fields such as stem cell biology [32] and cancer cell biology [33] but is more commonly used in microbiology to study interaction between microbes in biofilms [34] or between microbes and mammalian cells *in vitro* to understand pathogenesis [35] since the spatial arrangement of cells and clusters of cells has profound implications for the function of these complex communities.

1.2 Cell isolation methods

1.2.1 Physical isolation methods

Physical isolation methods include techniques in which their working principle is based on the physical properties of the cells, such as their size, shape or density. These techniques usually require contact with the cells to manipulate them and they can be summarized below:

1) Dilution to extinction: to isolate a single cell from a population a common and inexpensive technique is to dilute the sample such that when a small volume (for example 200 microlitres) of the sample is pipetted into the well of a 96 well plate, there is likely to be zero or one cell in each well. This technique is used for microbes [36] and mammalian cells [37] to discover new strains and create single cell clones (pure cultures), respectively, but is extremely labour intensive, and does not guarantee single cell isolation.

2) Micropippette aspiration: One way to isolate single cells is to mechanically 'pick out' a single cell from a sample. An early approach to isolate a single cell from a heterogeneous mixture is based upon using micro-pipettes or glass capillaries/pipettes to physically hold and manipulate a single cell [38]. In this case, the micromanipulator system commonly includes an inverted microscope and micro-pipettes, placed on a motorised micro-translation stage. These micro-pipettes, formed from ultra-thin glass capillaries, are connected to an aspiration-release unit. The desired cell can be 'lifted' out of the sample using a micro-pipette employing suction (aspiration) then the micropipette or sample stage is relocated and the 'picked' cell is released into a suitable collection device for study or further culture [39]. This technique avoids the need for expensive manipulation and selection equipment, and does not require a microfluidic system, but it suffers limitations such as low yield caused by cells sticking to the surface of the tip and physical damage to cells since there is mechanical contact between the cell and the micromanipulator, and a generally slow process resulting in low throughputs.

1.2.2 Acoustic methods

Acoustic methods describe techniques that demonstrate cell sorting based on the presence of an acoustic field. These techniques include both static (where there is no

flow) and microfluidic techniques, with the choice depending on the final application and the sample volume.

As the wavelength of ultrasound is about 1 mm, it allows the control and separation of multiple, large particles within a rather large volume based on a tightly focused ultrasound microbeam [40-41]. Furthermore, the low intensities that are needed for acoustic trapping lead to a very small impact on the viability of the trapped micro particles [42-43]. On the other hand, the large wavelength makes the selective trapping of single cells as well as the smaller cells with only acoustic forces a challenging process also due to the large trapping region [41]. Acoustic trapping is limited in terms of flexibility when applied to single cell trapping because of the need for enhanced standing wave patterns that depend on the geometry of the trapping system [40].

Current methods use long ultrasound pulses for grabbing a single cell and short pulses for interrogating the target cell, which leads to difficulty in performing the measurement of the physical properties at the same time with the trapping. Recently, a study has demonstrated that short ultrasound pulses can be used to generate an acoustic trapping force that is comparable to that with long pulses by adjusting the pulse repetition frequency (PRF) [44]. Furthermore, concerning the feasibility of a single beam-based acoustical tweezers, it has been demonstrated only recently [45-46] and future studies on this technique may allow the potential of this approach to be better understood.

1.2.3 Electrical and magnetic methods

Electrical and magnetic methods describe approaches that exploit an external electric or magnetic field to apply a force to manipulate the cells.

Although electro-based and magneto-based trapping systems work for cell sorting, when it comes to single cell isolation there are few reports in the open literature. One recent study demonstrated the use of dielectrophoresis to characterise *Mycobacterium smegmatis* single cells, explaining how the cells respond dielectrophoretically when exposed to an electric field [47]. One of the aims of this study was to relate the membrane altering mechanisms to cell death, drug-tolerance, and drug-resistance.

Again here, the main advantage of these methods is the fact that they are real-time, and quantitative techniques that can be integrated with other techniques and in case of the dielectrophoresis that it is, in most cases, label free. However, the need for a demanding and expensive set-up restricts their potential applications in scientific labs that need a simple and low-cost cell manipulation technique. Furthermore, for magnetic separation, the need to label the cells to be separated out, typically attaching particles of polarized charges to the cell's surface, also restricts the potential applications [48].

1.2.4 Optical methods include techniques that exploit optical forces to isolate cells.

A popular isolation technique that can demonstrate selective cell isolation, and is compatible with live cells, is laser capture microdissection [49]. This can extract sections of tissue from histopathological sections and can also dissect out single cells for genetic or protein analysis. This technique is mostly performed on fixed cells or tissue, although has been demonstrated to work for live cells [49] but it is of low throughput and high cost, and it presents the risk of potential damage to cells due to absorption of the high energy laser light used for dissection. Laser capture microdissection uses the absorption of energy to cut around a cell of interest to free it from the surrounding matrix, followed by a pulse of light which causes a shockwave to expel the cell of interest.

Optical tweezers is another optical method that uses the momentum of light to capture single cells in suspension, and move them in three dimensions. This technique of optically trapping and manipulating microscopic particles forms the basis of this thesis.

1.3 Introduction to optical tweezers

The first demonstrations of optical tweezing were based on the use of high Numerical Aperture (NA) microscope objectives to achieve a tight focus of the laser beam [8]. The main working principle of the technique is illustrated in figure 1.1.
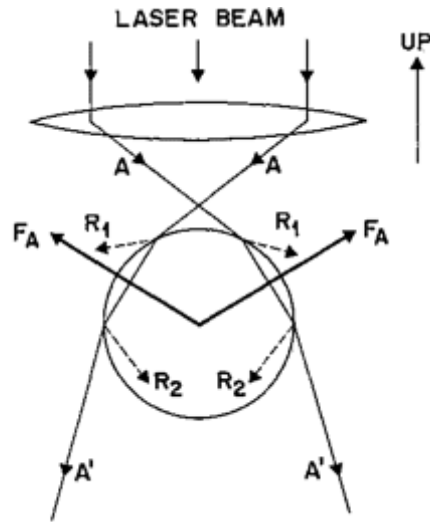
Figure 1. 1: Working principle of Optical Tweezers as presented in Ashkin's work in 1986 [8]. A collimated laser beam is tightly focused by a high NA objective lens. The rays A refract through the particle (circle) resulting in forces F_A. The net force on the particle, due to the refraction of both rays labelled A, is directed upward, towards the beam focus. The rays R_1 and R_2 represent scattered rays.

This approach requires dedicated and bespoke optical microscope configurations, and this reduces the flexibility of the tweezing device by introducing practical restrictions on the range of potential applications that could be demonstrated. The high NA approach also has sample limitations: Trapping in deep samples or trapping through turbid media can be challenging because of spherical aberrations in the optical trap and difficulties in forming a high intensity focus due to extreme scattering, respectively. The need for a high NA objective also restricts the field of view, so to achieve a larger field of view, a strict co-axial alignment between a lower NA imaging objective and the high NA tweezing objective, is needed. This leads to restricted movement and positioning of the sample stage.

Studies that aimed to address these restrictions suggested optical tweezing using optical fibres as an alternative approach in order to decouple the trapping optical system from the imaging system. Decoupling of the trapping system and the imaging lens can be applied to manipulation of cells and particles under a variety of microscopy modes, widening the variety of the potential applications [50-51].

In addition to decoupling the imaging optics from the trapping system, another factor that affects the range of the applications is the overall size of the system. In fibre-based trapping systems, a smaller fibre outer diameter allows the use of the system in a wider range of applications, for example decreasing the overall diameter of the fibre tweezer can lead to a less invasive device, useful for *in vivo* or *in situ* applications, or the use of smaller microchannels in a sample chamber and easier integration into lab-on-a-chip

devices. Additionally, a smaller device may enable a more portable device, or the use of multiple fibres in more complex trapping experiments.

1.4 Aim and objectives

The main aim of this thesis is the development and demonstration of a self-contained, portable, multicore-fibre trapping system that incorporates end-facet micro-mirror patterns to direct the guided light to form a tweezing location near the end of the fibre. This single fibre optical tweezing approach increases the flexibility of the trapping system as there is no longer a dependence on a high numerical aperture objective lens to create the trap. It gives the opportunity to easily combine optical tweezing of single cells in suspension with other generic microscopy techniques, since the need to modify the optical configuration of the microscope to incorporate a tweezing beam and associated optics is not required.

There is a clear need for an optical tweezer that is decoupled from the imaging system so that trapping is not always limited to the thin (~200 μm) samples restricted by the working distance of high NA objectives, nor limited in the field of view that is visualised whilst performing trapping. This thesis addresses this need by developing an optical tweezer on the end of a single optical fibre. The approach chosen is based upon the fabrication technique presented in [9], etching mirrors on the fibre cores so that the beam direction is changed due to total internal reflection (TIR). In this thesis a four-core fibre with machined mirrors is used to create a small diameter, single fibre optical tweezer.

The objectives of this research are to optimise the Focused Ion Beam (FIB) fabrication of the mirrors, build a robust, portable system capable of cell trapping and manipulation under different analytical microscopes, characterise the beam propagation characteristics, investigate potential stable trapping of some exemplar cell types, and quantify the trap strength.

To clearly state the terminology that describes the fibre-based trap of this thesis, and to avoid potential confusion throughout the chapters, a "tweezer", optical tweezer or OT means a conventional, microscope objective-based optical tweezer system. The machined, multicore fibre based tweezer/ 3D trap that is developed in this thesis will be referred to as the "MCF trap", and will sometimes be referred to as a two-beam or a four-beam trap depending on how many of the four cores of the multicore fibre are used.

1.5 Multicore fibre based trap

The main working principle of the MCF trap investigated in this thesis is based on the formation of a Total Internal Reflection (TIR) geometry at the end of the fibre, as previously proposed and demonstrated by Liberale *et al.,* in 2007 using a bundle of four optical fibres [9], and shown in figure 1.2.
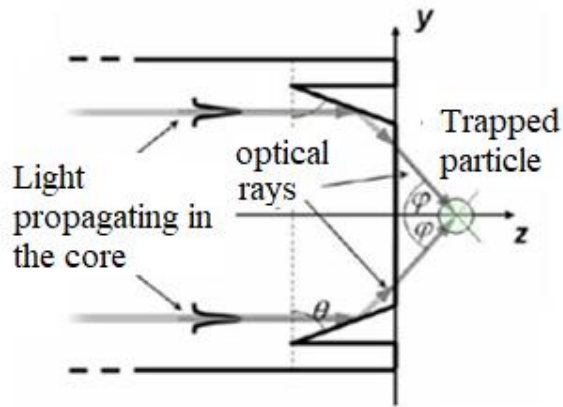
Figure 1. 2: Propagation of the laser beams as they exit the mirrored-shaped core facets. The beams undergo Total Internal Reflection when they hit the core-air mirror interface (image taken from [9]).

The light propagating in the core is totally reflected inside the fibre before it leaves the fibre at an angle, relative to the longitudinal axis of the fibre. In this thesis, Focused Ion Beam machining technology (FIB) is used to fabricate mirror-shaped facets on the end of the fibre aligned to the fibre cores. The light exiting the machined cores overlap in a region approximately 20 μm away from the fibre end. The trapping effectiveness of this type of machined multicore fibre has been tested by trapping yeast cells. Rapping of other exemplar cell types (with diameters ranging between 8-20μm) is also presented in this thesis.

Previous work described the use of four separate machined single-core fibres glued together in a glass capillary [9]. This demanded high precision in the assembly of the fibre-bundle, and as a result was a time-consuming fabrication process. In this thesis the replacement of the separate fibres with a single multicore fibre simplifies the preparation of the optical probe and increases the deployment flexibility of the trapping system. This thesis develops the techniques to fabricate, characterise and test these devices. FIB is used in preference to polishing or chemical etching to fabricate the mirrors due to its precision, flexibility and optical quality surface finish.

The fibre trap demonstrated in this thesis is a portable and flexible optical system, able to 3D optically trap and manipulate individual cells and particles, allowing the use of

this system together with additional microscopy techniques, such as Raman and fluorescent microscopes. A more detailed comparison between existing fibre based optical trapping systems and the fibre trap described in this thesis is discussed in Chapter 2.

Potential future applications that could be made possible by the features of the machined MCF optical trapping system developed in this thesis include:

- Isolation of a single cell to selectively deposit it on to a specific area of interest. Studies that aim to control patterning of cells in a 3D in vitro structure demands a precise deposition of the single cell in a specific position (e.g. stem cells sector) [52] and typically relies on 3D printing of tissues [53]. To add a single cell, or a small number of cells of a specific type to build or add to an in vitro 3D tissue structure, demands a small flexible 'tweezer' probe that can be inserted into a sample with care and can deposit a cell at specific sites in the sample.

- Characterisation and identification of a single cell. There are cases, where different cell types exist in the same mixture and they cannot be distinguished visually by microscopy. For this reason, where identification of the cell is needed, then the cell needs to be held stable under an analytical microscope, to be studied in isolation, away from other cells and substrates that may interfere with the signal, and without being damaged.

1.6 Thesis outline

A summary of each chapter of this thesis is given below.

Chapter 1 has provided an overview of the motivation to research and develop an optical trapping system based upon a single optical fibre and has introduced the concept of the machined multicore fibre trap.

Chapter 2 describes current applications of optical tweezing in biology as well as the conventional techniques used to accomplish them. The importance of studying single cells in isolation rather than a group of cells in order to avoid cell-to-cell or cell-to-substrate interactions is also discussed. Conventional optical tweezers are described in detail, followed by fibre trapping. Dual beam fibre traps are discussed before moving on to describe the methods of fabrication and applications of single fibre traps.

Chapter 3 explains the different fabrication methods for machining optical fibres on a micron resolution scale. Focused Ion Beam machining, which offers a route to the fabrication of the optical tweezing system in this thesis, is described in detail.

Chapter 4 presents the main experimental set-up assembly needed for the optical trapping and manipulation experiments as well as the fabrication processes of its main parts such as the microfluidic channels on the surface of the microscope slides and the fan-out device. Furthermore, the beams exiting the machined cores are also characterised in terms of propagation angles and divergence, so that the experimental values can be compared with the theoretically expected ones. In this way the mirror machining process can be also evaluated.

Chapter 5 explores the optical trapping of yeast cells using two machined cores and four machined cores of the same MCF. A comparison between these two traps is also presented in this chapter. The optical trap has been characterised in terms of efficiency and the beam propagation from the machined cores has been theoretically modelled. The work described in Chapter 4 and part of Chapter 5 has been published in Optics Express [54].

Chapter 6 demonstrates an initial aim to optically trap different types of cells and diverse particles, such as different mammalian cells, hollow glass spheres and bacteria. The use of the fibre trap with a commercial Raman microscope is shown and the Raman spectra collected from single trapped cells of different type are presented.

Chapter 7 discusses the main conclusions of this work and notes potential experimental future work of the machined multicore fibre-based optical tweezing system.

Chapter 2: Optical tweezing systems: Theory and applications

2.1 Introduction

The study of cell biology recognizes the cell as being an important structure of an organism and aims to understand it in detail. Many techniques have emerged to enable the detailed study of cells. Examples include i) new cell culture techniques, e.g. 3D cell culture [19], ii) microscopy techniques, from conventional light microscopy [55] to dark field [56], phase contrast [57], electron [58], fluorescence [59] and more recently super-resolution microscopy [60] and Raman imaging [61] and iii) cell handling techniques, as per discussion in Chapter 1.

Optical manipulation of cells, the focus of this thesis, has had an impact in many areas of cell biology (as mentioned in section 1.1). This includes determining cellular forces [13-15], control of cell-to-cell interactions [16-18], patterning of cell assemblies to build micro-tissues or micro-consortia [19], to sort [20-22], isolate [2, 24] and assist in the analysis [4-5] of cells.

However, conventional optical manipulation techniques depend on microscopy to trap and image simultaneously, thus the imaging microscope is constrained as it has to provide the manipulating beam and to collect the relevant image information. For example, in cases where it is required to count cells, or simply see a cell without much detail, then a bright field image may be sufficient. For more advanced analysis, for example to identify a specific cell for isolation from the rest of the group by its fluorescent signal, or for experiments to understand the chemical composition of a cell, then fluorescent microscopy and Raman microscopy is needed, respectively.

2.1.1 Fluorescence microscopy and optical tweezers

Where the experiment demands collection of a fluorescence signal (for identification) and optical trapping at the same time, then an optical tweezing system with fluorescence is required. Work that has demonstrated this has been published [62], however the technique that is used in this work that is based on a microscope objective to trap, and results in imaging limitations due to the small field of view arising from the high NA objective required for OT.

Only a single cell or a small number of cells can be visualised at one time using a high NA imaging objective. If the cell to be trapped is rare then a larger field of view,

capable of imaging hundreds or thousands of cells would be desirable to help locate it. For this reason, a more flexible trapping system may offer benefits to overcome such restrictions.

Further techniques such as Total Internal Reflection Fluorescence Microscopy [63-64] and confocal microscopy [65], have had OT incorporated into the microscope to help constrain the test sample. The combination of microfluidics and optical tweezers with epi-fluorescence microscopy to enable the analysis of rapid cytological responses in single cells have also been reported [25].

In all the above cases, where the experiment requires both trapping of cells and simultaneous imaging, the imaging objective is the same as the trapping objective. To extend the variety of the potential applications, the ability to decouple the trapping optics from the imaging optics would in turn allow the use of smaller NA imaging objectives to offer a larger field of view and the capacity to image at greater depths. A possible solution is a portable optical fibre based trapping system that can be used under any microscope. This offers enhanced flexibility compared with building a bespoke microscope setup, offering control of a trapped particle that is independent of the imaging optics.

2.1.2 Raman micro-spectroscopy and optical tweezers

Raman spectroscopy is a vibrational spectroscopy technique that provides specific information about the chemical structure of a molecule, by observing the Raman spectral "fingerprint". When combined with OT systems, it can provide the Raman spectrum of a single, trapped cell, since the cell can be 'grabbed' and isolated from the surrounding cells and the glass or plastic substrate [4, 5, 67-68], but at the expense of requiring a sophisticated bespoke Raman Tweezers system, where the Raman beam and Tweezing beam share the same objective lens , or are the same beam.

2.1.3 An imaging microscope

The basic structure of an imaging microscope, a key piece of equipment for a cell biologist, consists of an illumination source, where LED sources are becoming increasingly common, an objective lens that can vary in magnification according to the potential applications, a camera to capture the image and a structure to support the

sample that is going to be imaged (known as the sample stage). A simple configuration is represented in figure 2.1 below:
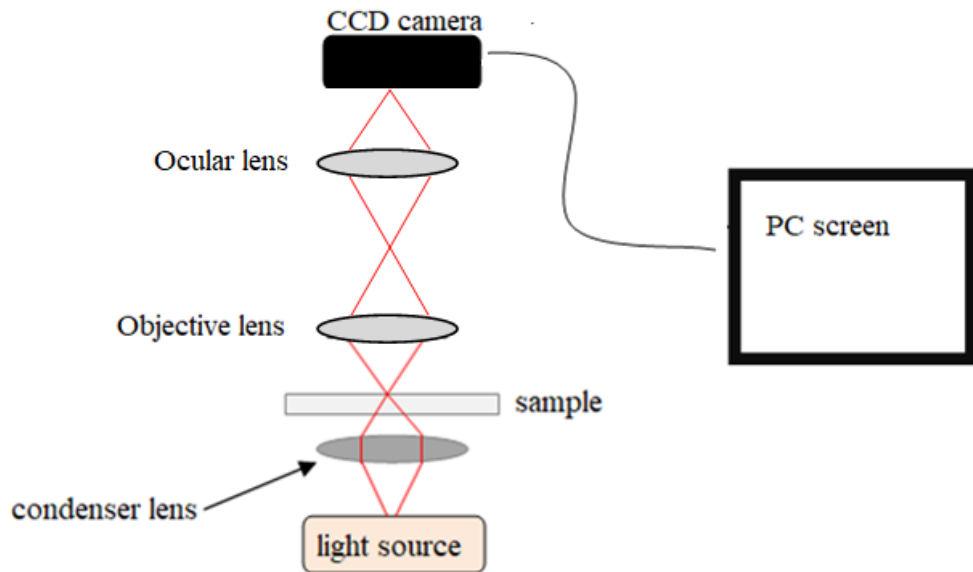
Figure 2. 1: Typical configuration of an optical microscope.

As the above diagram indicates, the light emitted from the light source is focused through a condenser lens onto the specimen (sample). The transmitted light from the sample is collected by the objective lens and focussed by the eyepiece (ocular) lens on the camera detector (CCD camera). This can be displayed on a screen or recorded for further analysis. This basic compound microscope can be modified with the addition of a laser beam and a few optical elements to make an optical tweezers system. However this is not always possible, especially in the case of commercial, enclosed, microscope systems. A conventional optical tweezer system is described below after the theory of optical tweezers.

2.2 Theory of optical tweezers

Optical Tweezers is a technique that uses a highly focused laser beam to optically trap, and manipulate microparticles. Assuming no absorption, the particle experiences a net force when it encounters a tightly focused laser beam. The net force is made of two components; a scattering force due to the scattering of photons from the particle, and a gradient force that is created due to the intensity gradient of the beam, which draws the particle into the highest intensity region of the beam, namely the beam focus. Both scattering and gradient forces depend on the wavelength of the laser beam (λ) and the particle size (radius, r) and the refractive index difference between the particle and the

surrounding media. Optical tweezing can take place in two regimes according to the relationship between the particle size and the wavelength of the laser beam: Mie regime (r>>λ) and Rayleigh regime (r<<λ). The Mie regime is based on Ray optics and refers to the case of having a particle that is up to 10 times larger than the trapping laser wavelength and a single beam can be traced through the particle. The Rayleigh regime refers to the case where the particle is smaller than the wavelength and can be described as a dipole that follows Rayleigh approximation. In this thesis the case of interest is the Mie regime (Ray optics approximation), as the wavelength used for optical trapping is 975 nm and the range of the trapped particles are biological cells, with diameters between 2-20 μm.1

2.2.1 Geometric ray approximation

In the Mie scattering approximation, the particle is generally considered as a transparent sphere, or lens, of higher refractive index than the surrounding medium, and larger than the wavelength of the trapping laser. The optical forces can be modelled using simple ray geometry. The incident laser Gaussian beam can be analysed by considering individual rays with appropriate intensity, momentum and direction. These rays propagate in a straight line within uniform, non-dispersive media and can be described by geometrical optics. Any ray carries momentum,p, given by

$$\mathrm{p} = \frac{n_{medium}\ P}{c} \qquad (2.1)$$

where the optical power of the light (P) travels in a medium with refractive index equal to n_{medium} and c is the speed of light in a vacuum [69].

Refraction of the incident light (rays A and B in figure 2.2) by the particle introduces a change in the momentum of the light, shown by the change in direction of rays A and B. Considering Newton's third law, this momentum change imparts an equal and opposite momentum change to the particle, which is translated into a force on the particle that is proportional to the light intensity (grey arrows A' and B', with the length of the grey arrows representing the magnitude of the force), resulting in a net force on the particle (blue arrows). In the case of a particle with higher refractive index than the refractive index of the surrounding medium, the optical force caused due to the refraction is towards the direction of the intensity gradient. Similarly, when the refractive index of the particle is lower than the medium index, the force is away from the highest intensity region.

Figure 2.2 (a) shows two peripheral rays from a tightly focused Gaussian beam and their refraction through a sphere of higher refractive index than the surrounding medium (paraxial rays are not shown). The rays undergo refraction and a change in momentum, resulting in a net force (blue arrow) which acts upwards towards the beam focus. This is the axial gradient force and acts to draw the sphere in the axial direction towards the highest intensity region. There is also a scattering force that acts on the sphere due to the change in momentum of photons scattered by the sphere. A trapped particle is held in an axial equilibrium position, close to the beam focus, where the scattering and gradient forces are balanced.

In figure 2.2 (b) a high index particle is shown to be at the periphery of a Gaussian beam. The intensity profile of the Gaussian beam is shown at the top of the figure. Two example light rays of different intensities A and B (represented by lines of different thickness) are shown to be refracted by the particle. Each of the rays refracts at the sphere surface and this leads to a change in direction of the rays, thus a change in momentum. The change in momentum of each ray, A and B, therefore results in a force on the sphere, shown by grey arrows A' and B' in the figure. The net force on the sphere is also shown, represented by a blue arrow. The gradient force component is directed into the highest intensity region of the Gaussian, whereas the scattering force component is along the direction of beam propagation.

Optical tweezers is a 3D gradient force optical trap, with lateral (or x-y) trapping due to the Gaussian intensity profile of the beam (show in figure 2.2(b), and axial (z trapping) due to the intensity gradient in z from tight focussing of the beam (shown in figure 2.2(a)).
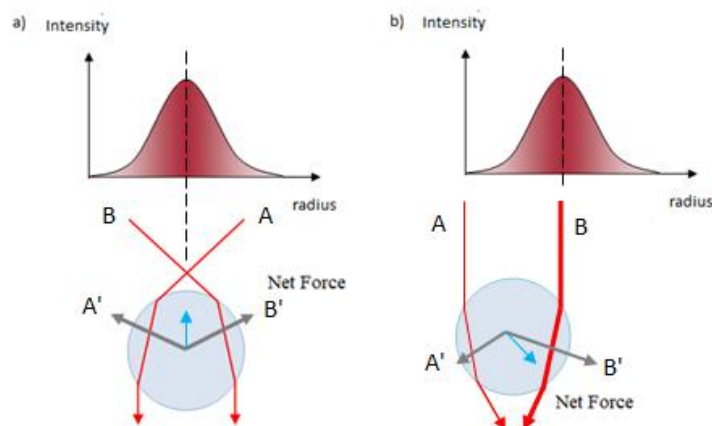
Figure 2. 2: a) Beam of light (red arrows) passing through a particle of refractive index n1 in a medium of refractive index n_{medium}. Here . we have axial trapping, which arises from tight focusing of the beam. b) Lateral trapping caused by using light with a gradient in the intensity profile (i.e a Gaussian beam). Two rays, A and B, of different intensities, represented as different line widths. The blue arrow indicates the restoring net force which in this case pushes the particle towards the highest intensity region of the beam.

2.2.2 Advanced imaging with optical tweezers

The majority of optical tweezers studies use the same objective lens to image and trap the particle, regardless of whether the optical tweezer is integrated into a commercial microscope, or if the tweezer and imaging system are custom built. A typical configuration for a microscope-based optical tweezers is depicted in figure 2.3.
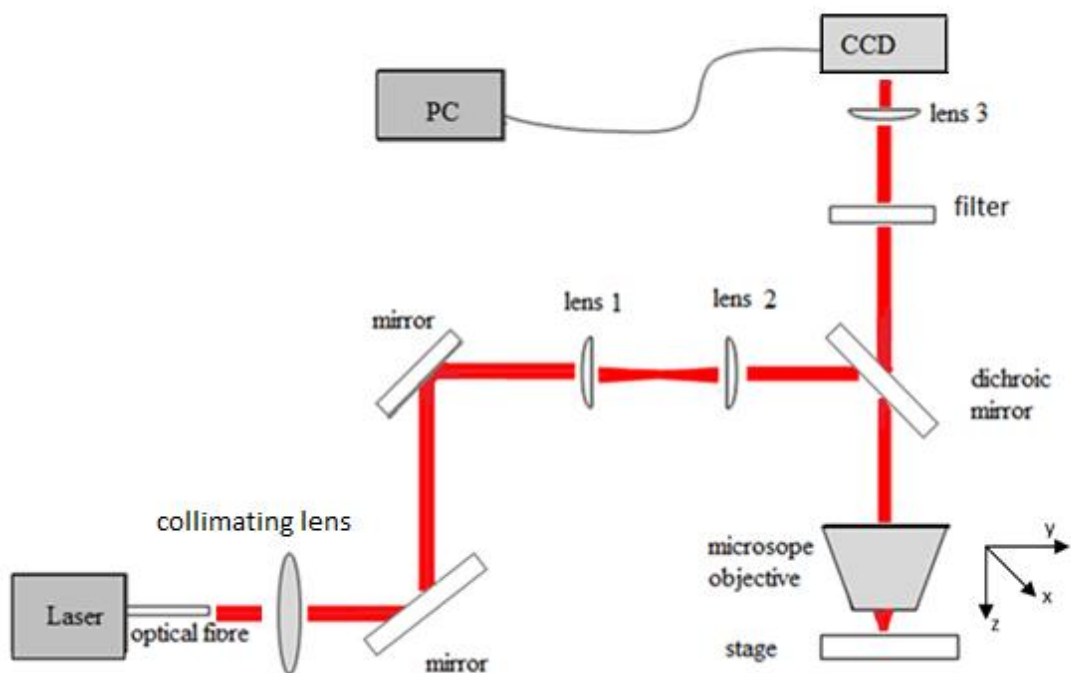
Figure 2. 3: Microscope-based optical tweezers set-up. The objective lens used for imaging and for trapping is the same. The red arrows indicate the trapping laser beam path and the blue arrows indicate the microscope beam path.

A similar approach has been used to incorporate optical tweezers into fluorescence or Raman microscope systems. Figure 2.4 shows a schematic of a fluorescent microscope with an integrated optical tweezer. In this case a HG (Mercury) arc lamp, an excitation filter and a dichroic mirror and emission filter are used to excite the labelled particles and image the emission [64]. In some cases, where an appropriate wavelength is used, the same beam is used for both trapping and excitation [4].
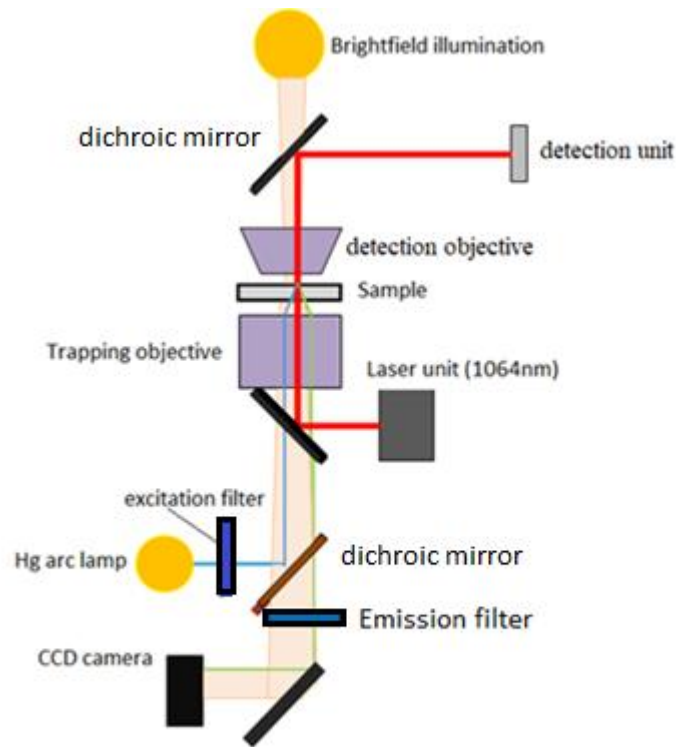
Figure 2. 4: Fluorescence microscope integrated with optical tweezing system. The red line indicates the path of the trapping beam. The blue line indicates the excitation beam, and the green line indicates the path of emission from the fluorescent particle.

However, the above-mentioned setups suffer from limitations in the variety of potential applications due to the restricted field of view as long as the microscope objective that is used for imaging, Raman, or fluorescent signal measurements is also used for trapping. Once again, decoupling of the imaging/measurement system from the trapping system would provide benefits in a range of potential applications.

To overcome these restrictions, a fibre-based optical trapping system has the potential to remove the trapping beams from the imaging system. Then a lower NA objective lens (or suite of lenses) for imaging to provide larger field of view to visualize more of the sample and deeper in the sample could be used. Furthermore, there would be reduced or no need for expensive parts (such as high specification lenses and mirrors) to build a bespoke specialist microscope because a fibre-based trapping solution could be used under a variety of microscopes, for example commercial fluorescence or Raman microscopes. Scattering due to the trapping beam may affect the image produced, so a filter before the camera may be the only additional optical element required in the microscope system.

The work in this thesis focuses on techniques that exploit optical fibres to deliver optical forces to trap and manipulate single cells and particles without modifying the microscope optical imaging system.

The benefit of the approach developed in this thesis is that it provides a flexible tool to combine microscopy and tweezing such that cells can be optically trapped or manipulated under a completely decoupled imaging system. The imaging system may be a custom-built, commercial, or state-of-the-art facility microscope, whilst the optical manipulation system is portable, can be incorporated into lab-on-a-chip devices and is capable of manipulating a variety of cell types from bacteria or yeast cells to mammalian cells.

To put this in context, a review of the key points of the development of optical trapping experiments based on conventional optical tweezers (where the laser trapping beam is focused through a microscope objective lens into the sample) and on optical fibre traps over the years, is presented.

2.3 Optical manipulation and optical tweezers

As Pyotr Lebedev proved experimentally in 1900, light is electromagnetic radiation which imparts pressure (a force) onto any surface exposed to it [70]. We now know this is due to photon momentum. Such interactions between electromagnetic radiation and matter via absorption and reflection can be denoted by the term ''radiation pressure''. Initial studies focused on the implementation of the scattering force to accelerate particles and to levitate them, and they described the need for a counter propagating force in order to stabilize the particle and hence optically trap it [8]. Counter propagating forces include gravity, an electrostatic force, or two opposed optical beams.

With the invention of the laser source in the 1960s, capable of providing a high intensity beams, new applications that made use of radiation pressure emerged. Laser sources presented significant advantages in comparison with conventional light sources, in particular their ability to focus their beam tightly, with a spot size on the micrometer scale.

This provides a high intensity which can import a meaningful force on micron-scale particles. Upon this critical point the basic idea of optical manipulation was formed, and was theoretically and experimentally tested by Ashkin, in 1970 [64] with the

demonstration of the acceleration of particles due to the scattering force in the early 1970s [8].

This first observation was the acceleration of transparent latex spheres of micro-meter diameters (0.59 - 2.68 μm) freely suspended in water, due to optical forces from a 515 nm wavelength visible laser beam, using milliwatts of power. Shortly afterwards, the first successful three-dimensional optical trap using two opposed, lightly focused 515 nm lasers was reported [64]. The same group in 1986 moved on to the demonstration of 3D optical trapping using a single tightly focused beam of 515 nm wavelength [8]. In this configuration the particle was drawn toward the maximum intensity region; the beam focus. Its equilibrium position was slightly below the beam focus, where there was balance between gradient optical forces and scattering optical forces. The significance of this work was formally recognised when Arthur Ashkin won 1/3 part of Nobel prize in Physics for the invention of Optical Tweezers (OT) and its applications in biology, in 2018 [71].

Optical Tweezers have seen widespread applications, such as building microstructures [72], particle confinement [10], cell sorting [20, 23,73-75], characterization of cellular mechanical properties [76-78], force measurement [79], spectroscopy [80-81], single molecule force spectroscopy and cell transportation [82-84]. Most of these experiments make use of a laser beam focused through a high NA microscope objective lens - a conventional, microscope based optical tweezer.

2.4 Fibre based optical traps and their applications

Conventional OTs rely upon the use of a high NA microscope objective in order to tightly focus the light and generate the necessary high intensity gradients in x, y and z, and thus stably trap the particle in the highest intensity region. However, this approach imposes restrictions on the variety of the potential applications due to the lack of flexibility of the microscope objective. To overcome these restrictions, studies that employ optical fibres instead of a microscope objective to deliver the trapping light are emerging [84].

In the 1990's replacing the microscope objective with optical fibres to deliver the trapping light was firstly demonstrated by Constable *et al.* [81], where the authors describe the use of two diverging, counter-propagating beams to optically trap a particle stably in 3D, as illustrated in figure 2.5. The replacement of the conventional OT, where the light is tightly focused, with fibres where the optical power is spread over a larger

area, leads to a less intense trapping beam and potentially less damage to a trapped particle. In Constable's study [81], the particle is trapped at the point where the optical forces are counter balanced.
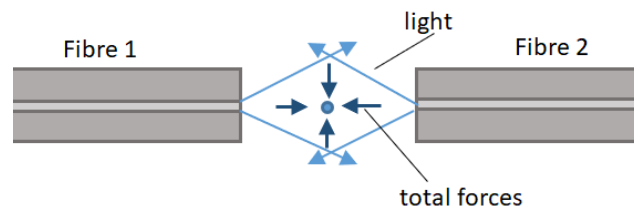
Figure 2. 5: Beam propagation in a two "counter-propagating" fibres experiment. The two fibres are configured with their cores aligned along a common axis. The particle is trapped at the point where the optical forces balance [81].

In figure 2.5 the gradient force (vertical dark blue arrows) due to the intensity gradient of the Gaussian beam draws the particle into the common axis of the fibres. The particle is held in a stable position between the two fibres due to the opposing scattering forces from the two beams (horizontal dark blue arrows).

This counter-propagating fibres based technique has been applied in studies such as cell stretching [1,85] whereby a cell is trapped and increasing laser power stretches the cells, with applications in understanding how cells mechanical properties are related to their biological functions [13] and cell rotation where a Gaussian beam from the one fibre and a rotating asymmetric mode from the opposed fibre [86] rotates the trapped cell to improve imaging. The dual beam fibre trap arrangement has also been shown to hold large structures such as 50 μm cells or linear arrays of multiple particles for trapping using Raman light [5]. The analysis of the optical forces of this type of trap is similar to the analysis of the forces of the conventional OT, with the difference due to the presence of two counter propagating beams. More specifically, the Gaussian beam intensity profile draws the particle into the same axis as the fibres and the scattering forces hold it in place between the two fibres.

An example of dual beam fibre trapping [9], is two opposing fibres delivering non-focused laser beams that induce forces additive on the surface, resulting in an overall force of zero acting on the particle. However, the different forces applying to different regions of the particle lead to the construction of the ''optical-stretcher'' device, which is able to stretch the particle along the beam axis. This device is applied to extended elastic objects such as cells, where the transfer of momentum of light occurs on the surface of the object. A major application of this device is the measurement of viscoelastic properties of materials including biological cells. This work studied the

deformation of human erythrocytes and mouse fibroblasts while other projects have made an impact in studying the differentiation and change in deformability between different stages of cancer progression [77].

Another approach for making an optical stretcher that aimed to overcome the limitations that the strict alignment of the fibres imposed, was to replace the fibres with optical waveguides. This approach demonstrated optical stretching of white blood cells using microfluidics and optical waveguides that were directly written into bulk glass by femtosecond laser pulses [87]. However, the use of waveguides, although it overcomes restrictions on the strict alignment of the fibres, does not provide flexibility in the trapping system. In applications that may require the deformability of the cell but at the same time the translation or rotation of the trapped cell, the waveguides cannot move together with the trapped cell as a 'free' fibre could inside a sample chamber or microchannel. At this point, it should be noted that high-throughput real-time deformability testing no longer uses optical stretching. Nowadays, hydrodynamic stretching [88] flowing the cells quickly through microfluid constrictions, is more widely used. Optical stretching is more common for small numbers of cells and in cases that the analysis demands other techniques to be carried out at the same time for example fluorescence or Raman imaging.

A study that aimed to demonstrate optical trapping of cells using a different fibre geometry allowing higher flexibility of the system was published in 2009 by Liu *et al*. [89]. As shown in figure 2.6, the design was two optical fibres with an angle between them:
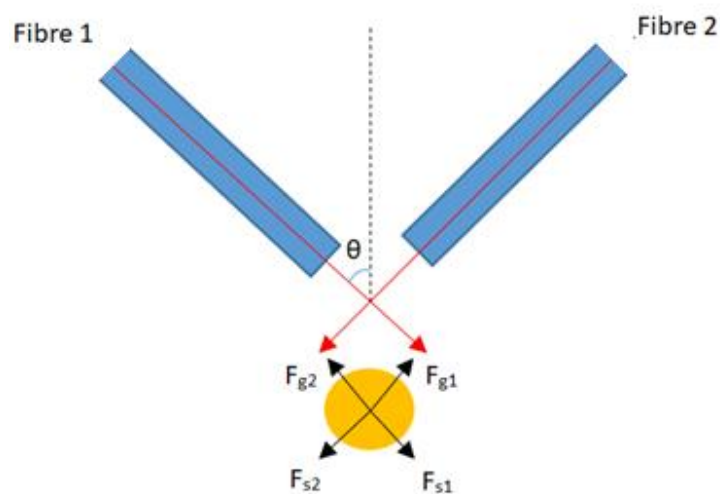
Figure 2. 6: Two inclined beams for optical trapping. The particle trapped at the point in the beam overlap region where the sum of all the forces is equal to zero (figure adapted from [89]). F_g and F_s are the gradient and scattering force respectively for ray diverging out of fibres 1 and 2.

Each individual fibre exerts an optical force upon the microparticle that can be resolved into a gradient and a scattering force. The gradient forces, due to the Gaussian intensity distribution of the beam, are shown as F_{g1} and F_{g2} in figure 2.6, and the scattering forces, F_{s1} and F_{s2}, due to the light exiting fibre 1 and 2, respectively. Typical optical forces are of the order of picoNewtons (pN). The scattering forces act in the direction of beam propagation while the gradient force is directed towards the higher intensity region of the Gaussian beam distribution. The particle is trapped in 3 dimensions at the point where the sum of all forces acting upon it is zero, which occurs in the region where the two beams overlap. In this way, there is free space between the fibre-end and the trapping area that permits the non-contact manipulation of particles of diameters less than tens of microns using optical access from only one side as opposed to counter propagating beams described above. Here, the angle of inclination between the two fibres has a threshold above which the trap is stable. Although optical trapping has been successfully demonstrated using this approach, this system still requires a careful positioning of the fibres and this imposes restrictions on the potential applications that would benefit from a more flexible optical system.

The use of a single fibre-based trap is expected to increase flexibility of the system compared to a dual fibre trap. The first single fibre trap was presented by Taguchi *et al.* [90] in 1997. This demonstrated optical trapping by using a focused beam emitted from a single tapered fibre with a spherical end 'lens' with a radius of several micrometres. The concept is depicted in figure 2. 7. The fibre shape brings the beam to a focus at a distance of 20 µm from the end of the fibre. Although the single fibre system had the flexibility to translate the trapped cell in the sample chamber, the yeast cells were trapped and they could be translated in 2D.
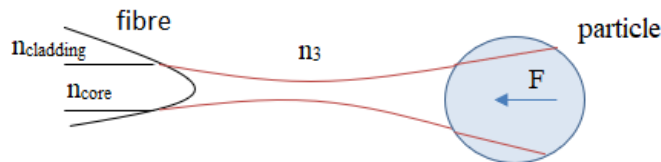
Figure 2. 7: Spherically tapered fibre used for particle trapping [90]. Polystyrene microsphere of 10 µm diameter immersed in water was trapped by a semiconductor laser beam, with minimum optical power 1.3 mW, where n_{core}, $n_{cladding}$ and n_3 are the refractive index of core, cladding and surrounding liquid, respectively. The gradient force due to the focusing of the beam draws the particle towards the fibre tip, as shown by the blue arrow.

The first example of a single fibre trap capable of 3D optical trapping was published by Taylor and Hnatovsky in 2003 [91] who developed a partially metalized, hollow-tipped, tapered fibre by selective chemical etching, with the resulting end tip feature shown in figure 2. 8. The height of the conical structure is 3 μm and the depth of the hole is 1 μm. The light pressure of the annular beam exiting the tip produces a scattering force that pushes a particle away from the tip, which is balanced by an attractive electrostatic force towards the tip, creating a stable 3D trap [92].

The particles trapped in this study were 2 μm solid glass microspheres immersed in water and the trapping distance from the fibre face was 1 μm. This poses restrictions in applications that include particles bigger than 3 μm in diameter, due to the inevitable physical contact with the probe, and at the same time is a demanding technique that requires the need of a well-controlled external electric field.
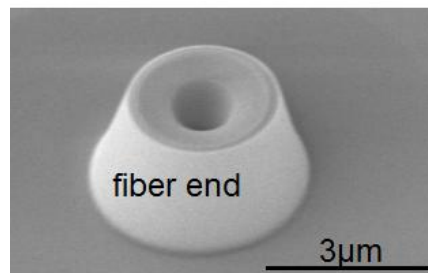
Figure 2. 8: Scanning Electron Microscopy image of a hollow tip end fibre [91]. A force created due to the annular beam of light pressure is balanced by an electrostatic force that acts towards the tip and that leads to the formation of a 3D trap.

The trapping distance was controllable in the work of Tam *et al.* [93] where a fibre-bundle probe was used to optically manipulate cells and particles in two dimensions. Step-index and graded-index fibres with NAs of 0.65 and 1.00 respectively, were used in their study. The final bundle included 50,000 fibres and each fibre was fabricated to have a lens element at its end-face to focus the light to a defined trap. The fabrication of the lens pattern was realised in three different ways: by chemical etching of the step-index fibre bundle to create wells and by depositing ball lenses into these wells, by fabricating a lens-shaped pattern on the end of each fibre, or by using a fibre bundle that consists of a gradient index material that makes each fibre self-focusing. Here, the number of optical traps that was formed is relative to the number of optical fibres in the fibre bundle, and a dense array of optical tweezers can be created. The number of the illuminated fibres depends on the magnification of the focusing objective and in this way by using different combinations of lengths; the size of the trapping area could be adjusted respectively. However, it should be noted that fibre traps similar to this that

include such high number of fibres requires a complex and time-consuming preparation process.

In 2013, a study that demonstrated stable trapping and manipulation of a 1 µm diameter polystyrene microsphere immersed in water, using both single and dual single-core fibres design was presented [94]. The optical fibres were tapered through aqueous hydrofluoric acid chemical etching in order to create a taper angle of 15° and tip diameters of 60 nm as illustrated in figure. 2. 9.
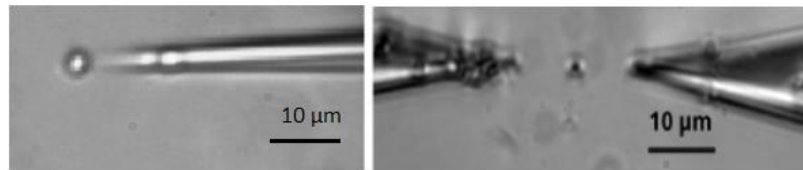
Figure 2. 9: Single and Dual nano-tip optical trapping design (images taken from [94]).

The beam profile as described in this work was reported to be Gaussian. Using a single fibre, particles were trapped very close to the tip end or in some cases stuck to the tip, using the gradient force along the axis of propagation. To achieve more stable trapping, and to increase the trapping distance away from the tip end, optical trapping experiments using two opposed etched-tip fibres was reported (Fig. 2. 9), where counterbalanced scattering forces were used.

In addition to the previously mentioned studies, other methods to modify fibre tips have been reported [95-99]. These included fabrication of axicon tips that were used to both trap and lyse mammalian cells [95] as well as fabrication of different polymeric structures at the fibre tip [96]. More recent work on multimode optical fibres has been presented by Cizmar *et al.* [97-98] to optically trap micro-particles using both static and dynamic intensity patterns, and in a similar way by Bianchi *et al*. to transmit digital holograms to image and optically trap 2 µm fluorescent beads [99]. However, this technique demands complex trapping pattern set up and programming. Cizmar *et al.* described as a first attempt in 2011 optical trapping and confinement of microparticles using multimode photonic crystal fibres [97]. Here, particles could be confined in the static intensity pattern that is formed by the superposition of several output modes. They could be manipulated by applying SLM modulation masks at the input fibre face, to control the arrangement of the output modes. However, this approach was limited to two-dimensional trapping.

A significant development in the field of fibre-based optical traps was the micro-fabrication of beam steering mirrors onto the fibre end-face. The first example of this was from Liberale *et al.* [9]. In their design, four single-core optical fibres with beam steering mirrors on their end-face were glued together and placed inside a glass capillary in order to form an optical probe capable of 3D trapping of a polystyrene bead, at a distance 35 μm away from the fibre end. A schematic of the concept and a micrograph of the end face is given in figure 2. 10. However, this concept demands high precision in manufacturing and alignment of the single core fibres inside the glass capillary, and the outer diameter of the probe ultimately reaches the millimeter scale, limiting its use in applications that require a small probe size. Furthermore, applications that require a flexible probe that can easily move inside microchannels, may not be realised using a rigid, large fibre trapping system similar to this.
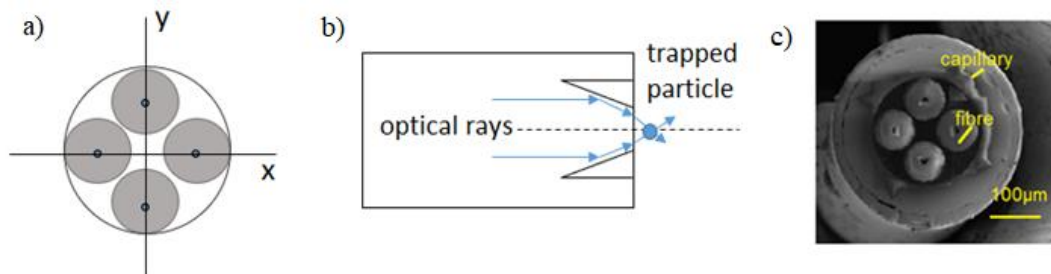
Figure 2. 10: a) Cross section of a bundle of four micromachined fibres, b) Beam propagation of the guided light exiting the mirror-shaped fibre facets on diagonally opposite cores, c) SEM image of the machined fibre-end facets cross section [9].

A further development came by exploiting two-photon lithography to fabricate micro-prism reflectors on the fibre-end of a fibre bundle of the same size as the Liberale probe, as shown in figure 2.11 [100], to trap a cell within the overlapping region of the beams.
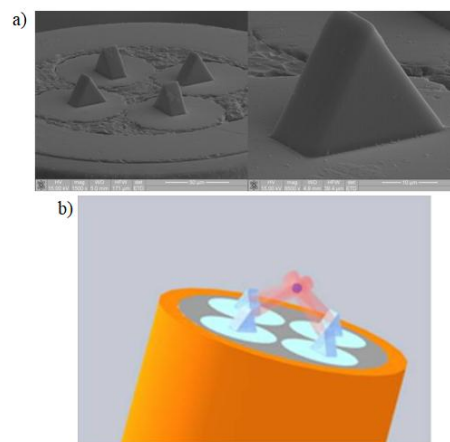
Figure 2. 11: a) Micro-prism reflectors on the fibre-end fabricated using two-photon lithography [51], b) Isometric representation of the four reflectors while trapping a particle on the overlapping area of the four beams, as described in [100].

To increase flexibility and to decrease the overall size of a single probe trapping system, the use of multicore fibres instead of fibre bundles started to be investigated. At approximately the same time as the fibre bundle was presented by Liberale *et al.* [100], Yuan *et al.* presented work that used a single, two-core (or twin core) fibre. Fusing and drawing were used to taper the fibres and this formed a small angle between the cores towards the tip which allows the electric field to cross and diverge [101]. This structure is the basis of a Mach- Zehnder interferometer. The two beams, which are represented as green and blue in figure 2. 12, have opposite optical phases.
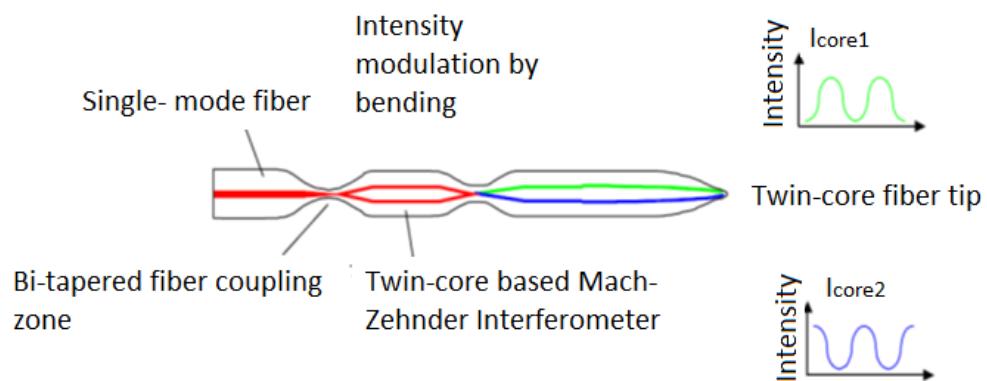
Figure 2. 12: Two-core fibre connected with Mach-Zehnder interferometer (image taken from [101]).

The wavelength of the laser beam in this experiment was 980 nm. Figure 2.12 shows a schematic of the experiment. Once the two fibres were spliced together (the single-core fibre with the double-core fibre), they were heated and drawn to bring the cores together in the 'bi-tapered fibre coupling zone' shown in figure 2.12. Following the same process, a twin-core fibre was spliced with the same two-core fibre to fabricate a Mach-Zehnder interferometer. The purpose of that interferometer was to modify the intensities of the two beams by bending the interferometer and thus to control the trapped cell orientation. The main advantages of this approach were the low optical powers required in the OT (less than 5 mW), and the small optical fibre tip size (3-5 μm in diameter). As the authors stated in their study, this configuration could be suitable for a potential integrated on-chip optical tweezers. However, the geometry means that the trapping distance was very close to the tip end, similar to earlier single core tapered fibre traps, and the trapped cells risked becoming stuck to the tip surface. Furthermore, the need to bend the fibre to control the power and the trap position is not very practical for trapping experiments.

In 2012, a new approach that combined the properties of the multicore fibres with the lensing of the fibre end-face, was presented [102]. Multicore fibres with four cores of 7 µm diameter each, with diagonal spacing 113 µm and core-core spacing 80 µm were used. The laser light used was a 1047 nm wavelength from a Nd: YLF laser (Fig. 2.13).

The lensing of the fibres was realised using a fusion arc splicer, which represents a fast, safe, affordable, and easy-to-handle way to modify a fibre end-face, compared to other techniques such as Focused Ion Beam (FIB) technology or chemical etching.
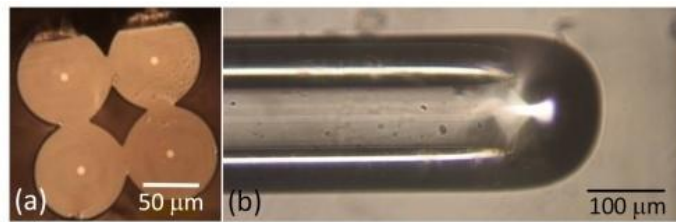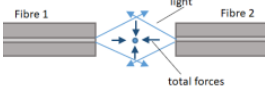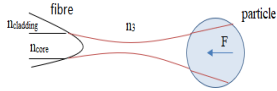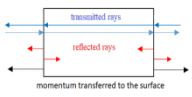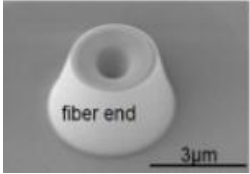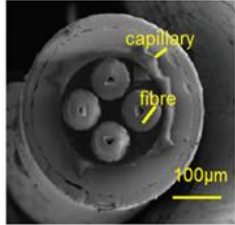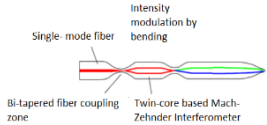
Figure 2. 13: Lensed multicore fibre fabricated through fusion splicer, to demonstrate optical trapping of a particle (taken from [102]).

An overlapping trap region in the far field due to light exiting the diagonal cores was noted. The position of that overlapping area varies depending on the surrounding medium. For example, when the surrounding medium was air then the distance away from the fibre-end was 250 µm, whereas when the medium was water the distance was 500 µm. When used with a coherent light source, this overlap of light from two diagonal cores results in generation of fringes in a large trapping region. Interference of light from four cores creates a lattice pattern. Arrays of one micrometre polymer spheres and *E. coli* bacteria have been trapped in the optical fringes and lattice, but only in 2D, against the surface of the sample chamber. Full 3D manipulation of a single particle was not demonstrated.

To summarise approaches to fibre trapping, Table 2.1 below, presents the key research developments in optical trapping using optical fibres, following chronological order:

Paper authors	Year	Trapping configuration	Main advantages	Main disadvantages
Constable *et al.*[81]	1993	Two-opposed fibres	Stable 3D trapping. No special or complex optical system required.	Restricted flexibility of the system. Precise alignment of fibres needed.
Taguchi *et al.*[90]	1997	Single etched tip fibre	Single fibre based optical system. No demanding preparation of the fibre tip.	2D trapping only (manipulation against a surface).
Guck *et al.*[13]	2001	Two-opposed fibres-Optical stretcher	Stable 3D trapping. No special or complex optical system required.	Restricted flexibility of the system. Precise alignment of fibres needed.
Taylor *et al.*[91]	2003	Single hollow metalized tip fibre	Single fibre based optical system. First 3D trap using a single fibre.	Restrictions in the cell diameter that can be trapped (up to 3µm). Need for an external electric field. Complex fabrication that requires several steps.
Liberale *et al.*[9]	2007	Bundle of machined fibres	Independent control of each of the cores.	Demanding preparation of the optical system. Large fibre diameter.
Yuan *et al.*[101]	2008	Twin core fibre	Small optical fibre tip size (3-5 µm in diameter).	Restrictions in the size of the cell that can be trapped. Need for bending of the fibre for variation of the power which is not practical.
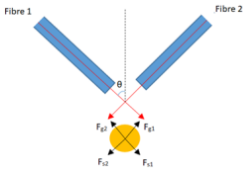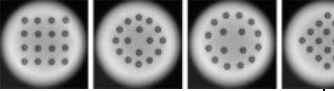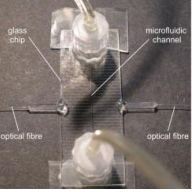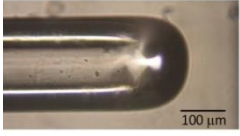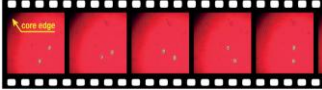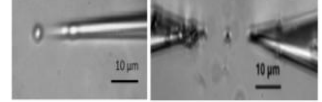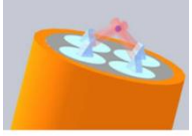
Liu *et al.*[89]	2009	Two inclined fibres	No need for the strict alignment of two opposed fibres.	Restricted flexibility of the system.
Cizmar *et al.*[97]	2011	Single multimode fibre	Allows complex optimization and manipulation through turbid media.	Demand for complex trapping pattern set up and programming
Bellini *et al.*[87]	2012	Two-opposed waveguides	Excellent alignment of opposing beams.	Restricted flexibility of the system. Microfluidic control of particle delivery required.
Barron *et al.*[102]	2012	Lensed multicore fibre	Fast, safe, affordable, and easy-to-handle machining process of an optical fibre system.	Not suitable for single cell trapping. 2D trapping only (manipulation against a surface).
Bianchi *et al.*[99]	2012	Single multimode fibre	Interactive holographic micromanipulation of micron sized beads. the same fiber can be used as a probe for scanning fluorescence microscopy	Not suitable for 3D control of manipulation.
Decombe *et al.*[94]	2013	Single and dual nanotip fibres	Very small size of the optical fibre tip (60nm).	Restrictions in the size of the cell that can be trapped. Trapped cell contacts tip risking physical damage.
Liberale *et al.*[100]	2013	Microprisms fabrication on fibre bundle	Independent control of each of the cores.	Restricted flexibility of the system due to large fibre diameter.

Table 2. 1: Summary of significant fibre-based optical trapping systems.

This review chapter has considered the use of optical traps and optical tweezers (OT) to hold and manipulate particles. A range of applications have been discussed where optical manipulation is an increasingly useful tool in supporting these studies. Difficulty in combining in-line optical trapping via the imaging optics can lead to restrictions in the breadth of applications to which it can be applied. By delivering the OT functionality via optical fibres there is a potential increase in flexibility. In the review trapping using single fibre modifications, dual fibres, fibre bundles as well as multicore fibres have been discussed. In this thesis it is proposed that multicore fibres offer a prospect for highly flexible single particle trapping systems.

2.5 Machined multicore-fibre based traps

An optical tweezing system based on the fabrication of micro-mirrors on the end-face of a multicore fibre (MCF) is explored in this work. The motivation for this approach is the need for a flexible, physically small and portable optical trapping system that is able to stably trap and manipulate micro-particles and cells under any microscope, overcoming limitations associated with the need for delivering the trapping power via the microscope imaging optics.

The working principle illustrated in figure 2. 14 focuses on the manipulation of the light delivered by the cores of the multicore fibre in such a way that they can be focused and act as a conventional high NA OT system. If the angles of the fabricated mirrors are slightly higher than the critical angle, then the beams undergo Total Internal Reflection (TIR) and they overlap (or 'focus') close to the fibre-end. As can be seen in figure 2. 14, which for simplicity depicts only one core of a multicore fibre, θ_{prop} is the propagation angle, related to the fibre end-face axis and φ is the angle related to the fibre axis (black dashed line). Controlling the mirror angle θ_{mir} will in turn control θ_{prop} and hence the trapping distance from the fibre end (d_{trap}). The full theory is described in Chapter 4.
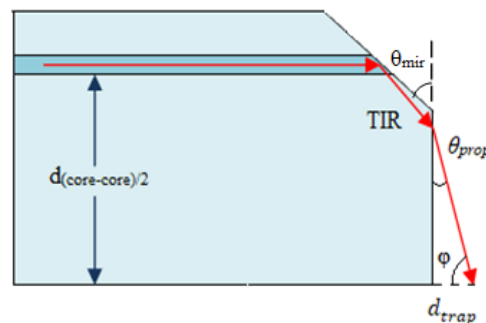
Figure 2. 14: Propagation of the laser beam resulting from the end facet mirror. The beam undergoes TIR when it reaches the fibre core-air interface and is redirected close to the fibre end atan angle ɸ with respect to fibre axis.

In this thesis, optical trapping of yeast cells, red blood cells, mammalian cells and characterisation of the trap has been demonstrated in the lab using a two-core MCF tweezing system and a four-core MCF system. The results of the two trapping systems are reported in Chapter 5 and 6. Furthermore, the combination of these devices with other microscopy techniques to demonstrate experimental examples, are described in Chapter 6. The use of the fibre trapping system to hold a cell beneath a Raman microscope provided the opportunity to collect the Raman spectrum from a single cell. Raman spectra of living yeast cells have been acquired. Raman spectra from mouse stem and Epiblast stem cells have also been captured. These proof-of-concept experiments open up opportunities for future use of our fibre trap for cell manipulation.

2.6 Discussion

Single cell isolation is of great importance as it provides the opportunity to study a cell whilst avoiding any influence from the surrounding groups of cells. Many techniques have been exploited to demonstrate single cell isolation, but optical trapping, more specifically optical tweezers, is the main field that will be examined further in this thesis.

Many technologies have been developed for studying and gaining a deeper understanding of biological cells. Optical trapping has been proven to be an extremely useful tool for many niche applications where single cells need to be manipulated, however the restrictions of conventional optical tweezers mean there is still room for enhancement. Fibre tweezers provide more flexibility, since the trapping becomes based on the tip of an optical fibre, rather than through light delivered via the imaging objective. Forming the required light manipulation structures on fibres has been reported where methods such as chemical etching, mechanical modification of the fibre tip, or fabrication of micro optics using techniques such as FIB etching have been used for applications including single and dual fibre trapping systems for single cell isolation [81,85,87,89,94], microassembly [97] or cell sorting [78]. The main drawbacks with these fibre configurations were the need for high precision in the alignment of the fibres, mainly for the case of the two opposed [81] or inclined fibres [63], the small trapping distance away from the fibre end for single tapered fibres [91], the need for a complex set up [9,100] or the need for external electric field [91].

There is an obvious requirement for a fibre-based tweezer that is able to trap large cells without contacting the fibre end, without a demanding preparation process, that is portable and can be used under any microscope system, that is small in size, and easy to

manipulate for studies that require single cell trapping and manipulation, such as isolation, sorting and analysis. In this thesis, FIB machining is explored as a technique to fabricate mirror shaped facets on to the end of a four-core fibre. FIB is used because it offers good precision which is relevant here since the emphasis of this thesis is to evaluate the fabrication procedure and the trapping geometry.

The optical trapping system that is developed in this thesis, demonstrates single-cell trapping and manipulation in 3D, using a flexible fibre-based probe that is deployed in a range of different imaging microscopes. The system is based on the fabrication of mirrors, or 'notches' on the end of the cores of a multicore fibre, similar to [9], causing total internal reflection of the guided light, but with the advantages of a multicore fibre. The multicore fibre offers a single, small diameter fibre, no need for strict alignment of two or four separate singlecore fibres, nor gluing of separate fibres inside a glass capillary but has the same advantages as a fibre bundle such as the freedom of independent transmission of different laser beam in each of the cores.

2.7 Conclusions

A variety of scientific work in the field of optical tweezing has been reported since Ashkin first demonstrated optical tweezers, in 1986. Limitations due to delivering the trapping beam via the microscope imaging optics led to the need for fibre-based tweezers development. Developments of fibre traps began with two opposing fibres or two inclined fibres and are routinely used successful in certain application areas, but they introduced other restrictions because of the need for strict alignment and for controlled microfluidics flow. Trapping based on a single fibre, such as lensed or tapered fibres is possible, however, this approach [4,24] has limitations related to the trapping distance, typically~1 μm away from the tip, thereby restricting the range of the cells that can be trapped. Novel approaches such as the use of fibre bundles instead of single fibres, aimed to overcome the abovementioned restrictions. In 2007, a novel approach of a fibre-bundle that could offer an increased trapping distance, the working principle of which was based on TIR, was presented. However, the fabrication of this optical probe demanded precise alignment of the single fibres inside a 1 mm glass capillary so resulted in a large overall diameter. This thesis describes the development of a small diameter (150 micrometre) single fibre, eliminating at the need for precise and demanding assembly. The thesis reports demonstrations that the MCF based trap can trap and manipulate a variety of different cell types. To make the MCF based trap, FIB technology is used to machine micro-mirrors on the end face of a MCF at such an

angle that allows the beams to undergo TIR until they exit the fibre and overlap at a distance away from the fibre large enough to trap large (20 μm diameter) cells without physical contact. The next chapter presents the main features of an optical fibre and describes the characterisation of the specific type of multicore fibre that is used in this thesis. Following that in chapter 4, FIB machining is used to create a range of mirror angles on MCF and the traps are experimentally tested.

Three-dimensional optical trapping of different types of cells and characterisation of the trap as well as the combination of the system with Raman microscopy and other microscopes for potential future biological applications, is presented later in the thesis.

Chapter 3: Fibre characterisation and mirror micro-fabrication techniques

This chapter begins with describing the basic working principles of an optical fibre as well as its main applications in various scientific fields. In this thesis, a four-core fibre is used as the basis of a novel optical trapping system for single cells. This special type of fibre is characterised and its specifications, such as the refractive indices of the core and the cladding, are presented. Knowing these specifications allows us to use geometrical optics to determine mirror angles for specific trapping distances. Additionally, this chapter describes the main fabrication techniques that have been used in this thesis to produce the required components for this novel trapping scheme, such as Ultrashort pulse laser machining and Focused Ion Beam technology.

3.1 Optical fibres

Optical fibres are transparent and flexible structures that work as waveguides to transmit light over long distances. They are commonly made of fused silica glass for low loss operation, or polymers for low-cost applications where higher losses are acceptable. Polymer fibres are most commonly used in biomedical engineering research due to their similarity with the extracellular matrix, where they are used to mimic biopolymers which are natural fibres in the extracellular matrix (micrometres long and nanometres thick) [103], however they are not commercially available in single mode version and they present low loss operations. Common optical fibres consist of an outer protective jacket, a cladding and a light guiding core, as shown in figure 3. 1. The core is usually circular in cross section and has a refractive index slightly higher than the cladding in order to confine the light in the core region, thus forming a waveguide. For low loss, fused silica fibres have a core that is commonly made from pure silica to achieve lowest loss while the cladding contains some additional dopants to decrease its refractive index, in order to form the required core-cladding refractive index structure. Depending upon the intended application, the core diameter can vary from the order of the wavelength of light to several millimeters.The jacket is the outer layer which is used to mechanically protect the glass fibre, and is most commonly made of polymers, such as acrylate, Fluoroacrylate, silicone, Polyimide, PA (Polyamide), PE (Polyethylene), PP (polypropylene), PVC (Polyvinyl Chloride), PVDF (Polyvinylidene Floride), PBT (polybutylene terephthalate) and PEEK (Polyether Ether Ketone).
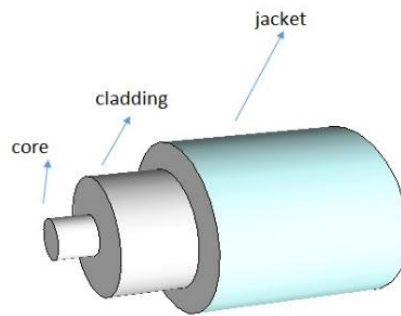
Figure 3. 1: Schematic of the structure of a typical optical fibre. A typical optical fibre cladding has a diameter of 125 μm and the core can range in size from 8-10 μm for single-mode and 50-100μm for multimode fibres.

Optical fibres are exploited in a wide range of applications. They are used for applications requiring transmission of images and illumination and have an important medical role as endoscopes [104-105]. Communication optical fibres are responsible for data transmission, ranging from Local Area Networks (LAN) to trans-ocean links and form the backbone of modern telecommunications [106]. Sensors capable of temperature, strain or pressure measurements based on optical fibres have been reported where they offer benefits in terms of size, sensitivity, and flexibility [107-109]. Moreover, techniques such as the inscription of Bragg gratings in the fibre can allow the fibre to be used as a sensor, for example to measure temperature or strain, and have found a wide variety of applications and are increasingly commercially available [110]. Furthermore, optical fibres have found niche applications in optical trapping and single cell manipulation as reviewed in Chapter 2, and they have demonstrated configurations that offer increased flexibility in some circumstances.

The guiding properties of the optical fibre core are largely determined by the core diameter, and in general optical fibres can be categorised as being single-mode or multi-mode. Single-mode fibres have a core diameter chosen such that only the fundamental mode propagates [figure 3.2b]. Typically, the core diameter is in the range of 8-10 μm, depending on the design operating wavelength. SMF-28 is a common single-mode communications fibre that is designed for low dispersion transmission of data over long distances. Multimode fibres typically have larger cores in the 50-100 μm range. This is much bigger than the wavelength of the transmitted light and therefore many different modes propagate along the fibre, as a result dispersion is higher and therefore they are mostly used for shorter distances. As figure 3.2 a,c illustrate, multimode fibres can be distinguished into two types: step index and graded index, depending on their design and fabrication. The step-index profile describes a refractive index that is uniformly

distributed throughout the core and decreases sharply at the core-cladding interface. The graded-index profile describes a refractive index that decreases proportional to the increase of the radial distance from the fibre optical axis. In this thesis single-mode step-index fibre is used because in optical trapping applications, a stable beam profile is desirable.
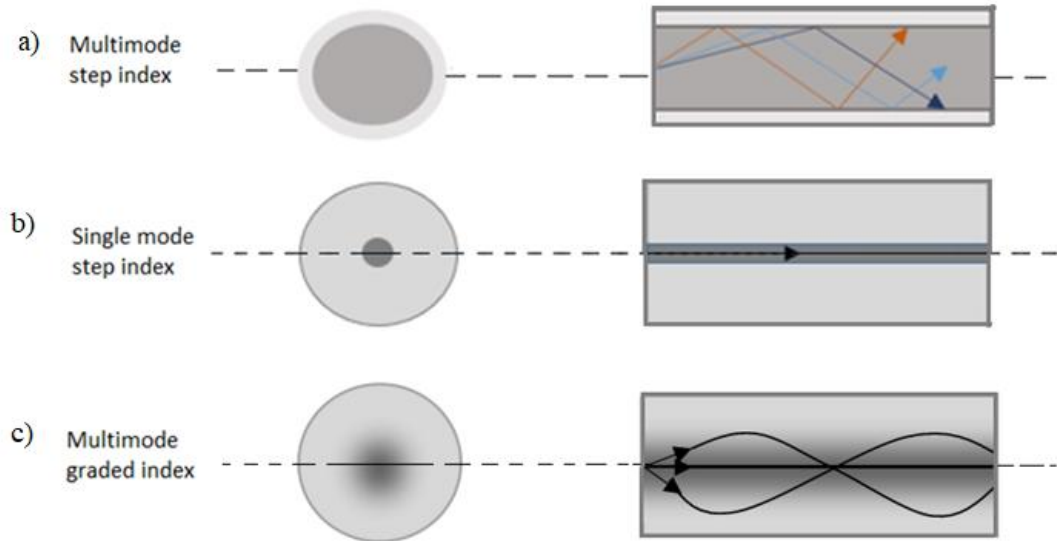
Figure 3. 2: Schematic of beam propagation in multimode (top and bottom image) and single mode optical fibres (middle image).

The working principle of a step index optical fibre (figure 3. 3) can be approximated as a result of total internal reflection (TIR) of the light when it reaches the core -cladding interface. This is a simplified model and a more accurate understanding can be developed using EM theory, however this ray-optics approach provides sufficient detail for the purposes of this thesis.
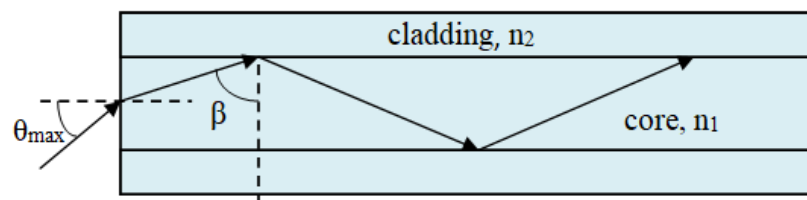
Figure 3. 3: TIR inside the core of an optical fibre. Here, θ_{max} is the maximum angle in which the beam undergoes TIR, n_1 is the refractive index of the core, n_2 is the refractive index of the cladding, and β is the angle of incidence at the core-cladding interface.

In practice the light reflection is not strictly at the core-cladding interface and the light penetrates slightly into the cladding, typically by a distance Δz (Fig.3.4), which is approximately five times the propagating wavelength [111]; this is known as the evanescent field. The evanescent field is an important parameter for this thesis as any attempt to redirect the light needs to act on the evanescent field as well as the light guided in the core.
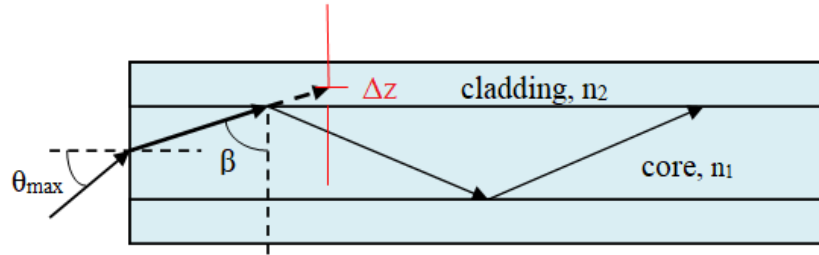
Figure 3. 4: Penetration of the energy into the cladding known as the evanescent field.

The factor Δz, a distance usually on the scale of micrometers (μm), can be calculated from Eq. 3.1 [112]:

$$\Delta z = \frac{\lambda n_1}{2\pi\sqrt{NA^2 - n_1^2 cos^2(\beta)}} \qquad (3.1)$$

where λ is the wavelength, n_1 is the refractive index of the core, *NA* the numerical aperture and β is the angle of incidence at the core-cladding interface as shown in figure 3. 4 [112]. The NA is defined as [113]:

$$NA = n_0 sin\theta_{max} = \sqrt{n_1^2 - n_2^2} \qquad (3.1)$$

where θ_{max} is the maximum acceptance angle for which the guided beam will still undergo TIR once it enters the fibre (shown in figure 3. 3), n_0 is the refractive index of the surrounding medium and n_2 is the refractive index of the cladding. At this point, β, as shown in figure 3. 4, will be almost equal to the critical angle $\theta_{crit} = \frac{n_2}{n_1}$.

When light propagates along an optical fibre, losses in power arise due to absorption and scattering. The attenuation *A*, often quoted in decibels (dB), can be found via:

$$A(dB) = 10\,log\left(\frac{P_{in}}{P_{out}}\right) \qquad (3.3)$$

37

where P_{in} is the optical power of the beam going into the fibre and P_{out} the optical power of the beam that exits the fibre. A typical value for the SMF 28 operating in the wavelength range 1525-1575 nm is 0.2 dB/km.

The attenuation is typically caused by Rayleigh scattering due to small variations in the core refractive index, bending, and absorption by the impurities of the core material, for example OH^- ions in the case of fused silica fibres. In addition to absorption, scattering effects and Fresnel reflections when the beam enters and exits the fibre lead to further losses in power [112,114].

The main approaches to minimize the losses depend on the source of the dominant losses. Rayleigh scattering and infrared absorption losses can be eliminated by using appropriate dopants and great lengths are taken to minimise losses in commercial fibre by careful control of the material composition.

If there is a need for multiple beams for signal transmission while using a single fibre then more than one core is required. Multicore fibres can be used for propagating several signals simultaneously. Where the core spacing is sufficient these cores are non-interacting and can guide different signals in each core, and thus have prospect as a multi-sensor component. Furthermore, in combination with microfabrication techniques such as Focused Ion Beam (FIB) technology or fibre-Bragg gratings (FBG) inscription, they can be applied to a wider variety of applications, such as strain or shape sensing, temperature sensing [115-116] or optical tweezing, which is the subject of this thesis.

Techniques that can modify the fibre open up a wider range of potential applications for these fibres. For example, UV lasers have been widely used for writing FBGs in the fibre cores, for applications in communications and sensors [117]. Micromachining of the fibre end surface into cantilevers for temperature sensing using picosecond laser machining has been demonstrated [118]. In another study, Focused Ion beam technology, which is a technique with an emphasis on precision and high resolution machining, has been used in microfabrication of structures to develop a Fabry-Perot refractive index sensor [119].

In conclusion, optical fibres are a useful tool to deliver light from a source to a specific predetermined location, due to their ability to guide the light along a flexible path. The transmission of the light can reach longer distances than electrical cables (telecommunication companies have reached transmission distances up to thousands of km), and if it concerns signal transmission, at higher bandwidth (up to 10 Gbits per

second (Gbps)), due to the low losses and dispersion at the same wavelengths. For example commercially available silica fibres allow 96% of the power to get transmitted after propagating through 1 km of optical fibre, which corresponds to a 0.2 dB loss. Optical fibres are widely used in telecommunication so they are commercially available, inexpensive and have tightly controlled specifications. Specialty fibres such as PCF [120], hollow cores [121], multicore fibres [122], are also increasingly available for a wide range of diverse applications.

3.2 Multicore optical fibres

The need for parallel transmission of different light beams along the same fibre, either for signal transmission or for sensor applications, has led to the development of fibres that include more than one core in their design. These fibres, known as multicore fibres, have found applications in industrial and scientific fields; in telecommunications to increase the capacity of optical networks, and in sensor applications, such as strain and temperature sensors, that can use different cores to transmit and receive the signal [123-124] or facilitate multi-measurement and operation.

Different MCF designs can be fabricated depending on the fibre characteristics and parameters as well as needs of the intended application. Similarly to the single core fibre described earlier, the MCF can be categorized as step-index and graded–index according to the refractive index profile, where in the first case the refractive index of all cores has a step between two constant values in the core and cladding interface (Fig.3.5(1)) while the second case shows a continuous profile in the refractive index of at least one of the cores (Fig. 3. 5(2)) [124].
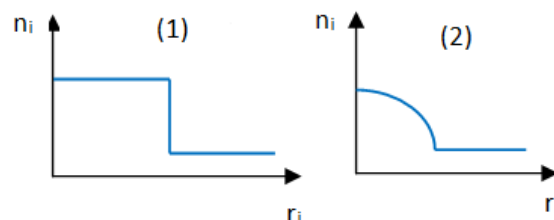
Figure 3. 5: Classification of MCF types, according to the refractive index profile. 1) Step index, where the profile shows a step for all cores, 2) Graded index, where the refractive index profile is continuous for at least one core.

Another important parameter of the MCF is the core to core distance that determines the extent of inter-core crosstalk and it is decisive for sensing applications of signals transmitted from different cores. Another important aspect for the final transmission

characteristics of the MCF is the fabrication method. As the research studies have shown through the years, one of the most important parameters that needs to be accomplished is to minimize the crosstalk providing at the same time the maximum core isolation [124]. The most common fabrication technique is the stack-and-draw technology of properly fabricated single core fibres [125] that is more widely used for fabricating a fibre bundle or optical probes [126].

The multicore fibre type that is used in this thesis, has four cores and distance between the two diagonal cores of 65±3 μm (Fig.3.6). This fibre is not commercially available and it has been fabricated in a research lab environment by taking four single-core fibre pre-forms (SMF28 type), and using a stack-and-draw technique to fabricate the MCF. Because of this, the distance between the two diagonal cores may vary along the length of the fibres, thus it may be different for optical experiments where different pieces of MCF are used. This small deviation has been added as an error in the final measurement of that distance.
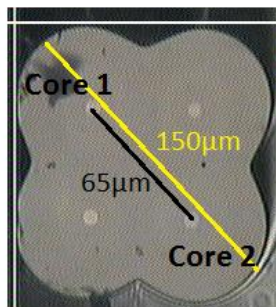
Figure 3. 6: Multicore fibre cross section as imaged under SEM. The diagonal core-core distance is 65μm.

Since this type of MCF is not a commercially available product with well-known properties, a characterisation of the relevant parameters was conducted. In particular, the refractive index of the cores is significant for a project that demands the alteration of the beam propagation through properly fabricated patterns on the core's surface. The refractive index has been measured using interferometry and more details are in the following section.

The main aim of this thesis is to modify the end-face of the four cores of the MCF in a way that the exiting laser beams will be focused into an overlapping region in order to trap a cell/particle. More specifically, mirror shaped facets are fabricated on the end of the cores at an angle (θ_{mir}) slightly higher than the critical angle, so that the propagating

laser beam undergoes Total Internal Reflection (TIR) through the core and exits the fibre at an angle equal to the θ_{prop} as depicted in figure 3.7 below.
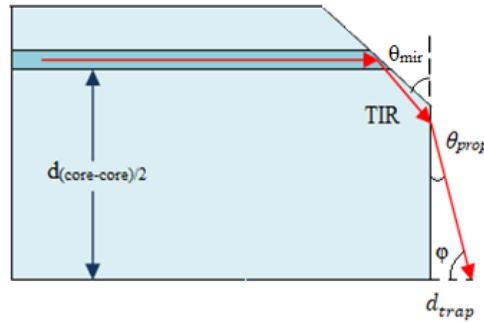
Figure 3. 7: The main working principle of the MCF based optical trapping system. Only one core of the MCF is shown here. The laser beam (red arrows) is incident upon the mirror-shaped face of the core and undergoes TIR, which alters its propagation. The beam exits the fibre in an angle equal to θ_{prop}. The trapping distance refers to the distance from the fibre end and is symbolized as d_{trap}.

To couple the laser light into the MCF cores, a fan-out device has been used to allow delivery of different laser beams to each of the cores. The fan-out device is responsible for connecting single core fibres with the cores of the MCF. The different types of fan-outs, as well as the actual devices that have been used for the work in this thesis, will be discussed in detail later in this chapter.

To summarize, the freedom of using each core independently and thereby delivering different laser beam intensity from every core of the MCF, makes this fibre an interesting component for an optical trapping system. Its small size together with the portability of the system (fibre and laser diodes), can potentially widen the scope of applications of the trapping system.

3.3 Experimental measurement of the multicore fibre refractive index

In the case of commercially available fibres, all the main characteristics of the fibre type, such as the core diameter, the cladding diameter, and the refractive index are well defined in the manufacturers' specifications. However, in case of the bespoke optical fibre used in this thesis, these parameters need to be measured. The main parameters that are important to model the proposed system and to determine the final mirror angles that will be fabricated on the end of the fibre cores are the distances between the cores, the core diameter and the effective refractive index of the core (n_{MCF}).

The multicore fibre used in this thesis (Fig. 3. 6), consists of a square array of four cores and was fabricated by drawing four separate single core SM 28-type fibre performs together. The core diameter was measured using the optical microscope to be 8±1 μm

and the diagonal core-core distance was measured to be 65±3μm centre of core to centre of core, respectively.

To measure the refractive index, a low coherence scanning Michelson interferometer was assembled with a length of fibre in one arm. The optical path length and physical length of the fibre are measured to calculate n_{MCF} and the main set up and process is described later in the section. Interferometry, in general, is a technique that uses the interference of waves to study potential changes in optical path length (for example displacement of a mirror in a traditional Michelson Interferometer) [127]. It is a technique that can measure optical distances ($l_{optical}$) in a system, with precision that is on the scale of the wavelength of light. In this way, the optical path length through a fibre can be measured and the geometric length ($l_{physical}$) that the light follows through an optical fibre can be measured physically. With this information the refractive index of that fibre, n, can be calculated as following:

$$n = \frac{l_{physical}}{l_{optical}} \qquad (3.4)$$

The configuration of the interferometer implemented in this thesis is shown in figure 3.8 and it is based upon a low coherence Michelson interferometer. It consists of a light broadband source 1550 nm (FWHM of 20 nm) that is used to measure the optical path in the fibre and a stable He-Ne laser source (633 nm), used for calibrating the external mirror scan displacement. The wavelength of the broadband source was chosen to be ~1550 nm in order to investigate whether the multicore fibre has the same properties as the SMF 28 single core fibres that it is believed to be based upon. The optical path of the 1550nm beam (blue line in figure 3.8) is split by a non-polarising 50/50 cube beam-splitter where it forms two beams. One beam travels towards a microscope objective that focuses the light into an optical fibre (signal arm) and the second beam propagates towards a moving mirror (reference arm) (Fig. 3. 8). The signal beam is focused onto a single core of the MCF, with the experiment realigned and repeated to obtain results for all four cores. The signal beam experiences Fresnel reflection at the front face and rear face of the fibre. The reference and signal beams recombine in the beam-splitter and the resulting interference intensity is captured by a detector. The measured signal consists of constructive or destructive interference of the two beams when the reflections in each arm are balanced to within the coherence length. Therefore, two sets of interference fringes are observed, associated with the front and back perpendicularly cleaved faces of the fibre, and this defines the optical path in the fibre.
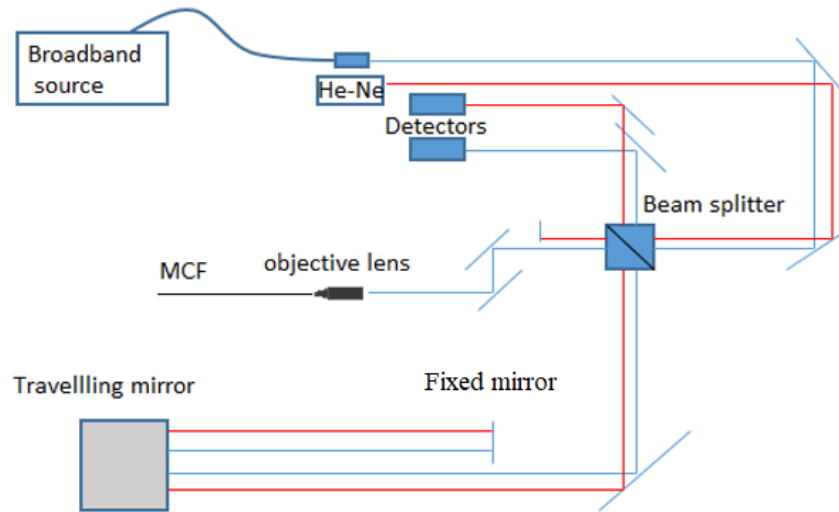
Figure 3. 8: Low coherence Michelson Interferometer consists of a broadband source, which is chosen to have a centre wavelength of 1550 nm (blue line), a reference He-Ne laser (633 nm) (red line), mirrors to direct the light and a beam splitter to form the interferometer. The 1550 nm beam splits into two at the beam splitter. One beam propagates towards the MCF and the other beam travels towards a moving mirror. When the travelling mirror (reference arm) changes position, a different interference between the two beams is reported when they recombine in the beam splitter. Two different detectors capture the two laser beams (633 nm and 1550 nm) after the recombination.

The path difference between the two beams (signal and reference) of the 1550 nm source (blue line in figure 3. 8), can be translated to a phase difference which creates an interference fringe pattern. The cycle of destructive to constructive, causes the intensity to undergo cyclic variation.

The physical length of the fibre was measured using the travelling microscope with an accuracy of 0.01 mm.

The x-axis of the data presented in figure 3. 9 indicates time. To proceed with the measurement process, the time axis needs to be transformed into position axis. For this purpose, a reference HeNe laser (stabilised 633 nm wavelength, red line in figure 3.8) that co-propagates along the measurement arm, has been used and an additional detector is included in the final set up to measure this signal. Figure 3.9a shows the interferrogram of the 1550 nm signal wavelength with the two reflections from the fibre-ends indicated. Figure 3.9b presents the reference HeNe laser signal which was used to calibrate the time axis into distance.

Matlab (ver. R2018b) was used to analyse the data (Appendix 3.1). The distance between the two reflections was automatically derived by the Matlab code from the HeNe (red) reference laser signal data which was used to translate the movement into units of distance using a fringe counting technique. Once the number of peaks (*N*) was

known, the optical path length could be calculated using Eq.3.5, where λ is the He-Ne laser wavelength (633 nm).

$$l_{optical} = \frac{\lambda N}{2}$$

(3.5)

a)

1st reflection
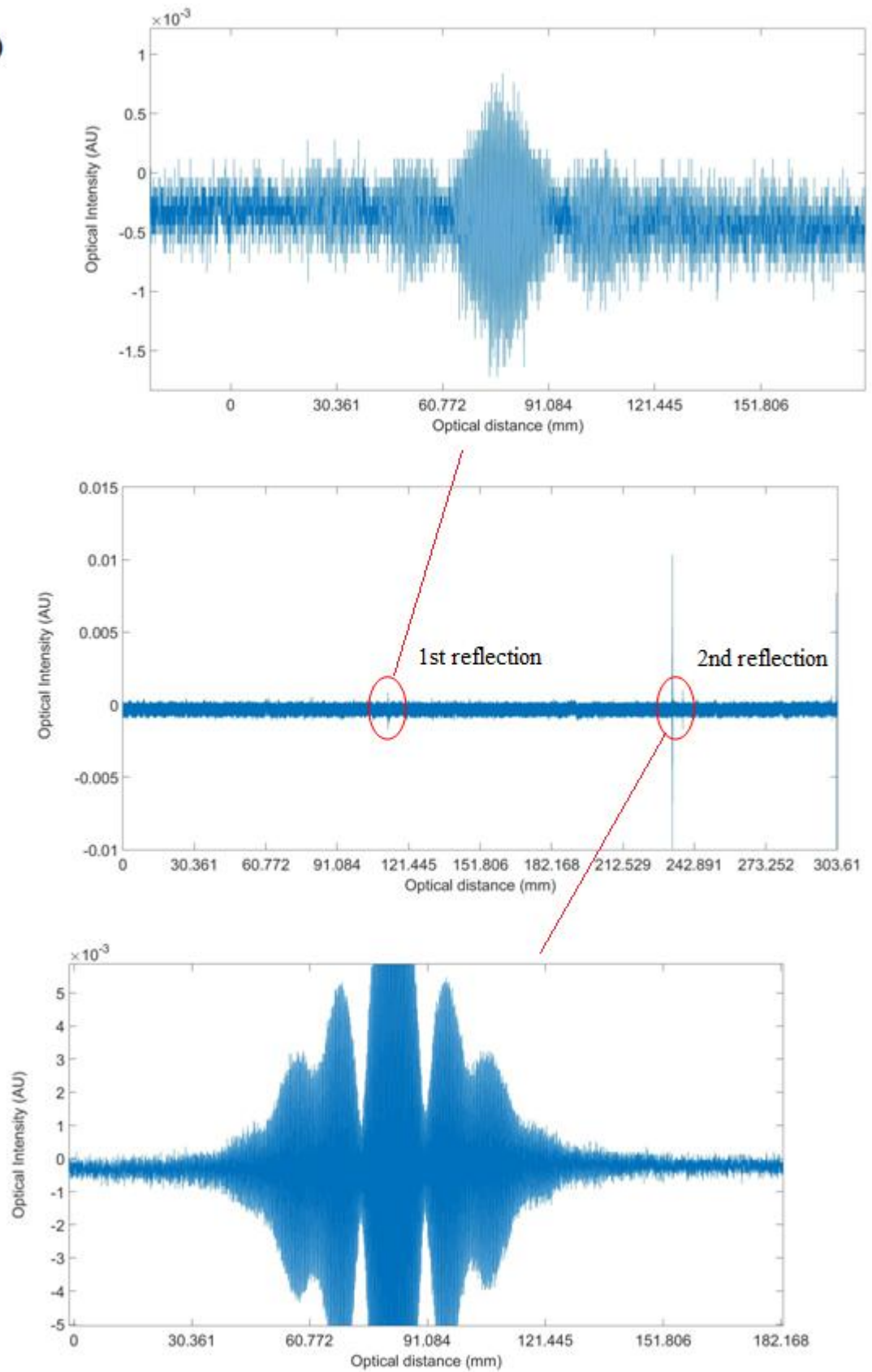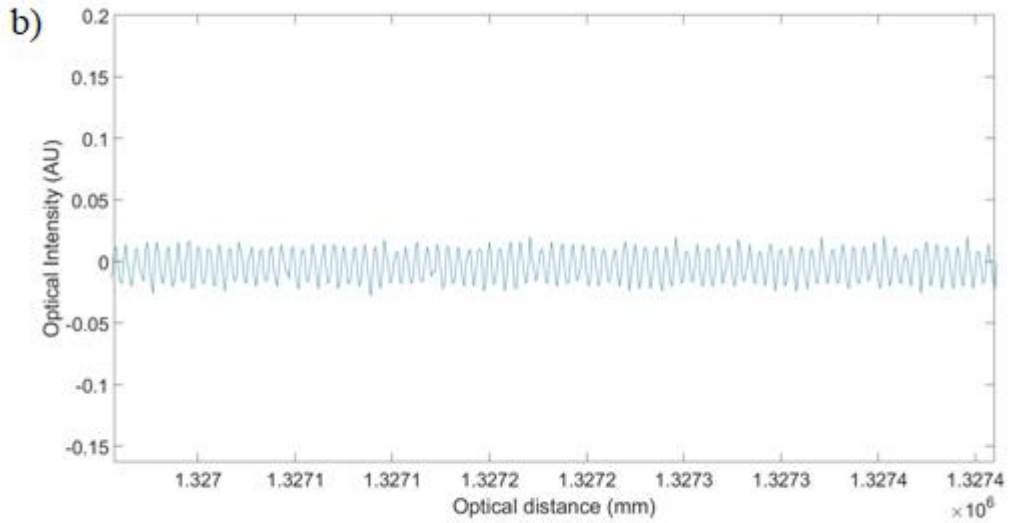
2nd reflection

Figure 3. 9: a) The two reflections when IR (1550nm) laser beam was propagating through the MCF, as captured by the detector. The two reflections correspond to the two perpendicularly cleaved ends of the fibre. As it is shown, the second reflection is much higher in intensity compared to the first reflection and this is possibly due to a better cleaving of the second fibre end face. In the zoomed graphs, it can be seen that the optical intensity forms a sinusoidal graph relating to the optical distance. b) The red laser signal as it is captured by the respective detector. The He-Ne laser had been used to calibrate the x-axis of the IR spectrum into mm.

The results for the average of four repeat measurements for the optical length using the 1550nm laser, for each of the four cores are presented below in Table 3.1. The physical length of the fibre was $l_{physical} = 17.5 \pm 0.1 \, cm$ with the uncertainty to be due to instrument (travelling microscope) accuracy, and so the refractive index for each core, given by the Eq.3.4, is also presented in Table 3.1.

$$L = \frac{\lambda N}{2} \qquad\qquad (3.6)$$

Core	Optical length (L)	Core refractive index n_{core}
Core 1	$11.9202 \pm 0.0155 cm$	1.468 ± 0.008
Core 2	$11.8439 \pm 0.0094 cm$	1.469 ± 0.008
Core 3	$11.9005 \pm 0.0771 cm$	1.470 ± 0.012
Core 4	$11.8724 \pm 0.1341 cm$	1.474 ± 0.018

Table 3. 1:Optical length and refractive index for each individual core of the MCF, as measured in the lab using the Michelson Interferometer.

46

The final value of the optical length for each core is the average of the four different measurements implemented for each core and the respective uncertainty is the standard deviation. The respective uncertainty of the refractive index of each core comes from the error propagation in Eq. 3.4. Calculating the average for the four cores, the effective index of the core is $n_{core} = 1.470 \pm 0.008$, where the uncertainty in this case is the standard deviation of the different measurements for each core. The typical refractive index for the core of a SMF-28 fibre is $n_{coreSMF\ 28} = 1.468$ at a wavelength 1550 nm, which agrees with the measured value obtained for the MCF within the experimental error. The 1550nm laser was chosen as a source, because the MCF that is used in this thesis was fabricated from the drawing of four single core SMF28 equivalent preforms that were are expected to be single mode at 1550nm. In this way, it is possible to compare the MCF refractive index with the value expected for SMF-28. Therefore, it can be assumed that the MCF properties are similar to SMF-28, and for the purposes of modelling, other specifications of the fibre can be approximated by using published SMF28 data. For example, the refractive index of the cladding can be considered equal to 1.463, as based upon the refractive index profile of a conventional SMF 28 fibre.

3.4 Fabrication techniques

Fabrication of micron-scale structures on the end of an optical fibre is a demanding and difficult process, in terms of combining a high precision with a desire for low cost of processing. Usually, cost increases as the precision of the technique increases. Some well-known fabrication techniques include, chemical etching [128-130], mechanical polishing [131], ultrashort pulse laser machining [132] and Focused Ion Beam machining (FIB) [133]. Chemical etching, usually HF etching when considering fused silica, and mechanical polishing, are two techniques of relatively low cost but of limited applicability for complex 3D structures. Laser machining, mainly using picosecond or femtosecond laser pulses, can lead to highly controlled removal of material, however it may result in an unacceptable level of surface roughness which would then require post-processing techniques such as FIB etching or flame polishing to achieve optical quality finishes. Each of the ultrafast laser types (nanosecond, picosecond or femtosecond (ns, ps and fs, respectively)) have different advantages and disadvantages, and all these characteristics can be summarized as follows.

Laser machining with nanosecond (ns) pulses typically results in a lower surface finish quality in comparison to ps and fs laser systems in terms of damage and swelling around

the machined features due to heating and melting effects [134], however the exact details vary depending on the substrate properties. For example, Lee *et al.*, 2009, focused on the differences between processing with nanosecond and picosecond pulses applied to aluminoborosilicate glass [134]. Comparison of trepanned holes produced in glass using nanosecond and picosecond pulses revealed that the wall surfaces and the entrance holes produced by picosecond pulses were smoother than those by nanosecond pulses. The picosecond laser provided high quality processing at lower speeds compared to the nanosecond source. Furthermore, laser cutting of glass was presented by Loeschner *et al.* [135]. The investigations were carried out with a short nanosecond pulsed Nd: YVO_4 slab laser and a high repetition rate femtosecond laser. Irradiation of the material with short nanosecond pulses leads to the formation of micro defects [135]. Picosecond (ps) and femtosecond (fs) pulses result in reduced regions of damage to the material, due to the very small heat affected zone, however they are often considered as expensive methods, with expensive source and slow processing speed/throughput. The main differences between these two techniques tend to be subtle and they depend on the material. When the material is a metal, the fs laser offers topside burr, however with slightly better quality of features and smaller roughness [136]. Furthermore, fs lasers can process wider variety of plastics, while ps often require green and UV wavelengths to process plastics effectively, due to the presence of a higher nonlinear effect. In general, fs lasers provide slightly better quality of features, however, ps provide higher cut speed (125-150 mm/s [137], while for fs lasers is typically around 50mm/s [138]). Summarizing, the main aspects of the three categories of ultrashort pulsed lasers concerning material machining processes can be seen in Table 3.2 below.

Type of pulses	Machining speed	Cost	Precision	Heat affected zone
ns	very high	low	medium	high
ps	Medium	medium	high	small
fs	Low	high	very high	very small

Table 3.2: Comparisons of the main aspects in relation to machining for the three different types of ultrafast lasers: ns, ps and fs pulsed lasers.

A technique that can fabricate features with high resolution, using a beam spot size equal to 1 Å and leaving a smooth machined surface without a need for further polishing techniques, is Focused Ion Beam (FIB) machining. The cost of this technique is higher in comparison with the above-mentioned techniques, especially because of the

maintenance-related cost of the system, however it offers higher surface finish properties and great control over the machined geometry.

In this thesis, it is shown that it is possible to fabricate mirrors on the end face of a multicore fibre using FIB machining in order to demonstrate three-dimensional optical manipulation of micro particles and cells, using a single optical fibre. This technique was chosen as it offers a good approach to demonstrate and explore the suggested concept and prove the working principle, although it is an expensive technique.

3.4.1 Focused Ion Beam technology

FIB machining provides the opportunity to engrave patterns with very small dimensions (in the scale of nm), on the surface of materials. Other techniques that deliver similar results, such as optical lithography, require an intermediate sample surface preparation, such as deposition of photoresist at the top of the sample material or etching of the surface. In contrast, FIB does not require any special preparatory process, except the addition of a thin gold coating before the fabrication, in particular for non-conductive materials, so they can be visualised under SEM without charge accumulation. The gold coating creates a conductive layer on the sample and that reduces charging, minimises thermal damage and improves the secondary electron signal that is required for examination under SEM. The pattern fabrication using this technique can be achieved either by defect generation, by ion implantation or by sputtering of the local surface [37], and each of them apply to different substrates depending on the sensitivity of the target and scales.

The basic parts of the FIB setup include: an ion column, a vacuum chamber, the gas delivery system, and a user interface. The ion column is similar to the structure of a SEM, but instead of an electron beam, there is a gallium ion beam. The ion beam energy range can be varied between 10 - 50 keV and the respective ion current is 1 pA -10 nA. This range of values can provide both a fine beam for imaging purpose on sensitive substrates with high resolution and an intense beam for milling in a short time [139]. The working chamber operates at a low pressure in the range of 10^{-7} mbar. There is a motorized stage, to mount the sample upon which can be moved in five axes, and the process of placing the sample in, and removing the sample from, the chamber is rapid and straightforward [139-140]. The user interface is computer-based software that controls the loading and unloading of the sample, as well as the motion of the motorized

stage and the valves of the gas system. An imaging camera and the ion beam parameters are automated and controlled through this software.

The fabrication process is explained thoroughly in Chapter 4, applied specifically to the case of machining the mirror structures on the end of the four cores of the MCF.

3.4.2 Fan-out fabrication techniques

The use of a MCF in this project has many advantages in terms of flexibility and concurrent transmission of independent laser beams. However, there is currently no laser source that can be directly connected to a MCF. For this reason, an optical device to interface between conventional fibres and MCF, known as "fan-out", is required. In this device each core of the multicore fibre is aligned to a core of a single-core fibre, allowing each core in the MCF to be connected directly to a discrete single core fibre.

Several different approaches for the fabrication of a fan-out have been reported. Laser inscribed waveguides have been used to produce a three-dimensional fan-out device [141] (Fig. 3. 10). This approach can be developed for any number of waveguides with a range of geometries thus it can be used for the MCF described in this thesis, and has similarities to the one described below [141]. Although these are commercially available, concerns regarding their power handling ability meant that care was taken when using these for the work in this thesis.
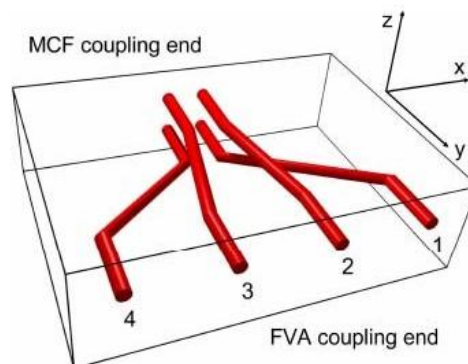
Figure 3. 10: Inscribed waveguides using femtosecond laser to produce a three-dimensional fan-out device that couples into a 4×1 fibre V-groove array (FVA) (image taken from [141]).

The development of a laminated polymer fan-out device that would interface between a seven-core MCF with an array of single core fibres was published in 2012 [142]. The pattern described here, is similar to that described in [141] with one difference being that the waveguide substrate material is a laminated polymer structure (Fig. 3. 11).

However, these fan-outs are not commercially available, thus was not considered an option for application within this thesis.
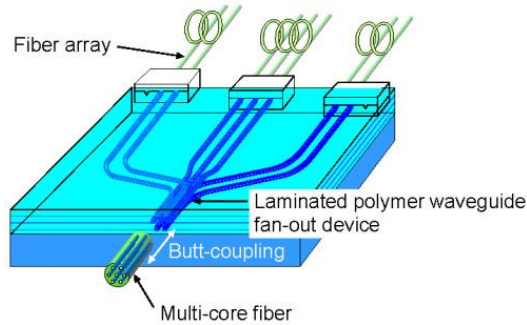
Figure 3. 11: Inscribed waveguides inside laminated polymer substrate to produce a three-dimensional fan-out device (image taken from [142]).

More recently, an optical connector based on tapered single core optical fibres in order to connect a seven-core MCF with seven separate fibres, was demonstrated [143] (Fig.3. 12). This is a low loss approach, however it is costly to manufacture because each taper requires its own fibre drawing process and therefore was not considered for the work in this thesis.
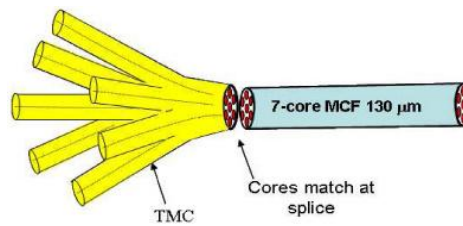
Figure 3. 12: Seven single core fibres tapered (tapered MCF connector (TMC)) and connected with a seven-core multicore fibre using a thermal splicer (taken from [143]).

Another approach is the use of a scalar domain diffractive optical element, a phase-only component, that can distribute diffraction orders that match the fibre core geometry [144] (Fig.3. 13). This approach was not adopted in this thesis as this requires precisely aligned free space optics and also for the aims of this thesis everything needs to be integrated.
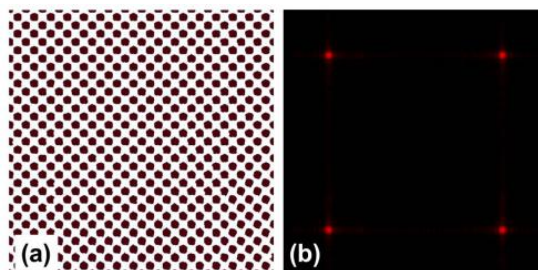
Figure 3. 13: (a) Phase profile of a 2×2 fan-out device. Black dots represent zero relative phase difference whereas white dots represent the π phase delay (b) Simulated output power (taken from [144]).

In this thesis, two types of fan-out device have been used to couple light from single core fibres into the cores of MCF to realise a single MCF-based optical trap. The first was based on HF-etched single-core fibres glued together, placed inside a glass capillary, carefully aligned to and glued onto the four-core fibre. The second fan-out type that was used for optical trapping experiments that required optical transmission to all four machined cores of the MCF was a commercially available product (3D OPtoFan^{TM}, Optoscribe Ltd.) that worked with more success due to the lower losses during the transmission of the laser beam and due to the fact that it was a commercially available product that did not demand any fabrication process before it use in the optical experiments. Both types of fan-out device are described in detail in the next chapter in section 4.2.1.

3.5 Discussion

The main specifications of an optical fibre are normally available in the corresponding manufacturers specification sheet. However, the multicore fibre that has been used in this thesis does not belong to this category of a commercial product and details of any previous characterisation were unavailable. For this reason, its specifications such as the refractive index of the cores had to be experimentally measured. The measurement of the core's refractive index was implemented using a custom built low-coherence Michelson interferometer and the refractive index value obtained was a good match with the respective value for SMF28 fibres. This supports the manufacturer claim that the cores are SMF equivalent, and therefore future calculations can be undertaken on this basis with confidence.

Concerning the potential fabrication techniques for machining of the mirror features on the end facet of the MCF, it needs to be highlighted that the main aim of this thesis is to investigate the proposed geometrical pattern for trapping purposes, thus the first aim was to minimise any potential error that may occur due to the fabrication process. For this reason, the fabrication technique of the mirror patterns had to be of high precision and accuracy. Focused Ion Beam technology was chosen to deliver these requirements, offering high precision in machining and minimising the resulting roughness of the surface compared to laser machining. This fabrication technique is understood to be a slower process in comparison with other techniques such as some of the ultrafast laser machining techniques, however for the perspectives of the study in this thesis, this fabrication technique was considered the most appropriate to prototype precision optical

structures on the MCF. Once the geometries and tolerances have been validated, there is scope in the future to machine these structures using faster processes such as laser machining or even nano-imprint lithography [145], allowing progress towards mass production. FIB milling is used in this work for bespoke design prototyping and testing.

The optical trapping system presented in this thesis, provides the freedom to connect different laser sources into each core of the fibre. However, this can only be achieved using a suitable fan-out component. In this thesis two types of fan-out have been used, one that is based on the HF-etching of four separate single-core fibres and their thermal splicing into a multicore fibre and a second device that is based on the laser inscription of four waveguides in a glass substrate that each connect a single laser source to a single core of the MCF. Both types of fan-out device are described in detail in Chapter 4.

3.6 Conclusions

The fabrication of microscale structures and patterns on surfaces, for example the end-face of optical fibres, and the demand for high precision machining in general has recently been of great interest [140]. In this thesis, FIB milling is used to fabricate precision structures on the end of a MCF in order to generate an optical trap, capable of single cell trapping in 3D, on the end of a single piece of fibre. This would enable optical trapping of single cells in a portable fibre-based setup, giving the opportunity to trap particles under a variety of microscopes that was not feasible with the conventional trapping systems. This has the potential to enable a wide range of studies at the single cell level such as cell isolation and analysis as previously explored in Chapter 1.

In the following chapter the development of the entire MCF-based trapping system, based on the fabrication of mirror patterns on the end face of the multicore fibre, the fabrication of the fan-out device, the assembly of the experimental trapping set up and its incorporation with a microscope to enable trapping and imaging of trapped cells, are described.

Beam geometry based on TIR at the FIB milled mirrors is explored using a geometrical optics approach. The FIB method was selected for making the mirror structures on the MCF due to its high machining precision, and is used to fabricate test fibres for subsequent trapping experiments.

Chapter 4: Fabrication, assembly and characterisation of a multicore fibre-based trapping system

This thesis investigates the development of an optical-fibre based optical trapping system that can trap and manipulate microparticles and cells using an approach that is independent from the microscope imaging optics. This chapter presents the concept and experimental implementation that is used to demonstrate optical trapping using a single multicore fibre with end face mirrors. The fabrication techniques that are required to manufacture bespoke components for this set-up equipment are described in detail starting with the optical fibre mirrors, followed by the fan out device, the laser coupling, and finally the fabrication of the microchannels and microwells on microscope slides to create sample chambers for trapping experiments. Characterisation of the fibre end mirrors and the optical properties of the beam exiting the modified multicore fibre, in terms of divergence are also described in this chapter.

After manufacturing, interfacing and characterising the multicore fibre system in this chapter it is then used in demonstration trapping experiments; these are discussed in detail in Chapter 5.

The overall experimental concept consists of the fibre trapping system and an associated imaging system to view the effect of the trapping, as depicted in figure 4.1. The optical trapping system includes the MCF with the machined mirror shaped facets, four 976 nm wavelength laser diodes (Thorlabs, PL980P330J, and controller CLD1015), a fan-out that is responsible for the connection of the MCF to the four single-core fibre pigtailed laser diodes, as well as a microscope slide with machined surface microchannels to mount the sample. More detail on the different types of fan-out that have been used in this thesis and on the fabrication of the microchannel on microscope slides are presented in section 4.5.1 and 4.7.1 respectively.

The imaging system includes a microscope objective (10×, 20×, or 40× depending on the experiment requirements), a CCD camera (Thorlabs DCC 1645C, USB 2.0, CMOS Camera, 1280 × 1024, Colour Sensor) to image the experiment from above, an illumination source from below for transmission microscopy and xyz micro translating stages for high-accuracy movement of the sample and the optical fibre to bring test objects into focus. The bespoke microscope system had the benefit that could be adapted for different measurements, such as trapping experiments, beam characterisation (section 4.3.6) and single cell fluorescence experiments (Chapter

section 6.5.1). The single cell Raman spectroscopy experiments (section 6.6) were performed on a different, commercially available microscope. The imaging microscope used for different experiments will be properly annotated in the respective individual sections later in the thesis. It is important to note that the objective and the CCD camera form a microscope imaging system and the objective lens is not used for trapping purposes.
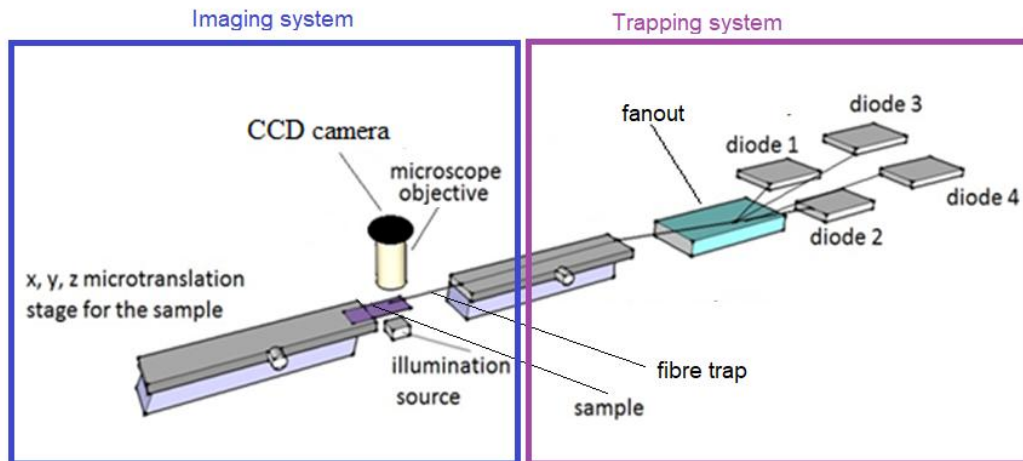
Figure 4. 1: Experimental set-up for the optical trapping experiments. The optical trapping system consists of the laser sources (diodes 1-4), their drivers, the interfacing fan-out and the MCF. The fan-out device is used to connect the four-core fibre to the four different laser diodes and to couple laser power into each core of the MCF independently. The imaging system consists of a microscope objective, a CCD camera connected to a PC, an illumination source for the sample and micro-translation stages to accurately move the sample. The sample used is typically based around a microscope slide often incorporating channels and reservoirs depending on the application.

The main objective of this thesis is to describe the formation of an optical trap based upon using a machined multicore optical fibre to form pairs of overlapping beams capable of holding particles or cells. All the techniques needed to fabricate and prepare the trapping set up, such as the technique to machine the fibre, to fabricate the interfacing fan-out used to couple laser light into the cores of the MCF, and to make appropriate sample holders with microchannels to mount the sample, are described in this chapter. Firstly, the fabrication of mirrors on the end of a multicore optical fibre is described in detail and the characterisation of light exiting the mirrors is presented to understand how the mirror angle affects the trap position and the beam propagation as well as how the experimentally measured trap position is compared with the theoretical trap position. Secondly, the integration of the MCF into the experimental set-up using a fan-out device is described and the total set up is characterised and analysed. Finally the

development of sample holders by implementing tests of a variety of microchannels patterns into a microscope slide is also presented.

4.1 MCF machining of mirror structures

As previously mentioned, the main aim of this thesis is the formation of overlapping beams, exiting an appropriately machined multicore optical fibre that will act as an optical trap. Below, the geometry of the mirror facets is described.

4.1 Calculations of mirror geometry

In this thesis, a four-core optical fibre is used as the basis of an optical trapping system, due to the annular distribution of light and its small overall diameter of 150 μm (in figure 4.2 a). These dimensions make this type of fibre suitable for the development of integrated 'lab on a chip' devices or to hold and manipulate cells in conventionally difficult to access locations, such as deep in a sample or in turbid media.

The basic fibre trapping system concept consists of forming mirrors at an angle θ_{mir} on the end of the fibre aligned with the individual cores, as illustrated in figure 4.2 b. The angle θ_{mir} has to be slightly higher than the critical angle so that the core-guided beams undergo Total Internal Reflection (TIR) at the media-mirror interface. The beams refract at the interface between the fibre-end face and the media and afterwards they overlap in the media to form a trapping region, tens of microns away from the fibre-end face (d_{trap}). The propagation angle θ_{prop} is the angle with respect to the fibre end-face and the φ is the angle with respect to the fibre axis. Figure 4.2 c presents an illustration of two beams exiting two diagonally opposite cores of the MCF.

The MCF that was exploited here consisted of four silica cores of refractive index $n_{core} = 1.470 \pm 0.008$ as measured using a Michelson interferometer and doped silica cladding of refractive index equal to 1.463 (Chapter 3, section 3.3). The critical angle, θ_{crit}, for TIR at a fibre core-water boundary (for a water-immersed fibre) was calculated to be 64.8°±0.3° using

$$\theta_{crit} = \sin^{-1}\left(\frac{n_{water}}{n_{core}}\right) \qquad (4.1)$$

where n_{water}=1.33 is the refractive index of water and $n_{core} = 1.470 \pm 0.008$ is the refractive index of the fibre core and the respective uncertainty is due to the experimental error discussed in Chapter 3.
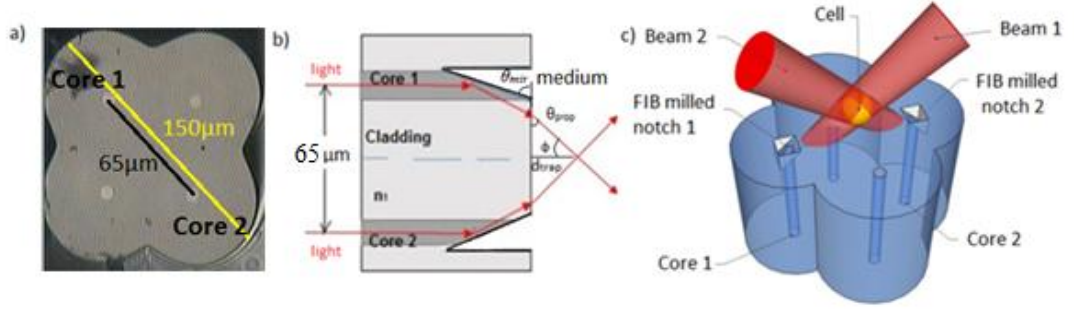
Figure 4. 2: a) Micrograph of the four-core fibre end-face as captured from SEM. Diagonally opposite cores, 65±3μm apart, are machined to form the steering mirrors, b) Cross-section of the fibre trapping system design. Light propagates along the core and undergoes TIR at the mirror/media interface at the FIB milled notches, followed by refraction at the fibre end face/media interface. The light from the two diagonally opposite cores converges in the medium at a distance d$_{trap}$ from the fibre-end face, c) 3D schematic of the propagation of the two beams exiting the machined diagonally opposite cores. A trapped cell (yellow sphere) is depicted in the overlapping area [54].

When the mirror angle, θ_{mir}, takes higher values than the critical angle of 64.8°, then the beam propagation angle, θ_{prop}, and the respective trapping distances, d_{trap}, vary accordingly.

For example, for a mirror angle equal to 67.5° the calculated NA related to the convergence of the two beams onto the trapping focus is

$$NA = n_m \sin(\varphi) = 1.039 \qquad (4.2)$$

where n_m represents the refractive index of the surrounding medium, in this case water (1.33), and φ represents the angle with respect to the fibre axis (as shown in figure 4.2b), which is calculated to be 51.4° using the geometry in figure 4. 2b.

The distance between the two diagonal cores of the multicore fibre is measured to be 65 ± 3 μm, and assuming that the off-set distance annotated as d in figure 4.3 is small and negligible, it can be assumed that the distance α is α≈$d_{core\text{-}core}$/2, as also shown in figure 4.3. The uncertainty in the diagonal cores distance is obtained from 1 standard deviation of the four different lengths/pieces of MCF used for different experiments. It is seen that this distance may vary, and this can be explained as this type of fibre is not commercially available but it was fabricated in a lab using stack-and-draw technology. According to the geometry presented in figure 4.3 [54], the trapping distance, d_{trap}, can be calculated geometrically as follows, with an uncertainty coming from the error propagation:

$$tan\varphi = \frac{d_{core-core}/2}{d_{trap}} \Rightarrow d_{trap} = \frac{d_{core-core}/2}{tan\varphi} = 25.9 \pm 0.5 \, \mu m \quad (4.3)$$
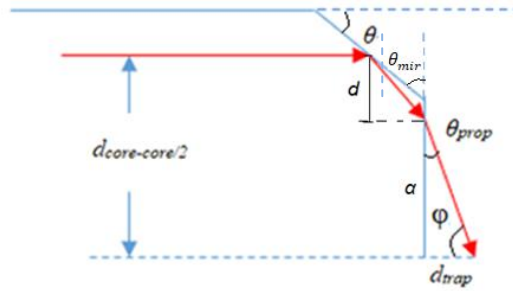
Figure 4. 3: Laser beam propagation through an optical fibre with end face mirror. Here, θ_{prop} is the propagation angle with respect to the fibre-end axis, φ is the propagation angle with respect to the fibre axis, $d_{core-core}$ is the distance between the diagonally opposite centres of the cores of the four-core fibre, d_{trap} is the trapping distance from the fibre end to where the particle is expected to be trapped, because this is where the two beams from the diagonally opposite, machined cores overlap, and, α is the distance between the d_{trap} axis and the point that the beam hits the medium-cladding interface before it exits the fibre.

A plot that shows the theoretical trapping distances d_{trap} (blue line) as geometrically calculated for a range of different mirror angles is presented in figure 4. 4. In the same figure the calculated NAs are also presented in orange line.
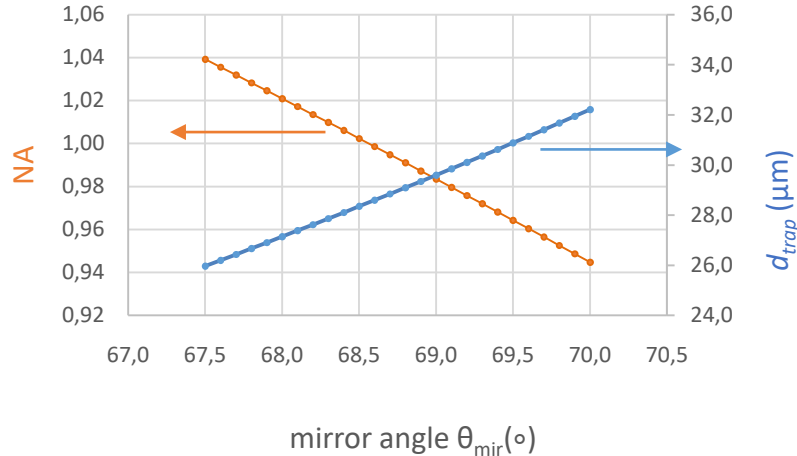
Figure 4. 4: Theoretical estimation of trapping distance d_{trap} (blue circles) and numerical aperture NA (orange circles) for a variety of mirror angles θ_{mir}, that take values slightly higher than the critical angle.

4.2 Mirror fabrication

To proceed with the fabrication of the required mirrors on the end facets of an optical fibre, a suitable fabrication technique is required. High (nm) precision and good quality surface finish are necessary to allow correct alignment and angle control and to provide

good optical quality reflecting surfaces. To realise the desired geometry with this level of precision, Focused Ion Beam (FIB) milling was chosen to be a suitable fabrication method. The FIB system used for the work presented in this thesis is the FEI Quanta 3D FEG (Fig. 4.5a) which consists of a Gallium ion beam source suitable for material milling and a Scanning Electron Microscope (SEM) that was used to image the process. These two beams are pre-aligned with an angle of 52° relative to each other as is depicted in figure 4.5b. The total length of the fibre that went into the chamber was approximately 15 cm, however it was wrapped in such way so that only 2-3 cm length was protruding outside the metal connector groove. The position of the sample in the vacuum chamber was controlled through the multi-axis stage position controllers. The control system allows for a SEM image to be monitored during the FIB processing allowing for any drift compensation. The main working principle of the FIB technique has been discussed in Chapter 3, section 3.4.1.
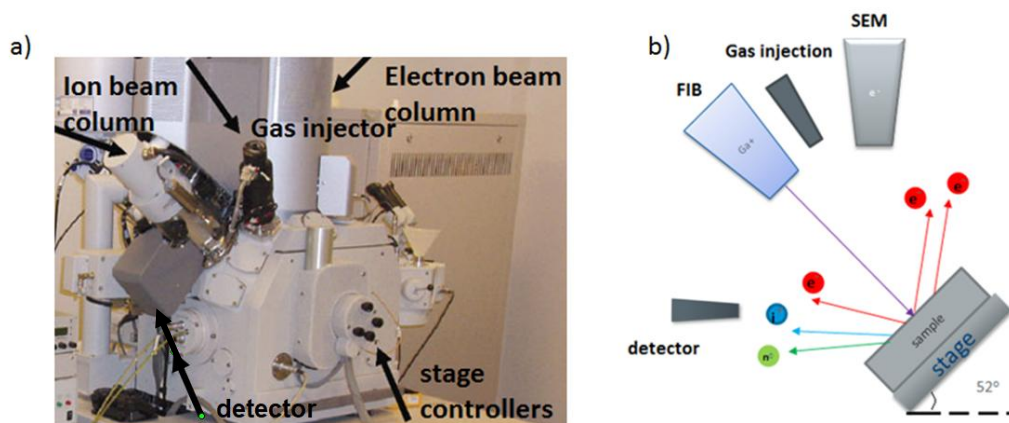
Figure 4. 5: FIB set up: a) Annotated photograph of the FEI Quanta 3D FEG used in this work, b) Schematic of FIB components. The set up includes the Gallium ion beam column for the FIB (labelled FIB), the electron beam for the SEM (labelled SEM), the detector that captures the scattered electrons to form an image of the whole process, and the stage on which the sample is placed. The gallium (Ga+) ion beam sputters a small amount of material and leaves the surface as neutral atoms (n_0) (green arrow) or secondary ions (i^+ or i^-) (blue arrow). The ion beam also produces secondary electrons (e^-) (red arrows) and the signal from these secondary electrons or the sputtered ions is collected to form an image.

4. 3 Initial experiments

Before fabrication of mirrors on MCF, some initial calibration studies were completed.

The first attempt to fabricate the mirror geometry was applied to two single-core fibres (Fig.4.6), glued together with UV curing glue and placed inside a glass capillary for stability and protection, to repeat the work by Liberale *et al.* [9] using only two fibres instead of four in the first instance. Two single mode, single core, SMF800 fibres

(SM800-5.6-125, Thor labs) have had the polymer jacket stripped off and have been perpendicularly cleaved and then cleaned along their length using isopropanol. Afterwards, they have been inserted inside a glass capillary (CM scientific Cat.Number:CV3040Q) of an inner and an outer diameter equal to 300 μm and 400 μm, respectively. The outer diameter of the SMF800 fibre type cladding is 125 μm. Once both fibres are inserted inside the capillary, glue was also added inside the capillary, then UV cured, to hold the two fibres in place. To correct for any height misalignment between these fibres a mechanical polishing of the resulting configuration was required. The main steps concerning the preparation as well as the mounting of the sample for FIB machining are described in detail in the following sections.
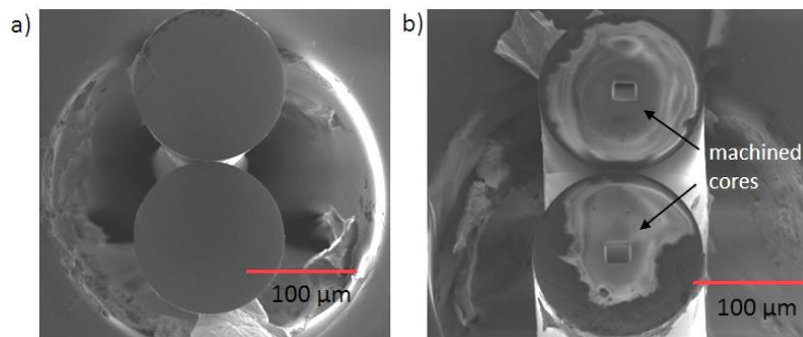
Figure 4. 6: a) Two single core fibres glued together in a glass capillary, mechanically polished and coated with gold. The inner wall of the capillary can be seen and is filled with UV curing glue and air. The outer wall of the capillary is outside of the microscope image. The capillary inner and outer diameters were given by the manufacturer as 300 μm and 400 μm, respectively. b) Mirror structures (machined cores) fabricated onto the core surface of the two fibres, using FIB technology.

This approach has potential to work in a similar manner to Liberale's fibre bundle and was an initial approach that provided experience in defining the mirror angles as well as defining the machining rates and parameters for the FIB process. However, some difficulties that were encountered during the preparation of the optical, mainly related to the fragility of the capillary during the mechanical polishing, led to the use of a MCF instead. The fibres shown in figure 4.6 have not been used for optical trapping experiments demonstration or further analysis.

4.3.1 Preparation of the fibre for FIB etching

As also mentioned in the previous section for the case of the single core optical fibres, the main steps to prepare generally an optical fibre for the FIB machining process, before mounting it in the FIB chamber are the following: Firstly, the polymer jacket needs to be stripped from the fibre. Then the fibre needs to be cleaved perpendicularly

to the fibre axis using a mechanical fibre cleaver to provide a smooth surface and finally it is cleaned with isopropanol in order to remove any dust or residual jacket material.

To achieve good electrical conductivity between the fibre and the FIB and prevent charges accumulating on the fibre surface, the fibre surface was coated with a gold layer of ~200 nm thickness, using vacuum deposition (Edwards Auto 306). To further enhance the conductivity during the FIB process, a small portion of graphite paint was applied to the surrounding area of the fibre end to offer good electrical contact between the fibre and the grounded holder. Graphite is more suitable than silver paint that is commonly used for this purpose because it can be more easily removed from the fibre after the FIB machining process is completed. This minimises risk of damage to the fibre, and reduces potential contamination for subsequent experiments. The graphite was simply removed from the fibre by simply immersing the fibre in water.

4.3.2 Mounting the sample in the FIB chamber

The prepared sample (stripped, cleaned and gold-coated MCF) was mounted on the stage inside the vacuum chamber, and its exact position was controlled via the software driving the positioning system but also manually through the stage controllers, whenever needed. The sample positioning process was viewed on the PC screen displaying the images as captured by a detector. Once in the correct position, a SEM image of the sample was acquired for reference and measurement purposes. Once all the important measurements such as the adjacent and diagonal core-core distance measurement as well as the distance of the cores from the edges of the fibre were obtained, the FIB system was turned on and the sample was rotated automatically to 52˚ to ensure it was correctly aligned to the FIB beam gun. A software tool was used to define the pattern of fabrication and machining was monitored using live SEM imaging of the sample.

The initial step of mirror fabrication was to locate the cores of the fibres. As previously mentioned, the fibre surface was totally coated with a thin layer of gold and that made direct identification of the fibre cores impossible. For this reason, the first step was to define the core regions: to do so, the initial measurements of the dimensions of the fibre were implemented through the SEM. These measurements were used as the base to define the cores' regions in the SEM image. Appropriate circular patterns were defined using FIB software and the gold covering these areas was removed, to make the core regions visible (Fig. 4.7 a-c).
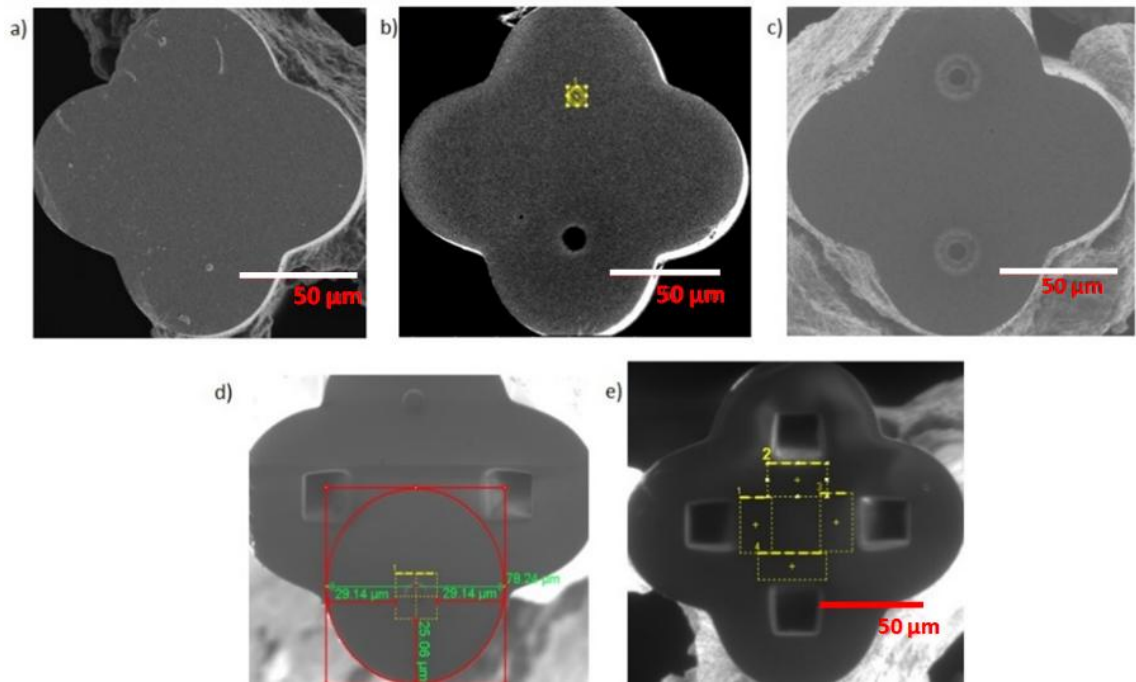
Figure 4. 7: SEM micrographs showing the steps of the FIB machining process. a) A cleaved MCF coated with gold. b) Software is used to define circular areas in the core region (yellow box).FIB removal of the defined circular areas of the gold layer from the core regions (the dark circular area towards the bottom of the fibre). This removal of the thin gold layer enables SEM imaging of the two cores and thus where the mirror structures are to be fabricated. c) After removal of a circular area of gold from two diagonally opposite core regions. The two other cores of the four-core fibre have yet to have the circular gold layer removed. d) Fabricated mirrors on two diagonally opposite cores. The red lines, yellow lines and green text are used to measure the distances from the fibre side edges to be defined as area to be machined. Yellow dashed lines represent the defined pattern to FIB machine the third core out of four in this case. e) Four cores have been FIB machined to create a mirror at each core. The fine yellow dashed lines represent the area where the thin layer of gold is to be removed from the area between the cores.

4.3.3 FIB milling process

Once the cores were located, the machining of the mirror structures could begin. The beam current for mirror fabrication was set at 7 nA, which was a value that was demonstrated to be capable of fabrication of patterns with low levels of debris and good surface finish. The fabrication was implemented for one core at a time. The first step, previously described when discussing the fibre mounting, involved removal of the circular region of the gold coating with diameter 10 μm centred on each core, to include the whole core area that is approximately 8 μm in diameter. The ion beam was then used to remove a 'slot' or 'notch' of material from a 18μm×18 μm area (Fig. 4. 7 d, e) aligned with the core to form the mirror components. The machining time for a single core was approximately 2 hours per core. As previously mentioned, the beam current that was used for the whole procedure was 7 nA, and this resulted in machining resolution of tens of nanometers, offering a good quality optical surface finish.

After mirror fabrication, a similar FIB process was followed to remove the 200 nm depth gold layer in the area between the two mirrors where the trapping beams are expected to emerge. This is to avoid absorption of the 976 nm trapping light by the gold during the optical trapping experiment. In early experiments where the layer of gold was not fully removed before the optical experiments it was clear that optical absorption led to heating effects that resulted in excessive flow due to the surrounding medium heating up as well as increased evaporation of the medium. The process of removing the 200 nm gold layer demands less than a minute, again using an ion current intensity of 7 nA (Fig. 4.7e). The resulting end face of the fibre, after the mirror fabrication as well as the removal of the gold, is shown in figure 4. 8.
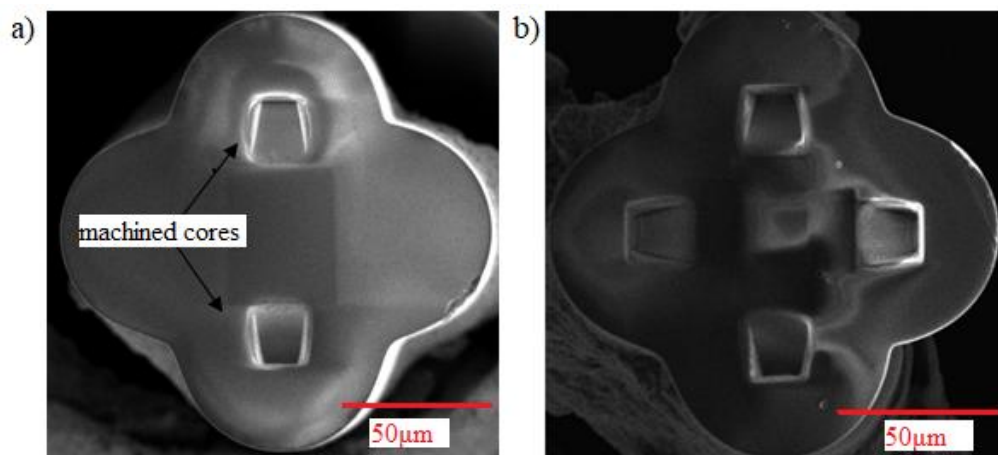
Figure 4. 8: SEM images of the fabricated mirrors on the end-face of a) two and b) four cores of a MCF. a) A rectangular area between the two cores appears in a darker shade than the surrounding area because of the region of gold removal to prevent absorption by the trapping laser light. This is also present but less easily visualised in (b).

An alternative technique to remove the gold layer after machining, whenever the FIB removal of the gold was deemed insufficient, was to use chemical etching. The fibre was immersed in a medium that consists of nitric acid and hydrochloric acid in a molar ratio 1:3, known as aqua regia, for 10-20 seconds, to successfully remove gold from the surface of the fibre. This technique was used in addition to the previously mentioned gold-removal technique in experiments where thermal effects due to residual gold were still evident.

In the early attempts of mirror fabrication, drift was a significant issue (Fig. 4. 9), possibly caused by a poor gold coating of the sample, and subsequent sample charging. For this reason, the sample was coated around all its sides and the fibre was mounted with its end-face very close to the metal holder-face (less than 1 mm) during subsequent attempts. In parallel to reassure that no unwanted drift will occur, the mirror fabrication

process was checked every 5 minutes and the beam was adjusted as necessary to compensate for any movement.
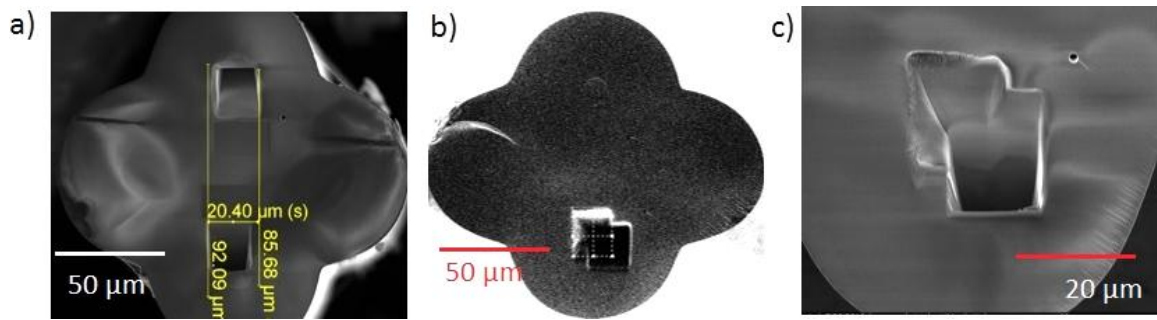
Figure 4. 9: Misalignment between the two machined patterns caused due to drifting of the beam. Better conductivity of the sample is needed to prevent misalignment of the expected fabricated patterns. a) SEM image showing the misalignment of the resulted patterns. The yellow lines indicate the left edge of the bottom mirror and the right edge of the top mirror, and their in-between distance that indicate the misalignment from the intended fabrication position. If there was no drift, the horizontal yellow line would take the value of the dimension of the pattern, 18º, thus the drift is of 2.4μm. b) FIB image that indicates the drifting of the pattern. The very fine, white, dashed lines indicate the pattern as initially defined through the FIB machining software and the dark shape, that looks like two overlaid squares, is the final pattern that was fabricated during the drifting c) SEM image of the same drifted pattern as b), zoomed in.

4.3.4 Evaluation of the fabrication technique

Once the issue of drifting was addressed, and the procedure to remove the area of gold between the cores was optimised to prevent absorption of the trapping beam, four MCFs were machined with different mirror angle pairs to evaluate the accuracy of the FIB technique. The fabricated angles can be measured after the process, using the SEM and more details in the measurement process will be presented in the next section. Table 4.1 presents the experimentally measured mirror angles for the four different MCFs. Several measurements for each core have been made using the SEM. One of these fibres had all four cores machined while the other three fibres had only one pair of cores fabricated into mirror shaped patterns. To distinguish these fibres and to maintain consistency and accuracy throughout the thesis chapters, we will name these fibres as follows:

Fibre Name	Fabricated mirror angles θ_{mir} (º)
Fibre 1 (used for the work presented in [54])	θ_{mir1} =67.5º θ_{mir2} =67.5º average 67.5º
Fibre 2 (4 machined cores fibre-pair 1)	θ_{mir1} =69.5º θ_{mir3} =66º average = 67.7º
Fibre 2 (4 machined cores fibre-pair 2)	θ_{mir2} =71º θ_{mir4} =69.5º average = 70.2º
Fibre 3	θ_{mir1} =67º θ_{mir2} =69º average = 68º
Fibre 4	θ_{mir1} =67.9º θ_{mir2} =71.5º average = 69.7º

Table 4. 1: Four different MCFs with fabricated mirror angle pairs. The fabricated angle as experimentally measured using SEM is mentioned and the average between the mirror angle value for each pair is also presented in this table.

4.3.5 Mirror angle measurement

As observed in experiments, FIB fabrication can result in minor fabrication errors (due to any uncorrected sample drift, for example) which can lead to a slight difference between the actual mirror angle and the desired angle. The milling and imaging resolution for the FIB technique is on the submicron scale (on the order of 10 nm) [146], however even for these relatively large features any small machining error can lead to a drift of the mirror angle. The machined mirror angle can be measured experimentally by observing the light exiting the fibre using the beam profile experiment that is described in detail later in section 4.3.6, but it can also be measured immediately post-FIB by imaging the fibre with a calibrated SEM. The SEM software has software routines that allows measurement of angles, corrected for the geometry of the system, an example of which is shown in figure 4.10. The fibre depicted in

figure 4.10 is Fibre 4 as named in Table 4.1 and the specific fabricated mirror angles were measured to be 67.9° and 71.5°, for a design value of 70° for both of them. The mirror that was actually measured using the SEM software tools was the angle annotated as θ in figure 4.3 and the respective θ_{mir} could be derived from the complimentary angle, equation 4.4

$$\theta_{mir} = 90 - \theta \qquad (4.4)$$
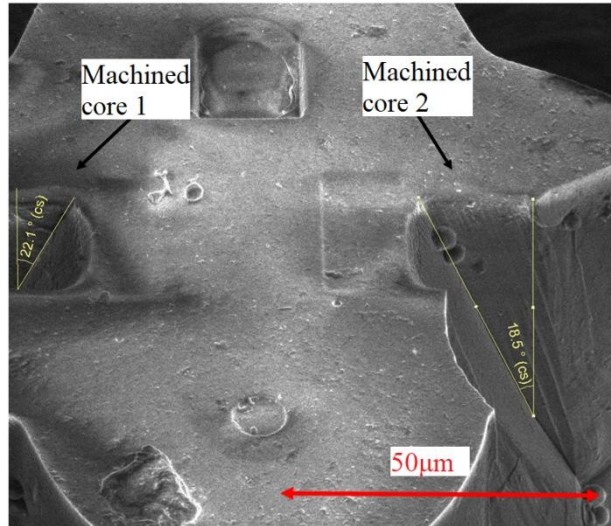
Figure 4. 10: Fabricated mirror angleσ measurementfor the two cores of Fibre 4. The angles were measured directly after the FIB machining using tools of SEM software. The mirror measured with the SEM was the mirror anotated as θ in Fig.4.3 and from this the θ_{mir} could be also calculated. The fibre edge on the machined core 2 point was broken giving better access to the mirror for measurement.

This deviation from the expected value of ±2.1° and ±1.5° for machined cores 1 and 2 respectively is believed to be due to residual beam drift during the machining process.

In the following section another important parameter of the beam characterisation, the beam divergence angle, will be experimentally measured and presented.

4.3.6 Beam direction and divergence measurement

Beam divergence is an important parameter in optics and, when it refers to a laser beam, it describes the rate at which the laser beam expands from its focus. In a similar manner the beam that exits the machined cores of the fibre trapping system will diverge, and the beam profile and divergence is of interest. Furthermore, as the cores of the MCF have been machined in such way to deliberately alter the propagation direction of the beams, this is also measured. Both beam propagation direction and beam divergence are required to develop an understanding of the trap geometry. Figure 4.11 indicates the two parameters, divergence angle (θ_{div}) and direction (θ_{prop}) of the beam, that are measured.
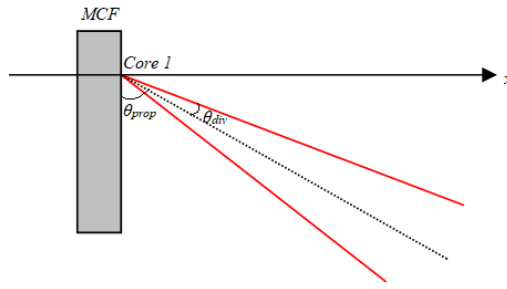
Figure 4. 11: Propagation and divergence of the beam exiting the fabricated core of the MCF. The direction of the beam is indicated by the propagation angle θ_{prop} and the dotted black line, and the divergence of the beam is indicated by the divergence angle θ_{div}, and the solid red lines. The x axis is parallel with the fibre axis while fibre face follows the axis that is vertical to x axis.

4.3.7 Beam divergence measurement- experimental setup

To evaluate the optical characteristics of the mirrors on the fibre end face, the profile of the beam exiting the machined core in water was measured. To do so, the fibre was mounted using a holder attached to an x, y, z translation stage as indicated in figure 4.12. The machined MCF is suspended in a water tank, and a frosted microscope slides, stuck on the side of the glass water tank facing the end of the fibre are used as a 'screen' so that the incident laser spot can be viewed from the opposite side of the slide from the MCF. A CCD camera is used to image the beam spot on the frosted slide as a scattered far-field image (Fig.4. 12).

As shown in figure 4.12, the light is coupled into the MCF using a fan-out device that interfaces between single core fibre and the MCF. More detail on this will follow in section 4.2.1.
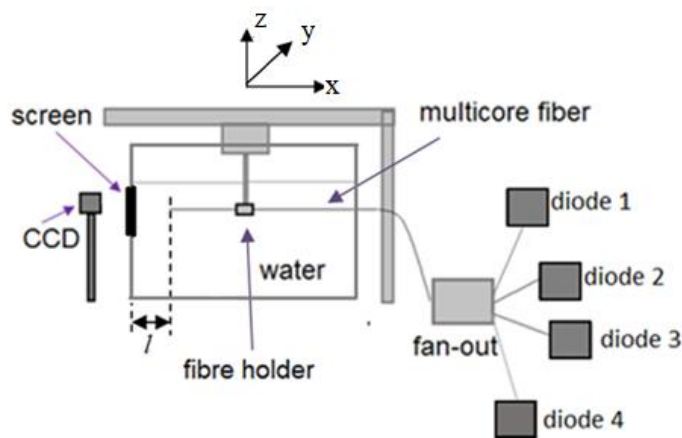
Figure 4. 12: Experimental set-up for the profiling of the beams exiting the machined multi-core fibre. The machined fibre is mounted inside a holder that has the ability to control the position of the fibre inside the tank. Microscope slides of frosted glass surface have been used as screen to image the beam spot. A CCD camera has been used to image the beam profile.

The fibre holder had the ability to move in the *x*, *y*, and *z* axes. An unmachined, single core fibre was initially used to define and calibrate the central axis of the system. This was based upon the fact that the propagation of the light exiting a cleaved single core fibre will be aligned with the fibre axis. Once the beam spot was identified, the fibre was moved away from the screen by known incremental steps. The displacements and the images of the corresponding beam spots were recorded, and the system optimised so that the central axis was well defined.

4.4 Beam divergence analysis

To obtain the beam direction and divergence from the stack of images, an analysis routine was developed (Appendix 4.1). This routine performs a Gaussian fitting of the intensity distribution of each of the beam spot images to determine the centre and width of the beam spot at different distances from the end face (*l* in Fig. 4.12). The general Gaussian equation used for this is given below and it refers to a single core of the MCF each time:

$$f(x) = a_1 e^{(-((x-b_1)/c_1)^2)} \qquad (4.5)$$

where the variables a_1, b_1, c_1 are given by

$$a_1 = \frac{A}{\sigma\sqrt{2\pi}} \qquad (4.6)$$

$$b_1 = \mu_x \qquad (4.7)$$

$$c_1 = \sigma\sqrt{2} \qquad (4.8)$$

And the coefficient, A refers to the amplitude of the Gaussian curve, σ is the spread of the distribution (a measurement of the spot size) and μ the mean value. The Gaussian distribution as shown above is normalised so that the sum over all values of *x* gives a probability of 1. Using several images with different displacements of the fibre-end from the screen for a single core of the MCF each time, it is possible to determine the beam direction and divergence. The intensity and Gaussian fit of one such beam profile, taken from one core of fibre 1 (a 2-machined core fibre) at a distance $l = 0.25$ mm, is shown in figure 4.13.
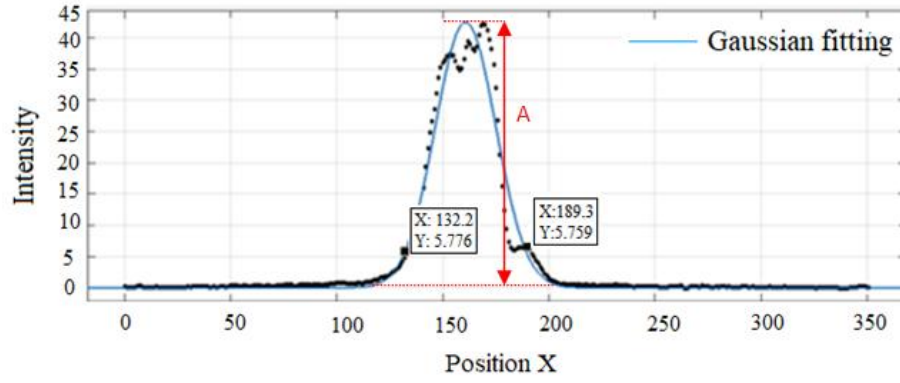
Figure 4. 13: Gaussian distribution fitting (blue line) based on the beam intensity profile indicated as black spots. The Gaussian distribution describes the intensity profile of the beam exiting one machined core of MCF 1. The amplitude A of the distribution as well as the X position of the maximum intensity are denoted in the graph. Both intensity and position axis are measured in Counts.

To calculate the divergence angle (θ_{div}) of an individual beam of the MCF, we need to obtain the beam diameter (measured here between X=132.2 and 189.3 pixels, based on the FWHM, $1/e^2$ technique) for two different distances of the fibre away from the screen, annotated as D_1 and D_2 in Eq. 4.9 below:

$$\theta_{div} = \tan^{-1}\left(\frac{X_2-X_1}{D_2-D_1}\right) \qquad (4.9)$$

where X1 and X2 are the respective beam diameters (measured to incorporate peak beam intensity) at two values of l, D_1 and D_2.

The divergence angle measurement method described above was followed for the two machined cores of Fibre 1 and for all the four machined cores of Fibre 2, and the respective results are summarised in Table 4.2.

Machined MCF		$\theta_{mirror\ fabricated}$ ($\pm0.2°$)	θ_{div} (°)
Fibre 1	Core 1	67.5°	4.4°
	Core 2	67.5°	6.5°
Fibre 2	Core 1	69.5°	3.6°
	Core 2	71.0°	1.2°
	Core 3	66.0°	5.6°
	Core 4	69.5°	4.1°

Table 4. 2: Divergence angle values of the individual beams exiting the machined cores of the MCF. Two machined fibres were measured, one MCF with two diagonal cores machines (Fibre 1 [54]) and one MCF with all four cores machined (Fibre 2).

The uncertainty of the fabricated mirror angle ($\theta_{mirror\ fabricated}$) is 1 standard deviation for the measurements implemented using SEM.

4.4.1 Propagation angle analysis

To proceed with the analysis of the propagation of the beam and to measure the direction that the beam follows when exiting the machined cores, an experiment described below, using the setup shown in figure 4.12, was implemented for Fibres 1 and 2, for two and for four machined cores, respectively.

As can be seen in figure 4.14 a, the spot shape of the beam that exits the machined cores is not circular when the fibre is normal to the screen, while the beam spot shape of a cleaved unmachined core has a circular beam profile. However, as the fibre angle with respect to the screen is varied, the shape of the beam changes until it finally becomes a circular shape. At this point the beam is normal to the screen and the angle rotated corresponds to the $(90° - \theta_{prop})$ (Fig. 4.14 b-c).
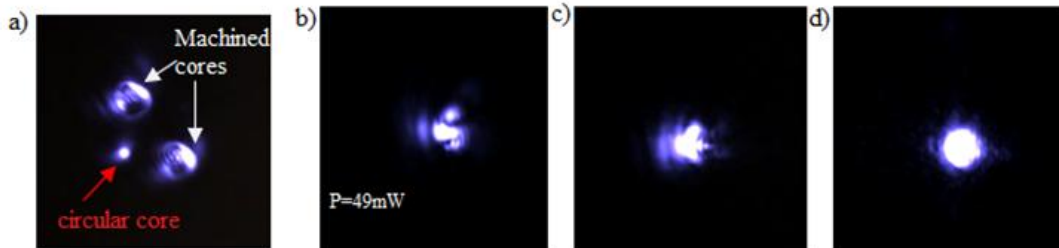
Figure 4. 14: a) Beam spots exiting an unmachined core of the MCF (red arrow) and exiting two machined cores from mirror shaped facets(white arrows) b) zoomed in spot of the beam exiting the machined core when the fibre is rotated by 0 degrees,c) beam spot when the fibre is rotated towards the fibre axis in an angle θ<(90° -θ$_{prop}$) d) beam spot when the fibre is rotatedin angle equal to 90° -θ$_{prop}$ and the spot shape appears circular.

Applying this experiment to the two cores of Fibre 1, the results displayed in Table 4.3 can be obtained. In the same table, the theoretically estimated propagation angles (using the measured value for θ_{mir}) are also displayed for comparison with the experimentally measured values. The uncertainty for the experimental estimation of the propagation angle is due to the rotary mount that was used in the lab to mount the fibre and implement the experiment (Manufacturer: Comar) and the uncertainty for the modeled value is due to error propagation.

FIB measured	Experiment	Modelled
ϑ_{mirror} (°)± 0.2°	$\vartheta_{prop.exp}$ (°)± 0.5°	$\vartheta_{prop.theor}$ (°)± 1
Core 1 67.5	52.3	51
Core 2 67.5	52.3	51

Table 4. 3: Propagation angle values of the individual beams exiting the machined cores of the MCF Fibre 1.

Once the beam divergence and propagation angles are measured, a beam propagation simulation can be developed. A Matlab model based upon the propagation of modelled Gaussian beams can be found in Appendix 4.2. This code required the estimation of additional parameters, such as standard deviation, mean of distribution and the amplitude symbolized in the code as $\sigma(x)$, μ_x and A respectively. Fibre 1, shown in figure 4.15 b, with two diagonally opposite mirror angles both of 67.5^o with measured divergences of 4.4° and 6.5°, and propagation angles of 52.3º for both angles, are inputted into the code and the simulation shown in figure 4.15(a) is generated.
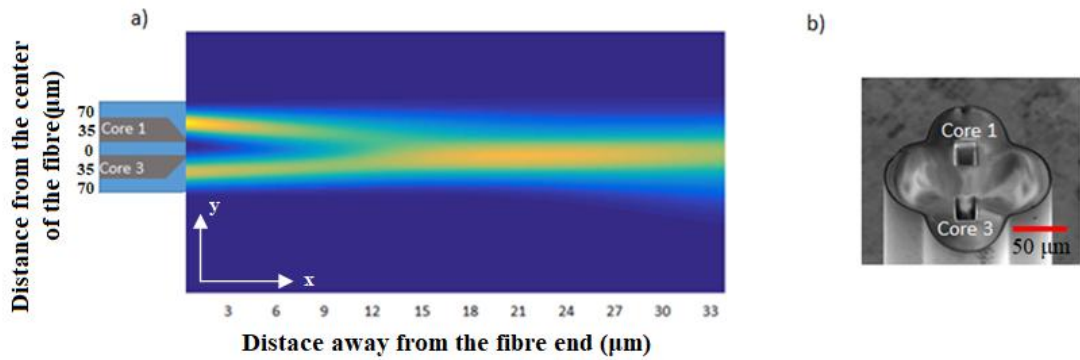
Figure 4. 15: Matlab simulation of the beam propagation exiting the MCF Fibre 1. As can be seen, the overlapping area is seen to be between 15 and 25 µm away from the fibre-end. b) A SEM image of fibre 1. The two cores 1 and 3 annotated in the machined Fibre1 to highlight the exact cores that the characterisation refers to.

In a similar manner to the above, results from Fibre 2 can be seen in figure 4.16. Fibre 2 has four machined mirrors, one at each core (1-4), of angle 69.5°, 71.0°, 66.0° and 69.5°, measured divergences of 3.6°, 1.2°, 5.6° and 4.1°, respectively, and experimentally measured propagation angles of 46.0°, 42.2°, 54.9° and 46.0°.

FIB measured	Experiment	Modelled
ϑ_{mirror} (°)± 0.2°	$\vartheta_{prop.exp}$ (°)± 0.5°	$\vartheta_{prop.theor}$ (°)± 1
Core 1: 69.5	46.0	47
Core 2: 71.0	42.2	43
Core 3: 66.0	54.9	55
Core 4: 69.5	46.0	46

Table 4. 4: Propagation angles of the individual beams exiting the machined cores of the MCF Fibre 2.

The details for two diagonally opposite cores (1 and 3, and 2 and 4) are used in the 2D simulations with the predicted beam propagation illustrated in Figures 4.16 (a) (cores 1 and 3) and (b) (cores 2 and 4).
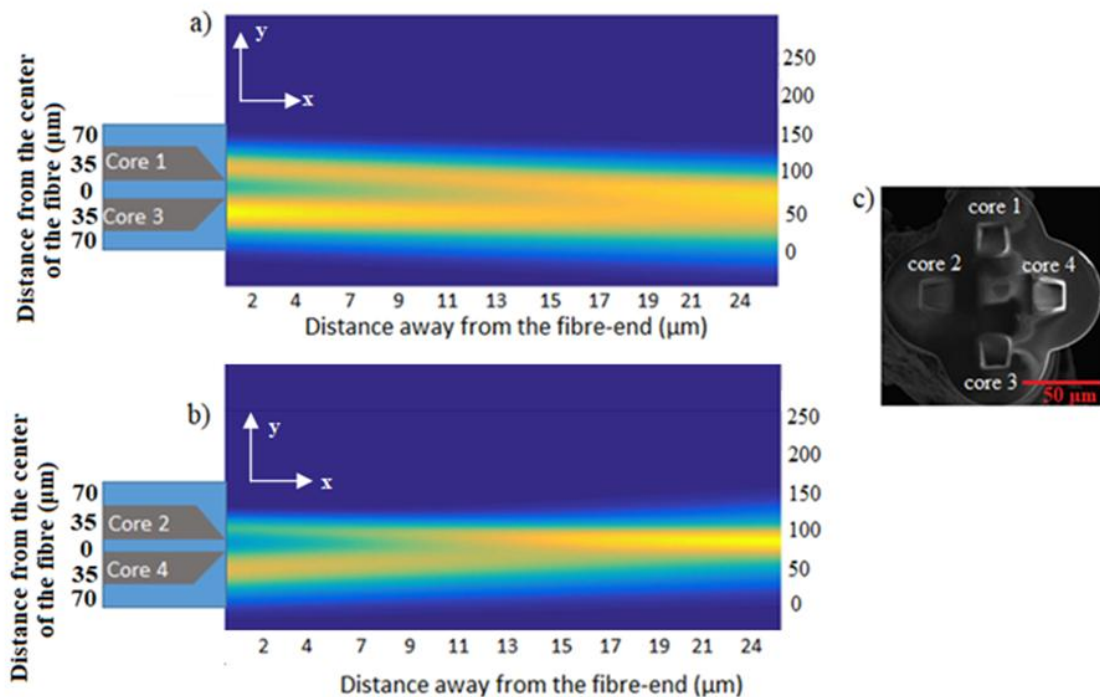
Figure 4. 16: a) Matlab simulation of beam propagation exiting from core 1 and core 3 from fibre 2. b) Matlab simulation of beams propagation from core 2 and core 4 from fibre 2. c) SEM image of fibre 2.

The difference in beam divergence from the individual beams exiting each machined core can be seen in the figure 4.15 a, and figures 4.16 a and b. There are evident differences in the divergence of the beams and resulting differences in the brightness of the beams. It is expected that in all these cases, if only one beam was tuned on then a microscopic particle of higher refractive index than the surrounding medium (water in this case), such as a yeast cell, in the vicinity of the beam, would be drawn into the region of highest light intensity (indicated by the yellow colour) due to the gradient force. Since it is not a tightly focused beam, but a diverging beam, the cell would be guided along the axis of beam propagation due to the scattering force, as discussed in Chapter 5.

When two diagonally opposite pairs of beams are turned on, resulting in overlapping beams, it is predicted that a particle would be drawn into the region of highest intensity (i.e. the overlap region) due to the gradient force, and trapped in this region so long as the scattering force is lower than the gradient force.

These predictions are tested experimentally and reported in the following experimental chapters.

72

4.5 Construction of the fibre trap system

The entire fibre trapping system is assembled from several parts, with different techniques required to connect the parts together. The fibre pigtail laser sources are connected to SMF by splicing, the SMF is connected to the MCF by using a fan-out device and the fibre trap is placed in a bespoke sample chamber to enable trapping experiments. These enabling technologies, required to construct a complete system, are detailed below.

4.5.1 Fan-out device

Figures 4.1 and 4.12 of this chapter include a fan-out component. The fan-out device is used to connect the MCF to 4 single core fibres suitable for connection to the laser diodes, so that every laser diode may transmit uniquely to each different core of the MCF. In this section the fan-out fabrication and testing is described.

Interfacing between conventional single core fibres and multicore fibres requires a fan-out component. Many approaches in designing and fabricating these fan-out devices have been published, as discussed in section 3.4.2.In this thesis, two types of fan-outs have been used. The first was based on four etched single-core fibres, placed inside a glass capillary, glued, polished and then aligned to the four-core fibre (Fig. 4. 17) [147]. This approach uses single-core fibres that are widely used in the lab and are commercially available at a low cost. This technique is described in [147] and it explains the interfacing of single-core fibres to a multicore fibre of a similar type as the MCF used for the work in this thesis.
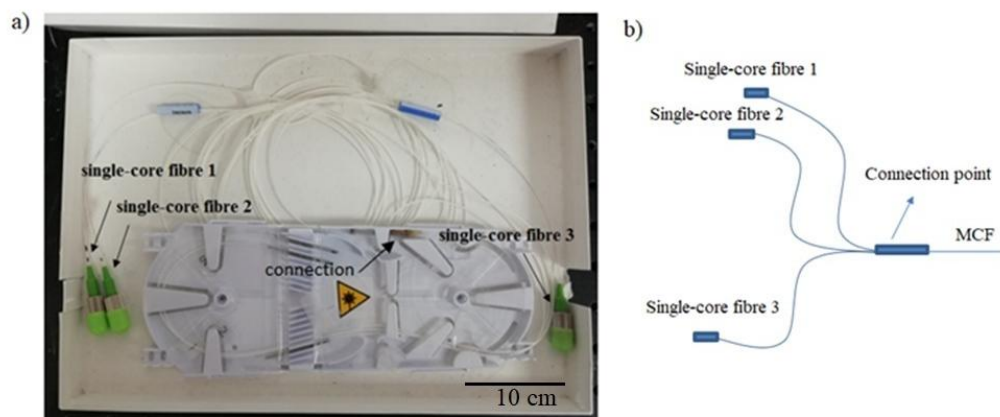
Figure 4. 17: a) Three-cores fan-out. This device was used for the optical trapping experiments that were based on two machined cores of the MCF, as well as for Fibre 1 characterisation experiments described in the previous section. It is secured in a protective sleeve labelled ''connection'' in the figure. b) Schematic of the basic concept of the three-single core fibres fan-out.

The above-mentioned type of fan-out, referred to as 'fan-out 1' was chosen as it was a device already available in the lab [148]. In this case it consisted of only 3 single core fibres and thus it could be used only for applications that required up to 3 cores of a MCF for the experiment to be implemented, therefore was well suited for experiments using Fibre 1 (the fibre with only two machined cores).

However, for applications that demanded 4 machined cores to be used simultaneously, this fan-out was unsuitable. For this reason, a second fan-out with four single core fibres coupled to the MCF was needed. The initial aim was to try to fabricate a fan-out similar to fan-out 1 type but with four single core fibres, in the lab. This "home-built" fan-out, named as 'fan-out 2', also aimed to include the exact MCF type that was also used for FIB machining (flower-shaped) rather than the circular-shaped profile that commercially available fan-outs use. More details in these different MCF types are presented in figure 4.23 later in the chapter.

The main fabrication steps can be summarised below:

Four single-core SMF800 (Thorlabs SM800-5.6-125) were stripped and cleaned with isopropanol, then immersed in 40% HF acid for 40 minutes, reducing their cladding diameter from 125 μm to 45-50 μm. A hollow square glass capillary (CM scientific ID 8510), with inner diameter 0.100 mm and outer diameter 0.150 mm was used to hold the four etched fibres tightly whilst UV curing glue was applied within the capillary (Norland products NOA 68) then set by UV illumination. To increase the robustness and eliminate the fragility of the device, the square capillary including the fibres was glued into a larger, thick-walled Borosilicate glass capillary (Sutter, B100-30-7) with inner and outer diameter 0.4 and 1.2 mm respectively. Finally, the structure was mechanically polished to yield a smooth, flat end face, as can be seen in figure 4.18.
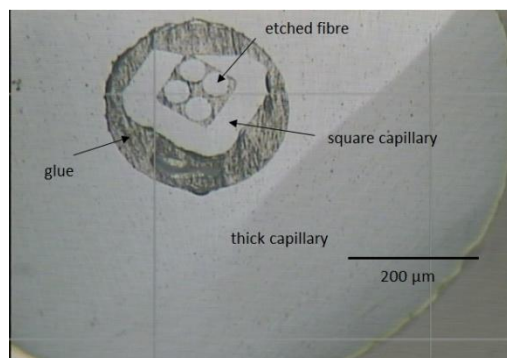
Figure 4. 18: Optical image of MCF-facing end of fan-out 2.Mechanically polished surface of four chemically etched single core fibres glued in a square capillary. A thicker borosilicate capillary was placed outside the square one, to decrease the fragility and eliminate the risk of breaking during the polishing. In this example the top left corner of the square capillary has been broken during the polishing process. The distance between adjacent cores is 50 μm.

A similar process was followed for the MCF fibre, where a piece of the MCF was stripped and glued inside the same type of borosilicate capillary prior to being mechanically polished. The results can be shown in figure 4. 19.
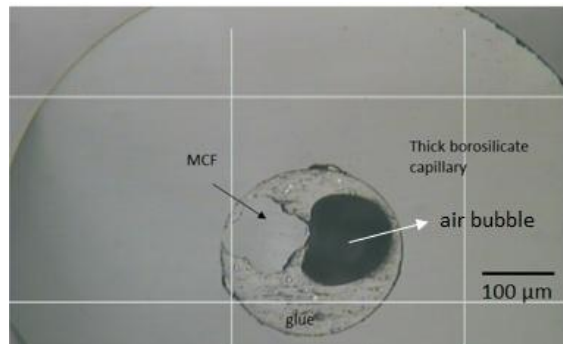
Figure 4. 19; Optical image of a multicore fibre glued in a glass capillary. The surface has been mechanically polished to have a clean and smooth surface. The thickness of the glass capillary wall was 0.7 mm while the inner diameter was 0.3 mm.

The second step of this fan-out fabrication was alignment and gluing of the two capillary parts. The two capillaries were brought close together and aligned so that the light in one of the single-core fibres was coupled to only one of the four cores of the multicore fibre. Using a combination of transverse and rotational alignment allowed the four cores of the MCF to be aligned to the four single core fibres. Once the optimum alignment was found, a small portion of a UV curing adhesive was applied around the connection area of the two capillaries and was cured using UV illumination. To manage the precise alignment, a set-up containing a multi-axis translation/rotation stage was assembled (Fig. 4. 20). Two micro-translation stages, one for each of the capillaries, were placed opposite to each other. A CCD camera was used to image the free end of the MCF. The free end of each of the single core fibres was connected to 976 nm laser diodes. This fibre coupled light could be used to aid the alignment process. The laser diodes transmit light and whilst the MCF is kept stable, the capillary with the single-core fibres is rotated around the fibre axis to achieve a combination of rotation (as indicated by the blue arrow in figure 4. 20) and translation alignment where a maximum power beam is emitted from the MCF.
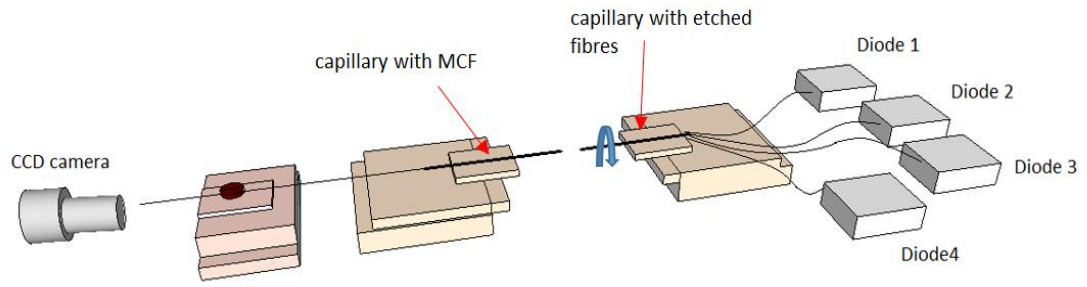
Figure 4. 20: Experimental set-up to align the two capillaries in order to build fan-out 3.The capillary enclosing the etched fibres rotates until each of the single-core etched fibre transmits light into a single core of the MCF. For this alignment procedure, every etched fibre is connected to a 976nm laser diode. A CCD camera is placed in front of the MCF cleaved end to image the fibre end face in order to assess the light transmission through the MCF.

The results of the beam output from the MCF on the CCD camera, can be seen in figure 4. 21.
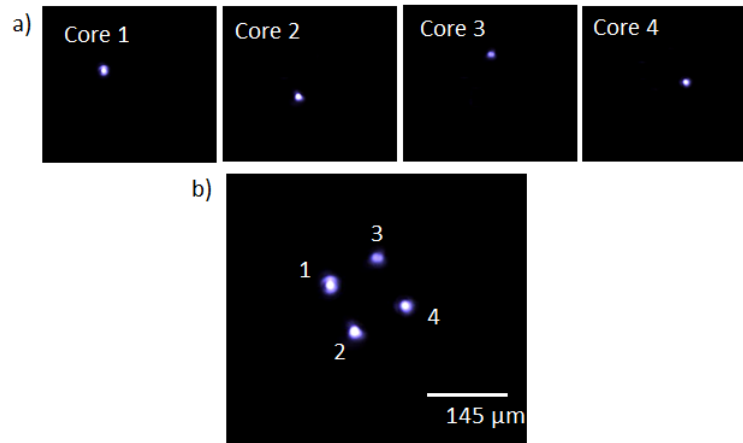
Figure 4. 21: Images from the CCD camera showing propagation of 976 nm after successful coupling in a) each core of the MCF separately, and b) all four cores simultaneously.

Although there was light coupled into all four cores as seen in figure 4. 21b, the output power of the transmitted light was insufficient for trapping purposes. The maximum power of the beam exiting the MCF was around 1.5 mW for maximum laser diode emission, whereas the minimum optical power required for optical trapping using this type of MCF arrangement is approximately 5-7 mW.

The high losses are potentially due to inaccurate alignment between the single core fibres and the multicore fibre. The alignment process was implemented manually, thus the human factor of an accidental slight movement of the stages that may occur after the application of the UV curing glue, or creep during the adhesive curing could lead to alignment errors that are significant in comparison with the μm scale of the core size.

Based upon this experience, more accurate alignment of the two fibre systems would be required to achieve lower loss coupling, by either using an automated rotation and

translation stages or by a very precise and accurate manual handling of the two translation stages. The initial objective was to fabricate a fan-out device similar to the 'fan-out 1' that could be used for all four machined cores. Because results from fan-out 2 were not sufficient for the implementation of optical trapping experiments an alternative fan-out was needed. Because of the long fabrication time for the manufacture of the in-house design of fan-out, it was decided to purchase 'fan-out 3' (Fig 4.22 a) and use this as a route to quickly achieve coupling into all four cores of the MCF.

'Fan-out 3'was a commercially available product (3D OPtoFan[TM], Optoscribe Ltd.), based on 3D laser inscribed waveguides (an example illustration is shown in figure 4.22b) to interface between the MCF and SMF as described in [141]. This manufacture approach uses femtosecond laser pulses to modify the local refractive index of a substrate at the beam focus and thus 'write' waveguides in 3 dimensions. A Ti: Sapphire laser system with a central wavelength of 800 nm can be used to inscribe the waveguides. The waveguides are created by moving the translation stage that holds the substrate material, in three dimensions, to trace out the required network of waveguides. This device had been used for 4-core optical trapping experiments.
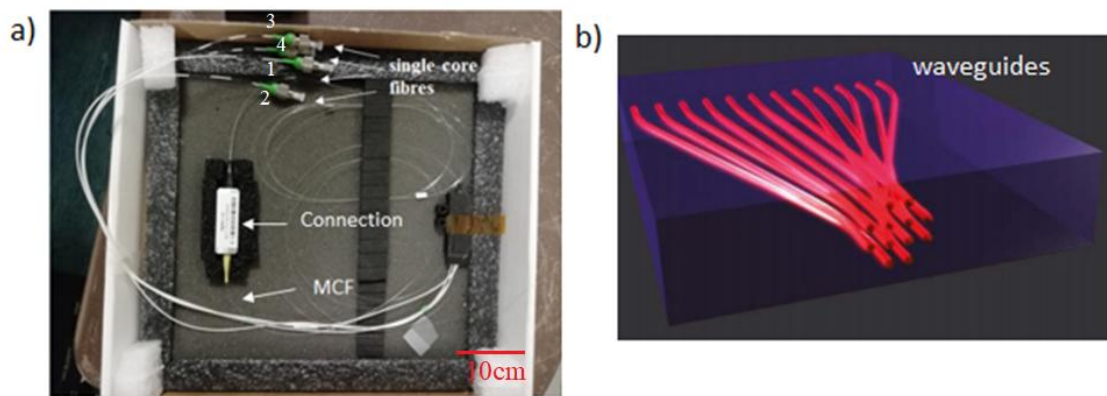
Figure 4. 22: a) Commercially available fan-out device (Optoscribe Ltd.) with four single core fibres inputs. The fibres have been annotated with different numbers to distinguish them during the experiments so laser power in each core of the MCF can be tuned. b) Schematic showing the 3D structure of inscribed waveguides in a silicon substrate (image taken from Optoscribe website), here corresponding to a 12-core example.

4.6 Optical fibre splicing

Both types of fan-out, 'fan-out 1' and 'fan-out 3' have been used to connect light from the laser sources into the cores of the machined MCF. However this requires splicing of MCF to MCF. Typically two splices are needed: Firstly, the connection of the fan-out MCF to a spare 'extension' length of the same MCF type that was used for mirror fabrication. The addition of this sacrificial length of MCF is an important step to extend

the available length of the MCF on the fan-out so that it can be cut back and cleaved as required for each new splice and thereby used for multiple experiments. Afterwards, the MCF extension is connected to the individual machined MCF samples.Both of these splices are implemented using thermal (arc) splicer and the details of this non-standard process are described in the following section.

4.6.1 MCF splicing

To allow testing of multiple probes, it is necessary to be able to splice MCF to MCF. Both types of fan-outs have been spliced in the same way to the machined MCF samples. The two different types of MCF that have been used are: 1) one that is 'flower-shaped' (figure 4.23a) and is also the type that is FIB machined to form the tweezing fibre, and 2) one with a circular facet (figure 4.23b) but with similar core-core distance as the 'flower-shaped'. The circular cross section fibre is the type used in both fan-out types used in this work. The circular shaped MCF is used in the commercially available fan-outs because it is a MCF type that can be also found commercially. The cross-sections of both MCF types are imaged below using an optical microscope (Fig. 4. 23).
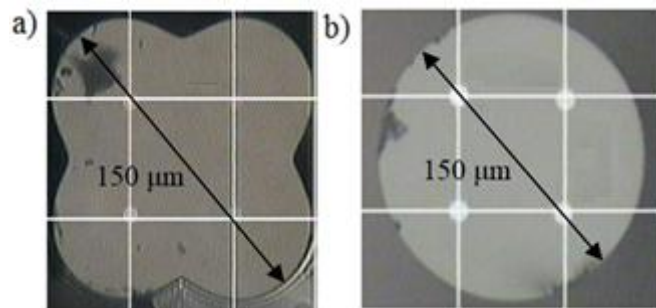
Figure 4. 23: a) Cross-section of the multicore fibre used for FIB machining to create the fibre trap. b) Cross-section of the circular multicore fibre that is used in both of the fan-out devices used in this project.. The diagonal diameter of (a) and the diameter of (b) are very similar and equal to 150±1 μm.

The process of connecting two multicore fibres with different cross-sections can be a demanding and difficult process, especially in terms of achieving suitable alignment to generate low loss splices. The fibre has to be correctly aligned in the x, y, and z axis, and also in the axis of rotation, aligned with the fibre axis.

In this thesis, a fusion splicer (FSM-100P+, Fujikura) that allows manual control of position and rotational alignment of the fibre was used in order to thermally splice the two types of MCF, including the dissimilar splice between the circular-shaped MCF of the fan-out to 'flower shaped' extension length of MCF. Before splicing the machined MCF to the fan-out, a longer length of unmachined perpendicularly cleaved flower-

shaped MCF was spliced on the end of the circular-shaped fibre of the fan-outs to avoid decreasing the length of the original fan-out fibre when many new splices of different machined MCFs are needed. An overview of the splicer and its application to the simpler case of two single-core fibres, is shown in figure 4. 24.

Figure 4. 24: a) Photograph of the fusion splicer used in this thesis. b) Screen showing the cross-section of two single-core fibres of 125µmcladding diameter, placed inside the splicer, before the splice. The X and Y indicate the respective cross sections of the fibres. c) The two fibres are manually aligned along their core axis. d) Image of the new fibre after the splice of the two single fibres.

To start, the free end of the fan-out MCF (round cross section) needs to be stripped, cleaned and cleaved and placed in the fibre splicer groove. In a similar way, the extension length of the 'flower-shaped' MCF needs to be stripped, cleaned and cleaved. The cleaved fibre is also mounted in the splice groove and at this point the splicing process can begin. The cleaving of the fibre surface is a very important aspect for delivering a good splice, because splice errors can arise due to poor cleaving.

In the splicer, the fibres are side illuminated, from two orthogonal directions, X and Y as shown in figure 4.24b. A video camera captures the images to be used as a guide for alignment. The FSM-100P can also image the end face of the fibres to allow also manual rotational alignment about the fibre axis to further increase the accuracy of the rotation. The rotational alignment can be achieved by rotating the two fibres until one

core of the fan-out MCF is aligned with one core of the flower-shaped MCF extension. This alignment requires high precision, otherwise transmission losses due to poor splicing may occur. For this reason, a visible red laser is used to monitor transmission of the light through the cores and thus minimise losses due to misalignment. Once the maximum output power through all four cores separately is known, then fibre rotation is optimised. Once the manual alignment in all x, y and z axes is complete, the software then automatically places the fibres at the correct separation before completing the splice.

In the same way, the free end of the 'flower-shaped' extension fibre is connected to the cleaved end of the FIB machined MCF.

4.6.2 Fusion splicing losses: calculations

As mentioned in the previous section, core misalignment during a splice can lead to transmission losses. In addition to this, any mismatch in the fibre refractive index can lead to an additional loss due to Fresnel reflections.

In this thesis the work is restricted to using the available MCF, therefore there is little that can be done to affect the Fresnel losses.

Losses due to misalignment can be modelled. In the geometry used here, a lateral misalignment of the fibre is most likely and is considered further. The transmission loss is approximated by T_1 given in Eq.4.10[114]:

$$T_1 = 2.17\left(\frac{y}{\omega}\right)^2 \text{ dB} \qquad (4.10)$$

where y is the lateral misalignment and ω is the normalized spot size (diameter of the beam spot).

To calculate the normalized spot size, ω, equation 4.2 [114] was used.

$$\omega = \alpha \frac{(0.65 + 1.62V^{-3/2} + 2.88V^{-6})}{2^{1/2}} \qquad (4.11),$$

where α is the core radius and V the normalised frequency, calculated as below using equation 4.3 [114,149].

$$V = 2.17\frac{2\pi\alpha}{\lambda}\sqrt{n_1^2 - n_2^2} \qquad (4.12),$$

where λ is the wavelength of the laser beam and n_1 and n_2 are the refractive indices of the core and the surrounding cladding, respectively.

For the 'flower shaped' MCF that has been used for the extension fibre and for FIB machining, the parameters take the following values after measuring them in the lab:

$$\alpha = 4 \text{ µm}, \ \lambda = 980 \text{ nm}, \ n_1 = 1.47 \text{ and } n_2 = 1.46$$

The normalized spot size and normalized frequency are therefore calculated to be:

$$\omega = 2.018 \text{ µm}$$

and
$$V = 9.51$$

so the loss in dB caused by the lateral misalignment is calculated, for 1 µm lateral displacement, to be equal to $T_1 = 0.532 \text{ dB}$ where a0.5 dB loss is equivalent to a percentage of loss of 11 % [114].

4.6.3 Optical loss characterisation

Once the MCF end of the fan-out is spliced, via the extension MCF fibre, to the machined MCF then the four single-core fibres of the fan-out can be connected to each of the four laser diodes sources. However, both splicing and fan-out connection are two processes that add to the overall losses of the system. More specifically, to estimate these losses, we take record of the output power in three different regions of the optical system: firstly, at the laser diode output, secondly at the end of the spliced extension MCF length of the fan-out and finally, at the end of the FIB-machined MCF that is spliced to the extension of the fan-out (Fig. 4.25). All the power measurements have been summarised at the Tables 1 and 2 in Appendix 4.3.
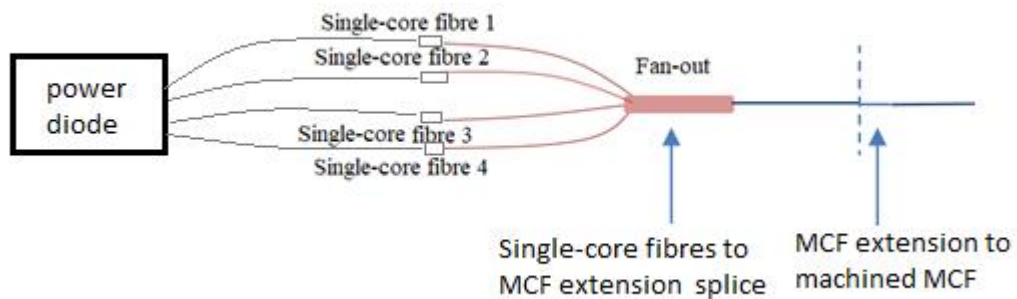
Figure 4. 25: Measurement of losses at two different points of the tweezing system after measuring the powers at the laser output. The first measurement of the output power of the trapping system took place directly after the fan-out extension MCF and the second measurement concerned the output power after the splicing of the machined MCF to the fan-out.

The measurement of the losses took place at two points in the MCF system. The first measurement concerned the fan-out losses and refers to the difference between laser power and MCF output and the second measurement concerned the splice losses which can be considered as the difference between fan-out output and the spliced machined fibre output.

Five different laser diodes have been used for the optical experiments in total, each for a different purpose and a record has been kept about the specific diode used each time in order to ensure correct device operation. The laser diodes used in this work each have maximum output power 330 mW and wavelength 976 nm (Thorlabs, PL980P330J, and controller CLD1015). The laser diode output powers have been calibrated by measuring the optical power in a range of drive currents from 0 mA to 400 mA (Fig. 4. 26). This calibration data was measured directly at the fibre of the laser diode output, i.e. before the splices and the fan-out.
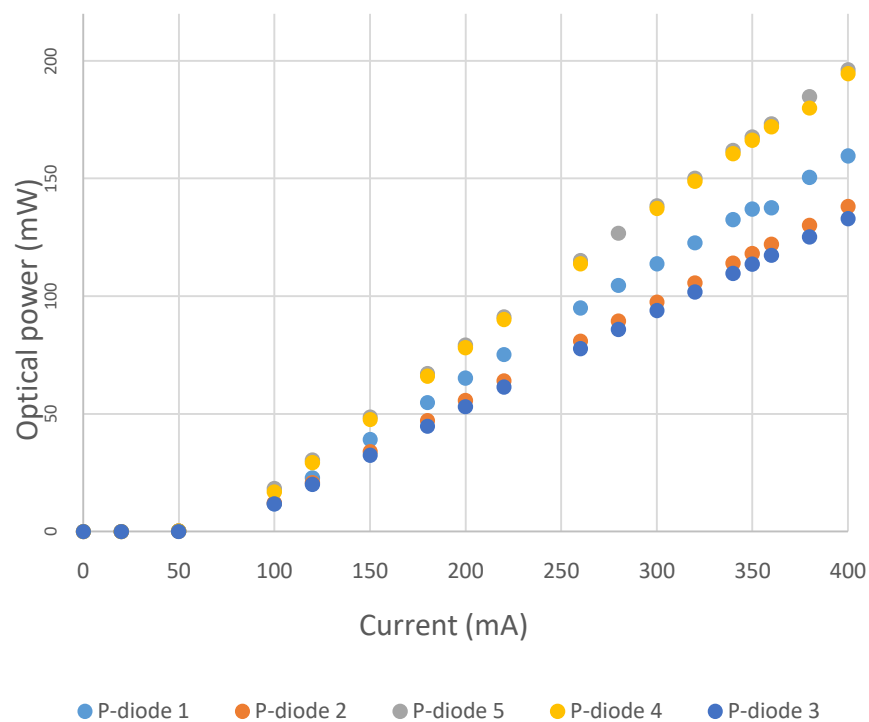
Figure 4. 26: Calibration of the 976 nm laser diodes' output power relating to the current, before the fan-out and the splices. Error bars for these measurements are too small to be included in the graph and they are equal to ±0.1mW and ±0.1mA, for the vertical and horizontal graph axis respectively.

First, the losses due to the connection of the MCF containing two machined cores (Fibre 1, as introduced earlier) to the etched fibres-based fan-out (fan-out 1, described in section 4.5.1) are presented in Table 4.5.

	Diode 1-Fan-out core 1	Diode 2-Fan-out core 2	Fan-out core 1-Machined core 1 (Fibre 1)	Fan-out core 2-Machined core 2 (Fibre 1)
Losses in dB	11 dB	6 dB	0.6 dB	0.1 dB
Output power as % of input power	8.0 %	21.5 %	85.8 %	97.1 %

Table 4. 5: Optical power losses for the MCF system containing two machined cores (fibre 1) and the etched fibres-based fan out device 'fan-out 1'.

In Table 4.5, losses due to 'fan-out 1' and splicing of the MCF (Fibre 1) can be seen. The fan-out consists of an 'extension' piece of MCF and the fan-out loss measurement was made after that MCF extension.

It can be noticed that the fan-out losses due to coupling the laser sources to the fan-out are significantly larger than the losses caused by the splicing of the machined MCF to the extension of the MCF.

In a way similar to the one followed for the fan-out 1 and Fibre 1, the losses related to the fan-out 3 and the machined Fibre 2 are presented below in Table 4.6. These losses measurements have been repeated for all four cores.

	Diode 3-Fan-out core 1	Diode 4-Fan-out core 2	Diode 2-Fan-out core 3	Diode 5-Fan-out core 4	Fan-out core 1-Machined core 1	Fan-out core 2-Machined core 2	Fan-out core 3-Machined core 3	Fan-out core 4-Machined core 4
Losses in dB	7 dB	6 dB	5 dB	5 dB	3 dB	5 dB	3 dB	3 dB
Output power as % of input power	17.7 %	20.2 %	31.3 %	31.4%	42.8 %	30 %	46.4 %	45.7 %

Table 4. 7: Optical power losses for the MCF (Fibre 2) with the four machined cores and the inscribed waveguide-based fan out device ('fan-out 2').

As can be seen in Table 4. 5 and 4. 6, the losses due to the connection of the fan-out to the laser sources are significant, showing optical transmission of 18 to almost 32%, whereas the losses due to the splicing of the machined MCF to the fan-out MCF extension reach up to 45%. Despite high losses, the final output power exiting the MCF cores is sufficient for the optical trapping experiments. However, for applications that need higher optical powers, or improved system efficiency, lower loss fan-out devices and splicing would be required. The waveguide-based fan-out shows smaller levels of losses in the output power. To increase in precision during the splicing of the machined MCF to the fan- out, greater precision in the alignment of the cores with the single- core

fibres need to be achieved, potentially through active alignment and monitoring of all the four cores simultaneously.

4.7 Laser machining of microfluidic channels

In this thesis, some trapping experiments need bespoke microfluidic channels fabricated on the surface of a glass microscope slide to contain the cell sample, define a trapping region, and control the motion of the fibre trap. Optical trapping experiments using machined MCF as described in this chapter, require a microfluidic structure with channels designed to hold the fibres in place, as well as reservoirs and deeper channels to deliver fluid containing microparticles.

A widely known technique suitable for glass machining is ultrafast laser material processing which is based upon the interaction of the laser pulses with the material-target [150]. This technique uses a focused laser beam to selectively remove material from a substrate. It can be categorized according to the laser pulse width into femtosecond (fs), nanosecond (ns) and picosecond (ps) laser machining and has previously been summarised in section 3.4. The main interaction that takes place during laser machining in ps regime is mostly thermal. Due to the short pulse duration there is good control over the volume removed and the size of the heat affected zone. However, cracks can appear on the surrounding surface, due to a sudden increase of temperature that introduces a shock wave, and this is one of the most important disadvantages of ultrafast laser machining technology [151].

In the focal region the beam heats the surface so that the material melts, vaporizes or undergoes chemical degradation [152-153]. Vaporization leads to material removal.

The relatively low cost, robustness and the rapid reproduction of bespoke structures machined on surfaces are cited as the main advantages of the ultrafast laser machining technique [154]. Furthermore, the volume of the removed material would not exceed 1 μm^3, which means micron-scale precision and control during the machining process can be achieved [155].

The approach that was chosen was ps laser machining as it combines high speed machining, micron scale resolution, and the ability to create bespoke microchannel patterns. Although not as accurate as FIB machining, it is significantly faster and therefore of lower cost. The reduction in machining accuracy is not an issue in the case of microchannels fabrication, where features smaller than 10 μm are not required.

The ultrafast laser used for making microchannel structures in our sample slides was the TrumpfTruMicro 5050 3C (Ytterbium doped YAG) picosecond laser. The laser provides a fundamental wavelength of 1030 nm and emits 6 ps long pulses. This wavelength can be converted into two other wavelengths, 515 nm (green) and 343 nm (UV) of 30 W and 12 W respective average power. The laser beam spot size for 1030 nm, 515 nm and 343 nm emission has been measured to be $16 \pm 2\,\mu m$, $30 \pm 2\,\mu m$ and $7 \pm 2\,\mu m$, respectively, using the knife-edge technique [118].

The borosilicate glass microscope slides (Fisherbrand™ , Catalog No.22-310397) used to create sample chambers for optical trapping experiments in this thesis were of dimensions 1.1 mm height, 25 mm width and 75 mm length. The main machining steps are summarised below.

The laser beam is focused onto the workpiece (i.e. the microscope slide) via a galvanometer scan head to quickly and accurately move the focused spot of 30 μm diameter, across the surface. A CAD file containing the desired pattern determines the pattern that the scan head follows.

To achieve the exact dimensions of the channels, optimised machining parameters such as the laser power and speed need to be determined for the chosen substrate material. This was done experimentally by testing different combinations of speed and power, in a sequence of array structures to investigate the resulting depth and roughness of the fabricated channels. The resulting machined depth was measured using the Leica microscope with an accuracy of 10 nm, by measuring the difference between the microscope surface level (as a reference) and the depth of the fabricated surface.

The optimised combination was 18.4 W power (80% of the total output power), 120 mm/s scan speed, 25 repetitions of the line scanning and 40 kHz frequency. The data from the testing of different combinations of power, speed and resulting machined depth can be found in Appendix 4.4. Another parameter which is crucial for the roughness of the fabricated pattern is the distance between the machined lines when raster scanning to cover an extended area. When a region is defined in the CAD file, hatch lines can be horizontal, vertical or spiral, depending on the suitability to the desired shape of the pattern each time. Thus, as shown from the fabricated arrays, if the distance between the lines is too large, then the roughness will be higher due to the presence of unmachined areas between the machined lines. For the fabrication of the

patterns used in this thesis the distance between the parallel horizontal lines was 0.003 mm (3 μm), allowing good overlap for a 30 μm beam diameter.

The minimum step that the computerised stage can achieve is 0.1 μm, as is defined by the translating stage software. The distance over which the focused beam has approximately the same intensity, known as Depth of Field (DOF) [156], can be given from

$$\text{DOF} = \pm 0.08\pi \frac{D_0{}^2}{M^2 \lambda} \qquad (4.13)$$

where D_0 is the laser spot diameter, M is the laser quality factor, and λ is the wavelength.

For the system used in this work, $\text{DOF} = 100\ \mu m$, which means that focal alignment better than 100 μm is required.

In summary, laser fabrication was used to make bespoke microchannel and reservoir structures on the surface of borosilicate glass microscope slides to assist with trapping experiments. A Trumpf Tru Micro 5050 3C Yttrbium YAG picosecond laser was used because of the relatively fast machining process, the flexibility this machining process provides. Surface features were written using power of 18.6 W, scan speed of 120 mm/s, 25 number of scans and 40 kHz frequency.

4.7.1 Fabrication of sample chambers

In this section, the micro-channel pattern that was designed to support MCF trapping experiments is described. Some initial work used a 'fibre bundle' of two machined single-core fibres (described in section 4.3) within a glass capillary that had an outer diameter of 1.2 mm whereas the multicore fibre had cladding diameter 150 μm and a jacket diameter equal to 242 μm, so a channel with appropriate width and the depth (at least 1.2 mm) was designed to fit both purposes.

The basic concept consisted of a micro-channel that covered half of the slide, a square shaped-trapping area with greater depth than the microchannel, and two circular-shaped glue areas. The dimensions and the depths of the pattern can be seen in Table 4.7 and the fabricated design in figure 4. 27.
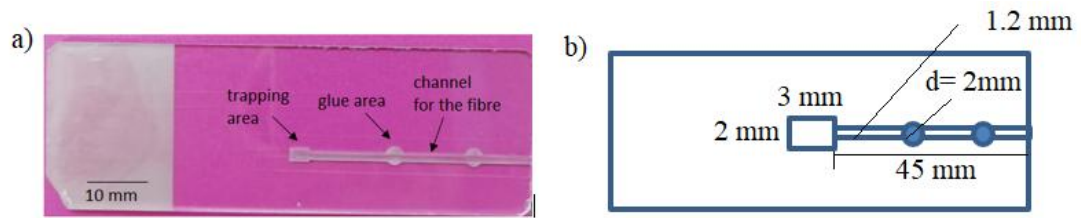
Figure 4. 27: a) Photograph of fabricated channel pattern on the surface of a microscope slide for optical trapping experiments using a bundle of fibres inside a glass capillary of outer diameter 1.2 mm or a multicore fibre of outer diameter of jacket 242 μm, b) Schematic indicating the dimensions of the machined patterns, d = diameter.

Feature	Width (mm)	Length (mm)	Depth (mm)
Trapping area	2	3	0.522
Fibre microchannel	1.2	45	0.381
Glue area	Diameter=2		0.150

Table 4. 8: Dimensions of the fabricated patterns on the surface of the microscope slide (all dimensions are given in millimeters). This slide was used for capillary-based fibre bundle experiments and MCF based optical experiments.

In Appendix 4.5 some initial work on the microchannels fabrication to demonstrate basic optical trapping experiments using two opposed single core fibres, that provides experience in both ps machining and optical trapping, is presented.

To summarise, picosecond laser machining has been used to make micro-channels on the surface of borosilicate microscope slides for trapping experiments with single-core fibres inside a glass capillary and for a multicore fibre based tweezing experiments. This technique has been chosen due to rapid and flexible machining process rate, its appropriate resolution and lower cost compared to alternatives. The machined MCF trap and associated chamber slide design are used in the majority of the trapping work in the following two chapters.

4.8 Discussion

In this chapter, the main techniques used for producing some of the parts of the MCF trapping system, such as the mirror modifications on the end of MCF, MCF splicing and interfacing and supporting technology such as fan-outs and microfluidic slides have been described.

A key enabling step for the implementation of any MCF experiment, including optical trapping is the ability to connect MCF to other components such as laser diodes. As long as there is no laser diode that can be connected directly to a MCF, the need for the use of a fan-out device remains. The fan-out devices that had been used in this thesis were of two different types, the etched fibre-based fan-out and the waveguide-based

fan-out. After measuring the power losses due to splicing of the fan-outs to the machined MCF, it had been found that the maximum loss for 'fan-out 1'was 11 dB and for 'fan-out 2' was 7 dB.

The etched fibre fan-out was used for two or three machined cores- based optical experiments and its fabrication was based on a glued stack of four etched single-core fibres, placed inside a glass capillary and attached to the four core fibre. This is an approach that uses single core fibres that are commercially available in a relatively low cost and their length can easily be extended by splicing onto more fibre, which can allow the use of the fan-out device for many different experiments. The attempt of developing a fan-out of this type for four cores, was implemented but the resulting performance was not sufficient for an optical trapping experiment due to fabrication errors. This could include variability in the chemical etching of the single core fibres, that may have resulting diameter variability of 1-2 μm which could in turn affect the core-core distance inside the glass capillary. Furthermore, the alignment of the four-core fibre with the four single core fibres was attempted manually and thus may not have reached the necessary level of accuracy. The alignment could also be subject to creep during the UV curing of the glue that was implemented between the two capillaries.

The fan-out device of the second type was used for the four machined cores experiments and it was a commercially available product, the fabrication of which was based on the inscription of waveguides through femtosecond pulsed laser writing.

The fabrication of the mirrors on the end face of the MCF, aligned to the cores, and of the correct angle to give the desired NA and trapping distance from the end face, has been implemented using Focused Ion Beam technology. With this technology a high precision fabrication was achieved and we have been able to eliminate the majority of fabrication errors that may occur during this technique, such as alignment drift for example. To eliminate a potential drifting effect, good sample grounding conductivity had to be achieved. To do this, a 200 nm thick layer of gold was deposited on the surface of the optical fibre while mounted on the holder inside the FIB chamber. At the same time, a small portion of graphite was added around the fibre to improve the grounding conductivity.

FIB machining is an expensive fabrication technique; however it can produce high fabrication precision for complex structures in comparison with other microfabrication techniques such as manual polishing, chemical etching or ultrafast laser techniques. The

beam current of the FIB was chosen to be high, so that the surface of the fabricated area was smooth, something that is necessary to provide a good internal reflector and to minimise undesired scattering of the laser light due to a high roughness.

Focus on using the machined MCF to demonstrate trapping of cells will be described in detail in the following chapters.

4.9 Conclusions

In this chapter, the main trapping set-up has been described in detail, including techniques to modify the MCF end face to incorporate turning mirrors. The aim of this thesis is to develop a single fibre based trapping system by fabricating mirror shaped facets on the end of the cores of a MCF. The technique chosen for the purpose ef the mirror fabrication is the Focused Ion beam (FIB) due o its high accuracy of the fabrication. The beam current was set at 7 nA to achieve low levels of debris and good surface finish and the machining time duration was approximately 2 hours per core. The pattern dimensions were 18μm×18 μm. Once the fabrication was completed, the mirror angles were measured through the SEM and uncertainty of the fabrication process was 1°-2° and it is believed to be due to residual beam drift during the machining process.

Propagation of the beam exiting the machined cores in water has been investigated, and a beam propagation model using Matlab has been presented. The divergence angle was experimentally measured in a water tank to be between 1°-7°, depending on any potential misalignments or drift throughout the FIB mirror fabrication process. The propagation angle of the beam exiting the machined cores has been experimentally measured and has been found to be in broad agreement with the respective expected one based on the actual FIB machined mirror angle. The experimental set-up used for the optical trapping experiments has also been presented and it consists of fibre trapping system and an associated imaging system to view the effect of the trapping. The optical trapping system includes the MCF with the machined mirror shaped facets, four 976 nm wavelength laser diodes, a fan-out to connect the MCF to the four single-core fibre pigtailed laser diodes and a microscope slide with machined surface microchannels to mount the sample. The imaging system includes a microscope objective, a CCD camera that images the experiment from top, an illumination source from below and xyz micro translating stages for high-accuracy movement of the sample. For the fabrication of the microchannel patterns on the microscope slides, ps laser machining was chosen as it combines high speed machining, micron scale resolution, and the ability to create

bespoke microchannel patterns. Although not as accurate as FIB machining, it is significantly faster and therefore of lower cost. The reduction in machining accuracy is not an issue in the case of microchannels fabrication, where features smaller than 10 μm are not required.

This experimental setup is used in the next chapter, Chapter 5, where optical trapping experiments of single yeast cells are presented. Experimental evaluation and characterisation of the optical trap strength and comparison of this value with other techniques of the existing literature is presented.

Chapter 5: Characterisation of multicore fibre optical traps

In Chapter 4, two different trapping fibre types were described, one having two machined mirrors and one having four machined mirrors, two systems that will be called throughout this chapter "two-beam" and "four-beam" trapping, respectively. In this chapter, optical trapping and manipulation of single yeast cells by two and four beam traps is demonstrated, and characterisation of the optical traps is presented. The characterisation of the trap includes estimation and/or calculation of the theoretical and the experimental d_{trap} and NA, maximum translation speed and maximum force for different powers. A comparison between the two and the four beams trap as well as comparison of the fibre systems with other fibre traps and conventional OT systems in the literature are also presented.

To maintain consistency between experiments and to ensure an accurate comparison between the efficiency of the two trapping approaches (two-beam or four-beam trapping), the same single fibre with four mirrors was used for both cases. Illuminating only two cores out of the four for the two-beam system, and illuminating all the four machined cores for the four-beam system respectively. In this way potential experimental uncertainties associated with the use of two different fibres (i.e. variation in splice losses, or differences in machining properties) are minimised.

5.1 Theoretical estimation and experimental observations of d_{trap}

Before moving on to the presentation and analysis of the optical trap, a theoretical estimation of key parameter, d_{trap} and for a variety of mirror angles, as well as some experimentally observed trapping distances and the respective calculated NA are described in this section. This section will provide an insight of what is expected to be seen throughout the experiments based on the designed mirror angle and it will highlight the main outcomes from the majority of experiments that demonstrate the working MCF.

Different mirror angles (θ_{mir}) all larger than the critical angle of 64.8° lead to different beam propagation angles (θ_{prop}), and thus result in different trapping distances (d_{trap}). The graph presented in figure 5.1 shows in solid blue line the theoretically calculated (i.e. expected) d_{trap} for different mirror angle values. The single blue data points that are presented in the figure refer to the trapping distances that were experimentally observed

in optical experiments of yeast cells using different machined MCFs, with different machined mirror angles.
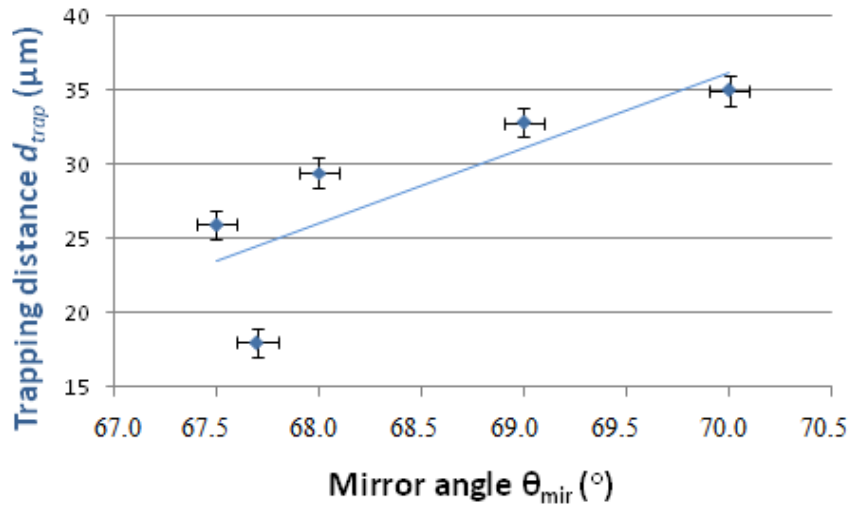
Figure 5. 1: Experimentally observed trapping distances (blue circles) of yeast cells, based on five different fabricated mirror angles. The theoretical estimation of d_{trap} is also shown as blue solid line, to highlight the deviation of the experimental values from the theoretical estimation.

The experimental trapping distance d_{trap} has been measured using the microscope images of captured yeast cells and it is measured from the fibre end face to the centre of the trapped cell. The resolution of this optical CCD imaging system and the pixel size as well as the differences in the 3 frames analysed leads to a position uncertainty of 1 μm. The NA can be calculated using Eq.5.1 for the fabricated angle.

$$NA = n_m \sin(\varphi) \qquad (5.1)$$

The error bars in x-axis come from the uncertaity in mirror angle measurement, while the respective error bars in d_{trap} in y-axis come from the uncertainty in d_{trap} measurement. As can be seen in the graph, the majority of the experimental values of the trapping distance are in broad agreement with the theoretical ones, with an exception of the 67.7° where the experimental value is much smaller than the theoretical one. This difference in the trapping distance could be explained due to the refraction of the exiting beam through the cells that are perhaps stuck to the fibre and nit visible under the microscope. This scattering can alter the resulting propagation of the beam and thus of the overlapping area position. This can lead to a different experimental trapping distance than the expected one for the same mirror angle.

It may be possible to generate traps with higher NAs by coating the fabricated mirrors facets with metal so that a greater range of mirror angles could be used. However,

92

detrimental heating has been reported in the presence of metal films and this has observed in this work when using metal coated fibres due to absorption of the 976 nm tweezing beam and therefore this approach has been avoided in this thesis.

The initial approach to determine the efficiency of the optical trapping systems was to trap Polybead Polystysterene microspheres (sizes 0.5μm, 1 μm and 3 μm, Thermo Fisher Scientific model [9003-53-6]) of refractive index $n_{microsp\ heres} = 1.59$. Use of uniform, manufactured particles aids experimental repeatability by avoiding variation between different particles, whereas with biological cells, intercellular variability in cell size, shape and composition is naturally present. Initially the use of polymer microspheres worked well, however damage to the fibre due to contamination by these particles was observed. It was noticed that after 4 or 5 experiments the polymer microspheres stuck to the fibre surface and in the mirror facet, which greatly affected the beam propagation and the formation of a stable trap. In an attempt to eliminate this issue, several approaches were investigated, such as adding surfactant to the sample to reduce the 'stickiness' of the particles and the fibre, and the use of an ultrasonic bath to clean the fibre after every optical experiment. However, despite using both of these approaches to mitigate the problem, the fibre surface remained contaminated. Furthermore, damage such as chipping of the fibre was observed after frequent ultrasonic bath cleaning. In addition, the cleaning process required dismantling of the fibre out of the set-up and then remounting after cleaning. This manual handling increased the risk of damage to the fibre. For these reasons, it was decided not to use polymer microparticles for the trapping experiments in this thesis and to find a less damaging alternative 'particle'.

The next rational option was to use cells, initially of a cell type that was relatively close to the microspheres' size, to investigate the efficiency of the geometrical mirror-based pattern and the repeatability of the results of optical trapping experiments. In this work yeast cells are used, as they are considered to be nominally uniform in structure and size.

Yeast cells have other advantages, they do not have a requirement to be cultured, they grow well at room temperature and conveniently, they can be suspended in water.

The yeast cell type used in these experiments; *Saccharomyces cerevisiae*, known as 'baker's yeast', exhibits a diameter typically in the range of 5-10μm. They are prolate spheroid in shape, but when optically trapped they appear circular under the

microscope. In this thesis, the yeast cells that were used for optical trapping experiments have been measured and their diameter found to be d=7μm±1 μm, where the uncertainty is associated with the difference between the highest and lowest value of the 10 different cells that were measured.

To evaluate the optical trap in terms of its strength, in other words the maximum force it can exert on a cell, a calibrated, conventional, microscope-based Optical Tweezing system (OT) was used. The OT force required to overcome the fibre trap force [54] for a given fibre trap power, was used to calculate the maximum MCF trap force and the quality factor (or efficiency of the trap) Q. The results derived from this method were used to compare the fibre trap with other published fibre-based trapping techniques as well as with conventional optical tweezers, in terms of trap strength and efficiency. Trapping force and Q will be defined in detail in section 5.4.

The maximum translation speed of the fibre in x and y directions (parallel and perpendicular to the fibre axis), for which the cell remained trapped, was also measured for different powers. These measurements are of practical use as they inform us how fast the fibre can move inside the microchannel while holding the cell stably in the trap, which is relevant for potential applications such as manipulation and deposition of single cells in a predetermined position on a substrate.

5.2 Two-beam and four-beam trap characterisation

Characterization of the two different trapping systems, one taking advantage of two machined cores ("two-beam trap") and a second that uses four machined cores ("four-beam trap"), was achieved by trapping yeast cells stably in three dimensions and by using a pre-calibrated conventional OT system to measure the trapping force F_{trap}, and the efficiency of the trap (Q). The machined fibre that was used for the trapping experiments (Fibre 2 as named in Chapter 4) had all four cores machined using FIB with mirror angles:

$\theta_{mirror\ 1} = 69.5^{\circ} \pm 0.2^{\circ}$, $\theta_{mirror\ 2} = 71.0^{\circ} \pm 0.2^{\circ}$, $\theta_{mirror\ 3} = 66.0° \pm 0.2°$ and $\theta_{mirror\ 4} = 69.5° \pm 0.2°$. These measurements have been made using the SEM, directly after the fabrication process, as discussed in detail in Chapter 4.3. The uncertainty of these measurements is given by 1 standard deviation of the three different measurements made with the SEM for each of the fabricated mirrors, as also mentioned in Chapter 4. A schematic of the mirror angle (θ_{mir}), propagation angle (θ_{prop}), and

the trapping distance (d_{trap}) is shown in figure 5.2 (a). A representation of the fibre end, with two exiting beams and a trapped particle, is illustrated in figure 5.2 (b).

For these machined mirror angles the beam characteristics φ and θ_{prop} as represented in figure 5. 2 (a) are calculated and shown in Table 5.1.
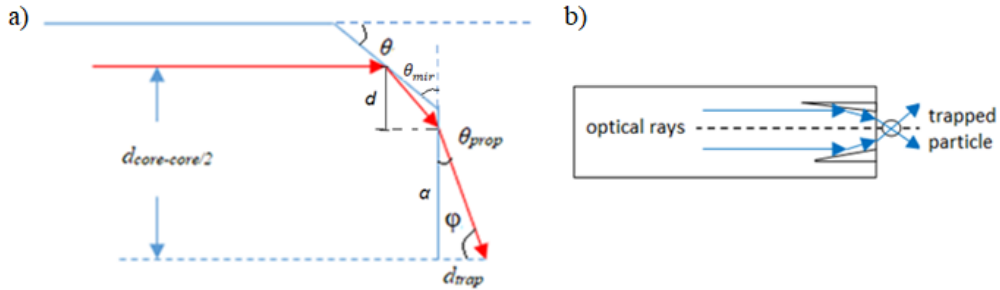
Figure 5. 2: a) Propagation of the laser beam through the machined mirror-shaped core immersed in water. b) Representation of the two beams exiting two cores of the machined-MCF, to optically trap a particle in the converging overlapping region, in water.

Core number	θ_{mirror} (°)± 0.2°	φ (°)± 0.2°	θ_{prop} (°)± 0.2°
Core 1	69.5	47.2	42.8
Core 2	71.0	43.1	46.9
Core 3	66.0	55.2	34.8
Core 4	69.5	46.9	43.1

Table 5. 1: Calculation of φ and θ_{prop} as are represented in Fig.5.2 a, for the machined mirrors, based on geometry and glass refractive index 1.46 and water refractive index. 1.33.

Figure 5.3a provides a schematic of the axis system concerning the fibre trapping based on the Matlab simulation described earlier in section 4.4.1. Figure 5.3b presents the cross-section of the machined fibre as imaged below the SEM, highilghting the machined cores 1-4 to discriminate them throughout the section. Figure 5.3a also indicates the axes system used in this thesis for the fibre trap. As can be seen, the x-axis refers to the axis that is parallel to the fibre axis, the y-axis refers to the axis that is perpendicular to the fibre axis and the z-axis refers to the axis that indicates the depth in the medium that the fibre immerses into. The yeast cell is trapped at a distance d_{trap}, as indicated in figure 5.4j and 5.5j and d_{trap} has been measured using image analysis of the captured video frames. This was achieved using 'Image J' software analysis. To convert the pixels to microns, the known diameter of the fibre (150µm) was used as a reference. The respective uncertainties of the trapping distances measured arise from the imaging camera pixel size, the ability to define the edges of the cell and the edge of the fibre face

and the different measurements of the same distance from different video frames. The exact set-up used to perform these experiments has been previously described in detail in first section of Chapter 4.
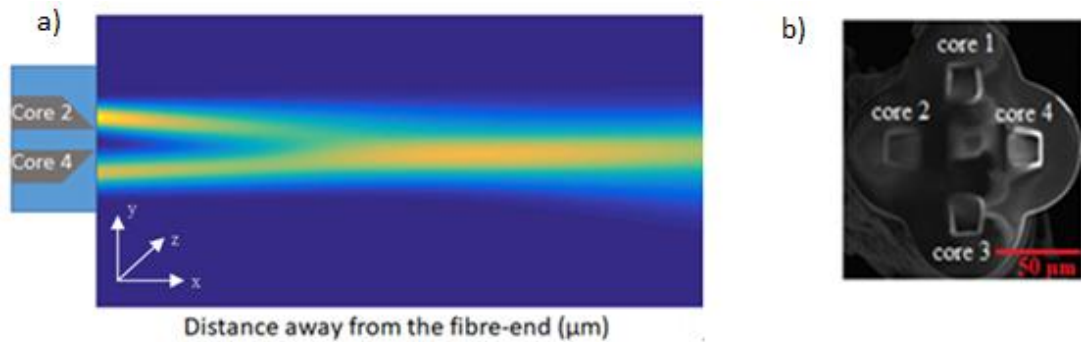
Figure 5. 3: a) MatLAB simulation of the two beams indicating the schematic of the axis system concerning the fibre trapping. The data used for this simulation are obtained from Chapter section 4.1.3, b) The four mirror shaped patterns on the end of the cores of the MCF have been named accordingly so that they can be distinguished throughout the text. For the two beam trapping, the cores illuminated were cores 2 and 4.

5.2.1 3D Optical manipulation of yeast cells

Two-beam trapping

For the two-beam trapping, the two cores used for the experiments were the diagonally aligned cores 1 and 3 (as named in figure 5.3 a and b) with mirror angles $\theta_{mirror\ 1} = 69.5° \pm 0.2°$ and $\theta_{mirror\ 3} = 66.0° \pm 0.2°$. The optical powers, were measured at the end of each core to be 5.3 mW±0.1 mW and 16.1 mW±0.1 mW for core 1 and core 3 respectively and the uncertainty is the device error. This difference in the power of each core is a result of the power losses due to splicing in the system. To check that manipulation of the trapped cell was possible in x, y and z directions without the cell falling out of the trap, the fibre was displaced along the three axes x, y and z by distances of 10's μm in each direction. At an average speed of 0.03 mm/s for all three axes the yeast cell remained stably trapped.

The initial 'feel' of the trap was strong (at the powers 5.3 ± 0.1mW and 16.1 ±0.1 mW) in all three dimensions, with a slightly stronger feel in x-axis direction, especially when demonstrating the experiments for maximum translation speed for practical applications (section 5.5). The cell could remain stably trapped in a stationary fibre trap for up to 6 min, after which evaporation of the medium started to affect sample flow. Yeast cells, in contrast with the microspheres, were much less 'sticky', and therefore less damaging to

the trapping system, thus their use in these experiments prolonged the viability of the trapping system.

Frames extracted from a recorded video showing three-dimensional trapping and manipulation of a single yeast cell using the two-beam trap are shown in figure 5.4. All the images have been cropped to be centred on the same spot in space to highlight the movement of the fibre in comparison with the position of the trapped particle. The axis along which the fibre is manipulated is highlighted in red in the axis label, the trapped cell highlighted by a red arrow and untrapped, neighbouring cells are annotated with a yellow number as a reference. The neighbouring cells change position with respect to the fibre end, in contrast with the trapped cell that remains in a stable position away from the fibre-end equal to the trapping distance. The trapping distance has been measured to be $d_{trap}=19.0\pm0.8\mu m$ for the cell shown in figure 5.4. To measure the trapping distance value, three different frames from the trapping video have been analysed and are presented in the next section and the average of these measurements is given as the final value. More specifically, the initial frame from the cell trapping in every different axis was used to measure the d_{trap} (Figure 5.4a, d, g) where there was no motion of the fibre that could potentially create flow in the medium and affect the trapping distance.

As mentioned earlier in the text, the uncertainty in d_{trap} can be traced to two sources: Firstly, it is due to the difference of the highest and the lowest trapping distance value between the three different measurements ($\pm0.7\mu m$) as well as due to the uncertainty based on the resolution of the imaging system ($\pm0.5\mu m$). To convert the pixels to microns, the known diameter of the fibre (150μm) was used as a reference. Therefore, combining these two, the resulting worst case uncertainty was $\pm$ 0.8μm.

The machined fibre is seen on the left-hand side of each image (Fig.5.4). Two of the cores are illuminated to make a two-beam trap. A yeast cell, indicated by a red arrow, is trapped. In this specific case, it is a 'doublet' or two cells stuck together, perhaps recently divided, which is trapped. As the fibre is manipulated along the x (image a-c), y (image d-f) and z (image g-i) axis it can be seen that the cell remains trapped at a fixed distance from the fibre and in focus, whereas the untrapped, neighbouring cells in the sample (marked 1, 2 and 3) change position due to the Brownian motion as well as due to residual fluid flow due to motion of the fibre through the sample. Here it needs to be noted that the image is refocused so the fibre and trapped cell remain in focus in the

image, whereas the untrapped cells move out of focus due refocusing (and due to their Brownian motion to a lesser extent).
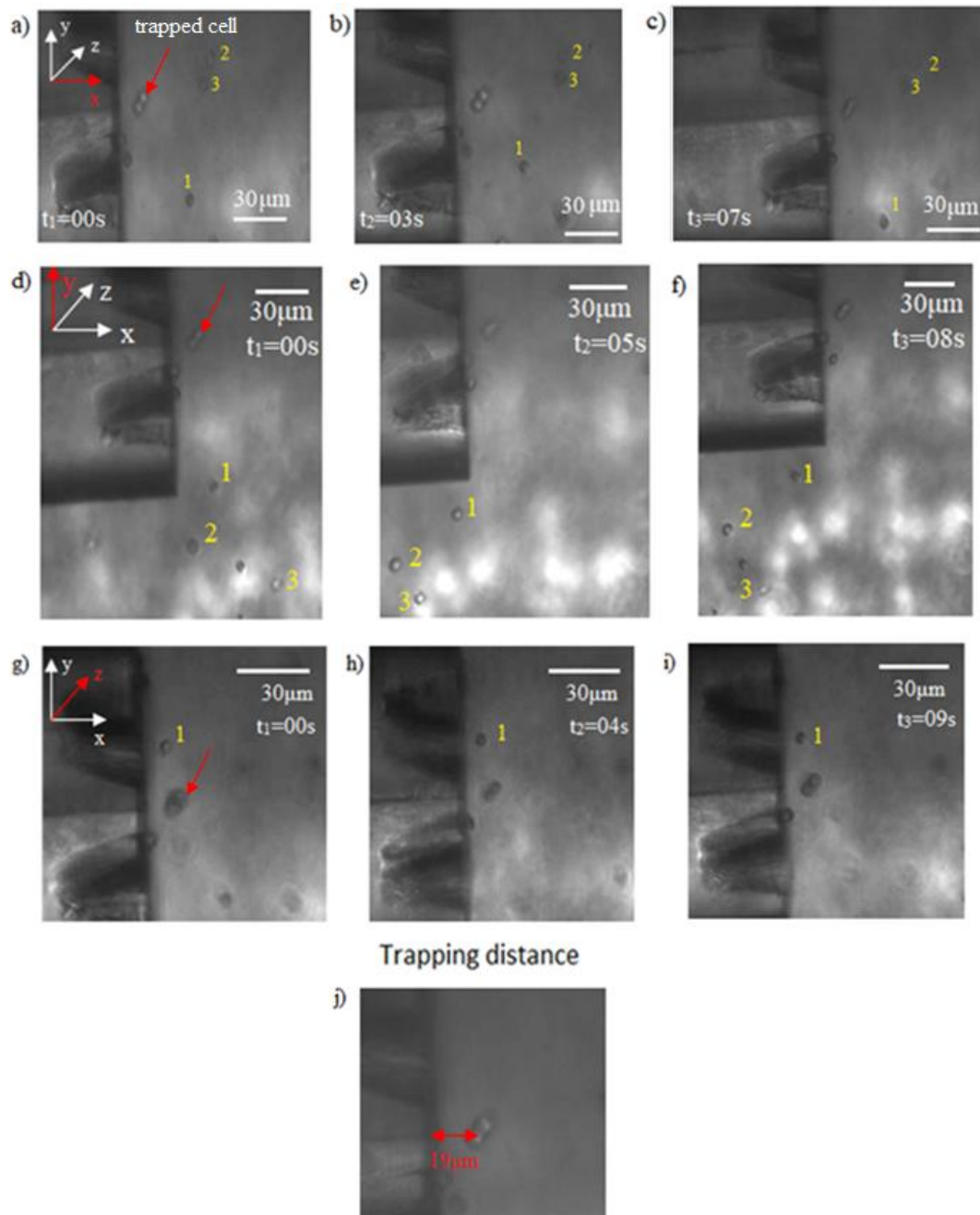
Figure 5. 4: Two-beam manipulation of two attached yeast cells in three dimensions, along (a-c) the x axis, (d-f) the y axis and (g-i) the z axis. The fibre is imaged from above the sample and the optical power for the two cores are 5.3 mW±0.1mW and 16.1 mW±0.1mW. The red arrows in a), d) and g) indicate the axis along which the fibre is moved, and as such the axis along which the cell is manipulated in each case. j) Trapping distance is indicated in red arrow, from the edge of the fibre to the centre of the cell, equal in this case to 19.0 ±0.8μm.

In more detail: Images (a-c) in figure 5. 4 show the trapped yeast cell moving together with the movement of the fibre along the x-axis (parallel with the fibre axis), while the untrapped cells, annotated 1, 2 and 3, change position with respect to the fibre-end. The

untrapped cells move position due to the flow of the medium created by motion of the fibre as well as Brownian motion.

Figures 5. 4 (d-f) show the movement of the fibre along the y-axis (perpendicular to the fibre axis). As can be seen, the trapped cell indicated with the red arrow stays in a stable position away from the fibre end in all three different time frames, in contrast to the neighbouring cells 1, 2 and 3 that move position due to Brownian motion and the flow created by motion of the fibre. Cell 1 has moved below the fibre in time frames t_2 and t_3, while cells 2 and 3 have come closer to each other in time frames t_2 and t_3.

In a similar way, Figure 5. 4 images (g-i) demonstrate manipulation along the z-axis, immersing the fibre deeper in the microchannel in the direction of gravity. As the fibre was moved along the z-axis, the image of both fibre and trapped cell became blurred as they moved out of the focal plane of the imaging system. The untrapped cells move position due to the flow of the medium created by motion of the fibre as well as Brownian motion.

Figure 5.4 image (j) shows the trapping distance as measured using Image J software. The trapping distance was measured for the trapped cell using the same fibre trap power for 3 different individual frames captured by the camera (d_{trap1}, $d_{trap\ 2}$ and d_{trap3}) and the results are presented in Table 5.2 together with the respective expected values for d_{trap} that were presented in figure 5.1. The uncertainty in the trapping distances measurements are due to the CCD system resolution and the pixel size.

2-beam trap (average mirror angle 67.7°)		
Experimental d_{trap}	Theoretical d_{trap}	Experimental-theoretical deviation
d_{trap1}=19.1±0.5μm		28%
d_{trap2}=18.4±0.5μm	$d_{trap\ theory}$=26.6μm	30%
d_{trap3}=19.5 ±0.5μm		26%

Table 5. 2: Different trapping distances for the cell trapped as shown in figure 5.4,measured for three different frames of the trapping video for the two-beam trap. The theoretical predictions of the trapping distance for these angles are also displayed together with their respective deviation. In each of the trapping distances in the table, the uncertainty is only the uncertainty due to the pixel size and the CCD resolution.

5.2.2 Four beam trapping

Similar to the previous section, Figure 5.5 presents time lapse images of the optical trap of a single yeast cell, but this time illuminating all four machined cores of the optical fibre. Following the same process as discussed for the two–beam trap, using the fibre diameter as a calibration dimension it is possible to measure the trapping distance. For

example, the trapping distance for the specific cell shown in figure 5.5 (j) was measured to be d_{trap}=18.0 ± 0.7 µm. The trapping distance was measured for 3 different individual frames (Figure 5.5 a,d,g) from the trapping video and experimental results are presented in Table 5.3.

The optical power required from each core to demonstrate the optical trapping was 2.5 ±0.1 mW, 5.0 ±0.1 mW, 5.3 ±0.1 mW and 11.8 ±0.1 mW for core 1, 2, 3 and 4, respectively. Similar to the observations with the two-beam fibre, the manipulation of a trapped yeast cell along the x, y and z axes was performed to get a 'feel' for the trap. The fibre and trapped cell were displaced through the three x, y and z axes distances of 10's µm in each direction with speeds of around 0.03 mm/s for all three axes readily achieved.

As before, the neighbouring cells indicate their changing position in comparison with the stable position of the trapped cell with respect to the fibre-end face. The cropped images result from the initial image maintaining the same field of view for all time frames.
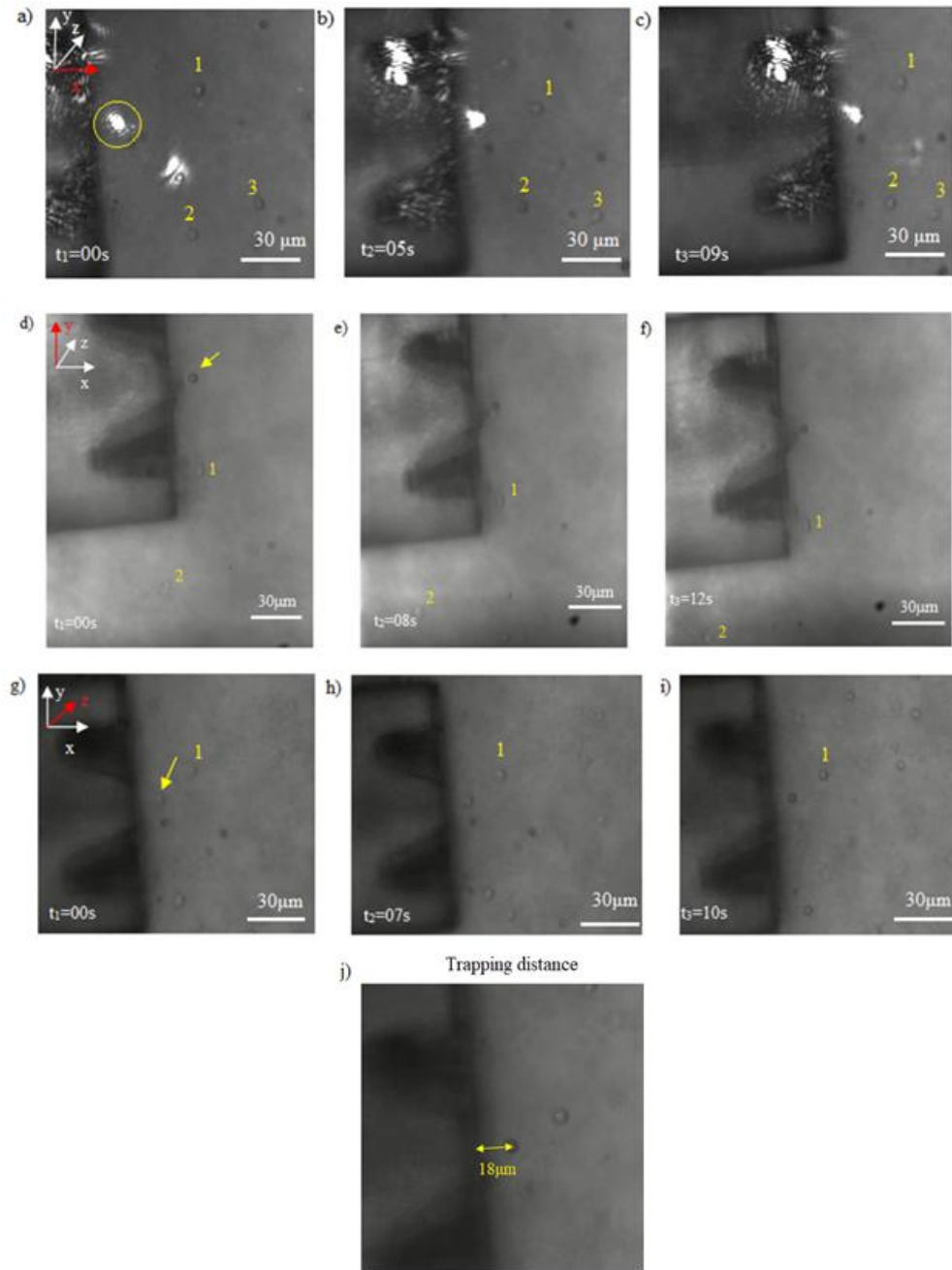
Figure 5. 5: Four-beam manipulation of a single yeast cell in three dimensions. The trapped cell is shown by a yellow circle in (a) and a yellow arrow in (d) and (g). Untrapped cells are annotated with yellow numbers. Manipulation is along the x axis (a-c), the y axis (d-f) and the z axis (g-i) indicated by the red arrows. (j) The trapping distance is measured to be $d_{trap}=18.0\mu m \pm 0.7\mu m$.

More specifically, Figure 5. 5 images (a-c) show movement of the fibre along the x-axis, in parallel with the fibre axis, and the denoted neighbouring cells 1 and 2 appear displaced with respect to the fibre end face, while the trapped cell remains at a stable distance away from the fibre-end and moves with it. This means that all the surrounding cells, except the trapped cell, are moving due to the flow of the medium arising from translating the fibre whereas the trapped cell remains held in the fibre trap despite the flow. As can be seen, cell 1 seems to move more to the upper area of the microchannel

between time frames t_2 and t_3, while cell 2 and 3 seem to move towards each otherbetween time frames t_2 and t_3.

In figure 5. 5 images (d-f), the fibre is moving perpendicular to its axis, in the y-direction. The trapped cell stays in a stable position relative to the fibre end, and follows the movement of the fibre. At the same time, it is observed that cell 1 changes position with respect to the fibre-end, following the flow of the medium, during time frames t_2 and t_3.

Similarly, figure 5. 5 images (g-i) present the movement of the fibre along the z-axis, immersing the fibre deeper in the microchannel. The fibre image and the trapped cell focus change as they are both moving out of the focal plane, while neighbouring cell 1 remains in focus for all three time frames illustrating the relative motion in the z-axis.

Table 5.3 presents the three different measurements done for the trapping distance (for the three different video frames a, d, g) together with the uncertainties of each measurement, as resulting from the CCD system resolution and the pixel size.

The theoretical trapping distance as geometrically estimated is also presented in the same table and an experimental-theoretical deviation percentage is also displayed.

4-beam trap (average mirror angle 69º)		
Experimental d_{trap}	Theoretical d_{trap}	Experimental-theoretical deviation
d_{trap1}=17.6±0.5μm		40%
d_{trap2}=18.0±0.5μm	$d_{trap\,theory}$=29.6 μm	39%
d_{trap3}=18.5±0.5μm		37%

Table 5. 3: Different trapping distances as measured for three different frames of the trapping video for the two-beam trap. The theoretical predictions of the trapping distance for these angles are also displayed together with their respective deviation. In this table, each of the trapping distance has as uncertainty only the one due to the pixel size and the camera resolution.

5.3 Maximum optical intensity of the fibre trap

The maximum operating total power of the trap for the two-beam optical trap, if we assume that the losses due to scattered light in the surrounding fluid are low, is 21.4 ± 0.1mW (5.3 ± 0.1 mW and 16.1 ± 0.1 mW for core 1 and core 3 respectively), while for the four-beam trap is 24.6 ± 0.1mW (2.5 ± 0.1 mW, 5.0 ± 0.1 mW, 5.3 ± 0.1 mW and 11.8 ± 0.1 mW for core 1, 2, 3 and 4, respectively.). At this point, it is observed that although the second trapping geometry used four trapping beams, the total optical power incident upon the trapped cell required for a stable optical trap is

similar to the total power of the two beam trap. This is an important observation since a higher total power can lead to a heating of the illuminated region and thus to an excess flow that affects the experiment.

The total intensity of the optical trap can be calculated from equation 5.2 below.

$$I = \frac{P}{A} \qquad (5.2)$$

Where I is the intensity, P is the total optical power and A is the cross sectional area of the overlapping in the yz plane region between the beams.

Two-beam trap

For the two-beam trap, the two beams exit the two machined cores with divergence angle $3.6° \pm 0.1°$ and $5.6° \pm 0.1°$ for core 1 and 3 respectively (Fig.5.3b) (see section 4.4 for how this was determined), where the respective uncertainty is due to error propagation in Eq. 4.9, and they have output beam diameter $19.4 \pm 0.4 \mu m$ and $18.4 \pm 0.4 \mu m$ respectively. The beam diameter had been measured at the overlap region (the fibre trap 'focal point') using two different techniques; the knife edge technique [157] and spot measurement using a CCD camera. The beam spot was measured at distances between the range of 0.5 mm -1 mm away from the fibre end and the related uncertainty arises due to the resolution of the CCD camera (0.5 μm) and due to the repeated measurements error (0.4 μm).

The overlapping cross section area, perpendicular to fibre axis, of the two beams is equal to $A = (295 \pm 12) \, 10^{-8} cm^2$. The uncertainty is due to the individual beam spot uncertainties. The area of the overlapping beam spots is larger than the cell area (which, for an 8μm diameter circular cell is approximately $\pi(4\mu m)^2 = 50.2 \, \mu m^2 = (50 \pm 14) \times 10^{-8} cm^2$), and the total intensity of the trap, at the overlapping area in the y-z plane, at a distance 19μm from the fibre end, will be $I = (0.0072 \pm 0.0004) \times 10^6 Wcm^{-2}$ with the uncertainty to due to error propagation.

Four-beam trap

The four-beam trap, as shown in figure 5.5, has a maximum total optical power of $24.6 \pm 0.1 mW$. Similarly to the two-beam trap, the overlapping region between the four beams is equal to $A = (295 \pm 12) \, 10^{-8} cm^2$, if we assume that the four beams fully overlap and consider the difference between the four beam divergences negligible. The intensity in this overlapping area is calculated to be $I = (0.0083 \pm 0.0004) \times$

10^6 Wcm^{-2}. The intensity for the case of the four-beam trap is very close to the one for the two-beam trap.

5.4 Characterisation of two-beam and four-beam traps

To evaluate the optical trap formed by the laser beams exiting the machined fibres, in terms of the force that the fibre trap can exert and trap efficiency, a calibrated conventional OT system was used to pull the particle out of the fibre trap, thereby allowing the trapping force exerted on the cell from the fibre trap to be evaluated. A dimensionless parameter known as the "trap efficiency factor" or Q is a 'figure of merit' for the comparison between optical traps in terms of efficiency, and is proportional to the trapping force divided by the total optical trapping power [158]. In more detail, Q is expressed in Eq. 5.3, where F is measured maximum trapping force exerted by an optical trap, P is the optical trapping power, n is the refractive index of the medium (for trapping yeast cells this is n_{water}= 1.33) and c the speed of light in a vacuum.

$$Q = \frac{Fc}{nP} \qquad\qquad (5.3)$$

Trap efficiency can be defined as the maximum force that the tweezers can exert for a given power. Trap stability here is used to indicate how long a cell can be trapped without falling out of the trap and trap stiffness, another way to characterise OT, is measured in pN/nm.

The fibre trap is characterised by measuring the maximum trapping force and using this to calculate efficiency, Q, in order to compare the two fibre traps and to make comparisons with other fibre traps and optical tweezers reported in literature. Fibre force measurement makes use of a conventional OT system operating at 976 nm and a microscope objective lens of 60× magnification and NA of 0.90. Briefly, but described in more detail later, the OT was calibrated with the same particles (yeast cells) and in the same media (water) as fibre force measurement. The maximum trapping force of the OT (F_{trap}) was determined from the Stokes' drag force (F_{drag}) calculated using Eq. 5.4 using the measured maximum velocity (u_{crit}). In this way the trapping force, F_{trap}, of the conventional OT as a function of incident power was calibrated. The OT set up is illustrated in figure 5.6, below.
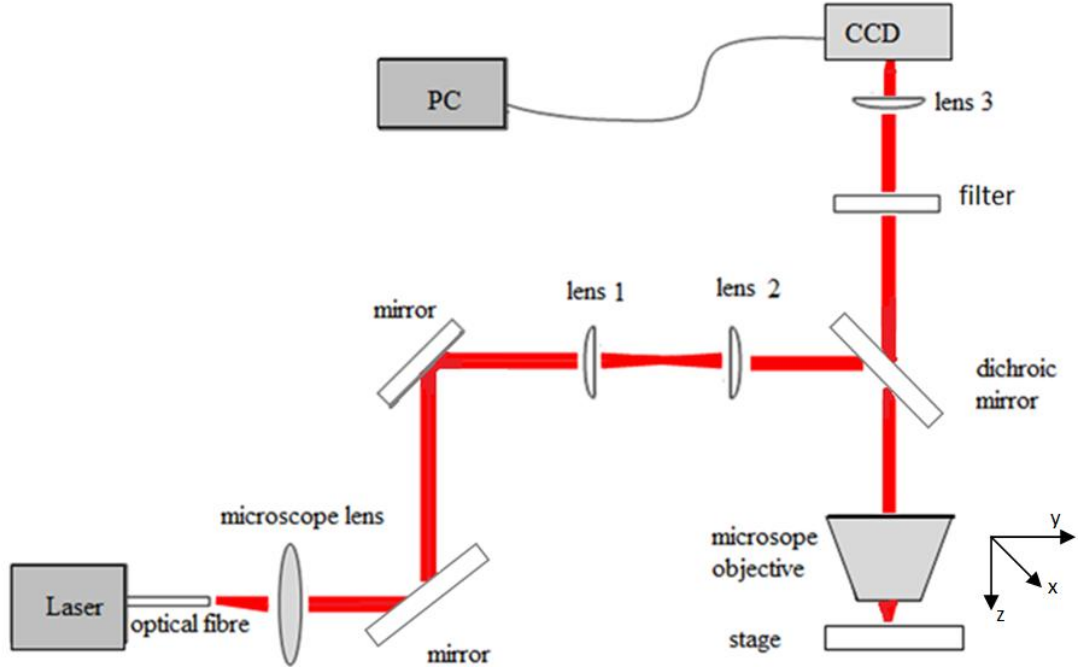
Figure 5. 6: Conventional OT used for the characterisation of the fibre trap, also presented in Fig.2.3 of Chapter 2.

To calibrate the OT so that it could be then used to measure the fibre trapping force, three different cells were trapped using a range of optical powers and translated in the x axis at increasing speeds using a motorized stage (Thorlabs Z825B) to acquire the average critical velocity (u_{crit}) for each power. Critical velocity is the maximum flow velocity that a cell can experience before the drag force exceeds the trapping force and the trapped particle falls out of the trap. These measurements provide calibration between maximum force and optical power.

The force of the OT (F_{trap}) at different powers was calculated by equating F_{trap} to F_{drag}, using Stokes' Law given by Eq. 5.4, where η is the viscosity of water and equal to 8.9×10^{-4} Pa and the trapped particle radius, r, is taken to be $3.5 \pm 0.5\mu m$ (Fig.5.7) with the uncertainty to be 1 standard deviation from the different measurements.

$$F_{trap} = F_{drag} = 6\pi\eta r u_{crit} \qquad (5.4)$$

The uncertainty related to the critical velocity, shown as error bars on the u_{crit} (blue) data points in figure 5.7 is associated with the maximum and minimum value of critical velocity measured for the three different cells trapped with the same optical power; this was measured to be ± 0.005 mm/s. Propagating this error in u_{crit} in Eq.5.4 results in uncertainty for the trapping force, F_{trap} has been calculated through error propagation and is presented in figure 5.7a.

The critical velocity of yeast cells for different optical powers in a conventional OT, using 60× objective lens, and the corresponding trapping force is indicated in figure 5. 7 below.

P (±0.1mW)	u_{crit} (±0.005mm/s)	F_{trap} (pN)
6.3	0.020	1.17 ± 0.33
9.0	0.025	1.47 ± 0.42
11.4	0.050	2.93 ± 0.50
12.8	0.055	3.23 ± 0.55
15.2	0.080	4.70 ± 0.72

Table 5. 4: Critical velocities and trapping forces for different trapping powers the conventional OT.
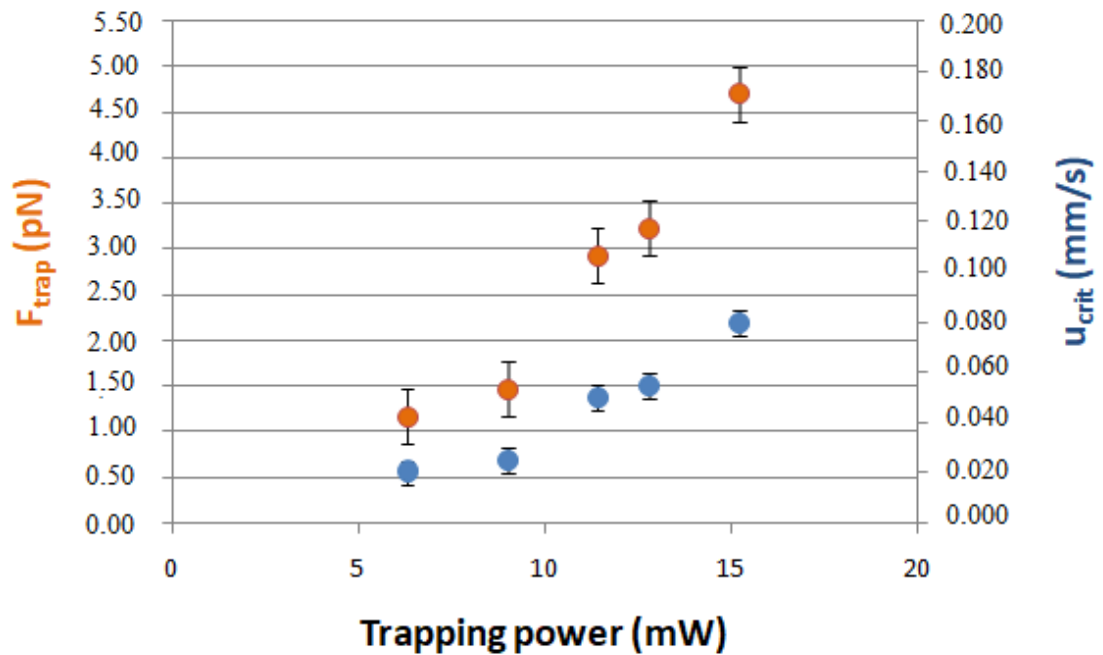
Figure 5. 7: Trapping power vs critical velocity (u_{crit}) (blue circles) for a conventional OT and vs trapping force (orange circles). This power vs force calibration of the conventional OT is used to measure the maximum force of the fibre trap.

The OT system with the 60× objective lens was then used for both the two-beam and four-beam trapping experiments. To use this calibrated OT system to characterise the MCF based tweezing system, a revised experimental set up, similar to the one described in figure 5.6 with the addition of the MCF trap, was developed (Fig.5.8).
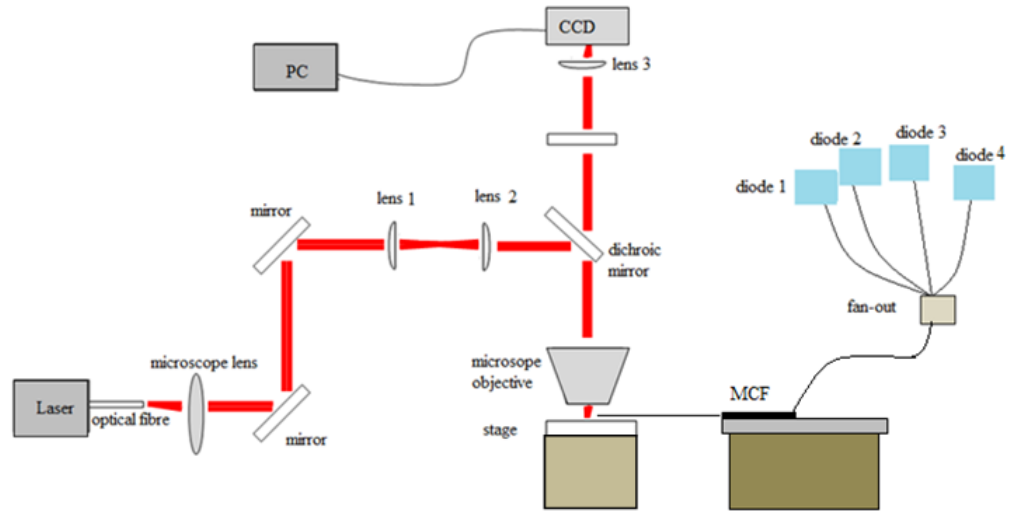
Figure 5. 8: Representation of the experimental set-up used for the characterisation of the fibre trap. A conventional OT system was used to measure the force of the MCF trap and consequently to calculate efficiency, Q of the MCF trap.

Once the single cell was trapped using the MCF trap, the conventional OT was activated, with its beam spot diameter calculated to be 1.32 μm and centred ~5-7μm away from the fibre-trapped cell. The calculation of the beam spot diameter was based on the wavelength of the laser beam (976 nm) and the NA of the microscope objective (0.9) and was given by the following formula:

$$spot\ diameter = 1.22 \frac{\lambda}{NA} \qquad (5.5)$$

The force associated with the output power of the OT required to pull the trapped cell out of the fibre trap and into the conventional OT trap (F_{trap}) provides an estimation of the strength of the MCF trap (F_{fibre}). This provides a characterisation method to measure the fibre trapping force (F_{fibre}) indirectly, using the conventional optical trapping system.

This experiment is performed using two and four beam fibre-trap powers between 23 and 32 mW and is repeated 4-5 times on different cells for each power. OT powers in the range of 1 mW to 8 mW were sufficient to 'break' the fibre trap.

The data in figure 5.9 present the relation between the optical power of the conventional OT required to "break" the fibre trap, with the power of the two and four beam fibre trap.
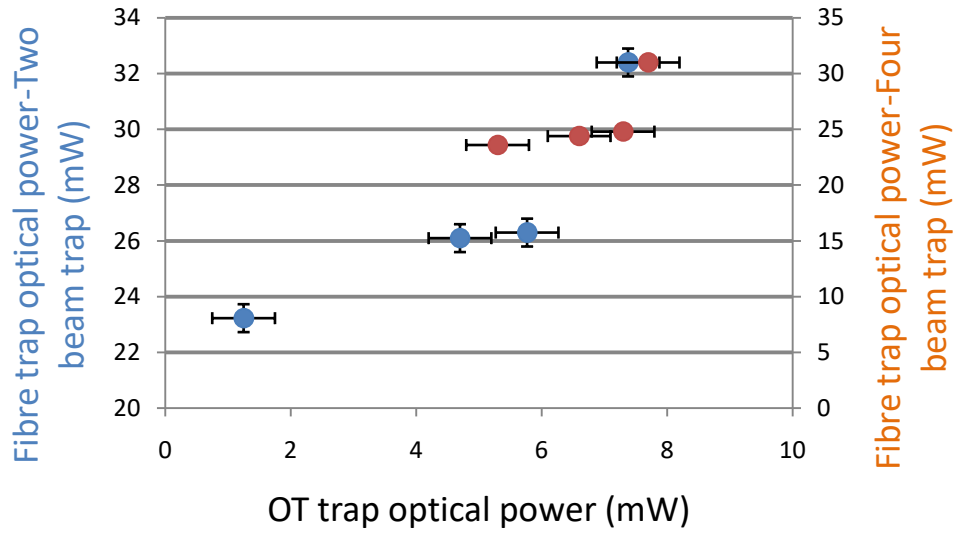
Figure 5. 9: Optical trapping power of conventional optical trap (OT) for yeast cells required to "break" the two (blue circles) and four beam (red circles) multi core fibre trap. The OT system has been pre-calibrated so that each optical power corresponds to a maximum trapping force for yeast cells in water.

The fibre optical power required to trap a single yeast cell is higher than the optical power that is needed to trap the same cell using the conventional OT system. This can be explained by noting that the optical fibre-based trapping system does not have single, tightly focused, gradient force trap generated by a high NA objective as is used in the OT. The fibre trap is made from (two or four) diverging beams which cross over and, within the overlap region, the balance of gradient forces and scattering forces produces an optical trap of equivalent strength to the OT but requiring a higher total power to achieve this. The trap efficiency, or quality factor, known as Q, is defined by Eq. 5.6.

$$Q = \frac{F_{fibre}\ c}{nP} \qquad (5.6)$$

where a value for F_{fibre} is arrived at by measuring the conventional OT power required to 'break' the fibre trap (figure 5.9), and taking F_{trap} from the OT calibration graph (Fig. 5.7, trendline based on the orange data points). F_{fibre} is measured in this way for several fibre powers and is shown as blue triangles for a two beam trap (Fig. 5.10) and for a four beam trap (Fig. 5.11).

The efficiency, $Q,$ for the two-beam and the four-beam trapping system is calculated using equation 5.6 and using the values of F_{fibre} and the total fibre optical power measurement, and is presented below as orange circles for a two beam and four beam trap, in figures 5.10 and 5.11, respectively.

P (±0,1mW)	u_{crit} (0,005mm/s)	F_{trap} (pN)	Q
19.8	0.010	0.76±0.39	0.008±0.004
22.1	0.010	0.90±0.47	0.009±0.004
23.0	0.015	0.91±0.33	0.009±0.003
23.5	0.015	1.09±0.36	0.010±0.003
29.9	0.020	1.80±0.51	0.013±0.003

Table 5. 5: Critical velocities, trapping forces and Q factor for different trapping powers for a two-beam trap.
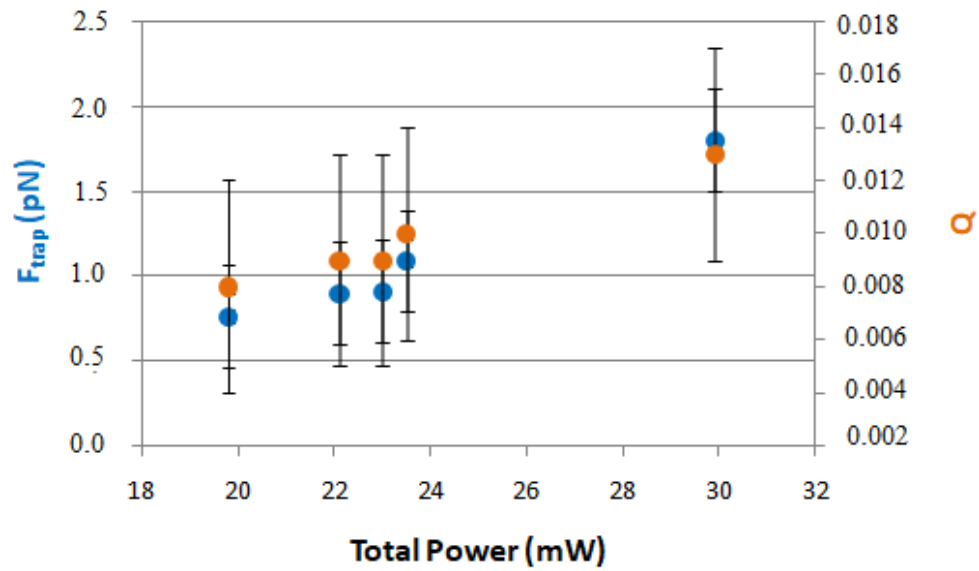
Figure 5. 10: Fibre trap force (F_{fibre}) for different total optical powers emerging from the MCF trap for a two-beam trap. Blue circles represent F_{fibre} and orange circles represent trap efficiency Q for the respective optical powers.

P (±0,1mW)	u_{crit} (±0,005mm/s)	F_{trap} (pN)	Q
23.6	0.020	1.61±0.42	0.015±0.004
24.4	0.020	1.74±0.49	0.016±0.004
24.8	0.025	1.99±0.48	0.018±0.004
31.0	0.025	2.37±0.24	0.017±0.001

Table 5. 6: Critical velocities, trapping forces and Q factor for different trapping powers for a four-beam trap
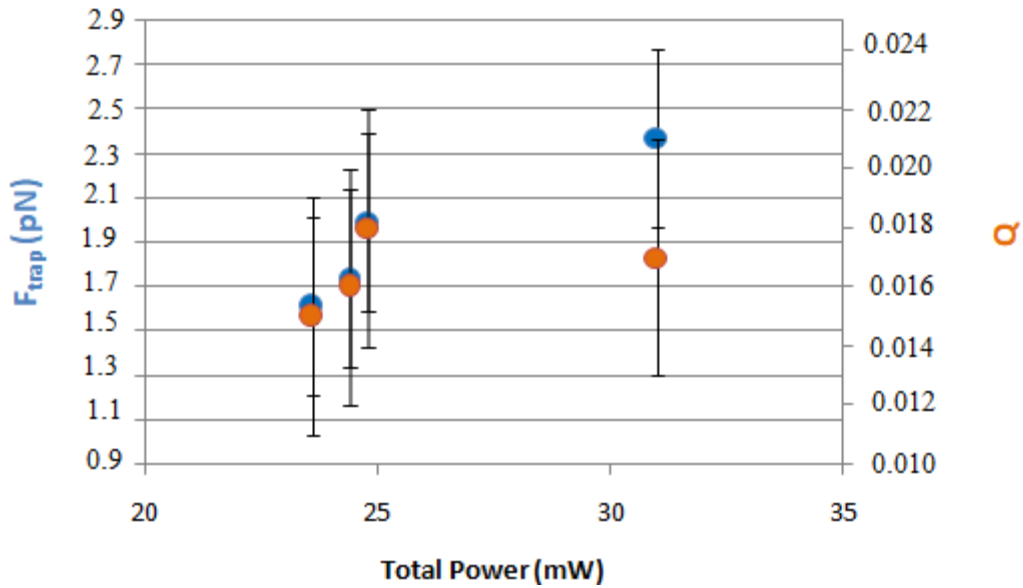
Figure 5. 11: Fibre trap force (F_{fibre}) for different total optical powers emerging from the fibre trap for four-beam trap. Blue circles represent the F_{fibre} and orange circles represent efficiency Q for the respective optical powers.

The above graphs show the trapping force and the trap efficiency Q of the two and four beam fibre trapping systems investigated. It is again noted that the total fibre optical power required to trap a single cell is similar for both systems, with the maximum optical power (power at which no excessive flow is created in the optical experiment yet) for the two core-based system to be 29.9 ± 0.1 mW and for the four core-based to be slightly higher, 31.0 ± 0.1 mW. Comparing the trapping force between the two systems, as well as the Q value, the four-beam trap demonstrates a greater trap strength for similar total powers. For example, for $P_{2core\ system}=23.5 \pm 0.1$mW and $P_{4core\ system}=23.6 \pm 0.1$ mW, the respective trapping forces are $F_{fibre\ 2cores}=1.09 \pm 0.36$ pN and $F_{fibre\ 4cores}=1.61 \pm 0.42$ pN. Similarly, for the same power, efficiency Q are calculated to be $Q_{2cores}=0.010 \pm 0.003$ and $Q_{4cores}=0.015 \pm 0.004$. The fact that the total optical power used to trap the cell in both cases is the same, as experimentally tested, means that the strength of the four machined cores fibre is stronger, due to four beam geometry and not due to a higher power. All the above uncertainties have been derived from error propagation.

Comparing the MCF based trap with other similar studies based on alternative fibre configurations, the trapping force appears to be in broad agreement with the performance reported in these studies that lie within the range of 0.5 pN and 5 pN [54,159-160]. The difference between the resulting trap force and those reported in the literature will be due to differences in the cells and particles trapped, the shape, size and

110

different beam geometries or beam intensity gradient profiles as well as the trapping powers used.

Geometries such as the two-opposed beams [81] demonstrate trap strength and stability at the level of $k = 1,72 \times 10^{-8}\,N/m$ for powers 5-7mW. Higher trapping powers and different trapping geometries may lead to higher levels of trap strength and stability, however the increased power leads to bigger risk of causing a damage to the trapped cells.

Compared with the conventional OT based trapping systems, the MCF based trap appears weaker, as OT studies in the literature present forces up to 35 pN (using a power of 80 mW) [161] for example. For powers similar to the powers used for the fibre trap (27-30 mW), the respective force was 10 pN [161]. The fact that the OT systems have a high NA objective to tightly focus the trapping light leads to a smaller, diffraction limited spot size, a high intensity gradient and thus higher trapping force in comparison with the MCF based trap.

The OT uses an NA lens of value 0.90 and a beam spot diameter of 1.32 μm as calculated using Eq. 5.4, which results in a stronger trap than the fibre. However, it should be noted that OT typically have an NA of 1.3, which in the case of this thesis would not allow increased working distance for practical reasons. The respective Q value for this NA OT system is on average Q=0.04, which is higher than the fibre trap Q values, but can be regarded as a weak conventional OT.

As previously mentioned, the four-beam trap is stronger than the 2-beam trap (by approximately 30%) due to the geometry compared to a two-beam trap of the same power. The average Q value for the two-beam trap and the four-beam trap is Q_{2cores}=0.0105 ± 0.0004 and Q_{4cores}=0.0154 ± 0.0004, respectively. Comparing these values with Q=0.04 for the 0.90 NA OT system used it can be seen that the OT is more than twice as efficient than the fibre traps, however, in the literature optical tweezers typically use a higher NA of around 1.3 and have much higher Q values, between 0.1 and 0.57 [161-163]. In general OTs are more efficient than fibre traps, however, the MCF trap allows additional flexibility in the trapping experiments and thus in the variety of the potential applications.

At this point it is noted that optical trapping using the MCF-based trapping system is analogous to trapping using a Laguerre Gaussian (LG) beam [164] in a conventional microscope-based OT. The LG profile is such that the on-axis intensity is zero, hence

the optical trap is stronger because there is no on-axis scattering force to push the particle out of the trap in the direction of beam propagation [158]. In a similar manner, our MCF design has no on-axis rays contributing to a scattering force along the direction of the fibre axis. In addition, and in contrast to the conventional, tightly focused beam of OT, the beams emitted by the fibres are diverging, which reduces the intensity gradient and the trapping strength compared to OT, however, the intensity of the fibre trap, as described in section 5.3, is on average 0.007×10^6 W/cm^2 and 0.008×10^6 W/cm^2 for 2-beam trap and 4-beam trap, for total powers 21.4 mW and 24.6 mW respectively, which is significantly lower than typical OTs (approximately 1.7×10^6 Wcm^{-2} for the same laser power and 0.09×10^6 Wcm^{-2} for the same trap strength in the OT system used in these experiments) and so the potential for optical and thermal damage of the test cell due to the trapping beam(s) is reduced.

5.5 Maximum translation speed for practical applications

In addition to the trap strength characterisation described above, a measurement of the maximum speed under which the fibre could be translated inside the microchannels with the cell remaining trapped, was performed. How fast the fibre can move inside the microchannels is an important parameter for applications that demand manipulation of the trapped particle via movement of the fibre, for example to transfer a single trapped cell to a predetermined location.

As a first step, the technique included movement of the fibre with the trapped cell along the x-axis (along the fibre axis) by small distances to stay within the field of view. More specifically, once the cell was trapped in either the two-beam or four-beam trapping systems, the stage and sample chamber moved by steps of distances of 0.5 μm using the motorised stage along the x-axis, so the fibre stayed in place with the trapped particle under the microscope so changes in trapping could be observed. The starting speed was 0.2 mm/s for the two-beam trap and 0.6 mm/s for the four-beam trap and it was increased by increments of 0.1 mm/s for both cases. The starting point of required speed for the four-beam trap case was higher and this can be explained as the fibre trapping power was slightly higher than the case of the two-beam trap as well as the medium flow was potentially higher than the one in the experiment of the two-fibre trap. As also mentioned previously, the initial 'feel' of the trap was slightly stronger in x-axis than in y-axis or in z-axis, and this is the reason why experiment in x-axis manipulation needed

to start with higher speed in the x-axis experiments. Each cell was tested three times, for the same optical power. The figure below represents the average maximum speed (u_{crit}) for each individual optical power and the respective measurement error is the standard deviation. The relation between the total optical power used for the fibre trap and the maximum speed of movement, for both the two and four beam traps is represented in figure 5.12 below. The power uncertainty as described earlier is $\pm$ 0.1mW which is not shown on this scale, as the symbols are smaller than the error bars.
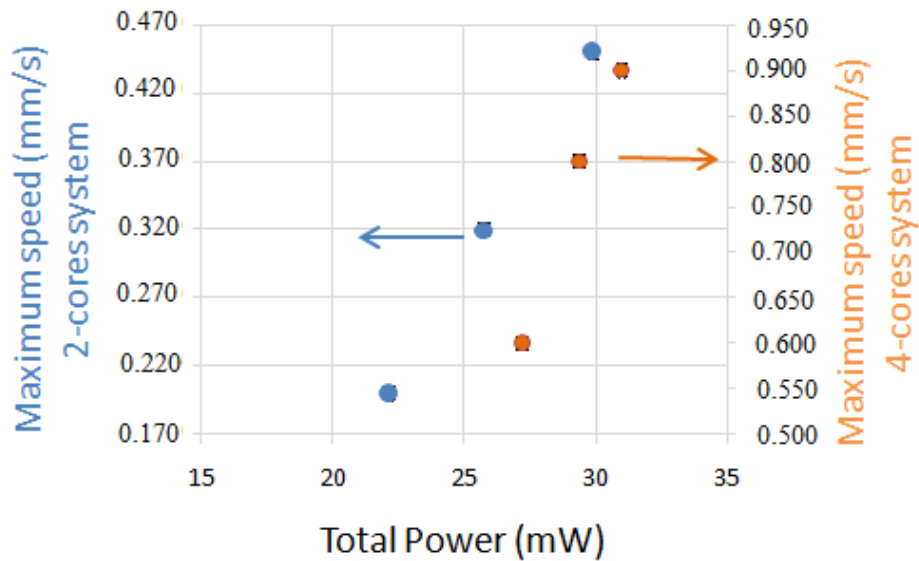
Figure 5. 12 Maximum speed in x-axis under which the trapped cells remain in trap, for different total optical powers. Blue circles indicate the maximum speed for the two-beam trap system and the orange circles represent the maximum speed using the four-beam trap.

Following from this the stage and sample chamber was translated along the y-axis, perpendicularly to the fibre axis and the relation between the total optical power and the maximum speed of movement for both of the trapping systems is represented in figure 5.13 below. Again, each experiment was repeated three times to verify repeatability. The starting speed for the two-beam and the four-beam trap was 0.02mm/s and 0.025mm/s, and this small difference in the starting point of speed can be explained as the fibre trapping power was slightly higher in four-beam trap than in the case of the two-beam trap. The error bars for these measurements in the speed axis depict the standard deviation for the three different measurements for each individual optical power.
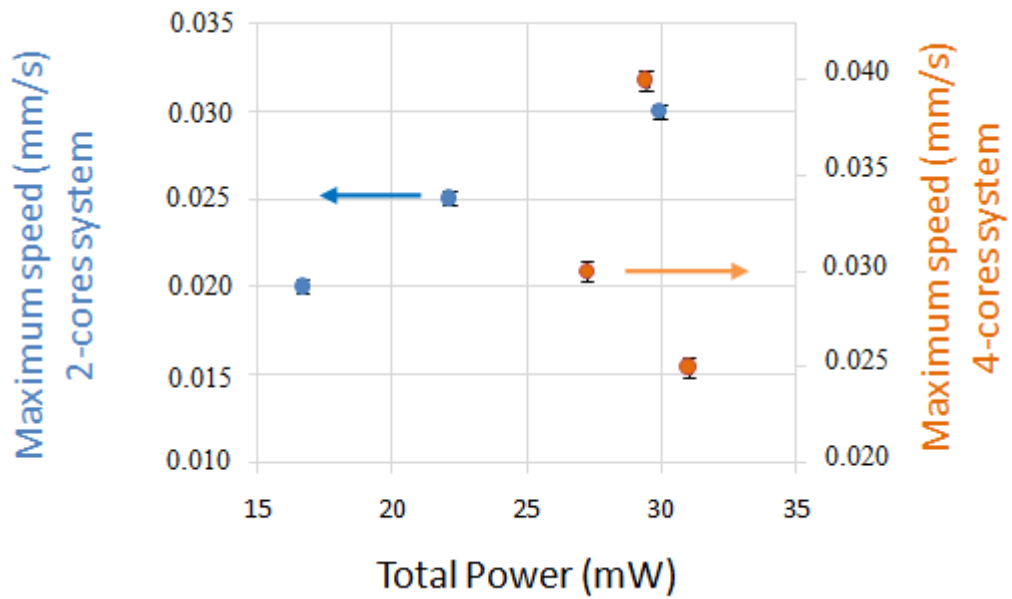
Figure 5. 13: Maximum speed in y-axis under which the trapped cells remain in trap, for different total optical powers. Blue circles indicate the maximum speed for the 2-core based trap system and the orange circles represent the maximum speed using the 4-core based trap system.

It has been observed that during these fast movements of the fibre along both x and y axis, an additional liquid flow was observed inside the sample. No external flow was deliberately added to the system and the only flow was created due to the movement of the stage.

Comparing x translation speeds with y translation speeds, cells can be translated in x an order of magnitude faster than in y. We believe this is due to the motion of the liquid directly in front of the fibre, in the area where the cell is trapped, that contributes to holding the particle in place when the fibre is translated in x. This motion of liquid (or 'hydrodynamic force') is either not present, or much reduced when compared with translating the fibre in y. As a result of this "hydrodynamic force" in addition to the trapping force, the maximum speed that is measured experimentally cannot be considered as the critical velocity of the optical trapping MCF system because it is not possible to separate these effects, however it is a useful indication of how fast the fibre can be moved while keeping the cell trapped.

Furthermore, as can also be seen from figure 5.12, the max speed in x between two-beam and four-beam traps is different, with the value for the four-beam case to be higher. When comparing this speed with how fast can cells be optically translated through a sample using conventional OT, it can be highlighted that an OT system requires optical powers more than 300 mW to achieve similar results [165].

114

5.6 Cell position tracking for trap characterisation

An optically trapped particle is confined in the trap but keeps moving within the trap due to the presence of Brownian fluctuations. The trapped particle is in a dynamic equilibrium between the optical forces, pulling the particle into the equilibrium position, at the region of highest light intensity, and Brownian fluctuations continuously pushing it in all directions, including out of the trap centre. The analysis of the thermal motion of the optically trapped particle in the optical potential can give us information on the shape of the trapping potential, and we can use it to track the particle's position. If the particle is held in a harmonic trapping potential (for example a conventional optical tweezer), its position distribution along an arbitrary axis orthogonal to the beam propagation direction is Gaussian. By recording a segment of video, we can track the position of the particle along an axis. The equipartition theorem relates the average energies of various forms with the total energy of a system.

The probability density of the particle position in a two-dimensional movement, in thermal equilibrium is defined in Eq.5.7:

$$\rho(x, y) = C e^{\frac{-U(x,y)}{k_B T}} \qquad (5.7)$$

where T is the temperature, k_B is the Boltzmann constant, $U(x, y)$ is the trap potential and C is a normalization constant.

The expected probability density for a Gaussian function is defined in Eq.5.8:

$$\rho(x, y) = C e^{\frac{-k_x}{2k_B T}(x-x_0)^2} e^{\frac{-k_y}{2k_B T}(y-y_0)^2} \qquad (5.8)$$

where k_x and k_y, are the trap stiffness in x and y directions, and (x_0, y_0) the equilibrium position. If the temperature is known, then the width of the Gaussian-shaped histogram(σ_x^2) is directly related with the trap stiffness as follows:

$$k_x = \frac{k_B T}{\sigma_x^2} \qquad (5.9)$$

Using some short segments of video data (up to 2 minutes trapping experiment), the position of single cells, held in the MCF trap, has been tracked by creating a Matlab

code with a view to sampling the probability distribution and generating an impression of the size and shape of the fibre trapping region. The videos used were of that level of time duration because for longer experiments there was high flow of the medium that led to disruption of the optical experiment. Furthermore, the videos were made to show manipulation, so the MCF or the stage were moving, so only short parts of videos, where everything was stationery, could be used.

Although the data are too few to be statistically significant, they can be used to make some observations about the overall trap dimensions in the xy plane which is the plane that we image and z is depth, such as conclusions about the size.

The videos that have been used for this analysis are yeast cells trapping videos that have been cropped in short segments of 1-2 minutes. The video image sequences are analysed using Image J software prior to the Matlab code. More specifically, code was developed to calculate the centre of the mass of the trapped cell based on frames from the trapping video, for each individual time frame and based on these points it derives the centre of the centres of mass which can be assumed equal to the time-averaged centre (the equilibrium position) of the trap. Once the centre of the trap is defined, the distribution of the centre of the mass of the cell for different time points around the centre of the trap can be estimated. By using equipartition theorem a value for trap stiffness, k_x and k_y, can be calculated from the variance in x or in y. The frame rate of the camera used to acquire the trapping experiments was 10 frames/sec and the pixel size was measured to be 0.3×0.3 μm square pixel, having as a reference a known dimension which in this case was the MCF diameter.

The code is presented in detail in Appendix 5.1 and the main steps can be summarised below, with two examples shown in figure 5.14. At this point, I would like to acknowledge Dr. Weiping Lu from IB3 Institute at Heriot Watt University for the initial guidance in this analysis.

First of all, video segments extracted from longer videos of cell manipulation in x, y and z were isolated and saved into separate image frames. These short segments showed the fibre held stationary, not translated, with a single cell trapped. The individual frames from the video segments were cropped to remove excess background from the captured image of the trapped cell (Fig.5.14 a,d) using the Image J software.

The initial image format is an RGB image and the first step after cropping the images in the video segment is to transform it into a grey image to avoid any complexity that the

different colour shades could potentially contribute to the process. The image in grey scale is depicted as a ring with its darkest areas in the periphery of the cell (Fig 5.14a).
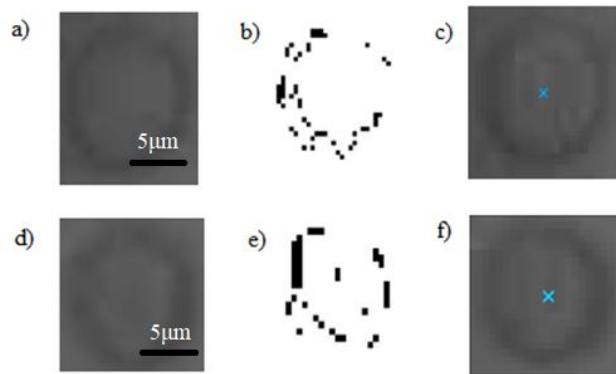
Figure 5. 14: Image processing steps to calculate centre of mass position of a trapped yeast cell for (a-c) 2-beam yeast cell trapping. (d-f) 4-beam yeast cell trapping: a,d) initial, cropped, RGB image of the trapped yeast cell, b,e) binary image as transformed using Matlab code c,f) RGB image from (a, d) marked with the centre of mass (blue cross) as calculated using Matlab code.

To simplify data processing these images were converted into a binary image format by defining a threshold of pixel intensity, where all the pixels that are of lower intensity than this threshold would take value 0 and all the pixels with intensity higher than the threshold would take value 1. In this way, a binary image that depicted a discontinuous ring of dark spots that correspond to the cell shape of the initial RGB image, was acquired. (Fig.5.14 b,e).

Once the binary image is obtained, then the centre of the mass could be measured, using the Matlab commands "regionprops" and "centroid" that return the centroids in a structure array of x and y coordinates. The resulting centre of mass is obtained in pixels thus required transforming into physical distances by using the pixel size calibration (equivalent to 0.3 μm in x and y dimensions). To make the representation of the centre of mass clearer, the centre of mass is presented here as blue cross marker in the RGB initial, cropped image of the cell (Fig.5.14 c,f).

Repeating the same code in a loop for all the time frames of a video segment, a number of different centres of mass, one for each video frame, is acquired. From these centres of mass, the time-averaged centre is obtained which can be assumed to be equivalent to the centre of the trap, as displayed in figure 5.15, symbolised as a diamond-shaped marker while the centres of mass are symbolised as circle-shaped markers. This value is again given in microns. The time-averaged centre (also known as the centre of centres) is at position (0,0) in the Cartesian co-ordinate system and it can be defined as the centre, or equilibrium position (x_0, y_0) of the trap.

117
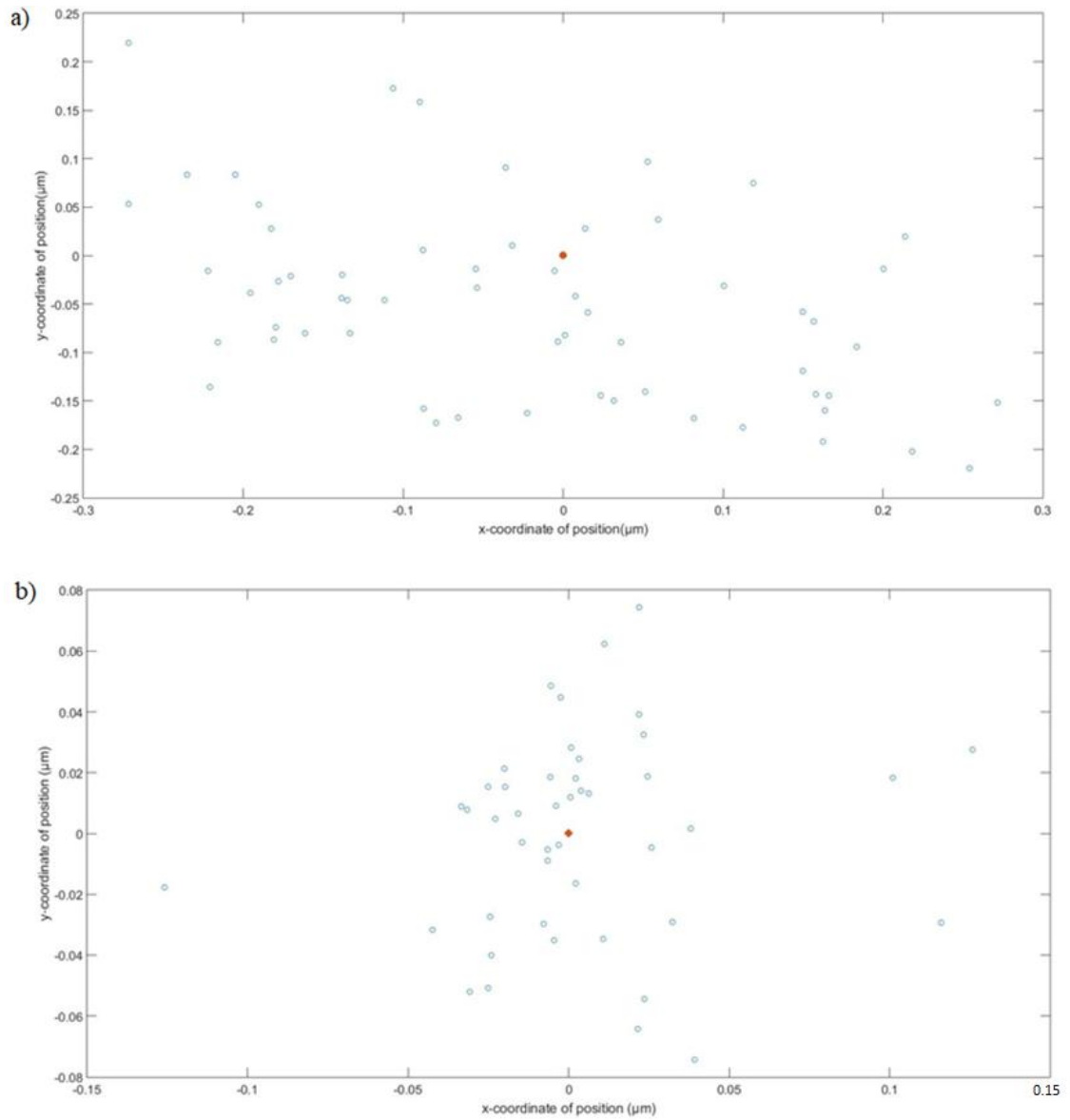
Figure 5. 15: 2D scatter plot of the trajectory of a yeast cell confined in (a)a 2 beam trap (21.4mW) from a video of 65 frames and (b) a 4 beam trap (24.6 mW) from a video of 47 frames. The centre of the centres, hence the assumed centre of the trap is shown by a star-shaped symbol.

The position of the yeast cell in x (Fig 5.15 a) and in y (Fig 5. 15 b) with time over the length of the video segment presented for a two beam trap, and in Fig 5.15 c and d for x and y position with time for a four beam trap. The yeast cell trapped in the four beam trap looks to be more confined in x and y than the two beam trap, which can be explained by the increased number of beams used and the trap geometry which allows for a more stable optical trap. This also agrees with results in section 5.1.3 where it was found that the four-beam trap demonstrates a greater trap strength for similar total powers. For example, for P_{2core} *system* = 23.5 ± 0.1 mW and P_{4core} *system* = 23.6 ± 0.1 mW, the respective trapping forces are $F_{fibre\ 2cores}$ = 1.09 ± 0.36 pN and $F_{fibre\ 4cores}$ = 1.61 ± 0.42 pN.

Similarly, for the same power, efficiency Q are calculated to be Q_{2cores} = 0.010 ± 0.003 and Q_{4cores} = 0.015 ± 0.004 that shows the 4 beam trap is stronger than the two beam trap.
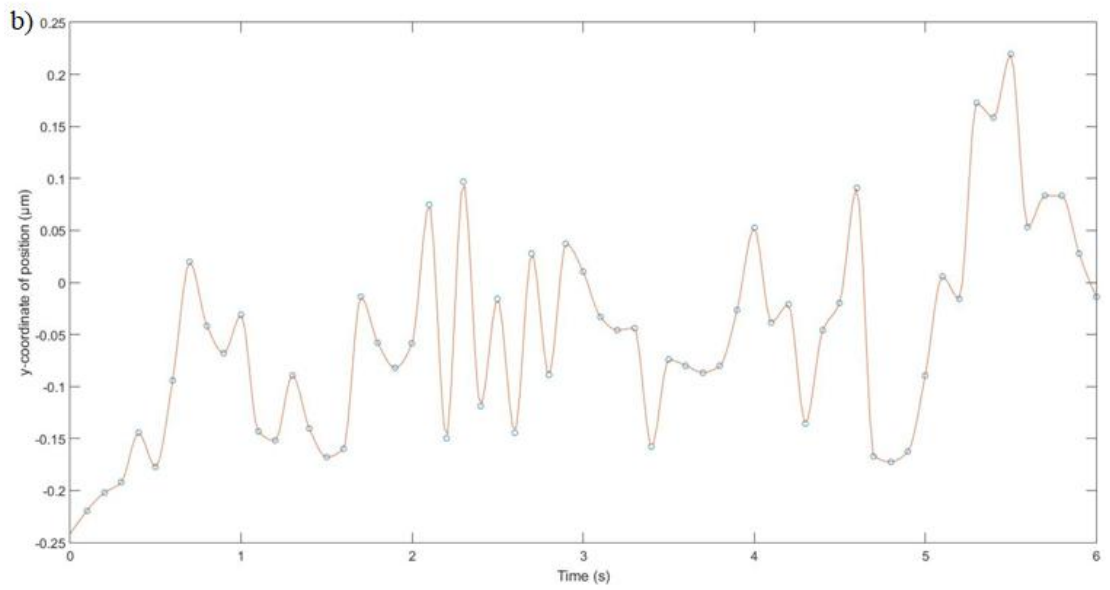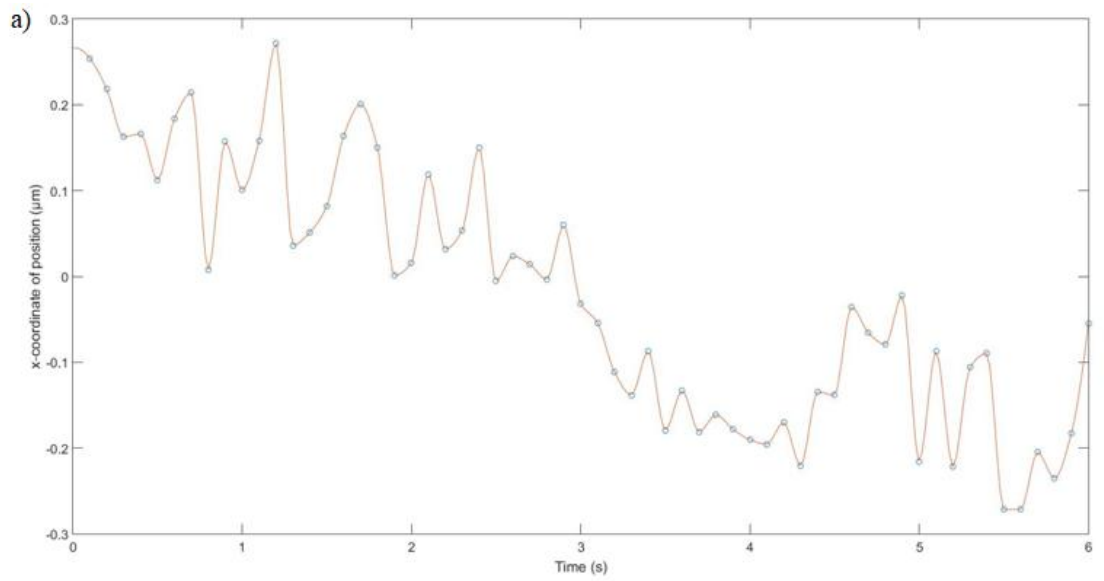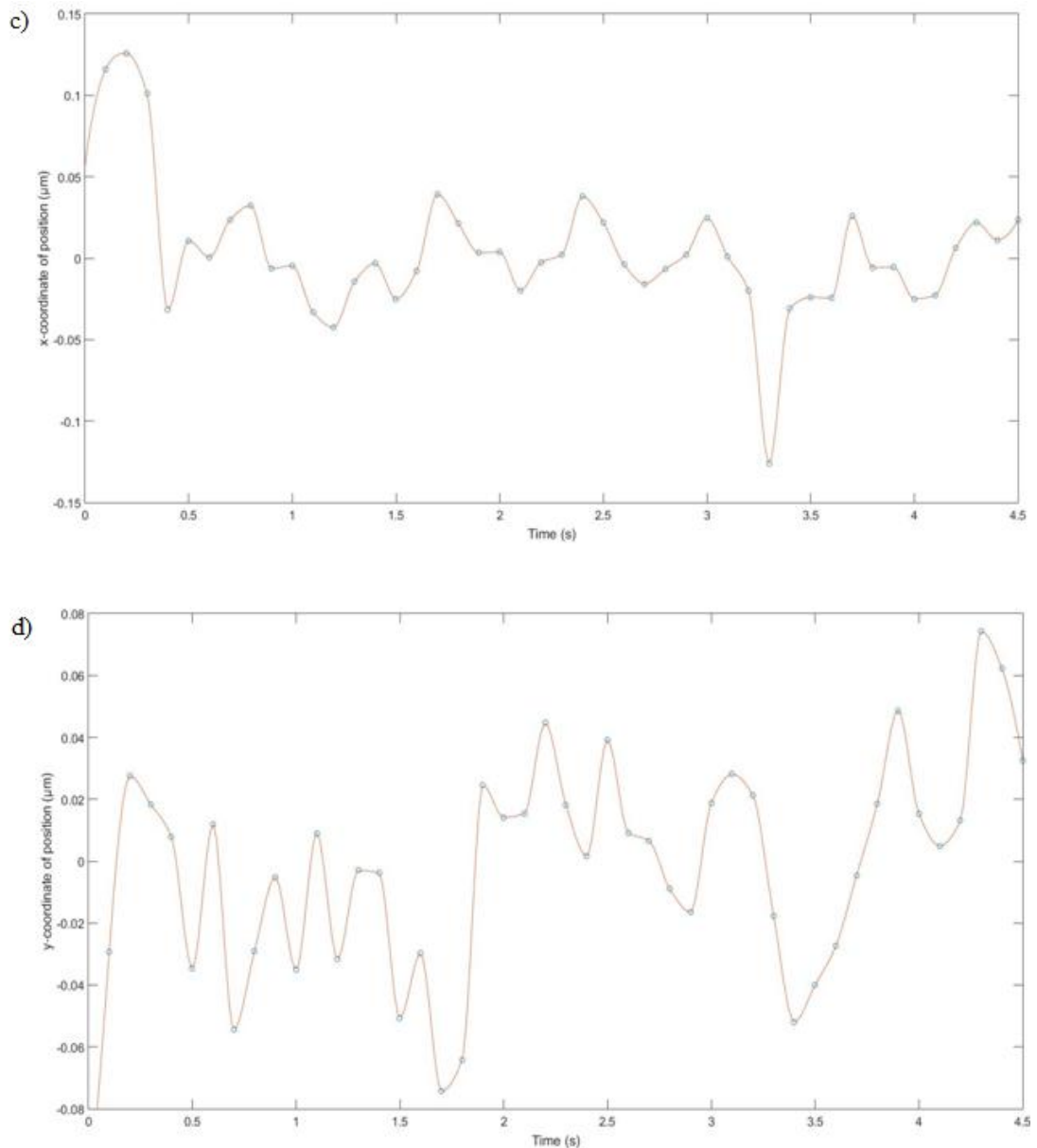
Figure 5. 16: a, b) Plot of x and y position, respectively, with time for the two beam optical trap, c, d) plot of x and y position, respectively, with time for the four beam optical trap.

As can be seen from the trajectory in x and y direction (where x is the axis parallel to the fibre axis and y the axis perpendicular to the fibre axis) the cell explores a larger distance in x direction compared to y. For the 2-beam trap (Fig 5.16 a and b) over the time period observed, the maximum distance travelled in x and in y is 0.56 and 0.46 units respectively and for the 4-beam trap is 0.26 and 0.15 units respectively for x and y. Mention error here. This difference in x and y direction denotes that the optical trap is not circularly symmetric since it appears that confinement of the cell in one direction is different to the orthogonal direction. The trap shape may be elliptical or asymmetric but an order of magnitude or more data points are required to determine this. Typically, a hundred thousand frames would be used to analyze an optical trap in this way. At this

point, we need to mention that this centre of mass tracking method has an error that has to do mainly with the camera resolution that captured the trapping video (±0.5 μm). Factors that may lead to larger uncertainty than the pixel size alone, such mechanical vibrations, or size or shape of cell changing due to rotation, can be considered as negligible during the short timescales considered.

Another way to visualise the motion of the particle inside the trap is to connect the different time points with a line to show the path a particle takes, as shown in figure 5.17 below. This type of figure could indicate if there are any 'hot spots' or multiple trapping locations inside the MCF trap, as the particle would linger in one position for a period of time then due to Brownian kicks, 'hop' into another stable position. Figure 5.17a shows that the yeast cell crosses the trap several times over the 65 second video (2-beam trap). In figure 5.17b the particle is located in the left hand side of the trap for approximately one half of the 47 frames video then moves across to the right hand side where it is located in the second half of the video, indicating that there may be two stable trap positions in this beam geometry.

The time resolution of the camera used in this work, and low number of data points means it is difficult to say if this is real, or an artifact of the sampling frequency (only 10 frames/sec), but it is worth noting at this point. For simplicity this thesis will continue to treat the two and four beam trap as a single trap, due to the data limitations to conclusively determine the trap geometry.
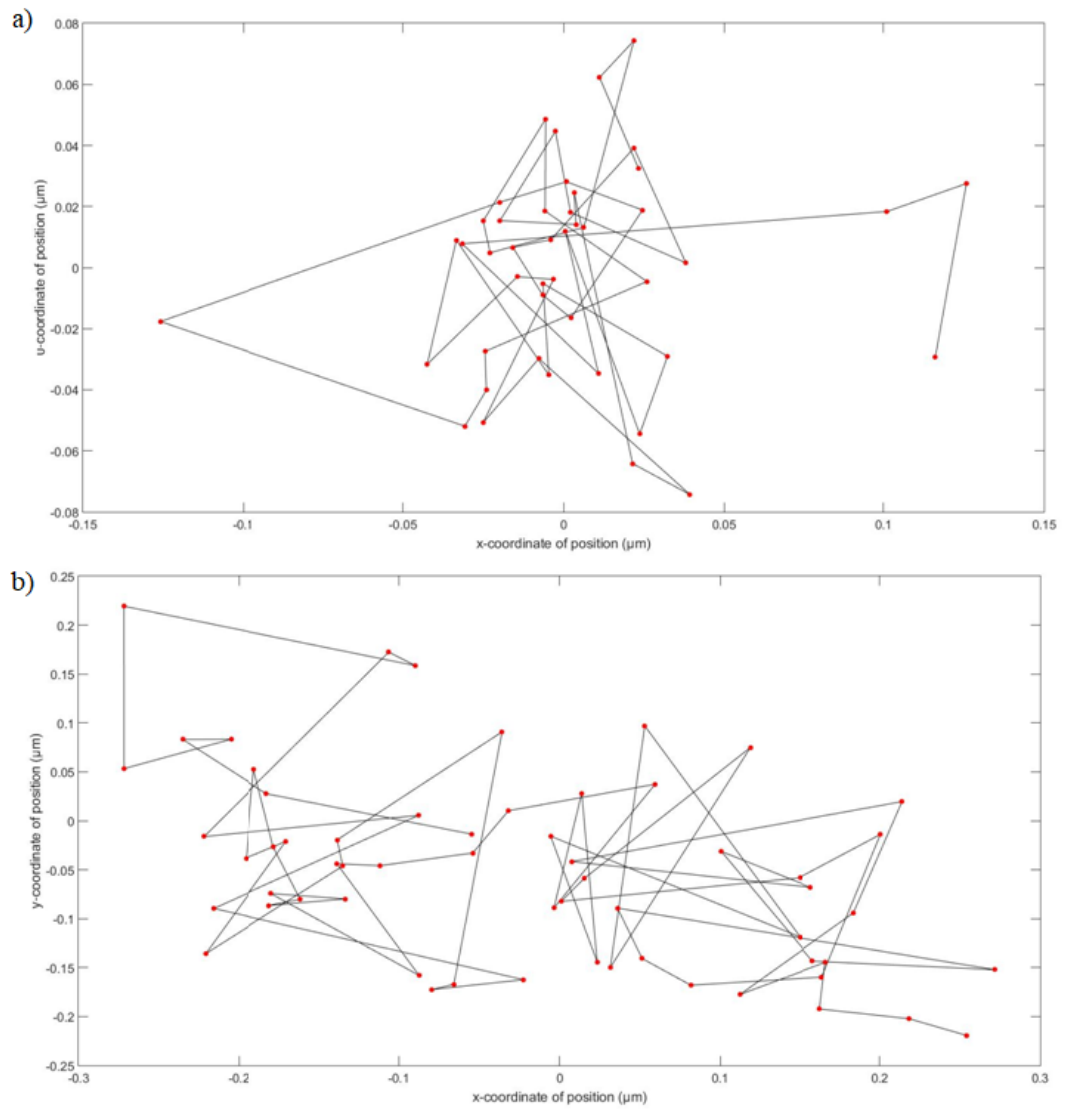
Figure 5. 17: Motion of yeast cell while in trap for a) two beam trap of power 21.4 mW from a video of 65 frames and b) four beam trap of power 24.6mW from a video of 47 frames.

Below the corresponding probability density of particle position in x and y is plotted in figure 5.18 for the two beam and four beam trap, to visualise the trap shape.
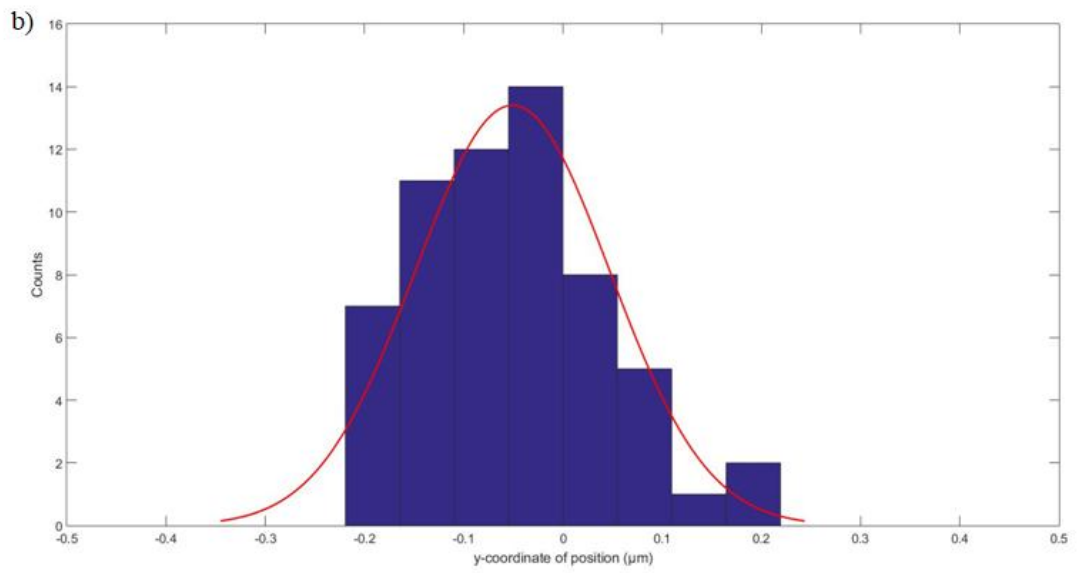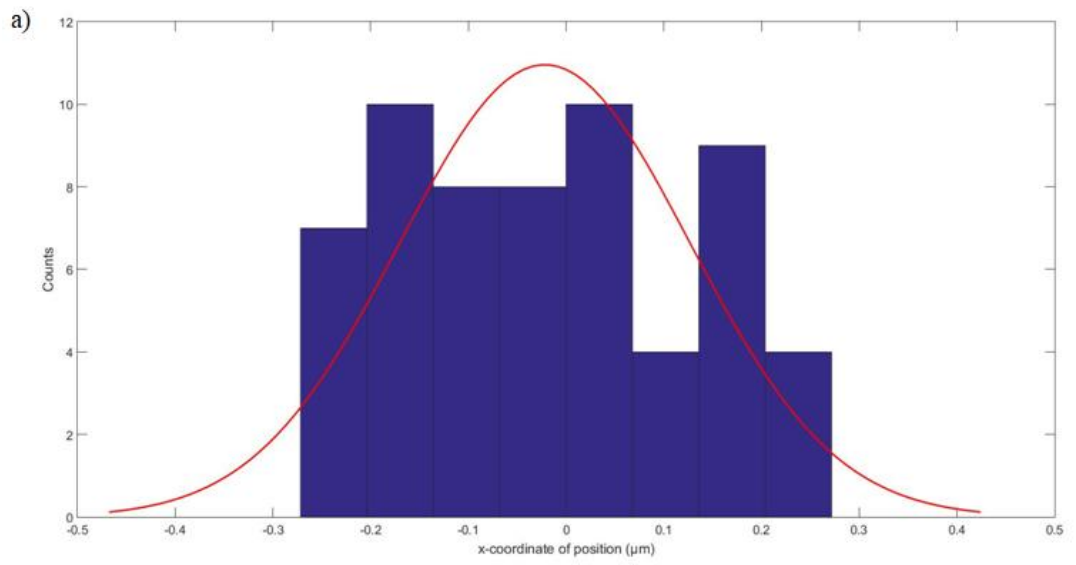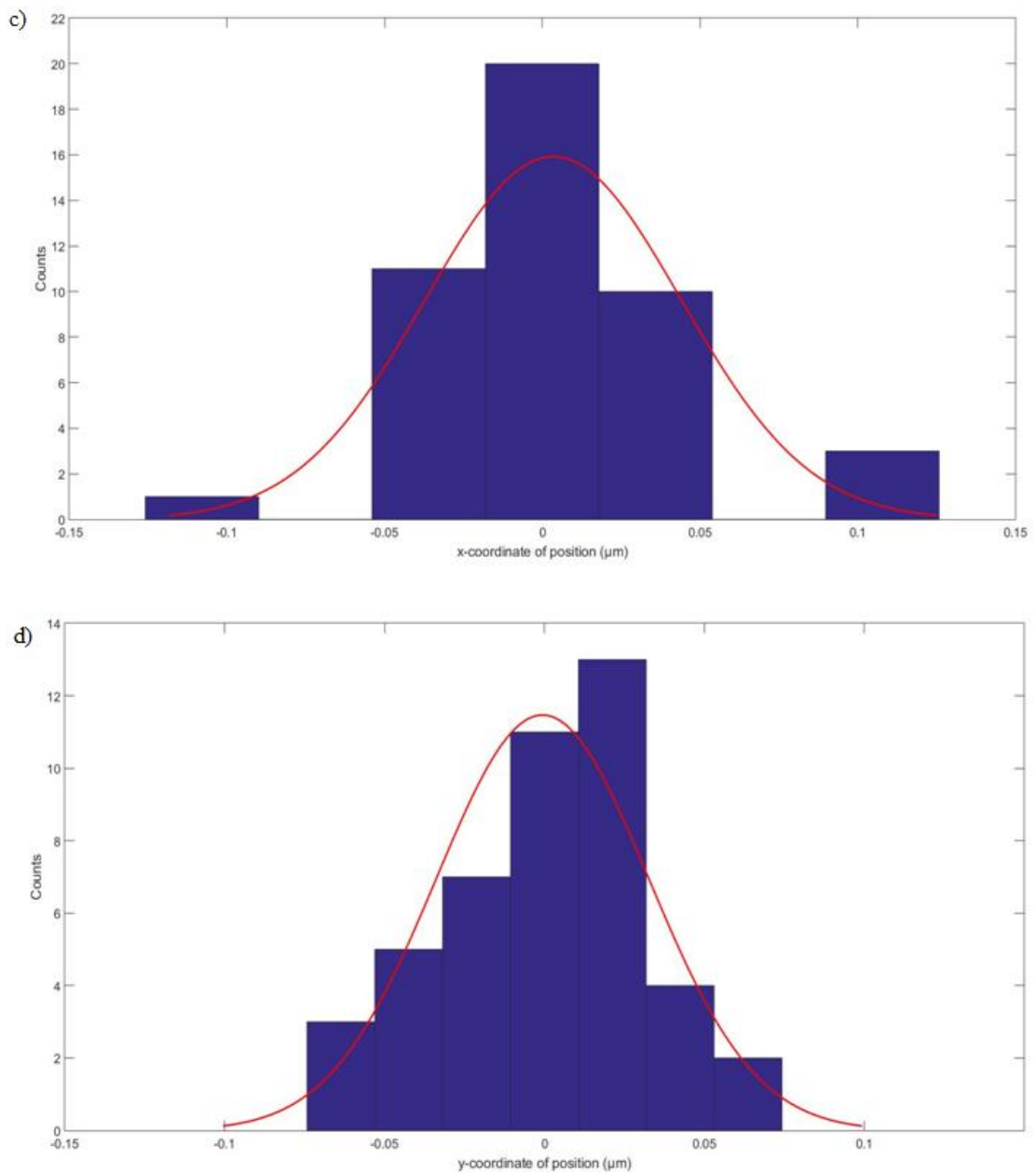
Figure 5. 18: a),b) Probability density of trapped cell trajectory in x and y direction respectively for the two-beam trap (give power), and c),d) for the four-beam trap (give power).

The gap between the bins in figure 5.18c may indicate that there in more than one stable trapping position (as mentioned above), but it could also be due to the small number of data points in comparison with the other studies, (only 47 data points in this case).

The standard deviation (σ) and the variance (σ^2) of the Gaussian fit, are two parameters that characterise the distribution and indicate the spread of the distribution. Given these parameters, then the trap stiffness in x and y could be calculated using the equipartition theory (Eq.5.8) mentioned earlier, with the temperature in the equation to be the room temperature during the experiment, equal to $20^{\circ}C \pm 3^{\circ}C$, but the data available is

insufficient to calculate variance and stiffness with confidence, due to the short segments of video available and for this reason are not included in this thesis.

The number of frames that are used for this analysis differ depending on availability of suitably trapped cells in recorded video. Longer video segments are beneficial as the accuracy of this analysis depends on the number of frames available. However, it was not possible to obtain the thousands of frames needed for accurate conclusions, because of the evaporation that occurred after a duration of time in trap (approximately up to 2 min).

5.7 Discussion

This chapter presents the optical trapping of single yeast cells using both two-beam and four-beam trapping systems, proving stable trapping in three dimensions. Yeast cells have been used as a reference for the optical experiments of this fibre-based trapping system, due to their consistency in shape and size as well as due to their durability in normal laboratory conditions. Polymer microspheres were not deemed suitable due to their tendency to stick to, and contaminate, the probe features.

The trapping distance, d_{trap}, for the two-core -based system was experimentally measured to be 19.0 ± 0.8 μm away from the fibre-end, while the trap distance using the 4-beam trap was found to be 18.0 ± 0.7 μm. We suggest that this small difference in the trapping distance can be explained because of the use of the second pair of machined cores, which cannot be considered exactly identical to the first pair, which consequently leads to a slightly different trapping point, located at the meeting point of all diverging beams coming out of the machined cores. Furthermore, this difference can also be considered to lie within the limits of uncertainty if considering difference in trapping positions due to different cell size.

In comparison with conventional OT which, as an example from the literature, demonstrates forces up to 35 pN (using a power of 80 mW) [161], the MCF trap appears weaker ($F_{fibre\ 2cores}=1.09 \pm 0.36$ pN and $F_{fibre\ 4cores}=1.61 \pm 0.42$ pN for P=23.5 mW and P=23.6 mW respectively), however, the MCF trap allows additional flexibility in the trapping experiment configuration and thus in the variety of potential applications.

The trapping force of the MCF based trap, and thus the trap strength, appears to be in broad agreement with the performance of other fibre based trapping studies where the respective F_{fibre} lie within the range of 0.5 pN and 5 pN [54,159-160]. The geometry of the beams which create fibre traps appears to be an important factor for determination of

trap strength and the force that the traps can apply. The geometry of a dual beam (two-opposed beams) trap [6] demonstrates trap stiffness of $k = 1.72 \times 10^{-8} \, N/m$ for powers 5-7 mW. Higher optical trapping powers also lead to higher force levels, but increase the risk of causing optical driven thermal damage to the trapped cells. MCF fibre trap- made from a single fibre (not a dual fibre, or fibre bundle) offers a stronger trap (or equivalent strength trap) to the single pulled fibres, but can trap the cell away from the fibre so there is no contacts, plus there is no SLM programming required (as is the case with Cizmar *et al*'s multimode fibre and offers 3D trapping where studies based on lensed multicore fibres could not.

As the most important advantages of the MCF trap cam be summarized to be the higher flexibility in the experiments as well as the small size of the fibre together with the fact that the overall system can be portable and combined with other microscopic techniques that increases the variety of potential applications.

5.8 Conclusions

In this chapter, the investigation of single cell optical trapping using two types of optical fibre-based tweezing systems is presented. The first fibre trap is based on the exploitation of two machined cores in a multicore fibre and the second type is based on the use of four mirror shaped cores of the same MCF to realise a two-beam and a four-beam trap, respectively.

Yeast cells have been used as a reference for the optical experiments of this fibre-based trapping system, due to their consistency in shape and size as well as due to their durability under normal laboratory conditions.

Yeast cell were stably trapped and readily manipulated in x, y and z directions using a two beam trap and a four beam trap. The trapping distance was measured from video microscopy data and compared with theory.

The next chapter presents initial aim of demonstrations of optical trapping of different types of cells as well as examples of single cell applications that may be enhanced by using the MCF trap. To demonstrate wider applicability than to yeast cells, demonstrations of trapping of human erythrocytes (RBCs) and mouse embryonic stem cells (ES cells) has been presented using both 2 beam and 4 beam MCF traps, and cells from the human glioblastoma cell line, U87, have also been trapped using the 2-beam

fibre system. To demonstrate proof-of-concept for potential further applications of the MCF trap, trapping of single cells has been performed below a Raman microscope for single cells to obtain Raman spectra from the isolated cells.

Chapter 6: Demonstrations of single cell MCF trapping applications

Using the two- and the four beam fibre trap systems, as presented in Chapter 5, some preliminary optical trapping and manipulation demonstrations of a range of cell types in combination with different imaging microscopes, are presented in this Chapter.

Human erythrocytes (red blood cells, RBC), human glioblastoma cells (from the U87 cell line) and mouse embryonic stem cells (ES cells) have been trapped and observations are reported. Trapping of E.coli cells in suspension was attempted and the particle behaviour is qualitatively described. Finally, to test trapping of non-biological, low refractive index particles, using the MCF trap, the behaviour of hollow air-filled glass spheres in the fibre trap, is qualitatively described.

In a demonstration of potential future applications of the MCF trap, two cores have been used to trap a cell, allowing one of the other machined cores to deliver 480 nm wavelength laser light with the aim to excite fluorescence of the fluorescently labelled trapped cell. The ability to hold a single cell stationary was exploited in another set of demonstrations, to allow single-cell Raman microspectroscopy to be performed. It is shown that a Raman signal can be collected from a cell trapped using the machined MCF trap. These initial experiments pave the way for potential future work in cell identification or cell sorting based on an optical signature collected from a single trapped cell.

6.1 Two-beam MCF trapping of biological cells

Earlier, in section 5.1, trapping of single yeast cells was described and discussed. The optical trap was characterised in terms of trapping force and trap efficiency (a ratio of force divided by power). Yeast cells were chosen to work with as an alternative to polymer microspheres to characterise the trap. Uniform, synthetic microspheres would have given more repeatable and reliable results, but due to their 'stickiness' were not suitable for this purpose.

In this chapter, optical trapping of a range of different types of cells is undertaken, in order to evaluate the fibre-based optical trapping system, in terms of the capability to trap cells of different sizes, and accordingly to demonstrate these optical traps for a wider potential range of applications. To investigate the optical power required to trap a diverse variety of mammalian cells and to investigate the trapping distance (d_{trap}) to

ensure that one of the main benefits of the technique -contactless manipulation- is maintained, human red blood cells, human glioblastoma cells (U87) and mouse stem cells have been used to test trapping using the 2-core based MCF trap.

The optical trapping experiments have several common aspects. The size of each cell type was determined experimentally by taking the average diameter of 10 cells from a captured image of each cell. The uncertainty in this size arises from the spread in values in this sample set. The resulting average trapping distance is the mean value of the measurements of the three different frames of the d_{trap}, with the uncertainty based upon the spread of individual measurements (i.e. the minimum and maximum values of d_{trap}). Where images of cells in specific traps are presented in this chapter, the trapping distance shown on the figure is for that specific frame.

6.1.1 Trapping human erythrocytes (red blood cells)

Erythrocytes, also known as red blood cells (RBCs) are the most common type of blood cell in humans and are responsible for transferring oxygen to the body tissues through the blood flow and the circulatory system. RBCs are flexible and shaped as biconcave discs with a disk diameter for a typical human RBC of around 6-8μm in diameter and 2 μm thick, this is much smaller than other human cell types [167]. Trapping single RBCs is of interest for disease diagnosis [168] or to help detect cell damage due to blood storage prior to transfusion [169] or to sense molecular changes during oxygenation and deoxygenation [170].

In this experiment, several microliters of whole peripheral blood are taken by pricking the finger of a healthy donor with a lancet. Blood is collected in a heparinized capillary tube. The blood is diluted with phosphate buffered saline (PBS) in a volume ratio 1:10. The buffer maintains pH and osmotic levels, so cells do not shrink, swell or burst during the experiment.

Optical trapping of RBCs can be seen in figure 6.1. The fibre ('Fibre 2', 'fan-out 3' as described in Chapter 4.5.1) is held inside the inscribed microchannel containing the PBS/ RBC solution and is imaged from above, using the setup shown in chapter 4, figure 4.1. The diameter of the cells that were trapped in this work was measured to be 8 ±1 μm. A cell is trapped in three dimensions, as shown in figure 6.1 with a total optical power of 24.6 ± 0.1 mW. Trapping distance d_{trap} was measured in three 3 frames (a,d,g) in the same way as for yeast cells in the previous chapter, from the captured video, giving a mean value for d_{trap} and an associated uncertainty in the measurement of

d_{trap} =12.0 ± 0.7 μm. The uncertainty in d_{trap} can be traced to two sources: Firstly, it is due to the standard deviation for the three different measurements (± 0.5μm) as well as due to the uncertainty based on the resolution of the imaging system (± 0.5 μm). As discussed in Chapter 5, the cell undergoes Brownian motion within the optical trap and this motion results in a different d_{trap} measured for different frames of the video and thus contributes to the uncertainty in d_{trap}, assuming there are no other vibrations in the lab.

Figure 6. 1: Two-beam manipulation of a single RBC in three dimensions, along the x axis, parallel to the fibre axis (a-c), the y axis, perpendicularly to the fibre axis (d-f) and the z axis, in depth (g-i).The red arrow in the coordinate axis indicates the axis along which the fibre and the cell are translated, in each case. i) The trapping distance is measured from the centre of the cell to the fibre end face, and was measured to be 12 μm in this image.

As can be noticed in figure 6.1 (images a-c), the trapped cell (indicated by a red arrow) remains a fixed distance away from the fibre end, which is equal to the trapping distance, while the neighbouring cells labeled 1, 2 and 3 appear to move further away

from the fibre end during the movement of the fibre along the x-axis (parallel to the fibre axis).

The non-trapped cells do not experience an optical trapping force; and movement is due to PBS and Brownian motion.

Similarly, for the movement of the fibre along the y axis (perpendicularly to the fibre axis), the trapped cell shown in figure 6.1 (images d-f) remains at a stable trapping distance away from the fibre end while the neighbouring cells change position. Again here, the non-trapped cells noted as 1 and 2 are not trapped and they change position following the medium flow.

Concerning the movement of the fibre along the z-axis (by changing the depth of immersion), the trapped cell remains the same distance away from the fibre and it also remains in the same plane of focus as the fibre. In these images the fibre has been kept in focus and the neighbouring cells (cells 1, 2 and 3) appear to move in and out of focus. These cells are not subject to the fibre trapping force and do not follow the movement of the fibre but instead they move in the medium independently from the fibre movement due to Brownian motion and also due to any flow in the sample created by motion of the fibre.

An observation also made in this trapping experiment was that an RBC, when trapped, tended to flip (change orientation and hence appearance from circular to disc-shaped) depending upon the flow of the surrounding medium and thus the orientation of the cell depends upon the direction of any incident flow. The d_{trap} was measured in frames from sections of video where there was no detectable fluid flow and the trapped RBC looked circular in shape.

6.1.2 U87 human glioblastoma cell line

U87 cells are a human primary glioblastoma cell line mostly used for brain cancer research [171]. They have epithelial morphology when grown in culture. In order to trap them, they were prepared in suspension by Dr Yasmine Tawil from the laboratory of Prof. Nick Leslie at the Institute of Biological, Chemistry and Bioengineering at Heriot-Watt University.

Cells were suspended in MEM media (Eagle's Minimum Essential Medium) supplemented with 10% Foetal Bovine Serum (FBS), 1% Non-essential amino acids, 1% Glutamax, 1% Anti-mycotic/Anti-biotic and 1% Sodium Pyruvate. The cells have a

'sphere like' morphology and their size is known to vary between 17 and 25 μm in diameter. The diameter of the cells that were trapped in the experiments described here were measured to be 19 ± 1 μm.

Figure 6.2 shows one example of three-dimensional trapping of a single U87 cell using the two-beam trap, at a distance d_{trap}=12.5± 0.6 μm away from the fibre end when measured from the centre of the cell. This trapping distance is the distance as depicted in figure 6.2 (j) and the source of uncertainty here is due to three different measurements (frames 6.2 a, d, g) as well as due to the CCD system resolution. The total optical power exerted upon this trapped cell is 28.1 ± 0.1 mW. The fibre and the fan-out used for these experiments were 'Fibre 2' and 'fan-out 3', as before.

Like before, the field of view remains fixed and any change in position of the fibre is due to its translation.
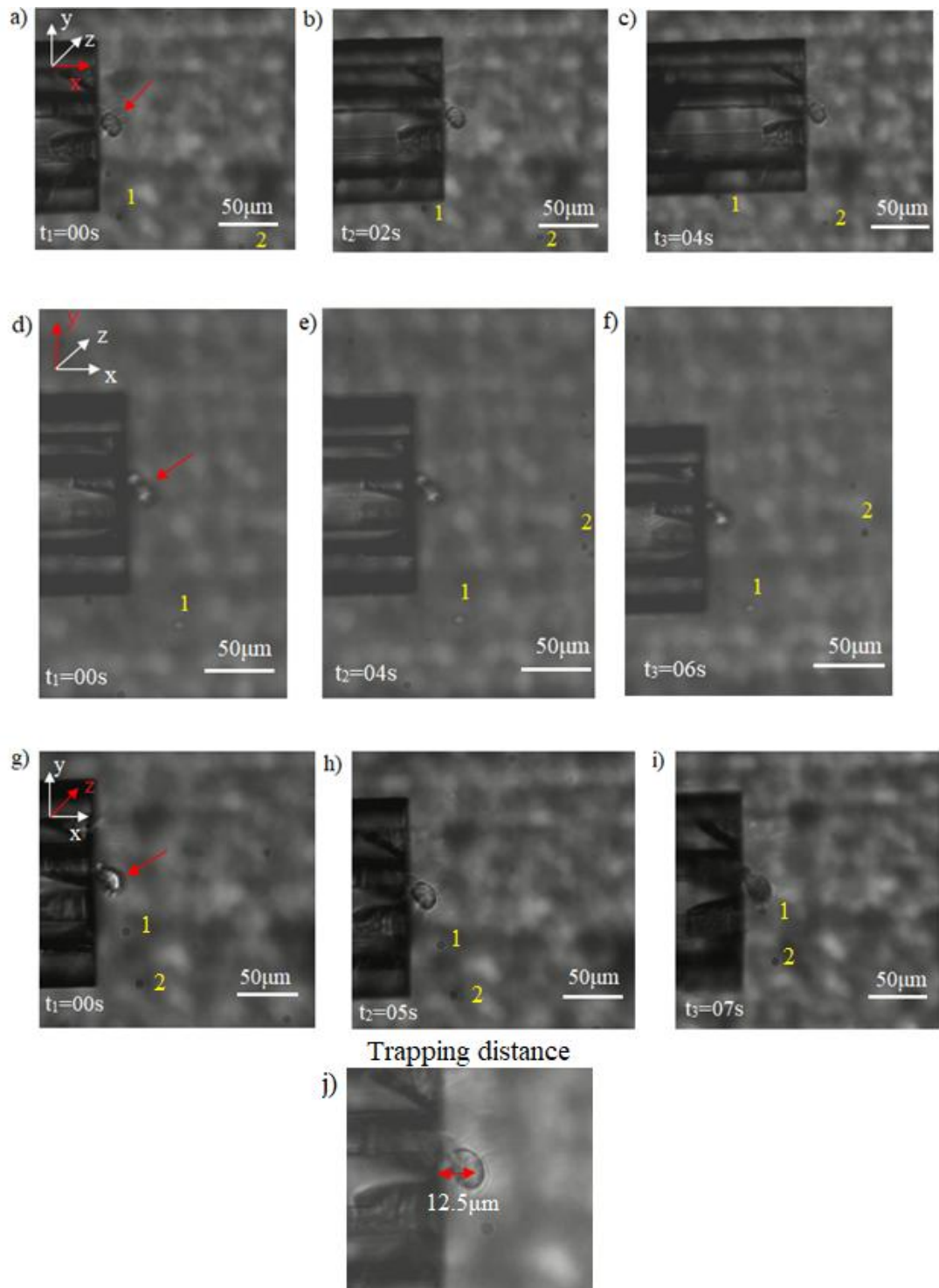
Figure 6. 2: Two-beam manipulation of a single U87 cell in three dimensions, along the x axis, parallel to the fibre axis (a-c), the y axis, perpendicular to the fibre axis (d-f) and the z axis, in depth (g-i).The red arrows in the coordinate axis indicate the axis of trapping that is studied in each case. i) The trapping distance from the centre of the cell to the fibre end.

As can be seen in figure 6.2 (images a-c), the trapped cell that is highlighted by the red arrow remains a stable distance away from the fibre face, which is equal to the trapping distance, during the movement of the fibre along the x axis (parallel to the fibre axis). In these images, particles in the medium (most likely cell debris), marked as 1 and 2, change position as they are not trapped, and move due to the medium flow.

In a similar way, figure 6.2 (images d-f) demonstrate the movement of the fibre along the y-axis (perpendicularly to the fibre axis), and the respective position of the trapped cell, which remains at a stable position with respect to the fibre face. The nearby particles 1 and 2 appear to be stable inside the medium without moving around or following the movement of the fibre. This suggests that the flow inside the medium was low during this experiment, thus the free cells did not show significant movement.

A similar case is noticed for the movement of the fibre along the z axis. The cell remains stably trapped, while the non-trapped particles 1 and 2 remain at a certain position inside the micro channel without moving, possibly due to a negligible amount of flow in the sample, due to its low speed of translation.

As figure 6.2 indicates, the cell is trapped very close to the fibre-end. This imposes limitations in the system's ability to trap cells larger than these due to the risk that they will contact the fibre-end face. However, an important point that can be examined in any future work is how the mirror angle could be varied so that the trapping distance is increased. Referring back to the geometrical approach of the d_{trap}, the largest d_{trap} for an average mirror angle of 70° was approximately 30 μm, which is in broad agreement with the experimental d_{trap} of U87 cell. In this case, larger diameter cells can potentially be trapped whilst avoiding direct contact with the fibre surface.

6.1.3. Murine Embryonic Stem cells (ES)

Embryonic Stem cells (ES) are derived from the inner cell mass of a blastocyst, an early-stage pre-implantation embryo and Mouse ES cells [172] were provided for testing by Prof. Ian Chambers of the MRC Centre for Regenerative Medicine, University of Edinburgh and were prepared by Dr Douglas Colby.
Mouse ES cells are 'sphere-like' with a size between 10-20 μm [173]. The cells used in the trapping experiments in this thesis were measured to be of diameter 13 ± 1 μm.

As seen in figure 6.3, a single ES cell has been trapped and manipulated in three dimensions. The trapping distance was measured to be d_{trap}=13.5 ± 0.5 μm and it refers to the trapping distance as measured in the specific trap demonstrated in figure 6.3. The total optical trapping power used was 27.8 ± 0.1 mW. The trapped cell has

remained stable during the movement of the fibre along the three axes. For the case of the ES cells, there were no neighbouring cells close to the trapped cell to use as a reference for the analysis of the trapping in 3 dimensions, however as it can be seen from figure 6.3, the cell remains at a stable position away from the fibre end for the time frames as the fibre is translated. Again, here the system used for trapping was 'Fibre 2' and 'fan-out 3'.
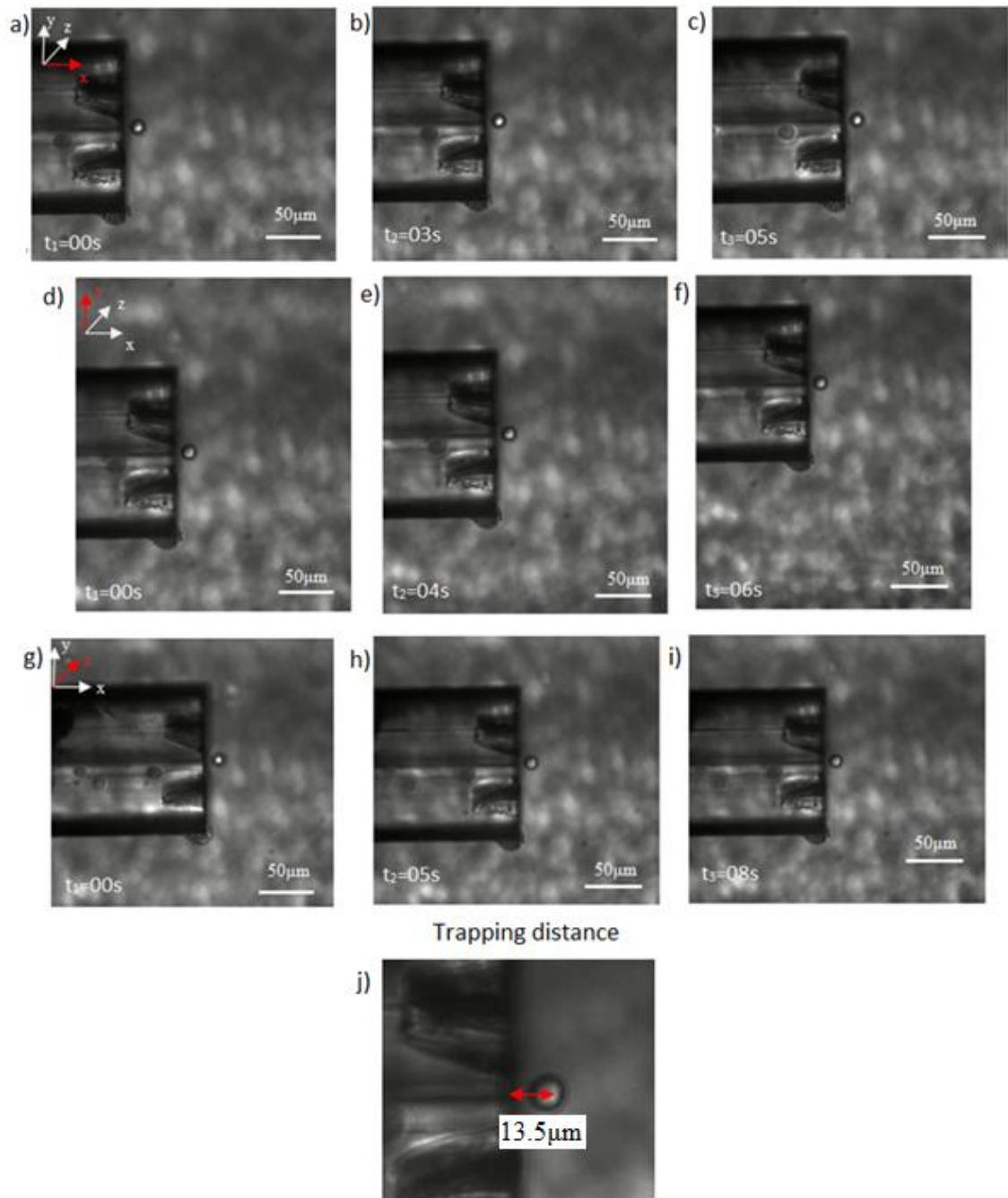
Figure 6. 3: Two-beam manipulation of a single mouse ES cell in three dimensions, along the x axis parallel to the fibre axis (a-c), the y axis, perpendicularly to the fibre axis (d-f) and the z axis, in depth (g-i). The red arrows in the co-ordinate axis indicate the axis of trapping that is studied in each case. i) The trapping distance measured from the centre of the cell, to the fibre end.

6.1.4 Trap strength measurement using three cell types

In a similar manner to the yeast cells, the characterisation of the trap strength for the cells mentioned above; RBCs, U87s and ESs was based on a pre-calibrated conventional OT system and the results for the trapping force and the trap efficiency Q for respective optical powers are presented in Table 6.1. As a reminder, Q has been previously defined in detail in Chapter 5.4.

The conventional OT system was precalibrated for every different cell type tested. The respective graphs for each cell type, of critical velocity (u_{crit}) plotted against conventional OT power are shown in figure 6.4 A range of trapping optical power is used to allow a best fit model to be applied to the data.
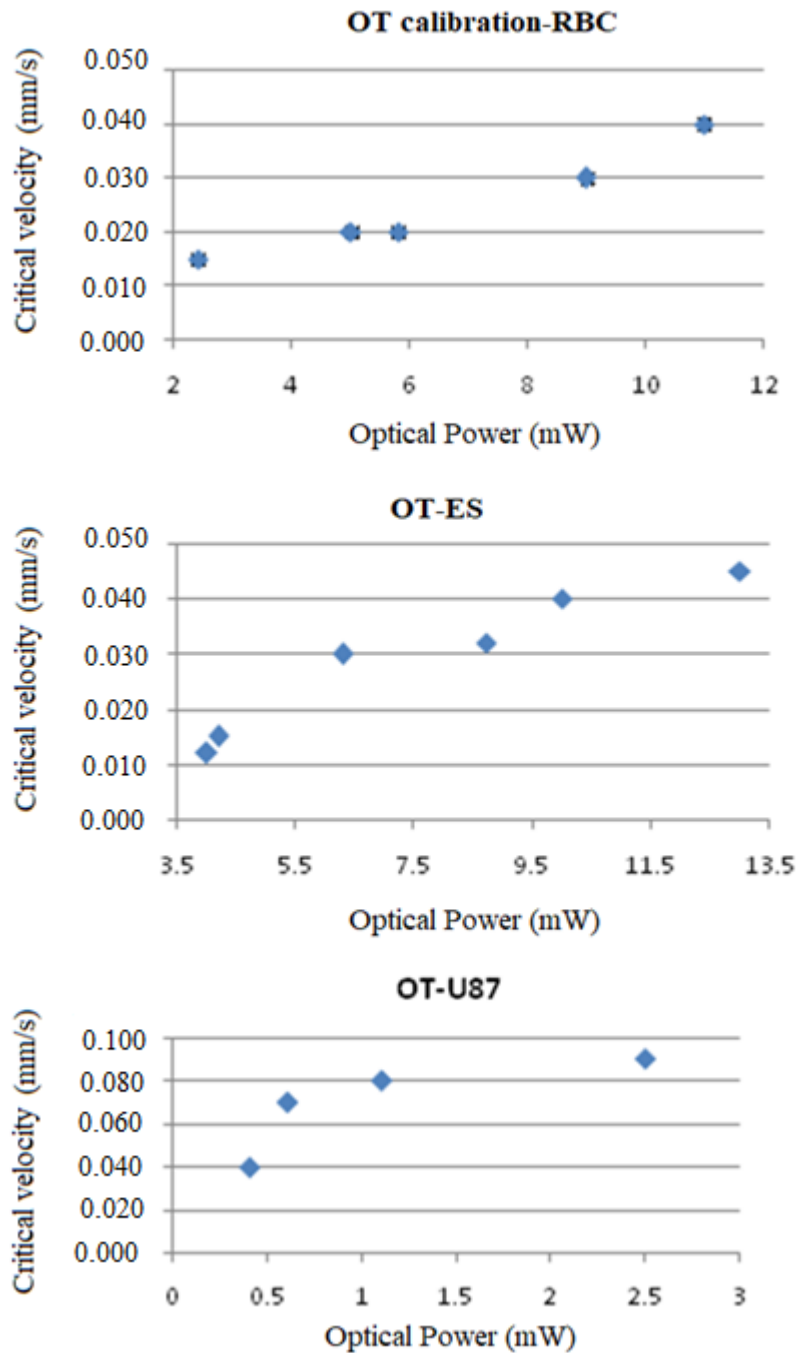
Figure 6. 4: OT calibration for the three different types of cells a) human Red Blood Cells (RBC), b) murine Embryonic Stem Cells (ES) and c) human glioblastoma cells (U87 cell line).

The method outlined in Chapter 5 section 5.4 that uses a calibrated OT to break the fibre trap, thus giving an estimate of the force of the fibre trap (Ffibre,), and the Q value of the fibre (Q_{fibre}) is followed here for trapping different cell types.. In this experiment the OT is calibrated for each cell type and from the measured critical velocity and Stokes Law (Eq. 5.4) the maximum trap force can be calculated for each optical power used. To measure F_{fibre} the OT is placed approximately 5 μm from the fibre trap, and the OT power is increased until the cell, initially stably trapped in the fibre trap, jumps from the fibre trap into the OT to be stably held in the OT. Using the graph of OT trap force

against OT optical power, the force exerted by the OT required to break the fibre trap is acquired and equated to the strength of the fibre trap, Ffibre. Once Ffibre and the power in the fibre trap (P_{fibre}) are measured, Q_{fibre} can be calculated from equation 5.3 in Chapter 5.

Cell Type	P_{fibre} (±0.1mW)	F_{fibre} (pN)	Q_{fibre}
RBC (d=8 ± 1µm)	24.6	0.6±0.2	0.005 ±0.001
U87 (d=19 ± 1µm)	28.1	4.4±0.6	0.035 ±0.004
ES (d=13 ± 1µm)	27.8	4.5±1.1	0.036 ±0.009
Yeast (d=7 ± 1 µm)	29.9	1.8±0.5	0.013 ±0.003

Table 6. 1: Maximum trap force (F_{fibre}) and Q (Q_{fibre}) of the two-beam fibre trap, measured using trapped RBCs, U87 cells, ES cells and yeast cells. d is the cell diameter.

Results of maximum trapping force of the two beam trap (F_{fibre}) and the efficiency of the two beam MCF (Q_{fibre}) for human RBCs, cells from the U87 human glioblastoma cell line and mouse ES cells, and the results for yeast cells (from Chapter 5) are shown in table 6.1. Three main parameters should be considered when interpreting the results; cell size, refractive index of the cells and refractive index of the surrounding medium. First, the cell size varies from 5-7 µm on average for the yeast cells,7-8 µm for RBC cells, 10-20 µm for ES cells and 17-25 µm for U87 cells, according to measurements and in agreement with literature. Additionally, the surrounding medium differs for each cell type. All cells are in an aqueous environment, with the yeast cell suspended in water (n=1.33), RBCs and ES cells suspended in PBS (n=1.34) [174] and U87 cells are suspended in MEM with additional supplements (n is approximately 1.34) [174]. Although the refractive indices of the media are very similar, this small difference could potentially lead to alteration of the propagation of the light during the refraction on the cell and during the scatter inside the medium. The refractive indices of the cells are assumed to be 1.39 for yeast cells [175], 1.38 for the U87, 1.399 for the RBC [176] and 1.375 for the ES cells [177].

Another factor to consider is the difference between the size of the cell and the size of the overlap region forming the trap. Smaller particles were observed to move around more in the trap. This will be examined more in the centre of mass analysis, later in this chapter. For a smaller particle, the smaller interaction cross section means that the particle will be affected by only part of the trapping beams, so the imparted force will be lower. It will only experience a scattering force from that fraction of the beam. If a particle is better matched to the trap size it can 'see' more of the beam, most of the light is scattered or refracted by the cell so the trap becomes more efficient, and thus Q_{fibre} is

measured to be larger for the larger cell types, U87 and ES cells, as presented in table 6.1.

In more detail, for the two-beam trap ('fibre 2', core 1 and core 3), the cross sectional area, in x-z plane, based on the beam spots is measured to be A=$(295 \pm 12) \times 10^{-8}$cm^2 (as discussed in Chapter 5). If considering the cell radius for each cell type, then the cell area (assuming a circular shape) for RBC, U87 and ES cells will be A_{RBC}=$(50.2 \pm 12) \times 10^{-8}$ cm^2, A_{U87}=$(295 \pm 31) \times 10^{-8}$ cm^2 and A_{ES}=$(132 \pm 20) \times 10^{-8}$ cm^2, respectively. Additionally, as it was measured in Chapter 5, the respective cell area value for the yeast cell was A_{yeast}=$(50 \pm 14) \times 10^{-8}$ cm^2. Based on these measurements, and if the differences in the refractive indices between the media and the cell types are considered negligible, then the order of the cells that undergo more efficient trapping (higher Q_{fibre}) to those that undergo the less efficient trapping is: U87 cells, ES cells, RBCs and yeast cells. This is in broad agreement with the Q_{fibre} values reported in Table 6.1. The larger ES and U87 cells, which better match the size of the trap are more efficiently trapped, with larger maximum force measured for a given trap power, and a larger value for Q_{fibre}, which was found to be 0.036 ± 0.009 and 0.035 ± 0.004, respectively. The smaller RBCs and yeast cells which only 'see' part of the trap as they are smaller than the trapping region experienced a smaller trapping force, F_{fibre}, and had a lower efficiency Q_{fibre}, of 0.005 ± 0.001 and 0.013 ± 0.003, respectively.

6.2 Four-beam MCF trapping of biological cells

Similar to the above study of two-beam trapping of RBCs, U87 cells and ES cells, measurements of d_{trap} and demonstrations of 3D manipulation are made whilst trapping RBCs and ES cells using the same 'fibre 2' as above, but this time all four cores were used to create a four-beam trap. The measurement of F_{fibre} by 'breaking' the fibre trap using an OT of known force is also made and based on that, Q_{fibre} is also calculated.

U87 cells have not been examined in this case because there were no available cells of that type during the period of the four-beam experiments, however conclusions can be made on the basis of available cells.

As before, cell sizes have been measured experimentally, and d_{trap} values are based upon the measurements of the trapping distance in the three different frames (a,d,g) of the same cell trapping experiment video.

6.2.1 Human erythrocytes (Red blood cells)

Optical trapping of single RBCs in three dimensions using a fibre with four machined cores is shown in figure 6.5. The total optical power is 29.9 ±0.1 mW and the measured trapping distance away from the fibre end-face $d_{trap}= 13.5 \pm 0.5$ µm.
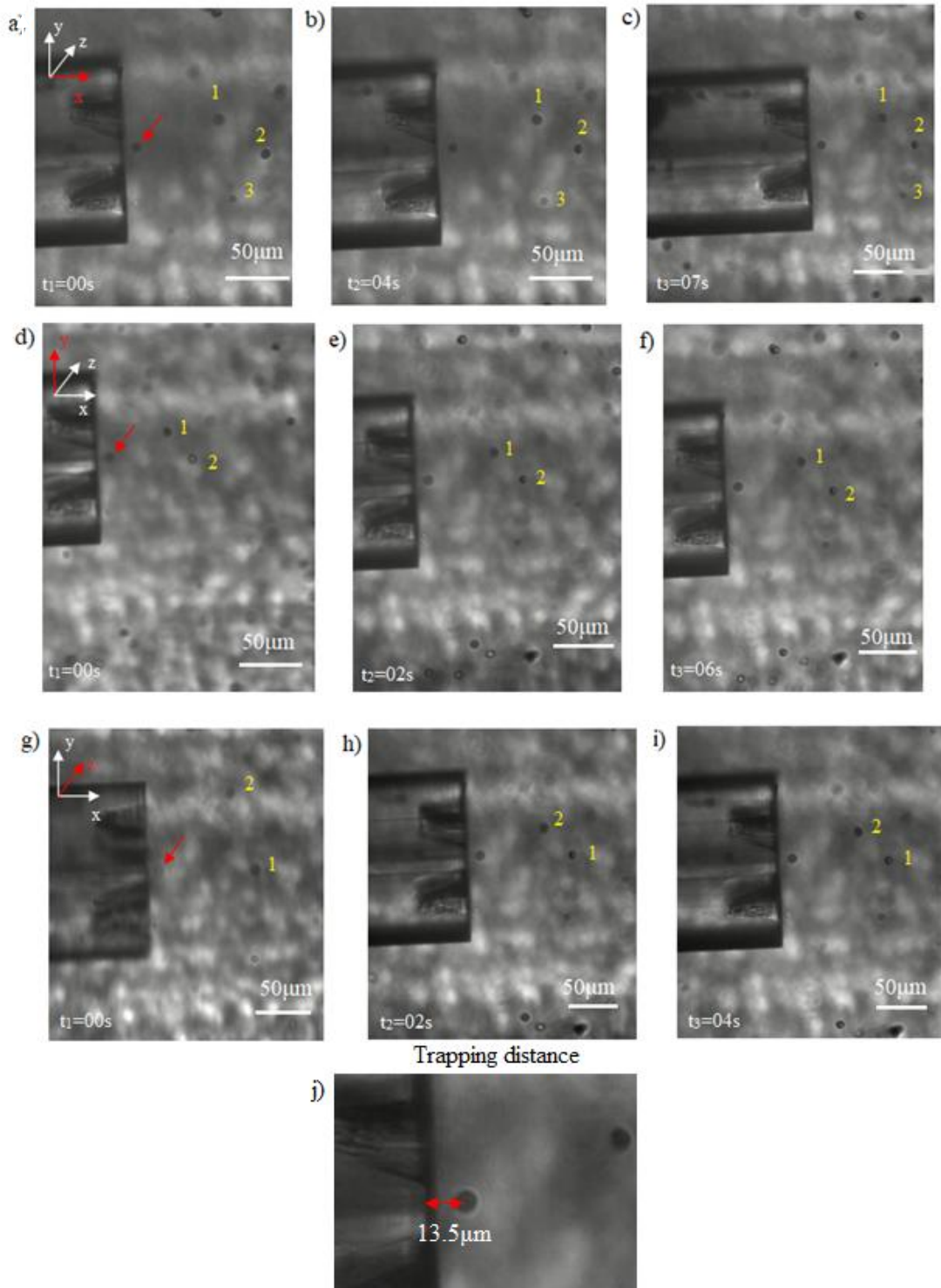
Figure 6. 5: Four-beam manipulation of a single RBC cell in three dimensions, along the x axis , parallel to the fibre axis (a-c), the y axis, perpendicularly to the fibre axis (d-f) and the z axis, in depth (g-i).The red arrows on the axis labels indicate the axis of trapping that is studied in each case. i) The trapping distance is measured from the centre of the cell to the fibre end.

Figure 6.5 images (a-c) show the movement of the fibre in the x-axis, parallel to the fibre axis, and the trapped cell (identified by a red arrow) that remains held at a stable distance away from the fibre end. In contrary, the non-trapped cells 1 and 2 are seen to change position with respect to the fibre end, which shows that they are not trapped. In

a similar way, figure 6.5 images (d-f) indicates movement of the fibre along the y axis, perpendicularly to the fibre axis, with the trapped cell again maintaining the same stable trapping distance away from the fibre face, while the free cells change position with respect to the fibre end, however the movement of the cells 1 and 2 is smaller than in previous cases, possibly because of the low flow of the medium. Figure 6.5 images (g-i) show the movement of the fibre along the z axis, moving in depth, holding the trapped cell at a distance equal to trapping distance and the non-trapped cells are seen to change position for the different immersion depths of the fibre, which indicates that these cells are not trapped but they follow the flow of the medium.

6.2.2 Embryonic Stem cells (ES)

Optical manipulation of a single ES cell in x, y and z directions using the four-beam trap, has been demonstrated (Fig. 6.6). The total optical power of the four cores is 32.6 mW and the trapping distance away from the fibre-end was measured from captured images to be $d_{trap}= 13.5 \pm 0.5$ μm.
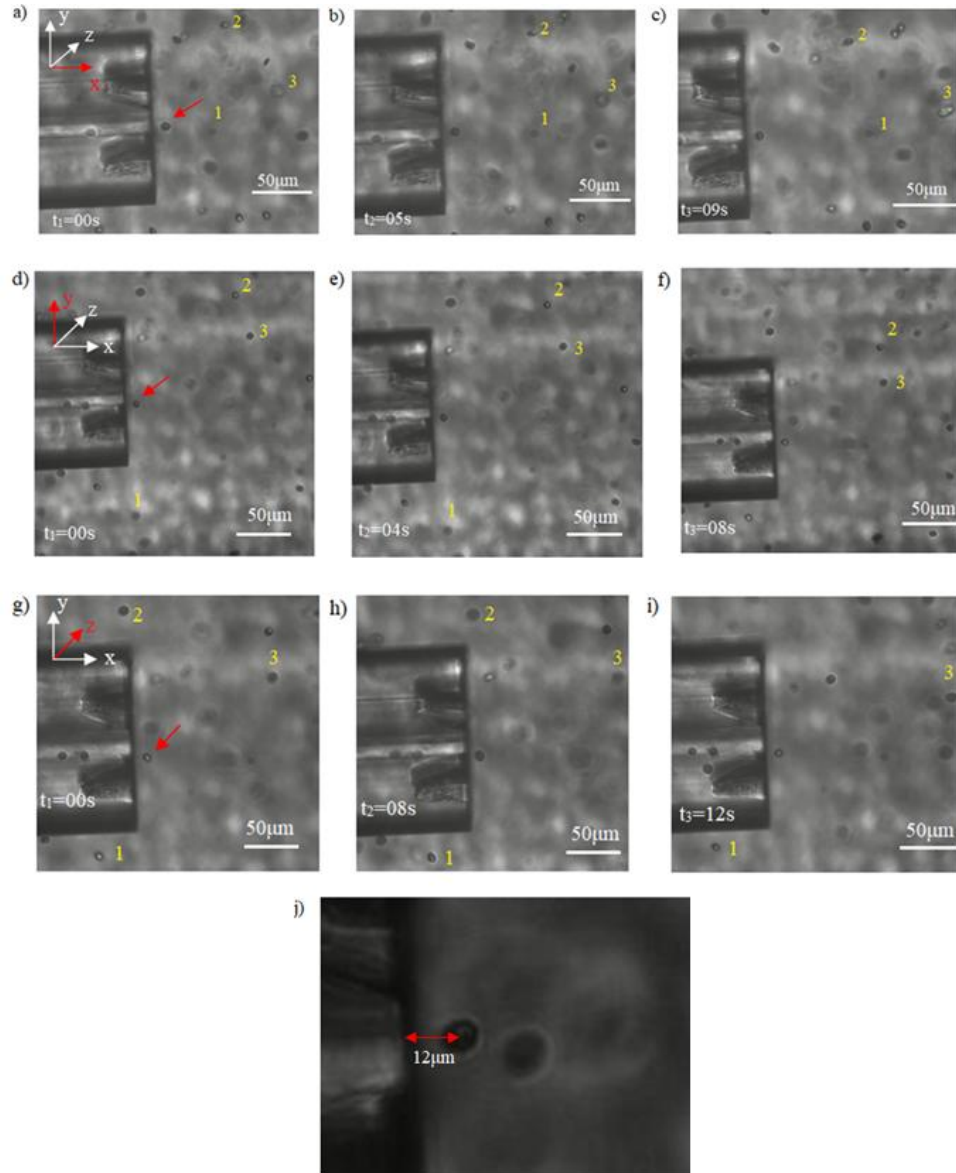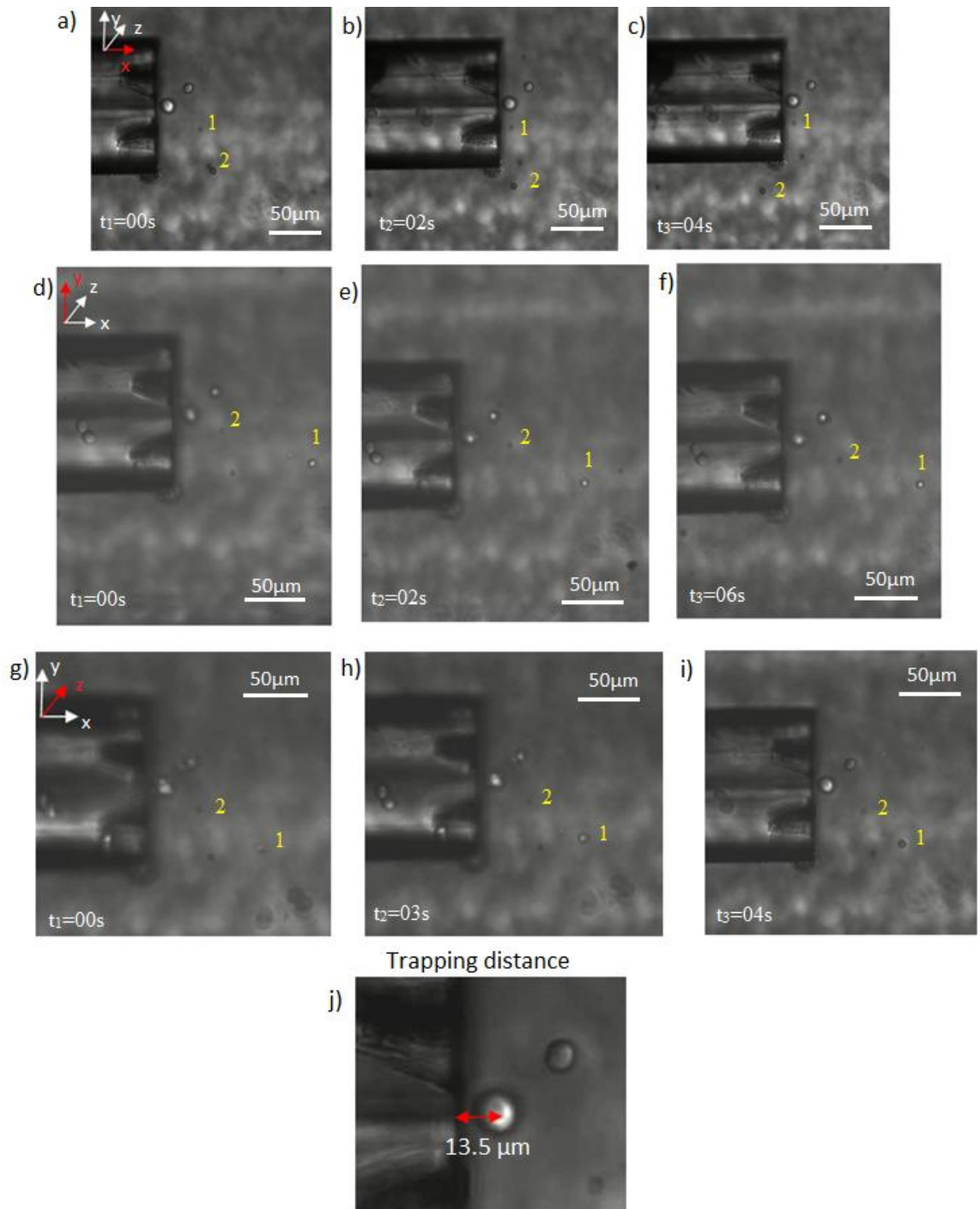
Figure 6. 6: Four-beam manipulation of a single ES cell in three dimensions, along the x axis , parallel to the fibre axis (a-c), the y axis, perpendicularly to the fibre axis (d-f) and the z axis, in depth (g-i).The red arrows in the axis label indicates the axis of trapping that is studied in each case. i) The trapping distance measured from the centre of the cell to the fibre end.

Figure 6.6 images (a-c) show the movement of the fibre along the x-axis, parallel to the fibre axis and the trapped ES cell (indicated by a red arrow) that remains at a stable position with respect to the fibre end. The non-trapped cells, or more likely cell debris, 1 and 2 change position relative to the fibre end, which denotes that they are unaffected by the optical trap. Similarly, Figure 6.6 images (d-f) indicates movement of the fibre along the y axis, perpendicular to the fibre axis, with the trapped cell again maintaining

the same stable trapping distance away from the fibre face, while the free cells change position with respect to the fibre end. Figure 6.6 images (g-i) show the movement of the fibre along the z axis, showing the trapped cell at a distance equal to trapping distance and the neighbouring cells 1 and 2 change position for the different immersion depths of the fibre, which indicates that these cells are not affected by the fibre trap but they follow the flow of the medium. As can be noticed in figure 6.6, there is a second cell close to the trapped cell that appears to be stable during the movement of the fibre along the three axes. However, this cell is not understood to be trapped, as it is not placed inside the beam path, but it could be that it potentially moves very slowly due to the low medium flow at this location.

The results of the characterisation method based on the pre-calibrated OT system for the RBCs and the ES cells can be found in Table 6. 2, following the same process as in the case of the two-beam trap in the previous section.

Cell Type	P_{fibre} (±0.1mW)	F_{fibre} (pN)	Q_{fibre}
RBC (d=8 ± 1μm)	29.9	1.14±0.34	0.009±0.002
ES (d=15 ± 1μm)	32.6	3.87±0.77	0.027±0.005
Yeast (d=7μm±1 μm)	31.0	2.37±0.24	0.017±0.001

Table 6. 2: Maximum trap force F_{fibre} and Q_{fibre} of the four-beam fibre trap, measured using trapped RBCs, ES cells and yeast cells

To explain the differences between Q_{fibre} and the trapping distances for the different cell types the different cell sizes, the small differences in the refractive index of the different media (water, PBS, MEM) as well as the refractive index of the different cells types can be considered negligible, as was the case for the two-beam trap discussion earlier.

Analysis of the trap strength based on the overlap area size and the respective cell sizes for the four-beam trapping area (A=(295 ± 12)×10^{-8} cm^2 from Chapter 5) and the respective size areas of the cells, A_{RBC}=(50 ± 12)×10^{-8}cm^2, A_{yeast}=(50 ± 14)×10^{-8} cm^2 and A_{ES}=(132 ± 20)×10^{-8} cm^2, suggests a similar trap area in the x-z plane as the two-beam trap, and that the larger ES cells will 'see' more of the trapping light therefore be trapped more strongly than the smaller RBCs and yeast cells.

The results of maximum force shown in table 6.2, show that indeed, ES cells are trapped more strongly (3.9 ± 0.8 pN for a 32.6 mW trap) than RBCs (1.1 ± 0.3 pN) and yeast cells (2.3 ± 0.2 pN), for albeit lower laser powers of 29.9 mW and 24.6 mW, respectively. Based on these force and power measurements, the fibre trap efficiency, Q_{fibre}, can be calculated. The most efficient trap (higher Q of 0.027 ±0.005)

is when the larger ES cells are used. The fibre trap is less efficient when smaller RBCs ($Q = 0.009 \pm 0.002$) and yeast cells ($Q = 0.017 \pm 0.001$) are trapped.

The average measured trapping distances for the three different frames of the same cell trapping experiment for both two-beam and four-beam traps are summarised in the graph below:
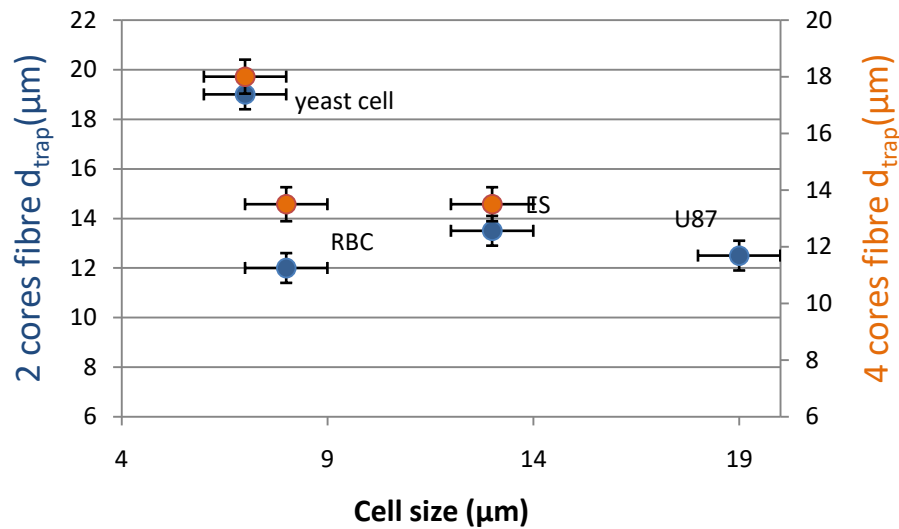
Figure 6. 7: Average trapping distance d_{trap} plotted against cell size. Blue circles are measurements from the two-beam trap and orange circles are measurements from the four beam trap.

The error in cell size in figure 6.7 shows the range of cell sizes measured in separate samples, and the error in y-axis shows the range of the trapping distances for the three different video frames.

The above graph indicates how the resulting trapping distance varies according to the cell diameter. In general, a cell can be trapped in any position inside the overlapping area of the beams, most likely in the highest intensity region. Each cell finds an equilibrium position within the trap where there is balance between scattering forces and gradient forces, leading to a stable trap position in 3D. The trap position is determined by beam geometry, cell dimensions and refractive index contrast between the cell and the surrounding medium.

6.3 Cell position tracking

As described in Chapter 5, image analysis was applied to videos of the trapped particle in a stationary (not translated) fibre to track the cell position in the x-y plane as it moves around the trap due to Brownian motion. This will help us understand how tightly confined the trapped cells are and how different cell types can move around in the trapping region. Tracking trapped particles for long periods has the potential to indicate

if the trap had the same level of stiffness in both the x and y directions, like a conventional OT, or if the trap does not have the same stiffness in the two orthogonal axes. However, as also mentioned in Chapter 5, stiffness cannot be calculated in our case, as the video frames that were analysed were not enough to allow us derive secure conclusions.

The frame rate of the camera used to acquire the trapping experiments was 10 frames/sec and the pixel size was measured to be 0.3×0.3μm square pixel, having as a reference a known dimension which in this case was the MCF diameter.

The same Matlab code as in Chapter 5 was used for the trapping experiments of red blood cells, ES and U87 cells and the respective results are summarized in the following figures for each cell type.
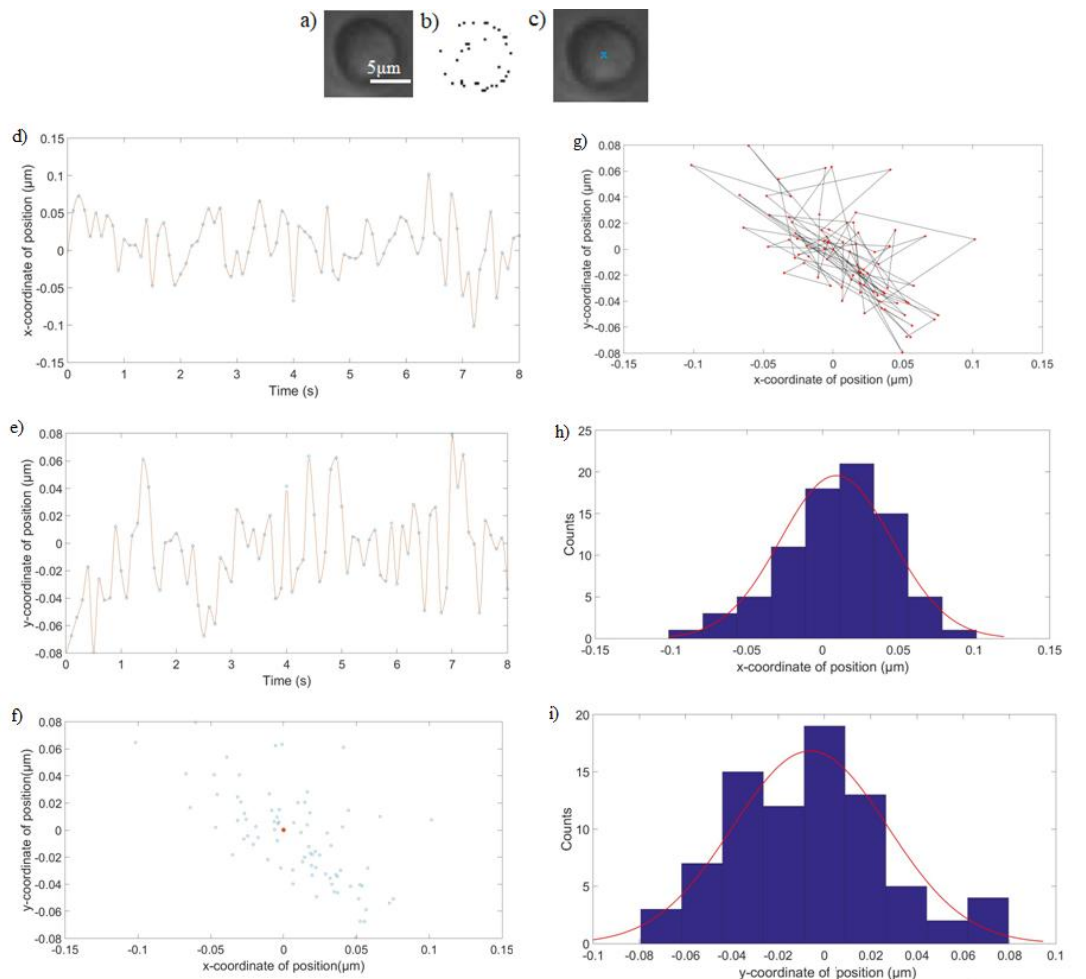
Figure 6. 8: ES cell position tracking analysis for the two-beam trap. a)Image of ES cell as imaged from the CCD, of a diameter of 13 ± 1μm, b) Binary image as created using the Matlab code, c) Centre of mass as calculated with the centre of mass analysis, d) x-trajectory of the cell while trapped, e) y-trajectory of the cell position while in trap, f)Centres of mass 2D plot, g) 2D plot of particle motion in trap, h) Distribution of the x-coordinate of position of the trapped cell and Gaussian fit (red curve), i) Distribution of the y-coordinate of position of the trapped cell and Gaussian fit (red curve).
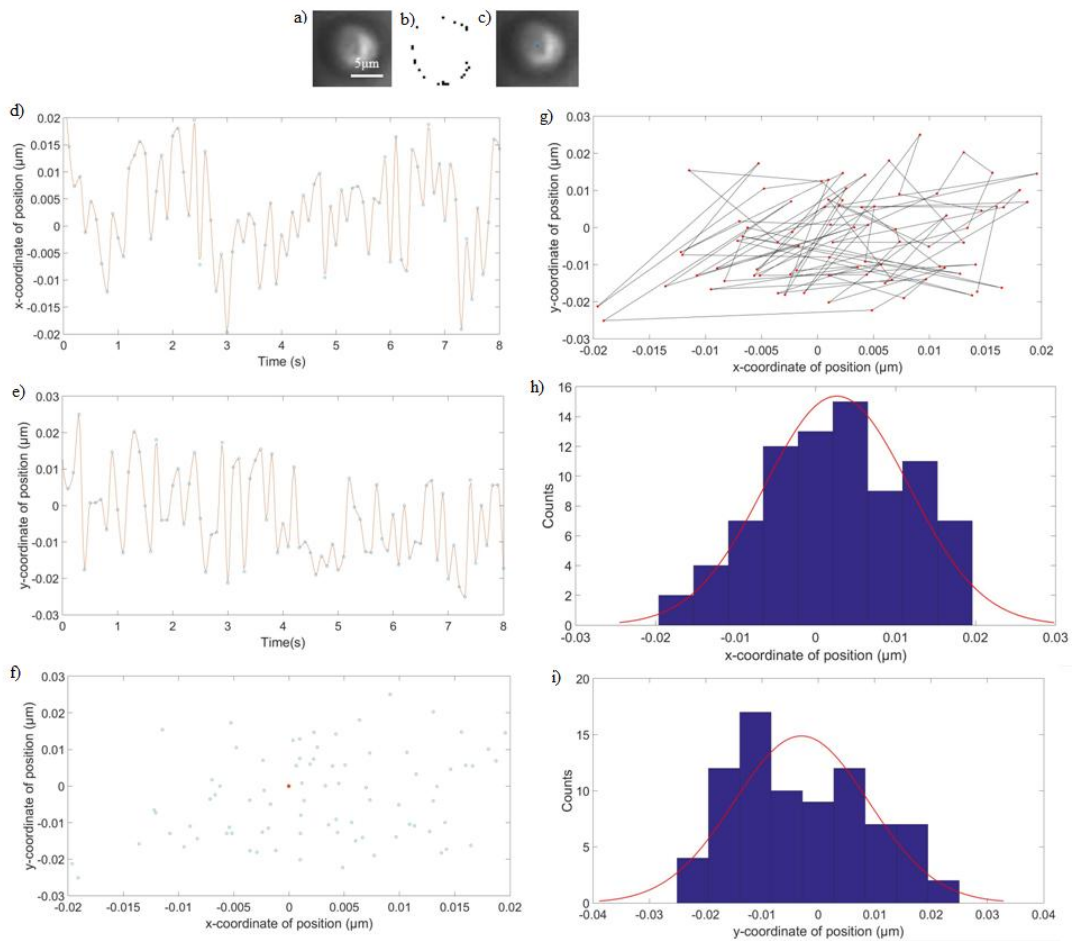
Figure 6. 9: ES cell position tracking analysis for the four-beam trap a)Image of ES cell as imaged from the CCD, of a diameter of $15 \pm 1\mu m$ b) binary image as created using the Matlab code, c) centre of mass as calculated with the centre of mass analysis, d)x-trajectory of the cell while being in trap and e) y-trajectory of the cell position while in trap. f)centres of mass plot. g) 2D plot of particle motion in trap h) Distribution of the x-coordinate of position of the trapped cell and Gaussian fit (red curve), i) Distribution of the y-coordinate of position of the trapped cell and Gaussian fit (red curve).
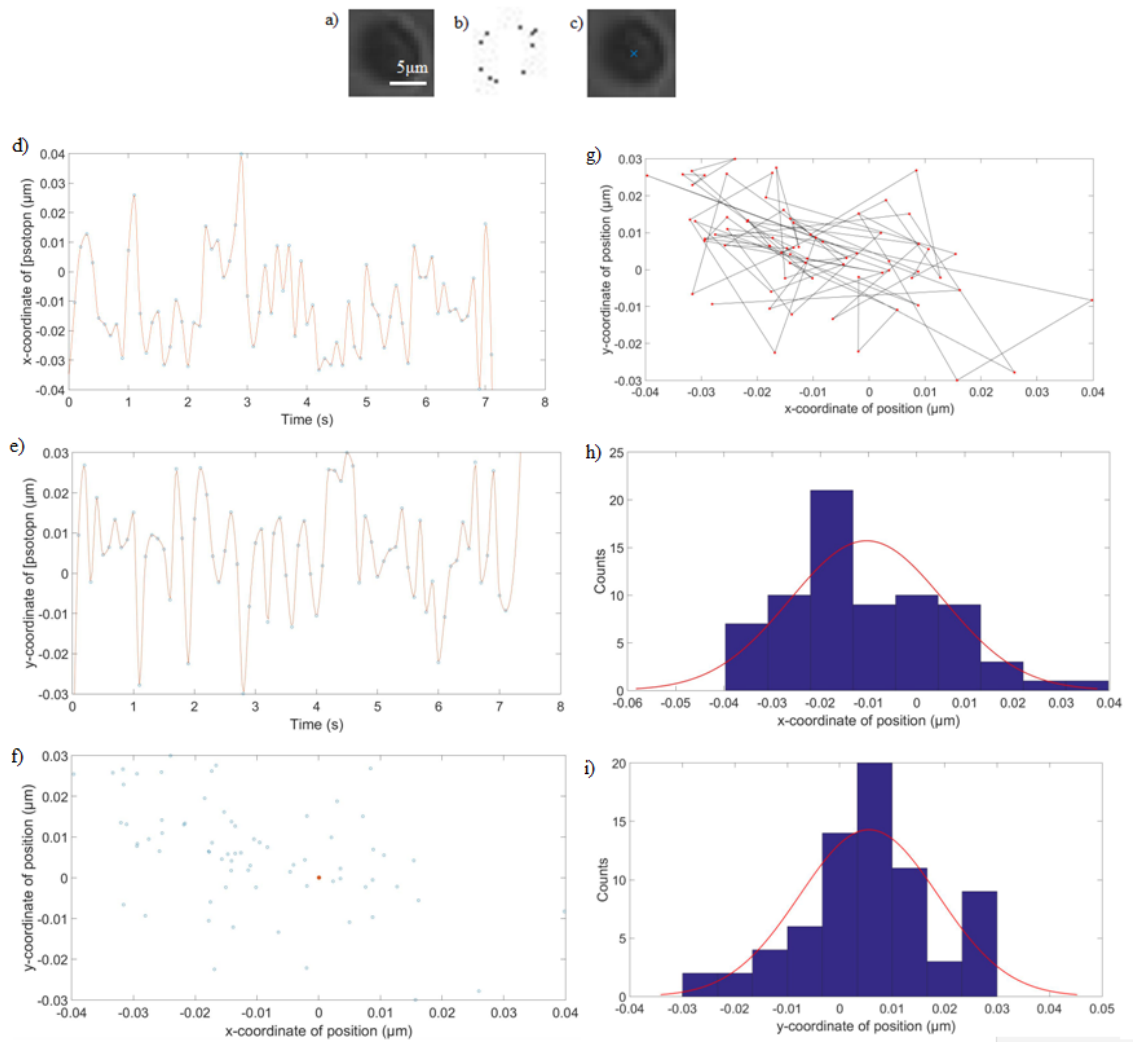
Figure 6. 10: Red blood cell position tracking analysis for the two-beam trap a)Image of ES cell as imaged from the CCD, of a diameter of $8 \pm 1 \mu m$ b) binary image as created using the Matlab code, c) centre of mass as calculated with the centre of mass analysis, d) x-trajectory of the cell while being in trap and e) y-trajectory of the cell position while in trap. f)centres of mass plot. g) 2D plot of particle motion in trap h) Distribution of the y-coordinate of position of the trapped cell and Gaussian fit (red curve).
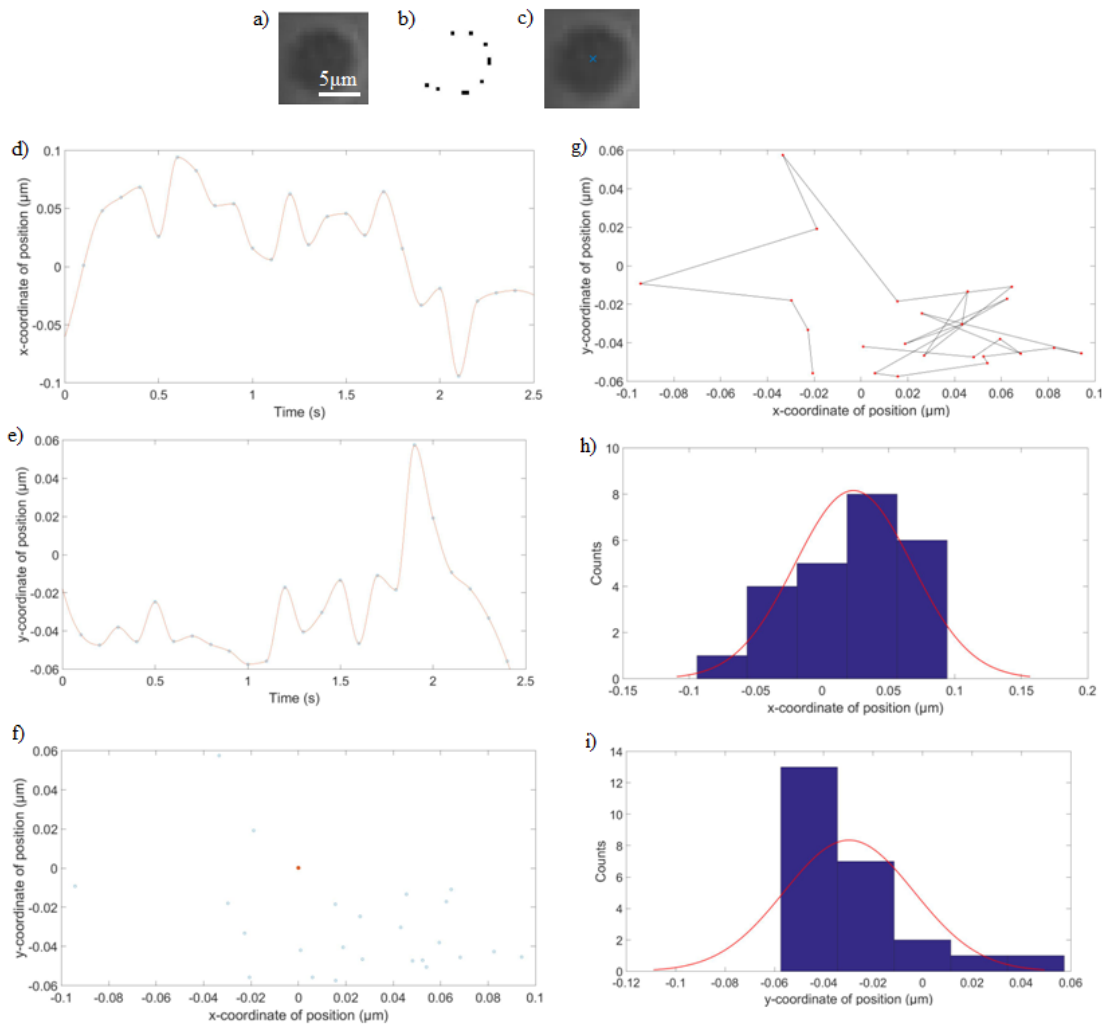
Figure 6. 11: Red blood cell position tracking analysis for the four-beam trap. a) Image of ES cell as imaged from the CCD, of a diameter of 8 ± 1 μm, b) Binary image as created using the Matlab code, c) Centre of mass as calculated with the centre of mass analysis, d) x-trajectory of the cell while trapped, e) y-trajectory of the cell position while in trap, f) Centres of mass plot, g) 2D plot of particle motion in trap h) Distribution of the y-coordinate of position of the trapped cell and Gaussian fit (red curve).
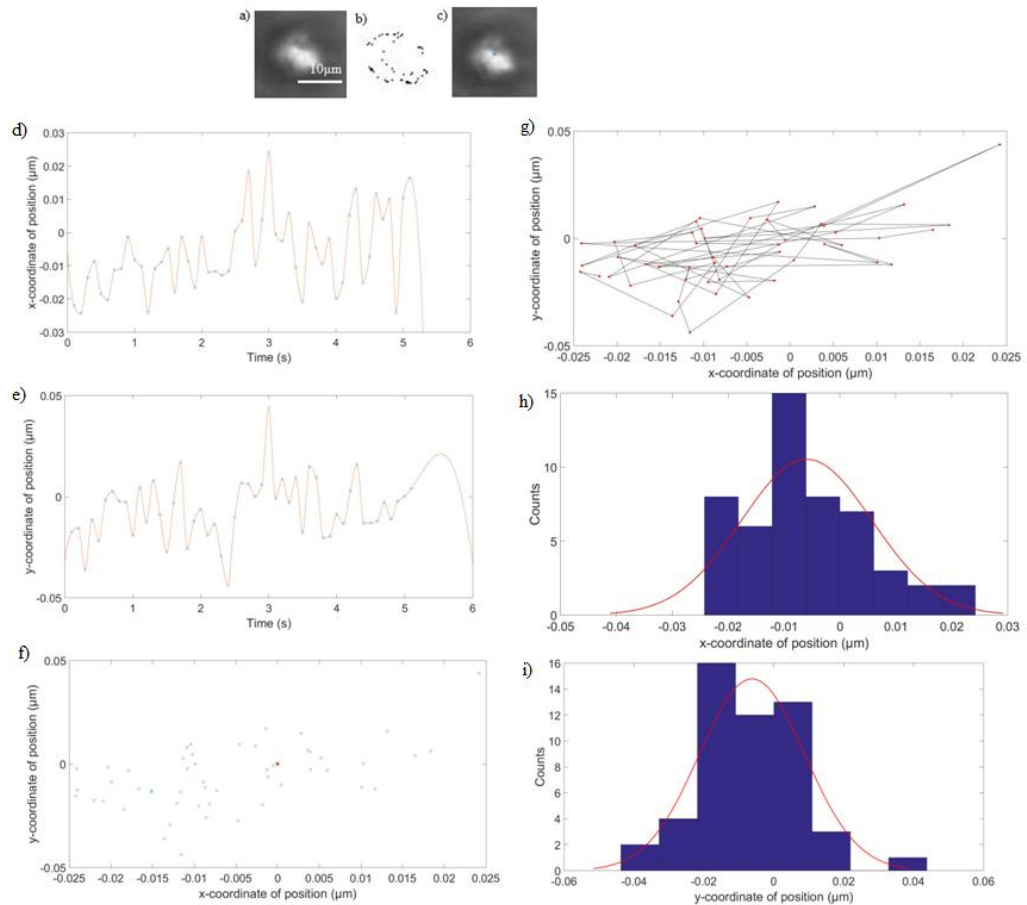
Figure 6. 12: U87 cell position tracking analysis for the two-beam trap a) Image of ES cell as imaged from the CCD, of a diameter of $19 \pm 1\mu m$ b) Binary image as created using the Matlab code, c) Centre of mass as calculated with the centre of mass analysis, d) x-trajectory of the cell while being in trap and e) y-trajectory of the cell position while in trap. f)centres of mass plot. g) 2D plot of particle motion in trap h) Distribution of the y-coordinate of position of the trapped cell and Gaussian fit (red curve).

6.4 Trapping diverse particles in the MCF

In this section, a range of other particles are used to test the trapping capability of the MCF trap. Bacteria trapping was tested using the four beam trap. Hollow glass sphere (low refractive index compared with surrounding media) trapping demonstration is also presented.

6.4.1 Trapping bacteria using a machined multicore fibre trap

Trapping individual cells is important because it offers the opportunity to study them in isolation, in a well-controlled environment, without any interfering interactions from other cells. This applies to the yeast cells and mammalian cells previously described, but also to bacteria, which are typically smaller, around 0.5 - 3 μm in diameter, depending on the species or strain [178].

Studies that describe optical trapping of bacteria using conventional microscope-based optical tweezing systems, have been reported. In 1987 [179], Ashkin *et al.* demonstrated optical manipulation of single, live, motile, unidentified bacteria and single, live *E.coli* bacteria using laser powers in the range of 1-5 mW showing no evidence of thermal damage to the cells. At powers exceeding 100 mW, a shrinkage in the size of the cell was observed. This was particularly evident in the case of *E.coli* bacteria. In 2003 Xie *et al.* studied and characterised *E.coli* bacteria by using a confocal microscope to simultaneously trap and excite fluorescence from a single cell. The laser power used in this study was approximately 20 mW and the wavelength was 785 nm [180]. However, the above-mentioned work uses microscope-based trapping techniques, and this is subject to the limitations previously mentioned in this thesis.

The ability of the MCF trap to isolate and manipulate individual bacteria was tested. *E.coli* bacteria from Prof. David Smith's lab at Heriot Watt University was cultured on an agar plate. After 24 to 48 hours at 37°C, visible colonies of *E.coli* appear. A small portion of a single colony is extracted from the plate and diluted in distilled water. This sample of *E. coli* bacteria in suspension is then pipetted into a sample chamber for trapping with the MCF.

Total optical powers in the range between 20 mW and 43 mW were observed to trap a group of *E.coli* bacteria, using the four-beam trap. After the trap was turned on, a dark 'cloud' gradually appeared to grow in the area where the beams overlap. The dark cloud was the accumulation of bacteria in the trapping region. The bacteria move into the trapping area due to Brownian motion, and powers of 20 – 43mW confined the cluster of cells in the trapping region. *E.coli* are rod-shaped bacteria of 0.25 -1 μm diameter and 2 μm length. This 'cluster' varied in diameter for different optical powers, but individual bacteria could not be distinguished or counted due to the imaging resolution (0.69) of the 0.40 NA objective used. The 'cloud' diameter and density, qualitatively measured by the scattered light in the images, was observed to increase with the increase of the total optical power, as shown in figure 6.13. The total time that the trap had been on was 1.5 min. Figure 6.14 indicates the relationship between the cluster size and the power.
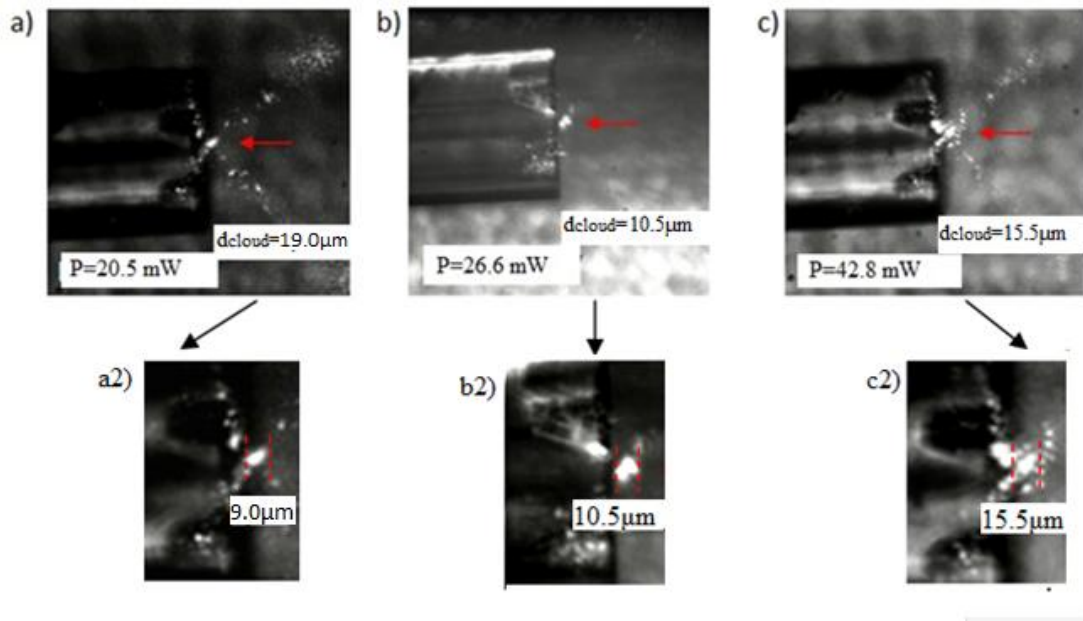
Figure 6. 13: *E.coli* 'cloud' formation for three different trapping powers a) P=20.53 mW, b) P= 26.67 mW and c) P=42.89 mW. a2), b2), c2) are the respective zoomed in images from a,b and c. Cloud diameter is seen to increase with respect to the total optical power.
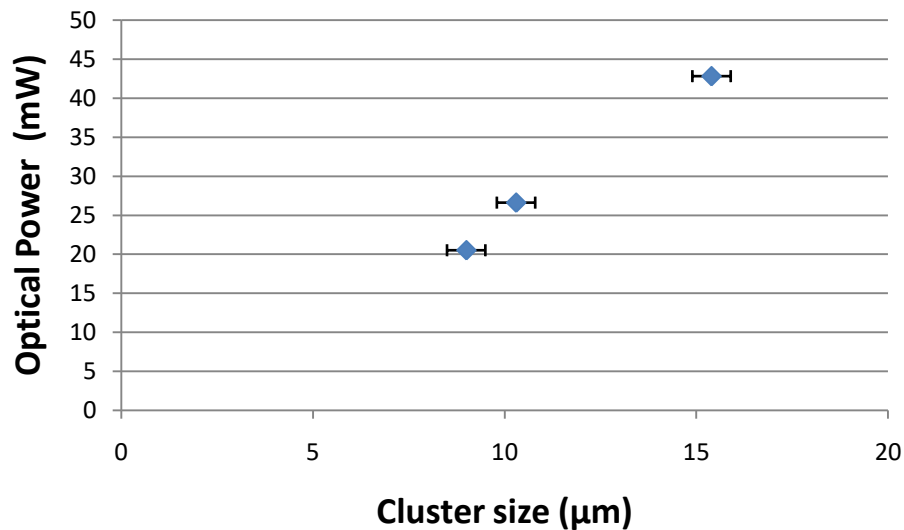
Figure 6. 14: Relation between optical trapping power and cluster size.

The overlapping region is much bigger than the size of the single bacteria so a single cell alone is unlikely to be confined and trapped in this volume unless the sample is extremely dilute, so single bacteria cell isolation was not demonstrated in this study. The number of trapped cells could not be quantified since the objective lens that was used for imaging was of a NA 0.40 which does not allow effective imaging of an individual bacterial cell on the micron scale. To improve this, a higher magnification objective lens would be required, which could not be realised in practice due to restrictions in the distance between the objective lens and sample surface. Trapping to confine a group of cells has some practical uses such as holding a group of cells within

152

a predetermined volume to monitor their signalling, growth or dynamics in response to a stimulus such as chemical or temperature are applications of interest to microbiologists [181] and for this reason trapping of a group or cluster of cells would be useful. Manipulation of the group is difficult and was not achieved, so other methods to translate the group or move it to a new location may have to be developed.

6.4.2 Trapping hollow glass spheres using a machined multicore fibre trap

Hollow air-filled microspheres, also known as microbubbles, are widely used in biological and medical research for imaging or therapeutic purposes [182]. However, optical trapping of such microbubbles is challenging, due to the lower refractive index of the particle because of the gas within comparison with the surrounding media. Trapping of low refractive index particles, such as hollow glass or polymer spheres filled with gas or gas filled liposomes, using conventional optical tweezers cannot be realized because the spheres are pushed away from the laser beam. When light hits the surface of a particle of lower refractive index than its surroundings, the particle scatters the light rather transmits it, as can be seen in the ray diagram in figure 6.15 a. Due to conservation of momentum, this results in a net force that repels the low index particle from the region of highest intensity towards the region of lower intensity, in contrast to an attractive force for a higher refractive index particle.
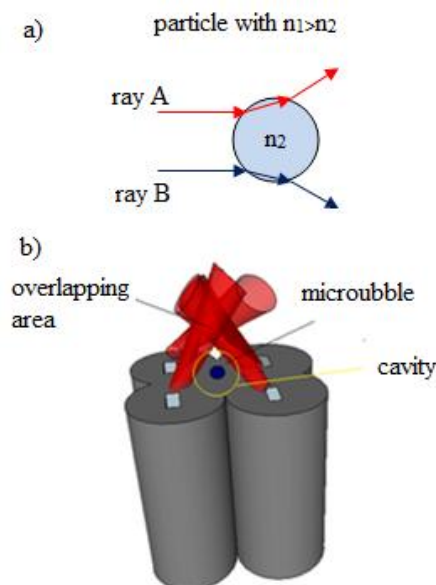
Figure 6. 15: a) Schematic showing interaction between ray a and ray b and a particle of lower refractive index (n_2) than its surroundings (n_1), b) Diagram of the optical trapping of a low-index microsphere (blue circle) using the four-beam trap. The particle, of lower refractive index than the surrounding media is trapped in the cavity formed between the overlapping area of the beams and the fibre end face (yellow circle).

153

Novel optical tweezer beam geometries and patterns have demonstrated optical trapping and manipulation of low refractive index microparticles. In 1998, Gahagan *et al.* used a strongly focused Gaussian laser beam containing a holographically produced optical vortex to optically trap low index particles (2-50 μm) in the dark centre of the beam [183]. In 2001, MacDonald *et al* presented optical trapping and manipulation of low index particles by trapping them in the dark fringes of an interference pattern [184]. In 1992, Sasaki *et al* trapped a water droplet (low index) in liquid paraffin (high refractive index), using a scanning laser technique [185]. The main concept was to use a focused laser beam of power 125mW, to scan a pattern circularly around the particle. The particle was trapped in the dark region, with the bright scanned circle surrounding it.

All of these studies demonstrated trapping and manipulation of low index particles [186-187] however they depend on a high NA objective lens.

We hypothesise that the MCF based trapping system can be used to trap low index particles, as shown in figure 6.15b. We aim to trap the low-index particle (blue circle, labelled 'microbubble'), not in the overlapping area as we have done for cells, but inside the cavity or 'cage' that is formed between the starting point of the overlapping area and the end of the fibre, as shown by the yellow circle labelled 'cavity' in figure 6.15b.

In this experiment, an aqueous medium containing hollow, glass beads with diameters ranging between 1 μm to 15 μm (Cospheric HGMS-0.67) were used. When the beams in two diagonal cores were turned on, the microsphere was repelled from the overlapping area of the two beams. By moving the fibre along the x-axis, parallel to the fibre axis, the microsphere keeps being repelled from the highest intensity region (the beam overlap area) into the cavity. Once the particle is between the fibre end face and the overlap area of the two beams, the third beam is turned on. This pushed the microsphere downward into the cavity, and finally the fourth beam below the microsphere is turned on, which repels the microsphere upwards into the cavity. With the four beams on, the microsphere is confined within this caged region. Figure 6.16 shows the motion of the microsphere as the four beams are turned on in sequence. The microsphere is stably translated afterwards in the x and y direction with a velocity of 0.01 mm/s and 0.02 mm/s respectively.

An important point to note is the initial position of the sphere before turning on the two first cores. The sphere needs to lie between the fibre end face and the area before the overlapping area, so that it can be guided towards the cavity.
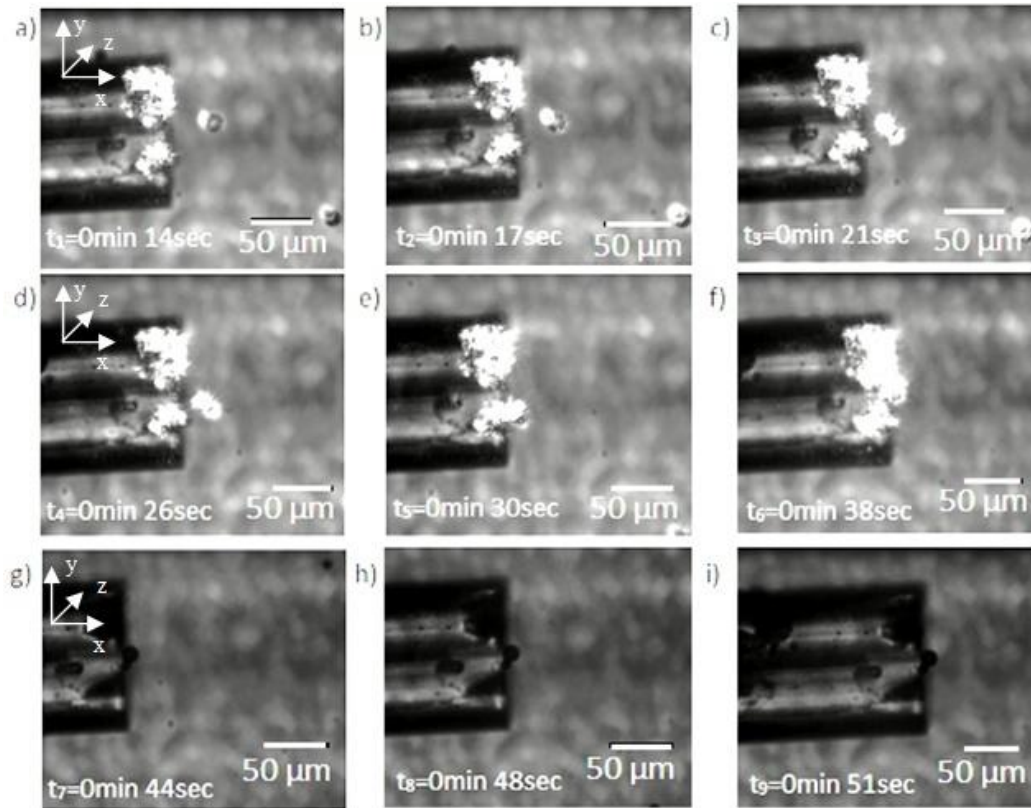
Figure 6. 16: Optical trapping of a single hollow glass (low refractive index) sphere of diameter 12μm inside the cavity formed between the overlap area of the four beams and the fibre-end. a)-d) The glass sphere is repelled by the two beams exiting the two diagonal cores and moves towards the fibre end face. e) and f) the third and fourth core are turned on to guide the low index sphere inside the cavity and capture it. g)-i) The stability of the trap is tested by moving the fibre along the x-axis. Scattered light is removed by the addition of a neutral density (ND) filter between the microscope objective and the CCD camera.

This method to capture and manipulation of low-index particles was repeated and observed a small number of times. Trap characterisation, to measure maximum trapping speed and trapping force, was not performed, so further experiments would be needed to quantify this method.

6.4.3 Cell growth observation

Many biological experiments require the test cell to remain healthy during and after the optical trapping, for example to allow for further examination or propagation. Furthermore, cell viability for a specific time under trap is an important parameter that can define the range of the potential optical experiments that an optical trapping system can demonstrate.

Cell division indicates that the cell remains healthy during the experiment. Saccharomyces cerevisiae is a budding yeast so it replicates by budding; a daughter cell buds from the mother cell during the cell cycle. Under optimal conditions (where nutrients are available and the temperature is 30-35º C), yeast cells can double their population every 100 minutes [188]. The normal budding event for a healthy yeast cell, from the creation of the daughter cell until its complete detachment from the mother cell, for a power of the level of the trapping power of the experiments of this thesis lies between 80-100 min for 1min 785 nm laser exposure, according to the literature [2].

A single yeast cell with a small bud was trapped using a two-beam trap of power 21.4 ± 0.1 mW and was held in place for 5 minutes to test if growth of the bud, or any morphological damage could be observed. Room temperature was controlled to be in 30°C. There were no nutrients in the water, but yeast cells were expected to have a store of energy that could support growth and division.

The observation is shown in Figure 6.17. There appears to be no visible damage to the mother or daughter cell after some time in trap, and budding appears normal and this experiment would be repeated for multiple cells and for more demonstrations if we would like to derive accurate conclusions. For these reasons, this section is presented as an initial aim of testing the viability of the yeast cells and not to conclude into accurate assumptions.
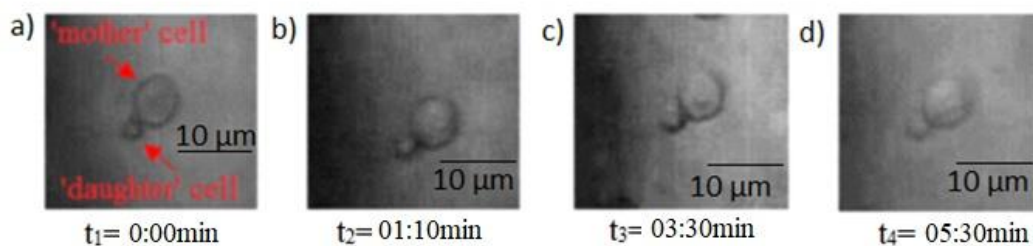
Figure 6. 17: Images of a trapped yeast cell during the cell division process. The images have been captured consecutively and the time between each image is shown.

The diameters of the mother and daughter cells were measured by converting pixels to micrometres (obtained using a micrometre calibration slide). Due to evaporation and flow in the sample, the growth could only be monitored for 5 minutes and 30 seconds.
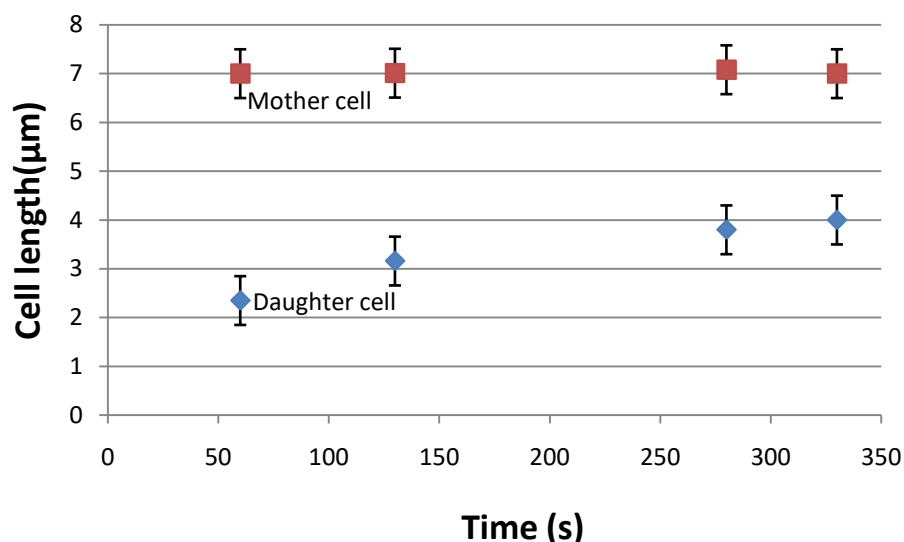
Figure 6. 18; Mother cell size (red square) and daughter cell size (blue diamond) with respect to the time elapsed in optical trap. Mother cell is approximately of the same size, while the daughter cell shows increase in size with respect to time.

As can be seen in figure 6.18, the mother cell shows small differences (lying within the uncertainty ± 0.5 μm due to pixel size) in measurements of the length for the four different measurements, which may be due to the change of focus that occurred due to evaporation or flow. Furthermore, the daughter cell appears to increase in length over time, with an increase in diameter from 2 μm to 4 μm in 5 min and 30 seconds, however, this could be a result of the change of focus during the time frames rather than a real change in size.

Ideally, yeast cell viability experiments would monitor the trapped cell until the daughter cell is totally detached from the mother cell and this experiment would be repeated multiple times for different cells. However, in the trapping experiments here, difficulties arose due to evaporation of the medium during the time scale of the experiments, and this prevented the observation of complete cell division. One solution attempted to overcome the rapid evaporation of the medium was to use an external syringe pump to replace water in the microchannel. However, adding water to the system resulted to a flow that was sufficient to overcome the trap strength, and the trapped cell was lost. In future, to fully test trapped cell viability, a sealed sample chamber that prevents evaporation would be used.

Since budding cannot be observed because evaporation in the sample chamber occurs well before the budding is complete, an alternative way to analyse the cell growth and examine if the laser power used for the trapping experiments is damaging for the cell or

157

not, would be to calculate the total energy deposited on the cell and compare it to the existing literature. For our case, the energy deposited on the cell is calculated to be 7.060 ± 0.001J for the 5 min 30 s exposure at 21.4 ± 0.1 mW. In other studies in the literature, for experiments implemented to test cell viability in yeast cells trapped with conventional of 1064 nm laser source for 15 min at 19 mW of power is found to cause no delay in reproduction or increased mortality, although it reduces the mean cell size. [189-190].

6.5 MCF trap applied to Microscope based diagnostics

6.5.1 Fluorescence microscopy

As discussed in Chapter 2, some of the most important and widely used techniques in life sciences are microscopy and spectroscopy. Microscopy is a technique that aims to view and image entire objects, or specific areas of these objects on the microscale that is otherwise impossible to view with naked eye. Many types of microscopes have been developed for different applications. The need for high resolution microscopes that can selectively image a biological specimen, or part of the specimen, with high contrast, led to the development of fluorescent probes such as fluorescent proteins (GFP-Green Fluorescent Protein being one such protein) and fluorescence microscopes.

The principle of fluorescence microscopy is based on the use of a fluorescent or phosphorescent marker to highlight specific aspects of the sample under test. Fluorophores are chemical compounds used to label specific structures. When a fluorophore (for example green fluorescent protein) absorbs light of a specific wavelength, it has the capability to emit this amount of energy at a longer wavelength. An optical emission filter is commonly used to attenuate the scattered illumination light from the emitted fluorescent signal.

Labelling a cell type selectively with fluorescent molecules and illuminating the sample with the appropriate excitation wavelength for the fluorophore allows these cells to be clearly identified via fluorescence when they are surrounded by other cell types that are unlabelled, or labelled with a different fluorophore.

The main techniques used to label cells (or more specifically cellular structures) are labelling with fluorescent dyes that are taken up by the cell and directly bind to the

structure of interest; immunofluorescence, where antibodies against the structure of interest, that have an attached fluorophore, are added to fixed cell samples; and protein tagging, which makes use of genetic engineering to modify cells so they make their own fluorescing molecules, for example GFP. These approaches offer the opportunity to tag specific molecules and thus to discriminate different cell types that may otherwise seem morphologically similar under the light microscope.

Here, trapped cells from the human glioblastoma cell line (U87 cells) and murine embryonic stem (ES) cells are labelled with Green Fluorescent Protein (GFP). This is a fluorescent protein that was first isolated from the jellyfish *Aequora Victoria.* The U87 cells were transfected and cultured by Yasmine Tawil IB3 Heriot Watt University (Nick Leslie's research group) in the Institute of Biological Chemistry, Biophysics and Bioengineering at Heriot Watt University. The ES green cells were from the lab of Prof Ian Chambers at University of Edinburgh and prepared by Dr Douglas Colby. The fluorescent protein has an excitation peak at 480 nm and emission peak at 507 nm [191-192].

To check that cell labelling was successful, the U87s and the ESs were imaged with a Nikon Eclipse E600 fluorescence microscope, using a ×10 objective. The FITC filter was used to image the green fluorescent cells. Green fluorescent cells of diameters in range of 10-20 μm are observed in the field of view.

However, the need to hold and examine single cells under a specialised microscope, for example to enable cell identification via fluorescence before a Raman signal is collected, would restrict the flexibility of the overall trapping system and the potential applications. The integration of the fluorescent microscopy in the machined MCF based tweezing system could address this demand.

To attempt simultaneous optical trapping of a single cell and fluorescence illumination of the trapped cell, the three machined cores of the MCF out of the four have been exploited. The two diagonal cores were used to deliver light of 976 nm wavelength to optically trap a single cell, while one of the other two machined cores was used to deliver 480 nm wavelength laser light to excite the GFP label in the trapped cell. As all three beams are directed towards an overlapping area, once the cell is trapped by the two diagonal cores, the third core is expected to direct the excitation light towards the cell and so it will excite only this particular trapped cell. The microscope used here is similar to that described in Chapter 5 section 5.1.3 with the addition of an emission

filter centred at 512 nm with bandwidth of 23 nm is placed between the objective lens and the CCD camera to give high contrast fluorescent image by transmitting only the wavelength of the fluorescent light (Fig. 6.19).
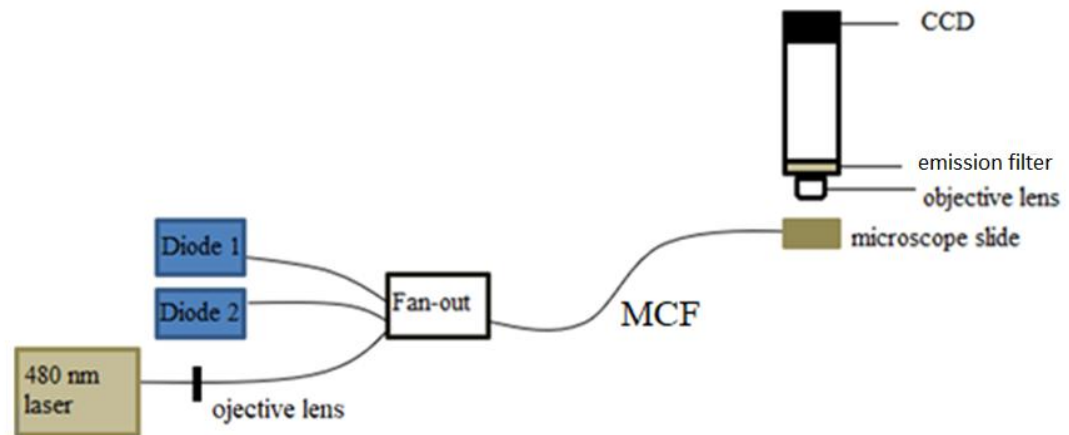
Figure 6. 19: Experimental set-up used for U87 cell trapping and fluorescence demonstration. It includes the machined MCF that connects with the two 976 nm laser diodes that are responsible for the optical trapping and a 480 nm laser (Argon ion) that is responsible for the excitation of the GFP labelled U87 cells. An emission filter is placed between the objective lens and the CCD camera, allowing only the fluorescent light to be captured from the camera.

Before trapping, fluorescence excitation was first tested by exciting fluorescein dissolved in water (Sigma Aldrich, 46960) that has an absorption peak at 480 nm and an emission peak at 507 nm, as well as water containing fluorescent beads of 5 μm in diameter (Bangs Laboratories, Inc., discontinued but similar to FCDG008), using a single core fibre that was perpendicularly cleaved. Figure 6.20 a and b show the image resulting from fluorescein sample and microbeads sample, respectively, illuminated by 2mW of 480 nm light. The position of the single core SM800 fibre is indicated by a yellow rectangle and its core by the dashed yellow line. Due to the emission filter in place before the camera, the light detected is the fluorescent emission from the samples.
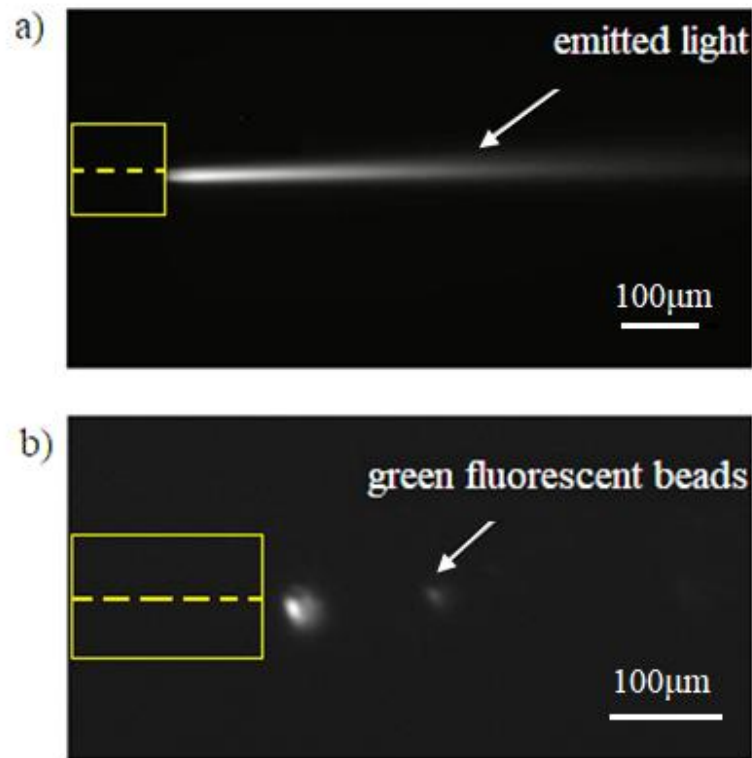
Figure 6. 20: a) Emitted fluorescent light from fluorescein due to propagation of 480 nm wavelength light from a single core SM800 fibre. b) Fluorescence emission from two green fluorescent 5 µm diameter beads, due to excitation by the 480 nm light emitted from the SM800 fibre.

After successful testing of green fluorescent samples using the single core fibre, and verifying the presence of a fluorescent signal, experiments based on the machined MCF for trapping and excitation beam delivery could follow.

U87 and ES green cells which have been genetically modified to express GFP have been used in optical experiments based on the machined MCF tweezing system that aim to demonstrate simultaneous stable optical trapping and selective fluorescence of the trapped cell using the fibre trap.

The optical trapping of these cells using one pair of machined diagonal cores has been investigated and is described in detail in sections 6.1.3 and 6.1.4. Figure 6.21 (a) shows the trapping of a U87 cell under brightfield in the setup shown in figure 6.19, figure 6.21 b shows the single cell with the white light illumination turned off and the emission filter in place, when illuminated with 2 mW of 480 nm laser light from the third core of the MCF. Figure 6.21 c shows the U87 GFP tagged cells imaged using a Nikon Eclipse E600 fluorescence microscope with FITC filter.
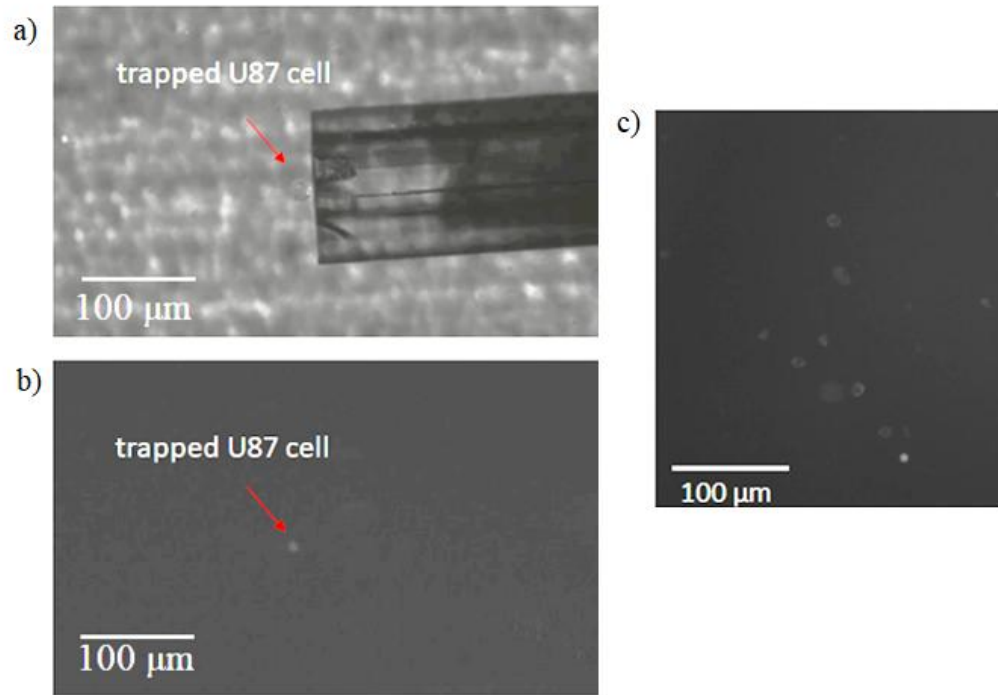
Figure 6. 21: a) Bright field image of a trapped U87 GFP cell of 18μm diameter, using the two diagonal machined cores transmitting 976 nm wavelength laser beam, a distance of 12.0 ± 0.5μm away from the fibre end, b) Fluorescence image of a trapped U87 GFP cell when illuminated by 480nm laser light from the third machined core, c) U87 cells imaged using a Nikon fluorescent microscope, with a × 10objective, having only the emitted fluorescent light captured.

The weak fluorescence signal produced from these cells corresponds to either a poor ability of the CCD to capture the emitted light but is most likely due to a small concentration of the GFP in the cell that leads to low intensity fluorescence. The image of fluorescent U87 cells in figure 6.21c taken using a fluorescent microscope, and in figure 6.21 b show similar levels of fluorescence. The irradiance of the Ar-ion for the respective power used for the excitation of the trapped cells in figure 6.21b (0.8 mW) is $I = 0.04 \times 10^5 W cm^{-2}$, the irradiance for the mercury lamp in figure 6.21c $I = 0.01 \times 10^5$ units. The emission filter in both cases were Nikon FITC filter 535/45 nm (Center wavelength 535 nm and bandwith 45 nm) used in figure 6.21c and 512/23 nm for figure 6.21b, which explains the similar intensity of the captured fluorescence.

To sum up, work in this thesis has demonstrated optical trapping and delivery of a fluorescent excitation beam onto the trapped cell. A weak fluorescent signal has been observed similar to the level of fluorescence seen with a commercial fluorescence source (a mercury lamp on a Nikon microscope). Further studies will be required to demonstrate that this technique can be used to identify fluorescently labelled cells, including experiments where unlabelled cells that generate no fluorescence signal are

trapped and illuminated with 488 nm, to confirm that the signal observed is the GFP reporter and not simply autofluorescence. As a future application, once a fluorescently labelled cell has been identified, a further experiment, for example Raman micro-spectroscopy, or translation of the cell for sorting, or isolation from other unlabelled cells, may be conducted using the MCF trap to hold or manipulate the cell.

In the next section, the combination of the MCF optical trapping with a commercial Raman microscope to generate a Raman spectrum of the trapped cells is described. Trapping a single cell under the Raman microscope allows one to acquire a Raman spectrum from the cell. The Raman spectrum has been used in the literature to characterise and analyse the chemical structure of a cell [193]. Raman microscopy has also been used to compare and discriminate two or more different types of cells that seem similar under a conventional microscope, as reported in the literature [193].

6.6 Raman spectroscopy

Spectroscopy is a characterisation technique based on the interaction of the sample-material with electromagnetic radiation. Spectroscopy, generally, can be based on emission, fluorescence, scattering, or absorption. Techniques like these are commonly used for both qualitative and quantitative analysis, to identify the chemical composition and the concentration of substances in the sample.

Raman spectroscopy is a technique that uses a monochromatic beam to illuminate the sample. As the laser light interacts with the material, it scatters. Inelastically scattered light, has a different frequency than that of the incident light and this is the so-called Raman scattering. When the incident beam frequency is higher than that of the scattered beam frequency, then Stokes lines appear in Raman spectrum and, when the incident beam frequency is lower than the scattered beam, anti-Stokes lines appear. Raman spectroscopy is a technique that provides information on vibrational and rotational modes of molecules and thus provides a structural 'fingerprint' where molecules can be identified in a sample. For this reason, the use of spectroscopic techniques in biology could provide information about the identity of the biological sample such as a tissue or cell.

The main drawback of Raman spectroscopy is the poor sensitivity due to the weakness of the Raman scattering signal. A famous technique that aims to overcome these limitations is called SERS (Surface Enhanced Raman Spectroscopy) and was

163

demonstrated by Fleishman *et al.*, in 1974 [194]. SERS uses a colloidal metallic surface onto which the sample is placed and when the metal absorbs the light, the plasmons on the surface are excited, and the electric field surrounding the metal is increased. Although this technique enhances the Raman signal, it is not appropriate for single cell characterisation because the metallic surface is not always compatible with biological samples and can damage their viability due to toxicity [195].

In the case of single cell Raman spectroscopy, several studies have been presented [5,196-197,68,198]. The major issues limiting single cell experiments under a Raman microscope is the uncontrolled movement of a cell in suspension due to Brownian motion. Furthermore, the background signal of the sample substrate can dominate the measured spectrum of both adherent cells and cells in suspension. For this reason, it is desired to hold the cell under test in a stable position at some distance away from the substrate. Optical tweezers, or trapping, have an important role to play in enabling this.

To date, the majority of the published studies that investigated the combination of optical trapping and Raman microscopy were based on systems that included a Raman microscope to both trap a cell and capture the Raman spectrum using the same laser beam [5]. Such a set up was used to demonstrate optical trapping and Raman spectroscopy of highly refractive and non-transparent particles in a liquid using an inverted confocal laser-tweezers-Raman-spectroscopy (LTRS) system. Here a 785 nm diode laser was used to optically trap particles and capture the Raman spectra of a number of particles including silicon, germanium, and $KNbO_3$ microcrystals that present a high refractive index and metal particles that show high reflection [5]. An inverted confocal Raman microscope has been developed to study chemical reactions of trapped particles [199]. By trapping the cells and lifting them away from the substrate, the fluorescence from the coverslip was avoided, thereby reducing the background signal [197]. However, this concept restricts the ability to further manipulate the cell and change its position relative to the microscope. To address this, a trap formed from two opposed fibres has been demonstrated to be able to hold and manipulate the cell in 3D below the Raman microscope, but limitations arise from the restricted space to set up the trapping system [68]. A more complex system that combined two ways of optical trapping with Raman micro-spectroscopy, was studied in 2011 by Dochow *et al.* [198]. The proposed system used two optical traps, both within a microfluidic environment, one based on a Quartz capillary and one based on a microfluidic glass chip. Single cells,

picked from reservoirs by optical trapping were sorted according to the Raman-based classification. This study demonstrated a more advanced process, however it needs special equipment and more complex and demanding experimental set-up.

The machined MCF optical tweezing system offers an alternative method to optically trap and stably hold a cell away from a substrate in a Raman trapping experiment. It additionally offers the ability to manipulate the trapped cell in 3D with respect to the microscope and the Raman excitation beam, using only a single fibre, thus avoiding the strict alignment needed by a dual beam trap.

In the work presented here, a micro Raman spectrometer (Renishaw InVia) with a 785 nm (near IR) excitation source, has been used. The 785 nm beam focused to a diffraction limited spot using a 10× NA 0.25 or a 20× NA 0.40 objective lens, is 3.83 μm or 2.39 μm, respectively, calculated using Eq. 6.1.

$$Spot\ diameter = 1.22 \times \frac{\lambda}{NA} \qquad (6.1)$$

Raman excitation power used in this work to acquire spectra, using a 20× objective lens was 92 mW. The power calibration of the Raman laser can be found in Appendix 6.1. A spectrum of Si that shows a characteristic peak at 520 cm^{-1} [200] is collected and used as a reference to calibrate the Raman system, before each experiment.

The main set-up is described in figure 6.22:
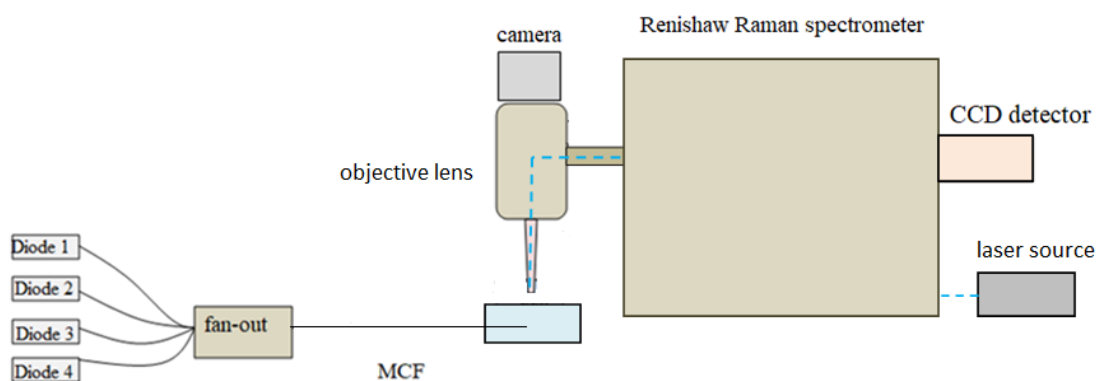
Figure 6. 22; Experimental setup for collecting the Raman spectrum from a single cell, trapped using the MCF. The Raman laser light of 785 nm wavelength is directed through the Renishaw inVia spectrometer and focused through an objective lens into the sample. The fibre and stage are manipulated in x, y and z until the trapped cell is in the correct position then the Raman spectrum is collected.

As can be seen from figure 6.22, the experimental set-up used to collect the Raman signals from trapped cells includes the machined MCF that traps the single cell so that

the cell can be lifted and held away from the bottom of the microscope slide, and the Raman spectrometer, including the Raman excitation laser source, the objective lens and camera and the CCD detector.

6.6.1 Single cell Raman spectroscopy of untrapped and trapped cells

To acquire a Raman signal from a single cell it is important to eliminate the background noise of the substrate to the cell signal. To determine the spectrum of a typical substrate, borosilicate glass microscope slides, the Raman beam was focused on the microscope slide with no cells on it. The results showing the acquired spectra from borosilicate glass are depicted in figure 6.23 as red lines, with 6.23a showing the spectrum from 200 – 800 cm^{-1} and figure 6.23b showing the spectrum from 900-1500 cm^{-1}. Two different key frequency areas have been captured to enhance the resolution.

The acquisition time of these spectra was 3s, with a spatial resolution of 1.10 μm using a × 10 microscope objective lens. To investigate if the signal from cells on a borosilicate glass substrate is strong enough to provide information for the cell, the Raman beam was focused on a freely suspended yeast cell settled on the same borosilicate glass microscope slide. These spectra are respectively depicted as black lines in the same figure 6.23. As can be seen in figure 6.23, the spectra for both slide and cell are very similar. This shows that the background signal due to the borosilicate substrate dominates and no information related to the cell structure can be acquired.
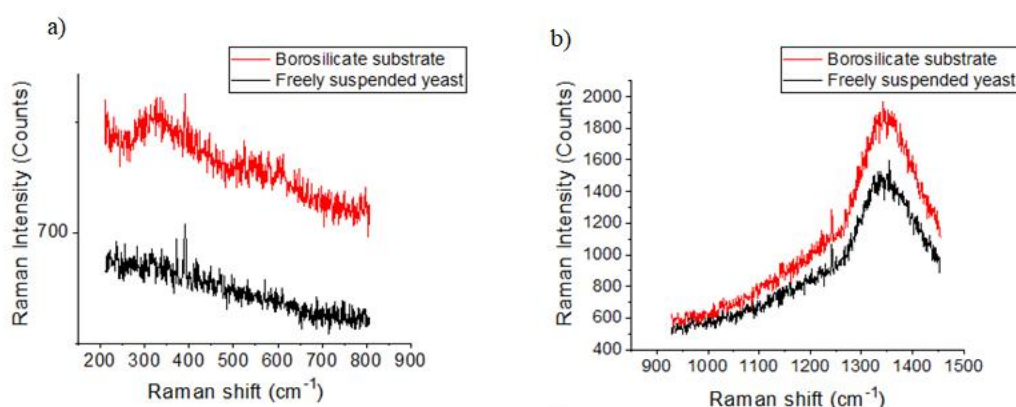
Figure 6. 23: Raman signals from a single yeast cell in water on a borosilicate glass slide (black spectrum), and from the surface of a Borosilicate glass slide without any cell sample (red spectrum). The Raman signal of the borosilicate control and the yeast cell on borosilicate for two different frequency regions centred at a) 520 cm^{-1}, b) 1200 cm^{-1}. The signal from the borosilicate glass substrate is dominant and no Raman spectra from the cells can be detected.

In a similar way, another substrate was investigated to examine if the background signal could be eliminated. Figure 6.24 presents Raman spectra for a Quartz glass microscope

slide (red lines) and for a yeast cell that is freely suspended in water on the same Quartz slide. As can be seen from this figure, the spectra are almost identical that again shows that the Quartz background signal still obscures any potential Raman signal from the cells.
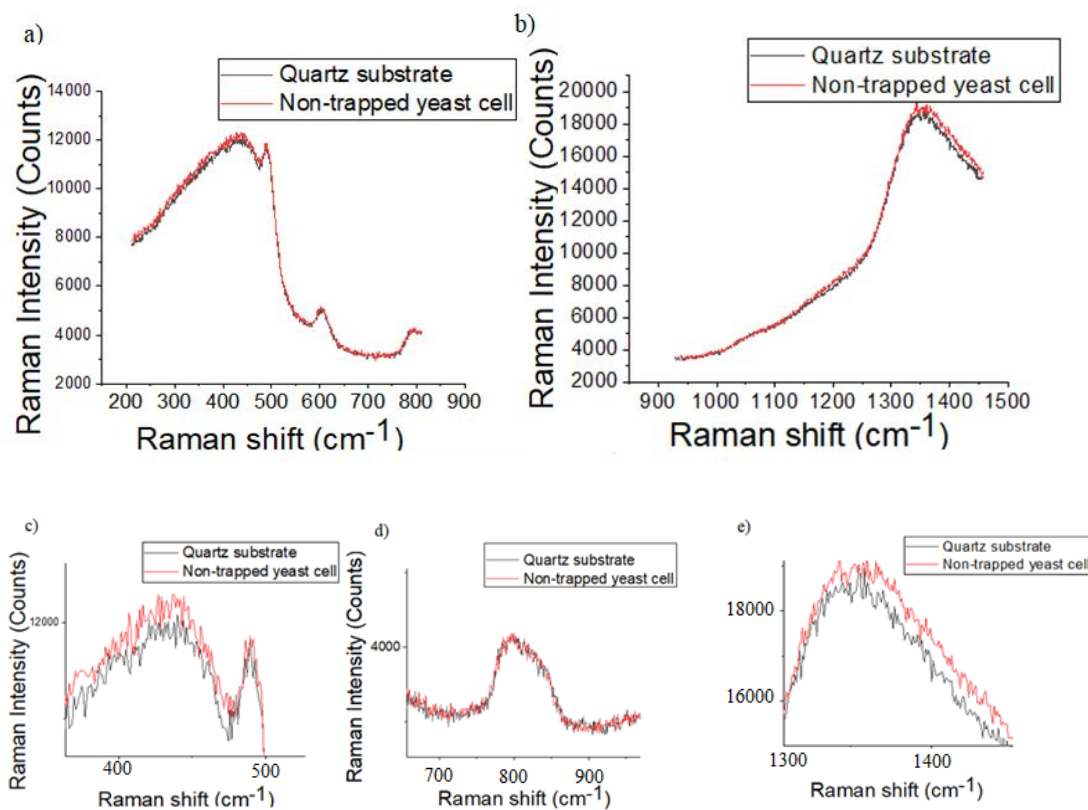
Figure 6. 24: Raman signals from a single yeast cell in water on a Quartz slide (red spectrum), and from the surface of a Quartz slide without any sample (black spectrum). The Quartz background Raman signal is dominant over the cell peaks for all the frequency regions.

To investigate if there are any peaks that identify the yeast cells that are potentially hidden in the spectra due to the high intensity counts of the background, the two spectra were zoomed in to the regions that some of the characteristic peaks of the yeast cells are located [5]. As these zoomed in images (Fig. 6.24 c-e) indicate, no characteristic peaks can be highlighted in the yeast cell spectra and not found in Quartz spectra.

To increase the information that can be acquired from the cell, a Raman spectrum was acquired from a yeast cell held using the MCF trap, a minimum of 75 μm away from the borosilicate substrate, at four different frequency regions. Furthermore, in the same plots, spectra of the same cell for different trapping powers are also presented for signal strength comparison (figure 6.25).
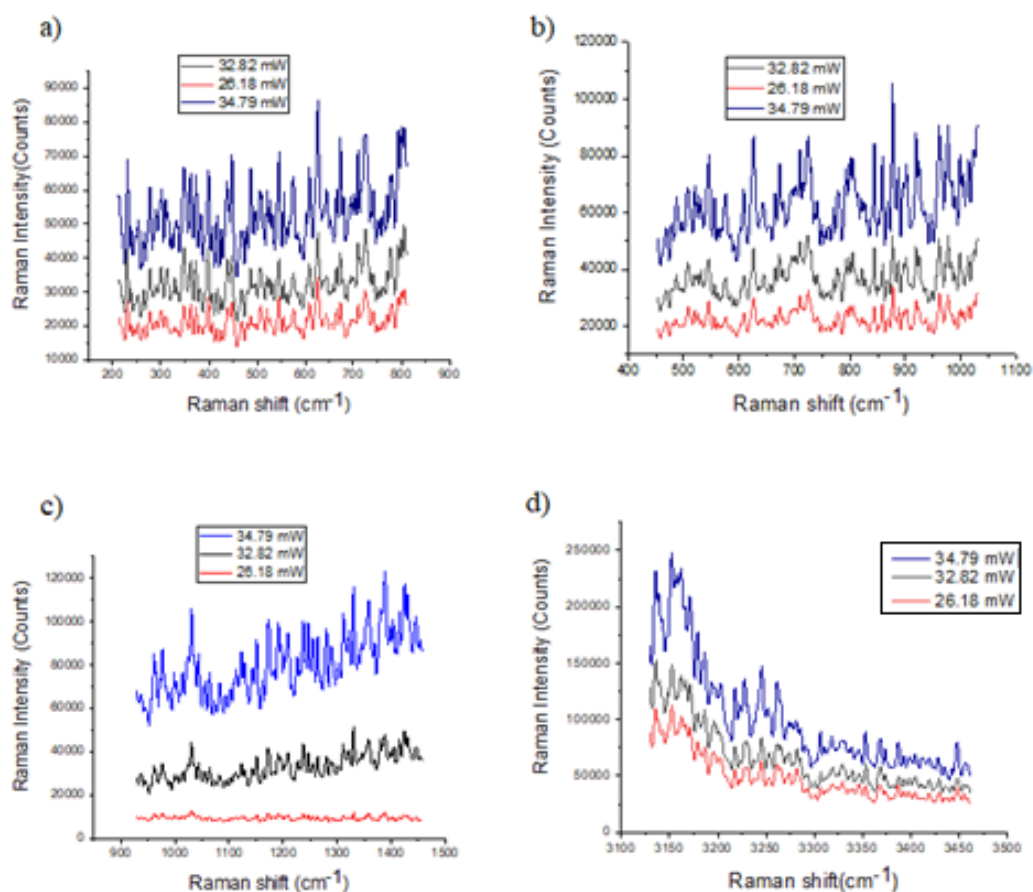
Figure 6. 25: Raman signal of a single, optically trapped live yeast cell in water, for three different total trapping powers, for the frequency regions a) 520 cm^{-1}, b) 750 cm^{-1}, c) 1200 cm^{-1}, d) 3300 cm^{-1}. Higher optical trapping powers of the four beam fibre trap lead to Raman spectra of higher intensity.

The Raman signal for the trapped cell in figure 6.25 that is away from the substrate does not contain the background fluorescence signal from the substrate at 200-1500 cm^{-1}. There is no broad peak of quartz at 400 cm^{-1} seen in figure 6.26 or of borosilicate and quartz at 1350 cm^{-1} seen in figure 6.25 (b) and 6.26 (b) respectively. The signal itself is stronger. For the trapped cell the counts are 20,000 for 200-1500 cm^{-1}. For the cell on glass the counts are 700-1000. For quartz are around 12,000. Assuming the same Raman excitation power, this is most likely caused by the additional laser light from the MCF trap. The main Raman peaks identified from examining figure 6.25 are presented in Table 6.3 below. The attribution of specific molecules or vibrational modes to the peaks within the trapped yeast cell spectrum have been made according to the literature [201-202, 54].

Raman peak (cm^{-1})	Vibrational assignment
777.05	Phosphotidylenatholomene
804.86	Phosphodiester
805.4	Phosphodiester
820.69	Tyrosine
960.64	Carotenoids
977.98	Proteins
1082.71	B1, 3 Glucans
1123.06	Mannans, B1, 6 Glucans, C-O stretching, N-H and O=C-N bending
1358.5	Phospholipids
1424.94	Phospholipids
3161-3448.29	OH stretching, N-H stretching and Amide II

Table 6. 3: Major Raman peak assignments for the yeast cells [201-202,54].

To sum up, acquiring Raman spectra from a trapped cell instead of cells attached to, or place on a substrate, allows enhancement of the resulting Raman signal as the cell is away from the substrate that gives high and dominant signal, as seen in figures 6.2. In addition, the trapping laser appears to contribute to the cell Raman signal enhancement by acting as an additional Raman excitation source, as seen in figure 6.25 when the Raman signal increases with increasing trapping power.

6.6.2 Single cell Raman spectroscopy of three closely related cell types; ES cells, ES green cells and Epi cells.

As explained, the Raman signal from single cells provides important information concerning the chemical structure within the cells. This information, derived from the respective spectra, can allow discrimination and categorisation between different cell types that otherwise appear similar in morphology if imaged by a conventional microscope.

The three cell types have been prepared by Douglas Colby from University of Edinburgh. Mouse ES [206-207] cells are made as describe in section 6.2.2. The self-

renewal efficiency of mouse ES cells is determined by the concentration of the transcription factor NANOG. ES green cells are ES cells that have been genetically engineered so NANOG is tagged with GFP [207]. NANOG, and hence GFP, is expressed only when cells are 'stem like'. When the ES cell differentiates, either spontaneously or deliberately, the ES green cells will no longer fluoresce green as the concentration of NANOG reduces and the cell become less 'stem-like' and more committed to a lineage. Epi cells are the mouse epiblast stem cells, which comprise a mixed population of progenitor cells committed to their lineages. Epi cells are no longer as 'stem-like' as ES cells, and no longer have the self renewing property of ES cells, however, the morphology of Epi cells is similar to the morphology of ES cells. Many scientists use protein tagging to identify cell types according to gene expression. In this case, GFP is used to identify stem cells by tagging NANOG with GFP, but tagging cells is a complex process that can disrupt the cell's normal function. An ideal method to distinguish cells without depending on fluorescent tagging is Raman microspectroscopy combined with PCA. If the spectra from ES cells and Epi cells form discrete clusters in a PCA plot, then this could be used to distinguish unknown cells in a sample of mixed ES and Epi cells. The benefits of this would be less dependence on costly, time-consuming fluorescent labelling of cells. In this section, it is investigated whether an ES cell can be distinguished from an ES green cell and an Epi cell using Raman spectroscopy simultaneously with MCF trapping.

Figure 6. 26 shows Raman spectra for the three cell types, representative of a single cell at a time. In the four different frequency regions (520 cm^{-1}, 750 cm^{1}, 1200 cm^{-1} and 3300 cm^{-1}), the differences between the Epi and the ES can be noticed, which are mainly differences in proteins and lipids. Table 6.4 and 6.5 present the vibration assignments, according to the literature, of the main characteristic Raman peaks seen in the spectra in figure 6.26 according to the literature [208-209].
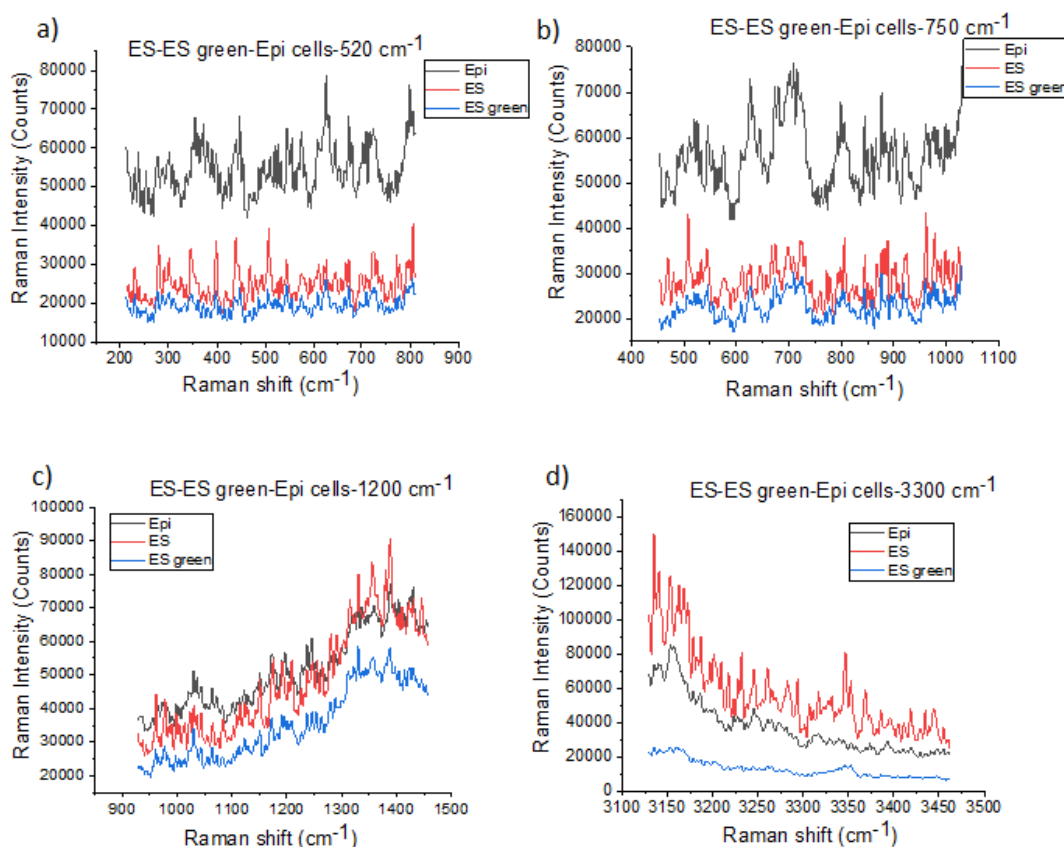
Figure 6. 26: Epi, ES and ES green cells Raman spectra, for four different frequency regions centred at a) 520 cm^{-1}, b) 750 cm^{-1}, c) 1200 cm^{-1}, d) 3300 cm^{-1}.The total trapping power of the MCF was 32.63 mW and the Raman laser power was 92 mW for 20× objective lens. Acquisition time for these experiments was 6 s.

Peak position (cm^{-1})	Major assignments
622.22	C-C twist of phenylalanine (proteins)
645.72	C-C twist Tyrosine (Proteins)
668.11	Thymine, Guanine (DNA)
708.57	Lipids
724.68	Adenine (DNA)
760.74	Tryptophane-proteins
772.71	U, C, T (DNA)
793.59	O-P-O stretch of DNA
820.69	Asym stretch of DNA
977.39	Proteins, lipids
1004.18	Sym rig Phenylalanine-proteins
1030.62	C-H in plane Phenylalanine-proteins

Peak position (cm⁻¹)	Major assignments
1102.45 1105.27	Stretching DNA
1125.86	C-N stretch of proteins
1148.22	C-C/C-N stretch of proteins
1205.53	Phenylalanine, Tryptophane -proteins
1279.43 1291.19	CH2 twist-lipids
1349.58	A, G (DNA)
1445.13	A, G, CH def (DNA)- CH def proteins- CH def lipids- CH def carbohydrates

Table 6. 4: Major assignments of Raman peaks for ES cells. The most characteristic peaks belong to proteins, DNA and lipids [208].

Peak position (cm⁻¹)	Major assignments
496.89	Glycogen
626.31	C-C twisting mode of Phenyalanine
645.72	C-C twisting mode of tyrosine
672.16	C-S stretching mode of cystine
715.62	C-N/Nucleotide peak
805.85	O-P-O stretch DNA
998.14	Symmetric ring of phenylalanine
1071.39	C-N stretching mode of proteins
1102.45	C-C stretching mode of lipids
1162.15	C-C stretching of proteins and carotenoids
1178.81	C-H in plane-Tyrosine
1197.26	Tryptophane and Phenylalanine
1226.63 1236.68 1244.9	Amide III

1270.36	
1323.61	Lipids
1403.77	Collagen/DNA
1454.76	Proteins, lipids

Table 6. 4: Major assignments of Raman peaks for Epi cells. The most characteristic peaks belong to proteins, DNA, carotenoids and lipids [209].

The highlighted peaks in figure 6.26 have been identified by eye after comparing the two spectra. A more accurate classification technique that can be applied to Raman spectra to present differences between different groups of spectra is Principal Component Analysis (PCA) [204-205]. This technique is a non-parametric technique that can process large amounts of raw data by compressing them into a smaller number of Principal Components (PCs), making the complex and numerous spectra easier to explore and visualise. These PCs contain most of the variance between two groups of spectra. PCA demonstrates the original Raman spectra by generating PCs through orthogonal transformation towards the direction of largest variation. This method allows us to display the cells in groups, reducing data by geometrically projecting them onto lower dimensions called principal components (PCs) in two dimensions (x axis is PC1 and y axis is PC2), showing that way if the existing differences between these two groups are enough discrete [205].

However, in our case, the comparison using PCA analysis does not provide accurate conclusions as the acquired spectra to be compared were not enough in number.

Habuchi *et al.* in 2003, aimed to obtain Raman spectra from single GFP molecules using SM-SERS (Single Molecule-Surface Enhanced Raman Spectroscopy) technique [210]. To demonstrate this, the individual molecules were absorbed on metallic nanoparticles to enhance the Raman signal. As denoted from these studies, characteristic Raman peaks of GFP are expected at frequencies: 1094, 1196, 1202, 1413, 1244, 1329, 1357 cm^{-1}. Concerning the Raman spectra of the cells that include GFP protein in the experiments of this thesis (the ES green cells), these peaks are of higher intensity in the spectra of green ES cells rather than in ES cells, which can be a first remark that the Raman technique can distinguish differences based on the existence or not of the GFP protein in the examined cell, and in that way the respective types of cells can be classified and characterized accordingly, however, of course this can also be done more easily by fluorescence. More interesting would be if differences in ES and

Epi cells can be detected by Raman and if PCA could be used to distinguish the cell type. This would mean that non-contact, non-damaging Raman could be used, instead of transfection and protein tagging, to distinguish cells that the literature has shown that it can work [209-211].

6.7 Discussion

This chapter presents the demonstration of optical trapping of murine embryonic stem (ES) cells, human glioblastoma (U87) cells and human erythrocytes (RBCs) with a two-beam trap using two of the four machined cores of the MCF trapping system, and trapping of ES cells and RBCs using four machined cores, proving stable trapping in three dimensions using both two and four beams. Keeping the trapping system constant, including the total trap power, and changing the cell type has enabled a comparison to be made between the trapping distance and the size of the cell. Bigger cells such as spherical mammalian cells, ES and U87 cells appear to be trapped slightly closer to the fibre end face than the smaller cells, such as yeast and RBCs. One explanation for the different trapping distances is the difference in the refractive index of the cells that leads to difference in the resulting refraction of the beam to the cell surface.

Trapping of particles much smaller than the overlap region (i.e. *E.coli* bacteria) was observed. Individual *E.coli* cells could not be imaged due to the resolution of the imaging microscope, but a cluster of trapped bacteria were trapped and imaged. The cells moved into the trap due to their Brownian motion were very weakly trapped in a 'cloud' in the beam overlap region. Neither the cluster, nor individual cells, could be manipulated through the sample in the same way that yeast cells were due to the weakness of the trap.

Trapping of low-refractive index particles (hollow glass spheres) has been tested using the four-beam trap. The trapping of hollow glass spheres cannot be implemented with a conventional optical tweezing system, due to the lower refractive index of the particle compared to the surrounding water; the particle is pushed away from the high intensity regions of light. To date tweezing arrangements to trap particles of low refractive index involved beam shaping by interference, using vortex beams or scanning beams. This thesis presents initial results in controllably manipulating such particles using the MCF trap.

This chapter also explores and presents potential biological applications of the MCF-based tweezing system and incorporates the MCF trap into different microscope systems. A cell was trapped using the two beam trap and fluorescence excitation light was launched into the third core of the MCF. The machined third core directed the 480 nm excitation light onto the trapped cell, with the aim to selectively illuminate the trapped cell. A fluorescent signal was observed, however further studies are necessary to develop this further and confirm that GFP has been imaged. The technique may allow experiments to excite fluorescence of a single trapped cell. With further development it may be possible to make use of the 4th core for light collection and potentially could lead to imageless trapping and fluorescence detection, without the need for a microscope.

In another study, the use of the four beam trap to optically trap single cells under a Raman microscope is reported

When collecting the Raman signal from a single cell using Raman micro spectrometry, the background signal of the borosilicate microscope slide glass, even of the Quartz glass, was very high so that no information concerning the Raman spectrum of the cell itself could be obtained. Trapping the cell and thus lifting it up from the substrate and then collecting the spectrum, helps to eliminate the substrate background signal and the cell spectrum can be obtained. Spectra of live yeast cells, mouse embryonic stem (ES) cells, embryonic stem cells expressing GFP (ES green) and Epiblast stem cells (Epi) cells have been captured, presented and discussed.

In this thesis many different cell types were tested to be trapped for different durations with no visible damage. In one instance a budding yeast cell was trapped for 5 minutes at a power of 21.4 ± 0.1 mW with no visible damage. For fluorescent imaging or Raman spectrum acquisition 5 minutes is more than sufficient time to collect a signal from a single, trapped cell.

The combination of trapping of a single cell together with analytical techniques such as Raman spectroscopy and other types of microscope, provides interesting alternatives in single cell imaging.

6.8 Conclusions

In this chapter, optical trapping in three dimensions of ES cells, RBCs and U87 cells using the two beam fibre trap as well as optical trapping of ES cells and RBC cells using the four beam fibre trap has been tested. These fibre traps have been

characterised, using a pre-calibrated OT system, to acquire the trap force and the efficiency factor Q.

Furthermore, in this chapter potential applications of the MCF optical trapping that could be of interest to the biological research community is presented; in particular the combination of MCF trapping of single cells with fluorescence excitation, and the combination of MCF trapping with Raman spectroscopy. In this chapter it is highlighted that a single but small fibre demonstrates some initial bio-experiments, holding different types of cells which vary on diameter, investigating this way the trapping distance (d_{trap}) to ensure that one of the main benefits of the technique -contactless manipulation - is maintained. Decoupling trapping from imaging is a benefit and this makes the variety of the potential applications wider, especially if combined with different characterisation techniques such as fluorescence excitation through the fibre. Raman spectroscopy can be also combined with MCF trapping so that the Raman beam is only used to acquire the spectra and not to trap. This allows us to reduce the background signal from the substrate and collect the spectra of the cells upon interest.

The final chapter summarises the main ideas presented in this thesis and also suggests future areas to explore to improve or add to the MCF trapping system developed in this thesis. Some ideas for further applications, to advance the work in this chapter but out of the scope of this thesis, are discussed.

Chapter 7: Conclusions and future work

7.1 Conclusions

This thesis describes the development of a four core fibre-based optical trapping system able to optically trap and manipulate microparticles and cells at the end of a *single* optical fibre. This geometry is suited for use in a wide variety of experiments using *unmodified* optical microscopes. The fibre system traps the cell by delivering the trapping light at the end of a multicore fibre using end-face beam turning mirrors to achieve the required beam paths. Because the trapping light is fibre delivered, no trapping light is delivered by the imaging optics and therefore any optical microscope is for imaging purposes only.

To date, the most common approach to optically trap cells and particles is to use an optical microscope to tightly focus the trapping light through a high numerical aperture objective lens and trap the particle in the highest intensity region point, [66]. However, this optical trapping arrangement limits the range of potential applications that optical trapping can be used for, due to the bulk microscope structure and the need for a bespoke microscope optical system capable of simultaneously delivering the trapping beam, and imaging the sample.

To overcome these restrictions, many attempts that replace the bulk optical lens with optical fibre have been reported and these are described in detail in Chapter 2, section 2.4.

The approach presented in this thesis is based upon micro-machining of a four-core optical fibre to incorporate micro optics on the end of the fibre. Focused ion beam machining (FIB) has been used to fabricate mirror patterns on the end of the multi-core fibre (MCF). These mirrors are designed with an angle slightly higher than the critical angle relative to the fibre axis, so that the light coming out of the machined cores gets redirected to form an overlapping region close to the fibre surface. A particle can then be trapped in this region.

This machined MCF optical tweezing system provides advantages in comparison with studies that use two opposed fibres [13] or two inclined fibres [89] to trap particles, by eliminating the need for precise multi-fibre alignment. Additionally, this approach avoids the use of a bundle of machined fibres [9], which offers advantages in terms of overall size of the fibre, flexibility of the system, and simplification in the assembly.

Also, if comparing with a tapered single fibre approach [91,94] the MCF trap holds the cell further away from the fibre end, while the tapered fibres have the cell in contact. Non-contact is an important parameter for the trapping, to avoid mechanical damage to a cell under study.

Moreover, optical trapping of a single cell using the machined MCF can be combined with other imaging techniques, so it can be applied to a wide variety of applications. For example, when combined with different types of microscopy, such as fluorescence or Raman microspectroscopy, it can be used help collect a signal from a single cell in a sample isolated from other cells.

The main findings of this thesis are summarised by presenting the key-findings from each chapter of this thesis below:

Chapter 3- Fibre characterisation and mirror microfabrication techniques: The two components of the MCF-based trap, besides the trapping laser sources and imaging microscope, are the machined multicore fibre and a fan out device to connect the MCF to the laser sources. The potential fabrication techniques that might be used to make these components are reviewed and compared. Techniques that are more commonly chosen for fabrication of microstructures on a glass material surface such as chemical etching, mechanical polishing, ultrashort laser pulse machining techniques and Focused Ion beam milling are discussed and potential fabrication approaches for the mirror structures needed in this work are described. Fan-out fabrication techniques to interface between single-core and multi-core fibres, such as waveguide laser inscription and chemically etched fibres attached directly to the MCF, are also described.

In this chapter, the measurement of the refractive index of the MCF core has been presented and analysed, as it is an important parameter that affects the final design of the MCF trap. The approach used to determine the refractive index was to use a Michelson interferometer to acquire a low coherence interferograms associated with two cleaved ends of a known length of optical fibre. The measured optical path length is compared with the respective physical length of the fibre to allow the effective refractive index of the fibre to me determined. The experimental value of the refractive index of the core of the MCF used in this thesis is $n_{core} = 1.470 \pm 0.008$, as measured at room temperature and for $\lambda = 1550 nm$.

Key-findings: Review of main techniques of micro-pattern fabrication and effective core refractive index measurement for the MCF.

Chapter 4- Fabrication, assembly and characterisation of a multicore fibre based trapping system: After reviewing the fabrication techniques in chapter 3, this chapter describes the techniques finally chosen for the fabrication of each part of the experimental set-up of the fibre trap, as well as the final assembly. As also mentioned in Chapter 3, FIB is a technique that removes material with a minimum resolution of 5 nm [133] and for this reason it is highly suitable for making the structures needed in this work, as to create bespoke structures on the end-face of the optical fibre, the fabrication technique should minimise the potential errors associated with the machining process. Laser machining was the technique chosen for the sample chambers microchannels fabrication and the technique chosen to make the fan-out was the chemical (HF) etching. The mirror angle is defined to be slightly greater than the critical angle so that the laser beam is always subject to total internal reflection when touching the mirror surface. The critical angle for a system where the effective refractive index of the core is 1.470 ± 0.008 and the medium where the optical trapping experiment takes place in water (n_{water}=1.33), is θ_{crit}=64.7$^\text{o}$ $\pm0.1^\text{o}$.

Furthermore, the experimental setup needed for the implementation of the optical experiments is presented. The setup consists of the MCF system that is connected to four separate laser diodes of 976 nm wavelength, each of maximum output power 330 mW, via a fan-out device. Two micro-translation stages have been used to mount the fibre holder and the sample. A laser machined microscope slide has been used as a sample chamber and contains a channel to hold the fibre. A CCD camera and a PC were used to image the trapping process using a home built microscope. In this chapter, the FIB fabrication process of the mirrors has been described and the characterisation of the beam exited the machined cores has been also made. Furthermore, an experiment that studies the divergence of the beam exiting the machined cores has been also presented in the same chapter. As the fabrication results show, the fabricated mirror angle was often measured to be slightly different than the designed angle, which in this case was defined to be 70°, due to a small drift during the FIB fabrication process. This is due to poor conductivity of the fibre, and can lead to a 0.5° to 4° difference in the resulting mirror angle, which in turn can potentially lead to a different d_{trap} and NA than the intended. Another step in the characterisation of the beam was the calculation of the propagation angle and the comparison between the theoretical estimations and the experimental values. More specifically, the Standard deviation between Theory and experiment turned out to be 0.5%-2.5% for the different fabricated cores.

Key-findings: Process to fabricate a machined MCF able to demonstrate stable optical trapping of single biological particles. Experimental set-up and characterisation of the beam.

Chapter 5-Optical trapping and manipulation applications: This chapter presents the results of the optical trapping experiments for yeast cells using the two-fibre traps: two-beam trap and four-beam trap. Firstly, characterisation of the two-beam and the four-beam optical traps based on a pre-calibrated conventional OT system has been described and the trap quality factor Q has been also calculated. As the respective results of the characterisation show, the four-beam trap is more efficient than the two-beam trap, with an efficiency Q_{4cores}=0.015 ± 0.004 whereas for the two-beam trap is Q_{2cores}=0.010 ± 0.003 for similar optical powers (23.5 mW). Comparing the MCF based trap with other similar studies based on alternative fibre configurations, the trapping force is in broad agreement with the performance reported in these studies that lie within the range of 0.5 pN and 5 pN [54,159,160]. If compared with the conventional OT, the MCF trap is weaker, as the OT studies present trap forces up to 35 pN [161]. The fact that the OT systems have a high NA objective to tightly focus the trapping light leads to the larger gradient forces and thus stronger traps in comparison with the MCF based trap. Comparing these values with Q=0.03 for the 0.90 NA OT system used, it can be seen that the OT is more than twice as efficient than the fibre traps, however, in the literature optical tweezers typically use a higher NA or around 1.3 and have much higher Q values, between 0.1 and 0.57 [161- 163]. In general OTs are more efficient than fibre traps, however, the MCF trap allows additional flexibility in the trapping experiments and thus in the variety of the potential applications.

In this chapter, the trapping distance has been measured experimentally and has been compared with the respective theoretical estimation. The standard deviation between experimental and theretical values is between 25-40% for the different traps. This can be explained due to the refraction of the exiting beam through the cells that are freely suspended in the medium, that they act like lenses. This scattering can alter the resulting propagation of the beam and thus of the overall overlapping area position. This can lead to a different experimental trapping distance than the expected one for the same mirror angle.

The NA values that were calculated based on the fabricated mirror angle are very close to the expected values.

Cell position tracking using a Matlab code has also been developed to provide information concerning the shape of the trap. The centre of mass of the trapped cell is identified and the trajectory of this position is plotted while the cell is trapped. Although the data was limited to short trapping durations some basic conclusions about the Gaussian-shaped distribution of the trap, and how confined the trapped cells are, can be presented.

Key-findings: Trapping force, trapping distance and trapping efficiency characterisation for yeast cells in 3 dimensions.

Chapter 6-Single cell applications of the MCF trap: This chapter presents an initial work to optically trap a variety of cell types; human red blood cells, human glioblastoma cells (U87s) and mouse embryonic stem cells (ES cells). Similar to the procedure used in Chapter 5, for yeast cells, d_{trap}, F_{fibre} and Q, as well as particle trajectory are measured to characterise and compare the trap properties for these diverse cell types. As well as trapping yeast and mammalian cells, experiments for trapping other particles some other particles have been also demonstrated. The aim to optically trap microspheres of diameters ranging between 1-15 μm as well as of *E.coli* bacteria forming a cluster, or 'cloud' of many loosely trapped cells using the machined MCF based tweezing system, has been demonstrated.

This chapter also describes the use of the MCF trapping with microscopy techniques such as Raman spectroscopy and fluorescent microscopy. Taking the spectrum of a single cell using a Raman spectrometer can be challenging due to high background signal, and tendency for the sample to drift out of the measurement volume. However, when the single cell is optically trapped and moved away from the substrate, then the background signal is minimised. Raman spectra of yeast cells as well as spectra from three closely related cell types; mouse embryonic cells (ES), mouse embryonic stem cells expressing GFP (ES green) and mouse embryonic stem cells that have differentiated into mouse epiblast cells (Epi), have been acquired and an initial comparison between the cell types has been presented.

Key-finding: 3D trapping of ES, U87 and RBC cells and characterisation of the trap. Collection of Raman signals from trapped cells and the analysis of the spectra which may lead to improved, no perturbative methods of characterising single cells.

To summarise, the aim of this thesis was to investigate, develop and characterise an optical trapping system based on the machining of special mirror patterns on the end of

a 4-core fibre. The main advantages of the suggested system can be summarised as the flexibility of the trap system as well as the decrease of its overall size that leads to potential use in a wider variety of applications.

In addition to the main demonstration, some examples of potential biological experiments, including trapping different types of cells as well as more specialised particles such as hollow glass microspheres have been discussed. However, this demonstration is only the beginning and further future research areas for MCF trapping fibres is suggested in the next section.

The main objectives of this thesis can be summarised as: Review fabrication methods to determine the best technique to fabricate bespoke end face mirrors on a fibre suitable for making a fibre trap, assemble a working, single, fibre trap based on a multicore fibre with machined mirrors capable of trapping single cells, characterise fibre optical trap in terms of the force it can exert, perform exemplar experiments to demonstrate the potential and the flexibility of the machined MCF trap. All these objectives have been examined and presented throughout this thesis as the above chapter review indicates.

7.2 Future work

7.2.1 Potential improvements of the fabrication techniques

The fabrication of the mirrors onto the fibre end has been demonstrated using FIB, which offers high accuracy and precision. This facilitated studies into the geometrical pattern by eliminating any significant errors due to fabrication. However FIB fabrication is slow, and therefore relatively expensive, and unsuitable for scaling up to mass manufacture, therefore alternative approaches are of interest.

7.2.1.2 Fabrication of mirror patterns using picosecond laser

In potential future studies of the MCF trap, in which the investigation of the main working principal is not the primary aim, then it may be possible to relax the manufacturing accuracy and tolerances. As such, further investigation of potential alternatives in the fabrication processes to create the mirror patterns would be of interest. A fabrication technique that would be less precise but also less time consuming and of lower cost, would be an alternative for studies that demanded higher number of

available optical probes or for commercial production of this optical tweezing system, where the cost of the fabrication using FIB could be prohibitive.

As mentioned in Chapter 3, there are many different machining techniques to fabricate patterns into a glass material. Picosecond laser machining is an alternative technique, potentially lower in cost and it shows high accuracy. The main working principle is presented as following.

The main recommended fabrication process is shown below in figure 7. 1. The optical fibre is mounted in a proper angle so that the cutting of the mirrors can be achieved. The beam scans the sample following the perpendicular direction, as the annotated blue lines indicate in the figure 7.1, and it removes material, leaving the fibre with a mirror shaped surface as intended.
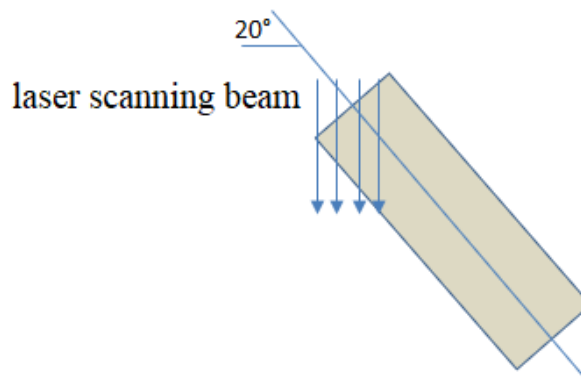
Figure 7. 1; The working principle of machining using picosecond laser is based on material removal by scanning the sample. The fibre is mounted in a holder that is able to control rotation in all axes so that it can be rotated by 20° in order to machine a 70° mirror.

To achieve the desired mirror angle, the most important aspects that need to be defined is the proper mounting angle of the fibre relative to the machining beam. Appropriate compensation for beam profile may be necessary. However, as long as the main aim is not only to fabricate the pattern but also to maintain a fairly low roughness of the machined surface, the machining velocity, pulse power, pulse overlap and machining wavelength all needs to be optimised.

Where laser machining surface finish is too rough then an option for improving the surface finish resulting from the picosecond laser process would be the use of FIB as a finishing technique. In this case, the use of FIB would be much lower cost because it will be used for substantially less time since only a few microns of material would need removal.

However, this laser machining process is still fabricating one fibre at a time, which poses restrictions to a potential mass production of the machined fibres. An alternative fabrication method that could overcome these restrictions would be nanoimprint lithography [145] that can offer rapid, massive and high throughput fabrication of patterns.

7.3 Future applications

As discussed, one of the main advantages of this approach to cell trapping is the possibility of isolating a single cell from a mixed population of cells and then examining it in isolation without the need of specially modified imaging microscopes. This offers the prospect of conducting a wide range of micro-biology experiments in a well-controlled environment, using conventional imaging techniques. Single cell experiments are becoming increasingly important to understand heterogeneity between cells in a population [212] and monitoring individual cells by holding them, stably, in the correct position using our MCF trap can contribute to this growing area. Another avenue for further use of the MCF trap is to examine the interactions between single cells.

7.3.1 Dynamics of two cells interacting

More complex biological experiments can be performed using machined MCF fibre traps. Using a microscope slide that includes a microfluidic channel that allows two separate tweezing fibres to be placed opposite to each other, but on a common axis, could be the basis for a cell-cell interaction experiment. This would consist of two opposed machined MCFs each one capable of trapping a single cell. Moving the two fibres closer would bring the two cells closer or into contact with each other and real time responses may be imaged by an appropriate diagnostic microscope; a bright field microscope if a response is hypothesised to be a change in morphology, a fluorescent microscope if the response is expected to be up regulation or down regulation of a fluorescently tagged protein; Raman micro-spectroscopy if there is expected to be a measurable change in the molecular constituents of either cell. This can be imaged by a range of diagnostic microscopes to study the interaction.

The same concept could be demonstrated by using a machined MCF to optically trap one cell, maybe a larger cell, and a conventional optical tweezing system to trap a second cell, possibly a single bacterium, which could not be trapped in the MCF. The conventional tweezers instead of a second optical fibre eliminates the need for alignment between two fibres and at the same time, the use of the conventional OT can widen the range of cell sizes that can be stably trapped. Having the freedom to trap a smaller cell such as a bacterium using the conventional OT can enable applications in experiments that explore the case where a single small cell is to be brought close to a larger cell and their interaction to be studied, for example the dynamics of an immune cell in response to a bacterial pathogen or the response of an epithelial cell to a toxic micro- or nano-particle.

7.3.2 Deposition of a single cell in a predetermined position

Another potential application that could be achieved using the proposed MCF trap would be to pick up individual cells and place them in a predetermined location. One example of this is where a pure culture from a single progenitor cell (such as bacteria, yeast, mammalian) needs to be created. Individual cells can be selected, isolated and manipulated to a new, uncontaminated location, using MCF traps. Given the correct conditions, the single cell will expand into a colony that may be used for further experimentation. Another application that can make use of MCF traps ability to isolate and manipulate single cells is to transport the trapped cell to a sample of cells, in order to examine the effect of the single cell on the existing population. The existing population may consist of a small number of cells (for example a micro-consortia) or a large population for example a 3D cultured spheroid. The cells can be monitored under a microscope to examine how their dynamics change in response to the new cell in the population.

The ability to manipulate single cells also will allow a researcher to build a structure of different cell types by manipulation of individual cells, one by one, in order to build up engineered microtissue structures. Using multiple reservoirs on a chip to store multiple cell types, or using fluorescence or Raman to first distinguish the cell types, one can envisage building a complex microtissue, cell by cell, composed of layers of different cell types. This would be a slower, but possible more precise method than 3D printing to 'write' complex 3D tissue structures.

As shown in Chapter 5 where the trapping experiments were presented, the maximum velocity that the trapped yeast cell could be translated within x and y direction was between 0.2 mm/s and 0.4 mm/s for optical powers 22 mW up to 29 mW for the two-beam trap in x direction and between 0.02 and 0.03 mm/s for y direction. For the four-beam trap, the maximum speed of translation for the x and y direction is between 0.6 and 0.9 mm/s for powers 27-31 mW and 0.025-0.04 for x and y respectively, as described in Chapter section 5. 5.

To proceed with an application like the above mentioned one, a design of bespoke devices that contain reservoirs so that we can define the path that the cell needs to follow is required.

7.3.3 Use of cores for excitation delivery and emission detection

An alternative way to perform Raman trapping or fluorescent trapping would be to use one core of the MCF excite the fluorescence emission or Raman scattering signal, and another core to detect any directly reflected signal and direct this to a suitable spectrometer instead of using the microscope imaging optics. A MCF incorporating a larger core would be able to collect more of the reflected signal from the trapped cell while minimising pickup from background objects. In chapter 6 we demonstrated selective fluorescent excitation of the trapped cell by using one core of the fibre to excite the fluorescence. Additionally, also in chapter 6, we observed that an increase in trapping power increased the strength of the Raman signal because the trapping light also acted as Raman excitation light.

7.3.4 MCF based trapping system in combination with microfluidics for cell sorting

Combining the trapping system with complex microfluidics geometries would give the opportunity for further sorting and study of single cells and for further understanding of cell properties and sample heterogeneity. Passive microfluidic sorting techniques, such as inertial focussing or the use of pores or channels as filters can be used as a first step to categorize the cells regarding their size, in the case of a sample with cells of many different sizes. As a second step, the MCF based tweezing technique could be used to trap a single sorted cell to investigate the fluorescent properties of labelled cells in the group or to collect the Raman spectrum and identify or characterise a cell using differences in the spectra between cells. Then the cell can be sorted by manipulation

into an appropriate collection channel or reservoir, by translating the fibre or by releasing the cell from the trap and controlling the flow so that the cell flows into the correct collection area. In such a manner, microfluidic circuits could be used with the MCF system for multi-step classifications/characterisation optical experiments. Additionally, the use of sealed microfluidic channels will reduce evaporation and lead to more stable trapping than observed in this thesis, where channels were written on a surface.

7.3.5 Adding reagents to cells

In some experiments, selective deposition of reagents to single cells inside a medium is needed. For example, there are cases in which an antibody needs to be selectively attached to a cell to transform the cell into an appropriate receiver of the drug under test [213] or in cases where it is desired to add cell proliferation reagents [214]. In these situations, the MCF fibre trap can be used. More specifically, this can be achieved using two MCF optical probes, one to stably hold the cell that the reagent will be added to and a second trap to hold the reagent microparticle. Bringing the two traps together will allow the reagent to approach the cell, in a similar manner to the "two cells interaction experiments" discussed earlier. A further way to deliver reagents controllably to trapped cells is to make use of hollow cored fibres. A fibre with four cores plus a hollow core may be fabricated to trap a cell in a manner similar to this thesis, and the hollow core may act as a microfluidic channel through which reagents may be delivered to a localised area at the end of the fibre where the cell is trapped. Further, the hollow core channel may be used to aspirate media to test, for cell excretions, for example, or to aspirate the trapped cell, for collection after treatment and downstream analysis.

7.4 Summary

This thesis describes the development of an optical trapping system that is based on the machining of micro-optics on the end face of a multicore optical fibre. Focused ion beam technology was used to fabricate mirrors of an angle slightly higher than the critical angle to allow the core-guided light to undergo total internal reflection. As a result, the emitted beams cross over (focus) close to the fibre end. An overlapping region between the two or the four beams that exit the fibre defines the region within which the cell or the particle is trapped due to the higher intensity of light.

Optical trapping of yeast cells, human red blood cells, human glioblastoma cells (U87s), mouse embryonic stem (ES) cells and mouse epiblast (Epi) cells, has been demonstrated in 3 dimensions. Evaluation of the optical trap in terms of maximum trapping speed, trap force and efficiency has been also presented. Raman spectra of yeast cells, ES cells (mouse embryonic stem cells), ES green cells (mouse embryonic stem cells expressing GFP) and Epi cells (mouse embryonic epiblast cells) have been collected.

The main advantage of using a fibre trap in single cell experiments, compared to a conventional optical tweezer, is the decoupling the imaging optics from the trapping optics, allowing trapping without the need of a high NA objective. The main advantages of using this MCF trap compared to other types of fibre trap described in the literature are the fact that this is a single flexible fibre of small diameter, only 150 μm, without the need for demanding bundle assembly. This portable MCF trap can be used under a variety of microscopes, such as Raman or fluorescent, and can further widen the range of potential applications.

References

[1] N. Bellini, K. C. Vishnubhatla, F. Bragheri, L. Ferrara, P. Minzioni, R. Ramponi, I. Cristiani and R. Osellame, "Femtosecond laser fabricated monolithic chip for optical trapping and stretching of single cells," Optics Express 18, 4679-4688 (2010).

[2] A. Keloth, O. Anderson, D. Risbridger and L. Paterson, "Single Cell Isolation Using Optical Tweezers," Micromachines (Basel) 9(9), 434 (2018).

[3] S. C. Grover, A. G. Skirtach, R. C. Gauthier and C. P. Grover, "Automated single-cell sorting system based on optical trapping," Journal of Biomedical Optics 6(1), 14–22 (2001).

[4] C. Xie, M. A. Dinnoand and Y. Q. Li, "Near-infrared Raman spectroscopy of single optically trapped biological cells," Optics Letters 27, 249–251 (2002).

[5] C. Xie, D. Chen and Y. Q. Li, "Raman sorting and identification of single living micro-organisms with optical tweezers," Optics Letters 30, 1800-1802 (2005).

[6] H. Zhang and K.-K. Liu, "Optical tweezers for single cells," Journal of the Royal Society Interface 5(24), 671-690 (2008).

[7] A. Ashkin, J. Dziedzic and T. Yamane, "Optical trapping and manipulation of single cells using infrared laser beams," Nature 330, 769–771 (1987).

[8] A. Ashkin, J. M. Dziedzic, J. E. Bjorkholm and Steven Chu, "Observation of a single-beam gradient force optical trap for dielectric particles," Optics Express 11, 288-290 (1986).

[9] C. Liberale, P. Minzioni, F. Bragheri, F. De Angelis, E. Di Fabrizio and I. Cristiani, "Miniaturized all-fibre probe for three-dimensional optical trapping andmanipulation," Nature Photonics 1, 723-727 (2007).

[10] O. M. Marago, P. H. Jones, P. G. Gucciardi, G. Volpe and A. C. Ferrari, "Optical trapping and manipulation of nanostructures," Nature Nanotechnology 8, 807-819 (2013).

[11] T. Čižmár, L.C.Dávila Romero, K. Dholakia and D. L. Andrews, "Multiple optical trapping and binding: new routes to self-assembly," Journal of Physics B: Atomic, Molecular and Optical Physics 43 (10), 102001 (2010).

[12] H. Melville, G.F. Milne, G.C. Spalding, W. Sibbett, K. Dholakia and D. McGloin, "Optical trapping of three-dimensional structures using dynamic holograms,"Optics Express 11(26), 3562-3567 (2003).

[13] J. Guck, R. Anathakrishnan, H. Mahmood, T. J. Moon, C. Casey Cunningham and and J. Kas, "The Optical Stretcher: A Novel Laser Tool to Micromanipulate Cells," Biophysical Journal 81, 767–784 (2001).

[14] S. Nawaz, P. Sánchez, K. Bodensiek, S. Li, M. Simons and I. A. T. Schaap, "Cell Visco-Elasticity Measured with AFM and Optical Trapping at Sub-Micrometer Deformations," PLoS One 7(9), 45297 (2012).

[15] W. H. Wright, G. J. Sonek and M. W. Berns, "Parametric study of the forces on microspheres held by optical tweezers," Applied Optics 33(9), 1735-1748 (1994).

[16] E. Townes-Anderson, R. S. St. Jules, D. M. Sherry, J. Lichtenberger and M. Hassanain, "Micromanipulation of Retinal Neurons by Optical Tweezers," Molecular Vision 4, 12 (1998).

[17] P. C. Ashok and K. Dholakia, "Optical trapping for analytical biotechnology," Current Opinion in Biotechnology, 16-21 (2012).

[18] A. J. Crick, M. Theron, T.Tiffert,V. L.Lew, P. Cicuta and J. C.Rayner, "Quantitation of Malaria Parasite-Erythrocyte Cell-Cell Interactions Using Optical Tweezers," Biophysical Journal 107 (4), 846-853 (2014).

[19] P. Jordan, J. Leach , M. Padgett, P. Blackburn, N. Isaacs, M. Goksör, D. Hanstorp, A. Wright, J. Girkin and J. Cooper, "Creating permanent 3D arrangements of isolated cells using holographic optical tweezers," Lab Chip 5,1224-1228 (2005).

[20] B. Landenberger , H. Höfemann, S. Wadle and A. Rohrbach, "Microfluidic sorting of arbitrary cells with dynamic optical tweezers," Lab Chip 12, 3177-3183 (2012).

[21] X. Wang, S. Chen, M. Kong, Z. Wang, K. D. Costa, R. A. Li and D. Sun, "Enhanced cell sorting and manipulation with combined optical tweezer and microfluidic chip technologies," Lab Chip 11, 3656-3662 (2011).

[22] L. Paterson, E. I. Papagiakoumou, G. Milne, V. G. Garcés-Chávez, T. Briscoe, W. Sibbett, K. Dholakia and A. C. Riches, "Passive optical separation within a 'nondiffracting' light beam," Journal of Biomedical Optics 12(5), 054017-054030 (2007).

[23] M. P. MacDonald, G. C. Spalding and K. Dolakia, "Microfluidic sorting in an optical lattice," Nature 426, 421–424 (2003).

[24] N. Auka, M. Valle, B. D. Cox, P. D. Wilkerson, T. Cruz Dawson, J. E. Reiner and S.J. Seashols-Williams, "Optical tweezers as an effective tool for spermatozoa isolation from mixed forensic samples," PLoS One 14(2), 0211810 (2019).

[25] E. Eriksson, J. Enger, B. Nordlander, N. Erjavec, K. Ramser, M. Goksör, S. Hohmann, T. Nyströmband and D. Hanstorp, "A microfluidic system in combination with optical tweezers for analyzing rapid and reversible cytological alterations in single cells upon environmental changes," Lab Chip 7(1), 71-6 (2007).

[26] A. Gross , J. Schoendube , S. Zimmermann, M. Steeb, R. Zengerle and P. Koltay, "Technologies for Single-Cell Isolation," International Journal of Molecular Sciences. 16(8), 16897-919 (2015).

[27] S. Ishii, K. Tago and K. Senoo, "Single-cell analysis and isolation for microbiology and biotechnology: methods and applications," Applied Microbiology and Biotechnology 86, 1281-1292 (2010).

[28] P. Hu, W. Zhang, H. Xin and G. Deng, "Single Cell Isolation and Analysis," Frontiers in Cell Developmental Biology 4, 116 (2016).

[29] A. Orfao and A. Ruiz-Argüelles, "General concepts about cell sorting techniques," Clinical Biochemistry 29(1), 5-9 (1996).

[30] B. Alberts, A. Johnson, J. Lewis, M. Raff, K.Roberts and P. Walter, Molecular Biology of the Cell. 4th edition, New York: Garland Science; 2002.

[31] D. Di Carlo , H. Tat Kwong Tse and D. R Gossett, "Introduction: Why Analyze Single Cells?" Methods in Molecular Biology 853, 1-10 (2012).

[32] Q. Wei and H. Huang, "Chapter Five - Insights into the Role of Cell–Cell Junctions in Physiology and Disease," International Review of Cell and Molecular Biology 306, 187-221 (2013).

[33] N. Nishida-Aoki and T. S. Gujral, "Emerging approaches to study cell–cell interactions in tumor microenvironment," Oncotarget 10(7), 785–797 (2019).

[34] M. E. Davey and G. A. O'toole, "Microbial biofilms: from ecology to molecular genetics," Microbiology and Molecular Biology Reviews 64(4), 847-67 (2000).

[35] G. B. Huffnagle, R. P. Dickson and N. W. Lukacs, "The respiratory tract microbiome and lung inflammation: a two-way street," Mucosal Immunology 10 (2), 299-306 (2017).

[36] S. J. Yang, I. Kang and J. C. Cho, "Expansion of Cultured Bacterial Diversity by Large-Scale Dilution-to-Extinction Culturing from a Single Seawater Sample," Microbial Ecology 71(1), 29-43 (2016).

[37] M. S. Cho, H. Yee and S. Chan, "Establishment of a human somatic hybrid cell line forrecombinant protein production," Journal of Biomedical Science 9, 631–638 (2002).

[38] K. Zhang, M. Gao, Z. Chong, Y. Li, X. Han and R. Chenand L. Qin, "Single-CellIsolation by Modular Single-Cell Pipette for RNA-Sequencing," Lab Chip 16(24),4742–4748 (2016).

[39] G. Wright, P. C. Morton, M. J. Tucker, C. L. Sweitzer-Yoder and S. E. Smith, "Micromanipulation in assisted reproduction: a review of current technology,"Current Opinions in Obstetrics and Gynecology 10, 221-226 (1998)

[40] G. Thalhammer, R. Steiger, M. Meinschad, M. Hill, S. Bernet and M. Ritsch-Marte, "Combined acoustic and optical trapping," Biomedical Optics Express 2(10), 2859-2870 (2011).

[41] F. Petersson, L. Aberg, A. M. Swärd-Nilsson and T. Laurell, "Free flow acoustophoresis: microfluidic-based mode of particle and cell separation," Analytical Chemistry 79, 5117-5123 (2007).

[42] J. Hultstrom, O. Manneberg, K. Dopf, H. M. Hertz, H. Brismar and M. Wiklund, "Proliferation and viability of adherent cells manipulated by standing-wave ultrasound in a microfluidic chip." Ultrasound in Medicine and Biology 33, 145–151 (2007).

[43] D. Bazou, R. Kearney, F. Mansergh, C. Bourdon, J. Farrar and M. Wride, "Gene expression analysis of mouse embryonic stem cells following levitation in an ultrasound standing wave trap," Ultrasound in Medicine and Biology 37, 321– 330 (2011).

[44] M. G. Kim, J. Park, H. G. Lim, S. Yoon, C. Lee, J. H. Chang and K. K. Shung, "Label-free analysis of the characteristics of a single cell trapped by acoustic tweezers," Scientific Reports 7, 14092 (2017).

[45] J.-L.Thomas, R. Marchiano and D. Baresch, "Acoustical and optical radiation pressures and the development of single beam acoustical tweezers,"Journal of Quantitative Spectroscopy and Radiative Transfer 195, 55-65 (2017).

[46] L.P.Gor'kov, "On the forces acting on a small particle in an acoustical field in an ideal fluid," Soviet Physics Doklady 6, 773 (1962).

[47] M. Elitas, N. Dhar, K. Schneider, A. Valero, T. Braschler, J. D. McKinney and P. Renaud, "Dielectrophoresis as a single cell characterization method for bacteria," Biomedical Physics and Engineering Express 3, 015005 (2017).

[48] F. S. Fritzsch, C. Dusny, O. Frick and A. Schmid, "Single-cell analysis in biotechnology, systems biology, and biocatalysis," Annual Review of Chemical and Biomolecular Engineering 3, 129-55 (2012).

[49] V. Espina, J. D Wulfkuhle, V. S. Calvert, A. VanMeter, W. Zhou, G. Coukos, D. H. Geho, E. F Petricoin and L. A. Liotta, " Laser-capture microdissection," Nature Protocols 1, 586–603 (2006).

[50] M. Wu, D. Ling, L. Ling, W. Li and Y. Li, "Stable optical trapping and sensitive characterisation of nanostructures using standing-wave Raman tweezers," Scientific Reports 7, 1-8 (2017).

[51] B. Redding, M. Schwab and Y. Pan,"Raman Spectroscopy of Optically Trapped Single Biological Micro-Particles," Sensors 15, 19021-19046 (2015).

[52] S. Wüst, R. Müller and S. Hofmann, "Controlled Positioning of Cells in Biomaterials—Approaches Towards 3D Tissue Printing," Journal of Functional Biomaterials 2. 119-154 (2011).

[53] 3D micro-organisation printing of mammalian cells to generate biological tissues," Scientific Reports 10, Article number: 19529 (2020).

[54] G. Anastasiadi, M. Leonard,L. Paterson and W. N. MacPherson, "Fabrication and characterisation of machined multi-core fibre tweezers for single cell manipulation," Optics Express 26, 3557-3567 (2018).

[55] J. P. M. Van Putten, C. T. P. Hopman and J. F. L. Weel, "The use of immunogold-silver staining to study antigen variation and bacterial entry into eukaryotic cells by conventional light microscopy," Journal of Medical Microbiology 33(1), 35-41 (1990).

[56] W. Qian, X. Huang, B. Kang and M.A.El-Sayed, "Dark-field light scattering imaging of living cancer cell component from birth through division using bioconjugated gold nanoprobes," Journal of Biomedical Optics 15(4), 046025 (2010).

[57] F. Zernike, "How I Discovered Phase Contrast," Science 121, 345-349 (1955).

[58] M. Knoll and J. Kügler, "Subjective Light Pattern Spectroscopy in the Electroencephalic Range," Nature 184, 1823–1824 (1959)

[59] M.J. Sanderson, I. Smith, I. Parker and M.D. Bootman, "Fluorescence microscopy", Cold Spring Harbor Protocols 10, 1042-1065 (2014).

[60] S. Cox, "Super-resolution imaging in live cells," Developmental Biology 401(1), 175-181 (2015).

[61] J. C. George Turrell, "Raman Microscopy: Developments and Applications" (Elsevier academic press, 1996).

[62] W. Lee, P. Reece and R.Marchington, "Construction and calibration of an optical trap on a fluorescence optical microscope," Nature Protocols 2, 3226–3238 (2007).

[63] J. Y. Walz, "Measuring particle interactions with total internal reflection microscopy," Current Opinion in Colloid and Interface Science 2(6), 600-606 (1997).

[64] M.I. Snijder-Van As, B. Rieger, B. Joosten, V. Subramaniam, C.G. Figdor and J.S. Kanger, "A hybrid total internal reflection fluorescence and optical tweezers microscopeto study cell adhesion and membrane protein dynamics of single living cells," Journal of Microscopy 223(1), 84-92 (2009).

[65] A. Hoffmann, G. Meyer zu Hörste, G. Pilarczyk, S. Monajembashi, V. Uhl and K. O. Greulich, "Optical tweezers for confocal microscopy," Applied Physics B 71, 747–753 (2000).

[66] A. Ashkin, "Acceleration and trapping by radiation pressure," Physical Review Letters 24, 156-159 (1970).

[67] C. M. Creely, G. Volpe, G. P Singh, M. Soler and D. V. Petrov, "Raman imaging of floating cells," Optics Express 13, 6105-6110 (2005).

[68] P. R. T. Jess, V. Garces-Chaves D. Smith, M. Mazilu, L. Paterson, A. Riches, C. S.Herrington and K. Dolakhia, "Dual beam fibre trap for Raman microspectroscopy of single cells," Optics Express 14, 5779-5791 (2006).

[69] H.C. van de Hulst, "Light Scattering by Small Particles", Dover, New York (1981).

[70] P. N. Lebedev, "Experimental examination of light pressure," Annalen der Physik, 1- 26 (1901).

[71] https://www.nobelprize.org/prizes/physics/2018/summary/

[72] R. Ghadiri, T. Weigel, C. Esen and A. Ostendorf, "Microassembly of complex and three-dimensional microstructures using holographic optical tweezers," Journal of Micromechanics and Microengineering 22, 1-8 (2012).

[73] K. Dholakia, M.P. MacDonald, P. Zemanek and T.Cizmar, "Cellular and colloidal separation using optical forces," Methods Cell Biology 82, 467–495 (2007).

[74] L. Paterson, E. Papagiakoumou, G. Milne, V. Garćes-Chávez, S. A. Tatarkova, W. Sibbett, F. J. Gunn-Moore, P. E. Bryant, A. C. Riches and K. Dholakia,"Light-induced cell separation in a tailored optical landscape," Applied Physics Letters 87, 123901 (2005).

[75] S. Kumar, I.Z. Maxwell, A. Heisterkamp, T.R. Polte, T.P. Lele, M. Salanga, E. Mazur and D.E. Ingber, "Viscoelastic retraction of single living stress fibers and its impact on cell shape, cytoskeletal organization, and extracellular matrix mechanics," Biophysical Journal 90, 3762–3773 (2006).

[76] J. Guck, S. Schinkinger, B. Lincoln, F. Wottawah, S. Ebert, M. Romeyke, D. Lenz, H. M. Erickson, R. Ananthakrishnan, D. Mitchell, J. Käs, S. Ulvick and C. Bilby, "Optical deformability as an inherent cell marker for testing malignant transformation and metastatic competence," Biophysical Journal 88, 3689–3698 (2005).

[77] J.A. Dharmadhikari, S. Roy, A.K. Dharmadhikari, S. Sharma and D. Mathur, "Torque-generating malaria-infected red blood cells in an optical trap," Optics Express 12, 1179–1184 (2004).

[78] M. Dao, C.T. Lim and S. Suresh, "Mechanics of the human red blood cell deformed by optical tweezers," Journal of the Mechanics and Physics of Solids 51, 2259-2280 (2003).

[79] K. Dholakia and P. Reece, "Optical micromanipulation takes hold," Nanotoday 1, 18–27 (2006).

[80] K.C. Neuman, E. H. Chadd, G. F. Liou, K. Bergman and S. M. Block, "Characterisation of Photodamage to Escherichia coli in Optical Traps," Biophysical Journal 77, 2856–2863 (1999).

[81] A. Constable, J. Kim, J. Mervis, F. Zarinetchi and M. Prentiss, "Demonstration of a fibre-optical light-force trap," Optics Letters 18, 1867-1869 (1993).

[82] S. Hu, S. Chen, G. Xu and D. Sun, "Automated transportation of multiple cell types using a robot-aided cell manipulation system with holographic optical tweezers," IEEE/ASME Transactions Mechatronics 22, 804–814 (2017).

[83] Y. Wu, D. Sun and W. Huang, "Force and motion analysis for automated cell transportation with optical tweezers," 2011 9th World Congress on Intelligent Control and Automation, Taipei, 839-843 (2011).

[84] H. Songyu, X. Heng, W. Tanyong, C. Shuxun and S. Dong, "Automated Indirect Transportation of Biological Cells with Optical Tweezers and a 3D Printed Microtool," Applied Sciences 9(14), 2883 (2019).

[85] J. Guck, R. Anathakrishnan, C. Cunningham and J. Kas, "Stretching biological cells with light," Journal of Physics: Condensed Matter 14, 4843–4856 (2002).

[86] S. Albert, T. Kolb, M. Haug and G. Whyte, "Optofluidic rotation of living cells for single-cell tomography," Journal of Biophysics 106, 1-8 (2014).

[87] N. Bellini, F. Bragheri, I. Cristiani, J. Guck, R. Osellame and G. Whyte, "Validation and perspectives of a femtosecond laser fabricated monolithic optical stretcher," Biomedical Optics Express 3(10), 2658-2668 (2012).

[88] H. Thirstrup, T. B. Rungling, M. Z. K. Al-Hamdani, R. Pathanchalinathan, M. H. Dziegiel, A. Kristensen, R. Marie and K. Berg-Sørensen, "Optical and Hydrodynamic Stretching of Single Cells from Blood," in Optics in the Life Sciences Congress, OSA Technical Digest (online) (Optical Society of America, 2017), paper OtM4E.1.

[89] Y. Liu and M. Yu, "Investigation of inclined dual-fibre optical tweezers for 3D manipulation and force sensing," Optics Express 17, 13624-13638 (2009).

[90] K. Taguchi, H. Ueno, T. Hiramatsu and M. Ikeda, "Optical trapping of a dielectric particle using optical fibre," Electronic Letters 33, 413-414 (1997).

[91] R. S. Taylor and C. Hnatovsky, "Particle trapping in 3-D using a single fibre probe with an annular light distribution," Optics Express 11, 2775-2782 (2003).

[92] E. McLeod and A. Ozcan, "Nanofabrication using near-field optical probes," Journal of Laboratory Automation 17(4), 248–254 (2012).

[93] J. M. Tam, I. Biran and D. R. Walt, "An imaging fibre-based optical tweezer array for microparticle array assembly," Applied Physics Letters 84, 4289-4291 (2004).

[94] J. B. Decombe, S. Huant and J. Fick, "Single and dual fibre nano-tip optical tweezers: trapping and analysis," Optics Express 21, 30521-30531 (2013).

[95] L. Yu, S. Mohanty, G. Liu G, S. Genc, Z. Chen and M.W. Berns, "Quantitative phase evaluation of dynamic changes on cell membraneduring laser microsurgery," Journal of Biomedical Optics 13, 0505081-0505083 (2008).

[96] R. S. Rodrigues Ribeiro, R. Queiros, O. Soppera, A. Guerreiro and P. A. S. Jorge, "Optical Fibre Tweezers Fabricated by Guided Wave Photo-Polymerization," Photonics 2, 634-645 (2015).

[97] T. Čizmar and K. Dholakia, "Shaping the light transmission through a multimode optical fibre: complex transformation analysis and applications in biophotonics," Optics Express 19, 18871-18884 (2011).

[98] I. T. Leite, S. Turtaev, X. Jiang, M. Šiler, A. Cuschieri, P. St. J. Russell and T. Čižmár, "Three-dimensional holographic optical manipulation through a high-numerical-aperture soft-glass multimode fibre," Nature Photonics 12, 33–39 (2018).

[99] S. Bianchi and R. D. Leonardo, "A multi-mode fibre probe for holographic micromanipulation and microscopy," Lab on a chip 12, 635-639 (2012).

[100] C. Liberale, G. Cojoc, F. Bragheri, P. Minzioni, G. Perozziello, R. La Rocca, L. Ferrara, V. Rajamanickam, E. Di Fabrizio, and I. Cristiani, "Integrated microfluidic device for single-cell trapping and spectroscopy," Scientific Reports 3, 1-6 (2013).

[101] L. Yuan, Z. Liu, J. Yang, and C. Guan, "Twin core fibre optical tweezers," Optics Express 16, 4559-4566 (2008).

[102] A. L. Barron, A. K. Kar, and Henry T. Bookey, "Dual beam interference from a lensed multicore fibre and its application to optical trapping," Optics Express 20, 23156-23161 (2012).

[103] A. Nicolae and A. M. Grumezescu, "Materials for Biomedical Engineering," Biopolymer Fibers, 1-20 (2019).

[104] D. Yelin, I. Rizvi, W. M. White, J. T. Motz, T. Hasan, B. E. Bouma and G. J. Tearney, "Three-dimensional miniature endoscopy," Nature Brief Communications 443, 765 (2006).

[105] L. Fu and M. Gu, "Fibre-optic nonlinear optical microscopy and endoscopy," Journal of Microscopy 226, 195-206 (2007).

[106] I. S. Amiri, S. Razalli B. Azzuhri, M. A. Jalil, H. M. Hairi, J.Ali, M. Bunruangses and P. Yupapin, "Introduction to Photonics: Principles and the Most Recent Applications of Microstructures," Micromachines (Basel) 9(9), 452 (2018).

[107] H. Bae and M. Yu, "Miniature Fabry-Perot pressure sensor created by using UV-molding process with an optical fibre based mold," Optics Express 20, 14573-14583 (2012).

[108] M. Silva-López, A. Fender, W. N. MacPherson, J. S. Barton, J. D.C. Jones, D. Zhao, H. Dobb, D. J. Webb, L. Zhang and I. Bennion, "Strain and temperature sensitivity of a single-mode polymer optical fibre," Optics Letters 30, 3129-3131 (2005).

[109] N. Gayraud, Ł.W. Kornaszewski, J. M. Stone, J. C. Knight, D. T. Reid, D. P. Hand and W. N. MacPherson, "Mid-infrared gas sensing using a photonic bandgap fibre," Applied Optics 47, 1269-1277 (2008).

[110] A. Othonos, "Fiber Bragg gratings," Review of Scientific Instruments 68, 4309 (1997).

[111] K. Thyagarajan and A. Ghatak, Fibre Optic Essentials (John Wiley & Sons, Inc., Hoboken, New Jersey, 2007), p. 260.

[112] B.Vojnovic and D. Volpi, "Notes on optical fibres and fibre bundles," (University of Oxford, 2012).

[113] C. S. Gardner and G. Papen, in Reference Data for Engineers (Ninth Edition), 2002

[114] J. M. Senior, "Optical Fibre communications: Principles and Practice," Pearson Prentice Hall, 2009, p.1127.

[115] M. Majumder, T. K. Gangopadhyay, A. K. Chakraborty, K. Dasgupta and D. K. Bhattacharya, "Fibre Bragg gratings in structural health monitoring—Present status and applications," Sensors and Actuators A: Physical 147 (1), 150-164 (2008).

[116] W.-C. Du, X.-M. Tao and H.-Y. Tam, "Fibre Bragg Grating Cavity Sensor for Simultaneous Measurement of Strain and Temperature," IEEE Photonics Technology Letters 11(1), 105-107 (1999).

[117] N. Singh, S. C. Jain and A. K. Aggarwal, "Fibre Bragg gratings writing technology using phase mask technology," Journal of Scientific and Industrial Research 64, 108-115 (2005).

[118] F. Albri, "High precision laser micromachining for sensing applications," (Heriot-Watt University, Edinburgh, UK, PhD thesis, 2014).

[119] W. Yuan, F. Wang, A. Savenko, D. H. Petersen and O. Bang, "Note: Optical fibre milled by focused ion beam and its application for Fabry-Pérot refractive index sensor," Review of Scientific Instruments 82(7), 076103 (2011).

[120] J. C. Knight, T. A. Birks, R.F. Cregan, P. S. J. Russell and P. D. de Sandro, "Large mode area photonic crystal fibre," Electronics Letters 34, 1347-1348 (1998).

[121] P. Russell, "Photonic Crystal Fibres," Science 299, 358-362 (2003).

[122] B. J. Mangan, J. C. Knight, T. A. Birks, P. S. J. Russell and A. H. Greenaway, "Experimental study of dual-core photonic crystal fibre," Electronics Letters 36, 1358-1359 (2000).

[123] https://www.fibercore.com/product/multicore-fiber

[124] A. M. Ortiz and R. L. Saez, "Multi-core Optical fibers: Theory, applications and opportunities," Selected Topics on Optical Fiber Technologies and Applications, Intech, 2017.

[125] I. Ishida, T. Akamatsu, Z. Wang, Y. Sasaki, K. Takenaga and S. Matsuo, "Possibility of stack and draw process as fabrication technology for multi-core fiber," Optical Fiber Communication Conference and Exposition and the National Fiber Optic Engineers Conference (OFC/NFOEC), Anaheim, CA, 1-3 (2013).

[126] OPTICAL FIBER MANUFACTURING: Stack-and-draw technique creates ultrasmall-diameter endoscopeshttps (www.laserfocusworld.com/detectors-imaging/article/16556900/optical-fiber-manufacturing-stackanddraw-technique-creates-ultrasmalldiameter-endoscopes

[127] B. H. Bunch and A. Hellemans, The History of Science and Technology, Houghton Mifflin Harcourt, 695 (2004).

[128] M. Mukhtar Wan, P. Susthitha Menon and S. Sahbudin, "Microfabricated fibre probe by combination of electric arc discharge and chemical etching techniques," in International Conference on Material Science and Engineering Technology, A. M. Research, ed. (Zhengzhou, 2012), 38-41.

[129] A. Barucci, F. Cosi, A. Giannetti, S. Pelli, D. Griffini, M. Insinna, S. Salvadori, B. Tiribilli and G. C. Righini, "Optical fibre nanotips fabricated by a dynamic chemical etching for sensing applications," Journal of Applied Physics 117, 053104 (2015).

[130] S. Mononobe, R. Uma Maheswari and M. Ohtsu, "Fabrication of a pencil-shaped fibre probe with a nanometric protrusion from a metal film for near-field optical microscopy," Optics Express 1 (8), 229-233 (1997).

[131] Y. K. Cheong, K. S. Lim, W. H. Lim, W. Y. Chong, R. Zakaria and H. Ahmad, "Note: Fabrication of tapered fibre tip using mechanical polishing method," Review of Scientific Instruments 82, 086115 (2011).

[132] I.- B. Sohn, Y. Kim and Y.- C. Noh, "Microstructuring of Optical Fibres Using a Femtosecond Laser," Journal of the Optical Society of Korea 13, 33-36 (2009).

[133] J. Orloff, M. Utlaut and L. Swanson, High Resolution Focused Ion Beams: FIB and its Applications, Springer Press (2003).

[134] S. Lee, A. Ashmead and L. Migliore, "Comparison of ns and ps pulses for Si and glass micromachining applications," in Solid State Lasers XVIII: Technology and Devices, vol. 7193 of Proceedings of SPIE, p. 10.

[135] U. Loeschner, S. Mauersberger, R. Ebert, H. Exner, J. Schille, P. Regenfuss, and L. Hartwig, "Micromachining of glass with short ns-pulses and highly repetitive fs-laser pulses," in Proceedings of the 27th International Congress on Applications of Lasers and Electro-Optics (ICALEO '08), pp. 193–201, October 2008

[136] What's the Difference Between Femtosecond and Picosecond Lasers? (https://www.machinedesign.com/mechanical-motion-systems/article/21836637/whats-the-difference-between-femtosecond-and-picosecond-lasers)

[137] C. Moorhouse, "Advantages of Picosecond Laser Machining for Cutting-Edge Technologies," Physics Procedia 41, 381-388 (2013).

[138] V. Matylitskya and F. Hendricksa, "Industrial femtosecond lasers for micro-machining applications with highest quality and efficiency " in 9th International Conference on Photonic Technologies LANE 2016 (Bayerisches Laserzentrum GmbH 2016), 1-4.

[139] J. Gierak, "Focused ion beam technology and ultimate applications," Semiconductors Science Technology 24, 1-23 (2009).

[140] S. Reyntjens and R. Puers, "A review of focused ion beam applications in microsystem technology," Journal of Micromechanics and Microengineering 11, 287–300 (2001).

[141] R. Thomson, H. T. Bookey, N. D. Psaila, A. Fender, S. Campbell, W. N. MacPherson, J. S. Barton, D. T. Reid and A. K. Kar, "Ultrafast-laser inscription of a three dimensional fan-out device for multicore fibre coupling applications," Optics Express 15(18), 11691-11697 (2007).

[142] T. Watanabe, M. Hikita and Y. Kokubun, "Laminated polymer waveguide fan-out device for uncoupled multi-core fibres," Optics Express 20(24), 26317-26325 (2012).

[143] B. Zhu, T. F. Taunay, M. F. Yan, J. M. Fini, M. Fishteyn, E. M. Monberg and F. V. Dimarcello, "Seven-core multicore fibre transmissions for passive optical network," Optics Express 18(11), 11117 (2010).

[144] A. L. Barron, A. K. Kar, T. J. Aspray, Andrew J. Waddie, M. R. Taghizadeh and H. T. Bookey, "Two dimensional interferometric optical trapping of multiple particles and Escherichia coli bacterial cells using a lensed multicore fibre," Optics Express 21(11), 13199-13207 (2013).

[145] H. Schift, "Nanoimprint lithography: An old story in modern times? A review," Journal of Vacuum Science & Technology B: Microelectronics and Nanometer Structures Processing, Measurement, and Phenomena 26, 458 (2008).

[146] J. Orloff, "Fundamental limits to imaging resolution for focused ion beams," Journal of Vacuum Science and Technology B. 14 (6), 3759 (1996).

[147] J. Cui, S. Zhu, K. Feng, D. Hong, J. Li and J. Tan, "Fan-out device for multicore fibre coupling application based on capillary bridge self-assembly fabrication method," Optical Fibre Technology 26, 234–242 (2015).

[148] G. M. H. Flockhart, W. N. MacPherson, J. S. Barton, J. D. C. Jones, L. Zhang, and I. Bennion, "Two-axis bend measurement with Bragg gratings in multicore optical fiber," Optics Letters 28, 387-389 (2003).

[149] W. A. Gambling, H. Matsumura and C. M. Ragdale, "Joint loss in single-mode fibres," Electronic Letters, 14(15), 491–493 (1978).

[150] I. Timbercon, dB vs. Optical Power Loss, 2018; http://www.timbercon.com/db-power-loss/

[151] J. Cheng, C-S Liu, S. Shang, D. Liu, W. Perrie, G. Dearden and K. Watkins,"A review of ultrafast laser materials micromachining," Optics & Laser Technology 46, 88-102 (2013).

[152] X. Liu, D. Du, and G. Mourou, "Laser Ablation and Micromachining with Ultrashort Laser Pulses," IEEE Journal of Quantum Electronics 33(10), " 1706-1716 (1997).

[153] A. K. Dubey and V. Yadava, "Laser beam machining- A review," International Journal of Machine Tools and Manufacture 48(6), 609-628 (2008).

[154] K. Sugioka and Y. Cheng, "Ultrafast lasers- reliable tools for advanced materials processing," Light: Science & Applications 3(4), 149 (2014).

[155] P. R. Hermana, A. Oettlb, K. P. Chena, and R. S. Marjoribanks, "Laser micromachining of 'transparent' fused silica with 1-ps pulses and pulse trains," in Conference on Commercial and Biomedical Applications of Ultrafast Lasers, San Jose, California (1999).

[156] S.-H. Lu and H. Hua, "Imaging properties of extended depth of field microscopy through single-shot focus scanning,"Optics Express 23(8), 10714–10731 (2015).

[157] M. A. de Araújo, R. Silva, E. de Lima, D. P. Pereira and P. C. de Oliveira, "Measurement of Gaussian laser beam radius using the knife-edge technique: improvement on data analysis," Applied Optics 48, 393-396 (2009)

[158] N. B. Simpson, D. McGloin, K. Dholakia, L. Allen and M. J. Padgett, "Optical tweezers with increased axial trapping efficiency," Journal of Modern Optics 45(9), 1943–1949 (1998).

[159] P. Minzioni, F. Bragheri, C. Liberale, E. Di Fabrizio and I. Cristiani, "A Novel Approach to Fibre-Optic Tweezers: Numerical Analysis of the Trapping Efficiency," IEEE Journal of Selected Topics in Quantum Electronics, 14 (1), 151–157 (2008).

[160] L. Yuan, Z. Liu, J. Yang and C. Guan, "Twin-core fiber optical tweezers," Optics Express 16(7), 4559–4566 (2008).

[161] N. Malagnino, G. Pesce, A. Sasso and E. Arimondo, "Measurements of trapping efficiency and stiffness in optical tweezers,"Optics Communications, 214 (1-6), 15–24 (2002).

[162] H. Cabrera, J. J. Suárez-Vargas, A. López, H. Núñez, G. Carvalho, G. Coceano and D. Cojoc, "Experimental determination of trapping efficiency of optical tweezers,"Philosophical Magazine Letters, 93(11), 655–663 (2013).

[163] A. Ashkin, "Forces of a single-beam gradient laser trap on a dielectric sphere in the ray optics regime," Biophysical Journal, 61(2), 569–582 (1992).

[164] L. Allen, M. W. Beijersbergen, R. J. C. Spreeuw and J. P. Woerdman, "Orbital angular momentum of light and the transformation of Laguerre-Gaussian laser modes," Physics Review A 45 (11), 8185–8189 (1992).

[165] L. Paterson, A. Keloth, C. Ross, P-H. Thiollier, J. Schuster, M.K. Winson & G.H. Markx, 2015. Isolation of single cells using optical tweezers. MaCuMBA General Assembly 2015, Marine Research Institute, Reykjavík, Iceland. [166] A. B. Matheson, L. Paterson, A. J. Wright, T. Mendonca, M. Tassieri and P. A. Dalgarno, "Optical Tweezers with Integrated Multiplane Microscopy (OpTIMuM): a new tool for 3D microrheology," Scientific Reports 11, 5614 (2021).

[166] A. B. Matheson, L. Paterson, A. J. Wright, T. Mendonca, M. Tassieri and P. A. Dalgarno, "Optical Tweezers with Integrated Multiplane Microscopy (OpTIMuM): a new tool for 3D microrheology," Scientific Reports 11, 5614 (2021).

[167] G. Tomaiuolo, "Biomechanical properties of red blood cells in health and disease towards microfluidics," Biomicrofluidics 8(5), 051501 (2014).

[168] T. J. Smart, C. J. Richards, R. Agrawal and P. H. Jones, "Stretching Red Blood Cells withOptical Tweezers," Optics in the Life Sciences Congress, Optical Trapping Applications 2017, San Diego, California United States, 2–5 April 2017.

[169] L. M. G. van de Watering and A. Brand, "Effects of Storage of Red Cells," Transfusion Medicine and Hemotherapy 35(5), 359–367 (2008).

[170] K. Ramser, J. Enger, M. Goksör, D. Hanstorp, K. Logg and M. Käll, "A microfluidic system enabling Raman measurements of the oxygenation cycle in single optically trapped red blood cells," Lab Chip 5(4), 431-436 (2005).

[171] M. Allen, M. Bjerke, H. Edlund, S. Nelander and B. Westermark, "Origin of the U87 MG glioma cell line: Good news and bad news," Science Translational Medicine 8 (354), 354 (2016).

[172] I. Chambers, D. Colby, M. Robertson, J. Nichols, S. Lee, S. Tweedie and A. Smith, "Functional Expression Cloning of Nanog, a Pluripotency Sustaining Factor in Embryonic Stem Cells," Cell 113 (5), 643-655 (2003).

[173] M. F. Pera, B. Reubinoff and A. Trounson, "Human embryonic stem cells," Journal of Cell Science 113, 5-10 (2000).

[174] V. T. Hoang, G. Stępniewski, K. H. Czarnecka, R. Kasztelanic, V. C. Long, K. D. Xuan, L.Shao, M. Śmietana and R. Buczyński, "Optical Properties of Buffers and Cell Culture Media for Optofluidic and Sensing Applications," Applied Sciences 9(6), 1145 (2019).

[175] B. Rappaz, F. Charrière, C. Depeursinge, P. J. Magistretti and P. Marquet, "Simultaneous cell morphometry and refractive index measurement with dual wavelength digital holographic microscopy and dye-enhanced dispersion of perfusion medium," Optics Letters 33 (7), 744-746 (2008).

[176] Y. K. Park, M. Diez-Silva, G. Popescu, G. Lykotrafitis, W. Choi, M. S. Feld and S. Suresh, "Refractive index maps and membrane dynamics of human red blood cells

parasitized by Plasmodium falciparum," Proceedings of the National Academy of Science USA 105 (37), 13730-5 (2008).

[177] M. Takagi, T. Kitabayashi, S. Ito, M. Fujiwara and A. Tokuda, "Noninvasive Measurement of three-dimensional morphology of adhered animal cells Employingphase-shifting laser microscope," Journal of Biomedical Optics 12(5), 054010 (2007).

[178] P.A. Levin and E.R. Angert, "Small but Mighty: Cell Size and Bacteria", Perspectives in Biology, Cold Spring Harbour (pubs) 7(7), 019216 (2015).

[179] A. Ashkin and J. M. Dziedzic, "Optical trapping and manipulation of viruses and bacteria,"Science 235 (4595), 1517-1520 (1987).

[180] C. Xie and Y. Li, "Confocal micro-Raman spectroscopy of single biological cells using optical trapping and shifted excitation difference techniques," Journal of Applied Physics 93 (5), 2982-2986 (2003).

[181] R. Di Giacomo, S. Krodel, B. Maresca, P. Benzoni, R. Rusconi, R. Stocker and C. Daraio, "Deployable micro-traps to sequester motile bacteri," Scientific Reports 7, 45897 (2017).

[182] K. Saralidze, L. H. Koole and M. L. W. Knetsch. "Polymeric Microspheres for Medical Applications," Materials (Basel) 3(6), 3537-3564 (2010).

[183] K. T. Gahagan and G. A. Swartzlander, "Trapping of low-index microparticles in an optical vortex," Journal of Optical Society of America B 15 (2), 524-534 (1998).

[184] M. P. MacDonald, L. Paterson, W. Sibbett, K. Dholakia and P. E. Bryant, "Trapping and manipulation of low-index particles in a two-dimensionalinterferometric optical trap," Optics Letters 26 (12), 863-865 (2001).

[185] K. Sasaki, M. Koshioka, H. Misawa, N. Kitamura and H. Masuhara, "Optical Trapping of a metal particle and a water droplet by a scanning laser beam,"
Applied Physics Letters 60 (7), 807 (1992).

[186] G. Rui, Y. Wang, B. Gu and Y.Cui, "Trapping of low-refractive-index nanoparticles in a hollow dark spherical spot," Journal of Physics Communications 2, 065015 (2018).

[187] P.H. Jones, "Trapping and manipulation of microscopic bubbles with a scanning optical tweezer," Applied Physics Letters 89, 081113 (2006).

[188] R. Salari and R. Salari, "Investigation of the Best Saccharomyces cerevisiae Growth Condition," Electronic Physician 9(1), 3592-3597 (2017).

[189] Z. Pilát, A. Jonáš, J. Ježek, and P.l Zemánek, ", " Effects of Infrared Optical Trapping on Saccharomyces cerevisiae in a Microfluidic System," Sensors (Basel) 17(11), 2640 (2017)

[190] F. Wetzel, S. Rönicke, K. Müller, M. Gyger, V. Rose, M. Zink and J. Käs, "Single cell viability and impact of heating by laser absorption," European Biophysics Journal 40(90), 1109-1114 (2011).

[191] W. Wardand and S. H. Bokman, "Reversible denaturation of *Aequorea* green-fluorescent protein:physical separation and characterisation of the renatured protein," Biochemistry 21(19), 4535-40(1982).

[192] D. C. Prasher, V. K.Eckenrode, W. W. Ward, F. G. Prendergast and M. J. Cormier, "Primary structure of the *Aequorea victoria* green-fluorescent protein, " Gene 111 (2), 229-33 (1992).

[193] H. Butler, L. Ashton, B. Bird,G. Cinque, K. Curtis, J. Dorney, K. Esmonde-White, N. J. Fullwood, B. Gardner, P. L. Martin-Hirsch, M. J. Walsh, M. R. McAinsh, N. Stone and F. L. Martin "Using Raman spectroscopy to characterize biological materials," Nature Protocols 11, 664–687 (2016).

[194] M. Fleischmann, P. J. Hendra and A. J. McQuillan, "Raman spectra of pyridine adsorbed at a silver electrode," Chemical Physics Letters 26(2), 163-166 (1974).

[195] A. N. Kuzmin, A. Pliss, C. K. Lim, J. Heo, S. Kim, A.Rzhevskii, B.Gu, K. Yong, S. Wen, and P. N. Prasad, "Resonance Raman Probes for Organelle-Specific Labeling in Live Cells," Scientific Reports 6, 28483(2016).

[196] C. Xie and Y.- q. Li, "Raman spectra and optical trapping of highly refractive and nontransparent particles," Applied Physics Letters 81 (6), 951 (2002).

[197] M. P. Houlne, C. M. Sjostrom, R. H. Uibel, J. A. Kleimeyer and J. M. Harris, "Confocal Raman microscopy for monitoring chemical reactions on single optically trapped, solid-phase support particles," Analytical Chemistry 74(17), 4311-4319 (2002).

[198] S. Dochow, C. Krafft, U. Neugebauer, T. Bocklitz, T. Henkel, G. Mayer, J. Albert and J. Popp, "Tumour cell identification by means of Raman spectroscopy in combination with optical traps and microfluidic environments," Lab on Chip 11 (8), 1484-1490 (2011).

[199] M. Houlne, C. Sjostrom,R. Uibel, J. Kleimeyer and J. Harris, "Confocal Raman Microscopy for Monitoring Chemical Reactions on Single Optically Trapped, Solid Phase Support Particles," Analytical Chemistry 74, 4311-9 (2002).

[200] P. G. Spizzirri, J.- H. Fang, S. Rubanov, E. Gauja and S. Prawer, "Nano-Raman spectroscopy of silicon surfaces," Material Science 34, 1-5 (2010).

[201] C. Xie and Y.Q.Li, "Study of dynamical process of heat denaturation in optically trapped single microorganisms by near-infrared Raman spectroscopy," Journal of Applied Physics 94, 6138 (2003).

[202] F. Adar, "Introduction to interpretation of Raman spectra using database searching and functional group detection and identification," Spectroscopy 31(7), 16-23 (2016).

[203] J. R. Lepock, H. E. Frey and K. P. Ritchie, "Protein denaturation in intact hepatocytes and isolated cellular organelles during heat shock," Journal of Cell Biology 218 (2), 1267-1276 (1993).

[204] X. Li, T. Yang, S. Li, D. Wang, Y. Song and S. Zhang. "Raman spectroscopy Combined with principal component analysis and k nearest neighbour analysis for non-invasivedetection of colon cancer," Laser Physics 26 (3), 1-9 (2016).

[205] I. T. Jolliffe and J. Cadima, "Principal component analysis: a review and recent developments," Philosophical Transactions of The Royal Society A Mathematical Physical and Engineering Sciences 374 (2065), 1-16 (2016).

[206] D. J. Illich, M.Zhang, A. Ursu, R. Osorno, K. P. Kim, J. Yoon, M. J.Araúzo-Bravo, G. Wu, D, Esch, D. Sabour, D. Colby, K. S. Grassme, J. Chen, B. Greber, S. Höing, W. Herzog, S. Ziegler, I. Chambers, S. Gao, H. Waldmann and H. R. Schöler, "Distinct Signaling Requirements for the Establishment of ESC Pluripotency in Late-Stage EpiSCs," Cell Reports 15 (4), 787-800 (2016).

[207] N. P. Mullin, J.Varghese, D. Colby, J. M. Richardson, G. M. Findlayand I. Chambers, "Phosphorylation of NANOG by casein kinase I regulates embryonic stem cell self-renewal," FEBS Letters 595, 14-25 (2021).

[208] I. Notingher, I. Bisson, A. Bishop, W. Randle, J. Polak and L. Hench, "*In Situ* spectralmonitoring of mRNA translation in embryonic stem cells during differentiation *in vitro*," Analytical Chemistry 76 (11), 3185-3193 (2004).

[209] N. Stone, C. Kendal, N. Shepherd, P. Crow and H. Barr, "Near-infrared Raman Spectroscopyfor the classification of epithelial pre-cancers and cancers," Journal of Raman Spectroscopy 33, 564-573 (2002).

[210] S. Habuchi, M. Cotlet, R. Gronheid, G. Dirix, J. Michiels, J. Vanderleyden, F. C. De Schryver and J. Hofkens, "Single-molecule surface enhanced resonance Raman spectroscopy of the enhanced green fluorescent protein," Journal of the American Chemical Society 125, 8446-8447 (2003).

[211] P. Schellenberg, E.Johnson, A. Esposito, P. Reid and W. W. Parson, "Resonance Raman scattering by the green fluorescent protein and an analogue of its chromophore," The Journal of Physical Chemistry B105, 5316-5322 (2001).

[212] S. J. Altschuler, L. F. Wu, "Cellular heterogeneity: do differences make a difference?" Cell 141(4), 559-563 (2010).

[213] P. Chames, M. Van Regenmortel, E. Weiss, D. Baty, "Therapeutic antibodies: successes, limitations and hopes for the future," British Journal of Pharmacology 157(2), 220-233 (2009).

[214] P. Larsson, H. Engqvist, J. Biermann, E. Werner Rönnerman, E. Forssell-Aronsson, A. Kovács, P. Karlsson, K. Helou and T. Z. Parris, "Optimization of cell

viability assays to improve replicability and reproducibility of cancer drug sensitivity screens," Scientific Reports 10, 5798 (2020).

3.1 Michelson Interferometry for refractive index measurement

Matlab code for IR spectrum

```
K=readtable('IR17multicore.dat');
x1=K{:,1};
A=[1:1:5000000];
y1=A;
plot(y1,V);
pks=findpeaks(x1,y1,'MinPeakProminence',0.007);
```

Matlab code for red spectrum

```
T=readtable('red17multicore.dat');
Fig.;
x=T{:,1};
B=[1:1:5000000];
y=B;
plot(y,V1);
D=[1855000:1:3845000];
V2=V1(1855000:3845000);
x2=V2;
y2=D;
plot(y2,x2);
 [pks,locs]=findpeaks(x2,y2,'MinPeakProminence',0.005);
 [pks,locs]=findpeaks(x2,y2,'MinPeakDistance',0.00008);
 stop
peakInterval = diff(locs);
sum(peakInterval);
stop;
AverageDistance_Peaks = mean(diff(locs));
```

4.1 Beam divergence code

```
clc;
I=imread('core0d1cropped.jpg');
imshow(I);
c=rgb2gray(I);
h=imshow(c);
hp=impixelinfo;
a=mean(c,1);
d=[0:1:298];
x=d;
y=a;
plot(x,y);

A=imread('backgroundcropped.jpg');
imshow(A);
f=rgb2gray(A);
g=imshow(f);
gp=impixelinfo;
b=mean(f,1);

e=[0:1:298];
x=e;
y=b;
plot(x,y);
v=minus(a,b);
```

```
plot(x,v)
```

4.2 Matlab for Gaussian beam-propagation simulation (for two beams)

```matlab
clc
x1=[1400:1:1970];

y1=[-220:1:380];
sigma2=0.056*x1-67;
sigma2;
beta=-0.076*x1+2.8e+02;
beta;
a=672./sigma2;
a;
fxy=cell(1,size(x1,2));

for j=1:1:size(x1,2)
disp(fxy);
   temp=a(1,j).*exp(-((y1-beta(1,j))./sigma2(1,j)).^2);
   A(j,1:length(temp)) = temp;
fxy{1,j}=temp;
end
B=transpose(A);%multiply by the power we used for the profile
B1=30.*B;
Fig.(1);
h1=pcolor(B1); set(h1,'EdgeColor','none');
x=[1400:1:1970];

y=[-60:1:540];
sigmacore1=0.02*x-14;
sigmacore1;
betacore1=0.041*x+2.2e+02;
betacore1;
alphacore1=640./sigmacore1;
alphacore1;
fxycore1=cell(1,size(x,2));

for j=1:1:size(x,2)
disp(fxycore1);
temp=alphacore1(1,j).*exp(-((y-betacore1(1,j))./sigmacore1(1,j)).^2);
A1(j,1:length(temp)) = temp;
   fxycore1{1,j}=temp;
end
B2=transpose(A1);%multiply by the power we used for the profile
B3=30.*B2;
Fig.(1);
h1=pcolor(B3); set(h1,'EdgeColor','none');
C=B1+B3;
Fig.(1);
h1=pcolor(C); set(h1,'EdgeColor','none');
ylim([200 500]);
```

Beam divergence-MCF with two machined cores

More specifically, for the fibre with the two machined cores, the calculations follow the procedure below:

Core 1: P=3.27 mW

Measurements have been taken for two different positions of the fibre-end away from the screen, for the first machined core, $D_1 = 1400 \ \mu m$ and $D_2 = 1470 \ \mu m$.

Running the Matlab code, the parameters for the D_1 are:

$$a_1 = 42.46$$
$$b_1 = 160.7$$
$$c_1 = 20.21$$

The maximum Y will be the

$$Y_{max} = Y\frac{1}{e^2} = 42.46 \times 0.135 = 5.732 \qquad (4.13)$$

We find the X_1 and X_2 for this Y_{max} :
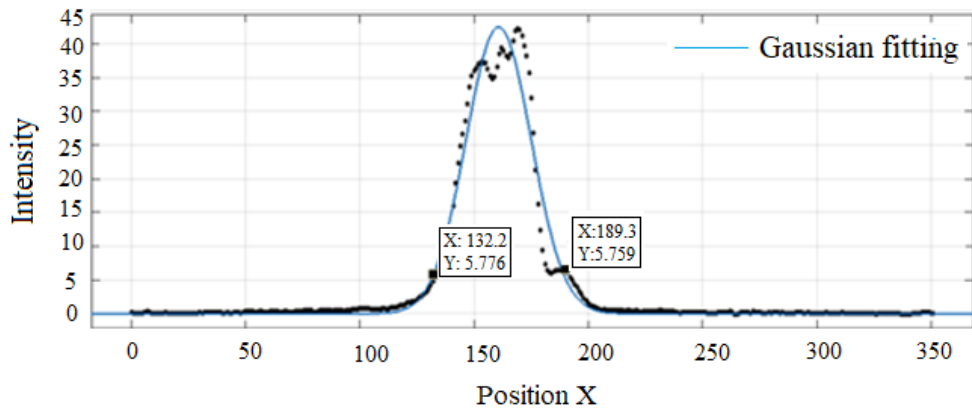
Fig. 4. 28: Matlab graph of the Gaussian fitting of the Intensity distribution of the first machined core of the MCF.

$$X_{1.1} = 132.2 \text{ and } X_{1.2} = 189.3$$
$$X_1 = X_{1.2} - X_{1.1} = 57.1 \times 0.782 = 44.65 \ \mu m \qquad (4.14)$$

The same process for the data of the second position of the fibre end away from the screen are derived as following:

$$a_2 = 41.95$$
$$b_2 = 157.8$$
$$c_2 = 22.21$$

The maximum Y will be the $Y_{max} = Y\frac{1}{e^2} = 41.95 \times 0.135 = 5.663$

$$X_{2.1} = 126.3 \text{ and } X_{2.2} = 189.2$$
$$X_2 = X_{2.2} - X_{2.1} = 62.9 \times 0.782 = 49.18 \ \mu m$$

Finally,

$$\vartheta_{div} = \tan^{-1}\frac{X_2-X_1}{D_2-D_1} = 3.74° \qquad\qquad (4.\,15)$$

Following the same process for the second machined core (Fig. 4. 23), for $D_1 = 1460\ \mu m$ and $D_2 = 1600\ \mu m$, the parameters respectively are $a_1 = 44.57, b_1 = 168.7, c_1 = 19.36$ and $a_2 = 43.35,\ b_2 = 165.2$ and $c_2 = 20.68$, and the resulting beam divergence $\vartheta_{div} = 1.21°$.
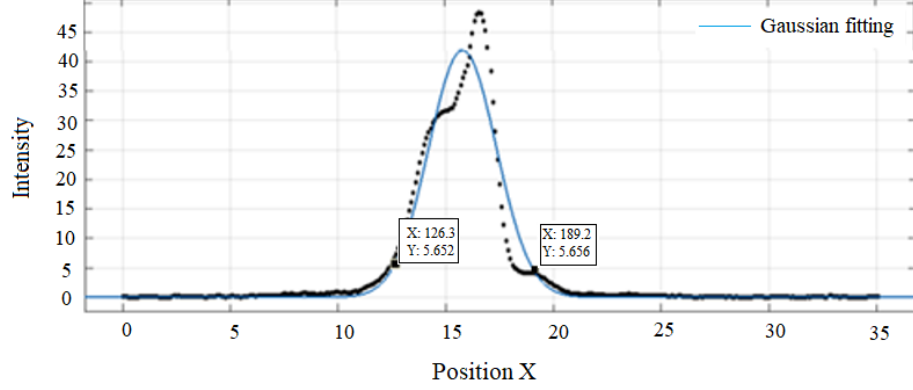
Fig. 4. 29: Matlab graph of the Gaussian fitting of the Intensity distribution of the second machined core of the MCF.

As previously explained for the MCF with the two machined cores, in a same way the beam divergence angle for the MCF with the four machined cores, had been calculated.

For the first core, for $D_1 = 1400\ \mu m$ (distance away from the screen)

$$c_1 = \sigma_1\sqrt{2} \Rightarrow \sigma_1 = 14.29$$

So, for a known a

We derive $A_1 = 1520.52$

And
$$b_1 = \mu_{x1} = 160.7$$

Similarly, for the second position $D_2 = 1470\ \mu m$,

$$c_2 = \sigma_2\sqrt{2} \Rightarrow \sigma_2 = 15.71$$

So, for a known a

We derive $A_2 = 1651.54$

And
$$b_1 = \mu_{x1} = 157.8$$

For these two set of data, position and μ and sigma,

$$\sigma(x) = 0.02 * x - 14$$

and

$$\mu(x) = -0.041 * x + 2.2 * 10^{\wedge}2$$

209

$$\mu(y) = -0.044 * y + 2.2 * 10^\wedge 2$$
$$\mu(z) = -0.04 * z + 2.2 * 10^\wedge 2$$

For the second core, for $D_1 = 1460\ \mu m$

$$c_1 = \sigma_1\sqrt{2} \Rightarrow \sigma_1 = 13.69$$

So for a known a

We derive $A_1 = 1529.06$

And
$$b_1 = \mu_{x1} = 168.7$$

Similarly, for the second position $D_2 = 1600\ \mu m$,

$$c_2 = \sigma_2\sqrt{2} \Rightarrow \sigma_2 = 14.63$$

So for a known a

We derive $A_2 = 1589.33$

And
$$b_1 = \mu_{x1} = 165.2$$

For these two set of data, position and m and sigma,

Following the same process for the second core,

$$\sigma(x) = 0.0067 * x + 3.9$$

and

$$\mu(x) = -0.025 * x + 2.1 * 10^\wedge 2$$
$$\mu(y) = -0.027 * y + 2.1 * 10^\wedge 2$$
$$\mu(z) = -0.024 * z + 2 * 10^\wedge 2$$

Beam divergence-MCF with four machined cores

Following the same process, for the core 1

$$A = 9396.79$$

$$\sigma(x) = 0.019 * x + 11$$

and

$$\mu(x) = -0.082 * x + 1.6 * 10^\wedge 2$$
$$\mu(y) = -0.069 * y + 1.4 * 10^\wedge 2$$

$$\mu(z) = -0.11 * z + 2.2 * 10\text{\textasciicircum}2$$

For the core 2

$$A = 10558.5$$

$$\sigma(x) = 0.008 * x + 13$$

and

$$\mu(x) = -0.047 * x + 1.8 * 10\text{\textasciicircum}2$$

$$\mu(y) = -0.039 * y + 1.5 * 10\text{\textasciicircum}2$$

$$\mu(z) = -0.061 * z + 2.3 * 10\text{\textasciicircum}2$$

Similarly, for the core 3

$$A = 10049.81$$

$$\sigma(x) = 0.032 * x + 7.3$$

and

$$\mu(x) = -0.033 * x + 1.6 * 10\text{\textasciicircum}2$$

$$\mu(y) = -0.028 * y + 1.4 * 10\text{\textasciicircum}2$$

$$\mu(z) = -0.043 * z + 2.1 * 10\text{\textasciicircum}2$$

Finally, for the core 4,

$$A = 710$$

$$\sigma(x) = -0.023 * x + 22$$

and

$$\mu(x) = 0.088 * x + 1.3 * 10\text{\textasciicircum}2$$

$$\mu(y) = 0.09 * y + 1.3 * 10\text{\textasciicircum}2$$

$$\mu(z) = 0.086 * z + 1.3 * 10\text{\textasciicircum}2$$

MCF with two machined cores

For the first core, for $D_1 = 1400 \ \mu m$ (distance away from the screen)

$$c_1 = \sigma_1 \sqrt{2} \Rightarrow \sigma_1 = 14.29$$

So, for a known a

We derive $A_1 = 1520.52$

And
$$b_1 = \mu_{x1} = 160.7$$

Similarly, for the second position $D_2 = 1470\ \mu m$,

$$c_2 = \sigma_2\sqrt{2} \Rightarrow \sigma_2 = 15.71$$

So, for a known a

We derive $A_2 = 1651.54$

And
$$b_1 = \mu_{x1} = 157.8$$

For these two set of data, position and μ and sigma,

$$\sigma(x) = 0.02 * x - 14$$

and

$$\mu(x) = -0.041x + 2.2 \times 10\hat{}2$$
$$\mu(y) = -0.044y + 2.2 \times 10\hat{}2$$
$$\mu(z) = -0.04z + 2.2 \times 10\hat{}2$$

Following the same process for the second core,

$$\sigma(x) = 0.0067x + 3.9$$

and

$$\mu(x) = -0.025x + 2.1 * 10\hat{}2$$
$$\mu(y) = -0.027y + 2.1 * 10\hat{}2$$
$$\mu(z) = -0.024z + 2 * 10\hat{}2$$

All the calculation steps for the four cores of the four machined core- fibre can be found in Appendix B. The resulting beam propagation for the two fibres can be seen in Fig. 4.24 and 25 below. The images have been stretched in x axis so that the propagation of the beams can be seen in detail.

4.3 Fan-out power measurements

I (mA)	P (mW)					
	Diode 1	Diode 2	Fan-out core1	Fan-out core 2	Machined core 1	Machined core 2
100	11.7	12.0	1.3	3.4	0.913	2.400
120	22.8	20.8	2.0	5.3	1.650	4.190
150	38.9	33.9	2.9	7.3	2.583	6.940
180	54.8	47.0	4.4	11.4	3.270	9.860
200	65.0	55.5	5.1	12.0	4.320	10.860

250	94.8	80.9	7.1	17.5	5.370	15.370
300	113.7	97.5	8.4	19.9	7.750	20.030
340	132.4	113.9	9.6	23.6	8.990	25.370
360	137.5	122.0	10.2	24.6	9.340	26.800

Table 1: Comparison between the power values of the laser beam coming out of the laser diodes, the fan-out before the spicing of the machined fibre and after the splicing, for the etched fibres-based fan-out type.

I (mA)	P (mW)											
	Diode 3	Diode 4	Diode 2	Diode 5	Fan-out core 1	Fan-out core 2	Fan-out core 3	Fan-out core 4	Machined core 1	Machined core 2	Machined core 3	Machined core 4
100	11.63	16.87	12	18.14	1.507	3.811	4.177	6.217	0.00661	1.503	1.953	2.56
120	19.9	29.18	20.8	30.28	2.759	6.199	6.595	10.11	1.207	2	3.355	4.188
150	32.26	47.61	33.98	48.68	4.802	9.889	11.12	16.05	1.969	3.128	5.256	6.98
180	44.73	65.89	47	66.97	7.079	13.55	15.18	22.11	2.887	4.193	7.233	10.09
200	53.04	77.9	55.56	79.09	9	15.95	17.87	25.91	3.453	4.894	8.33	11.89
250	61.31	113.7	80.92	115	13.35	21.88	24.36	34.24	4.961	6.549	11.36	16.35
300	77.63	137.2	97.52	138.5	14.52	27.66	30.6	42.21	6.476	8.226	14.07	20.06
340	85.74	160.44	113.9	161.8	15.58	32.15	35.38	49.12	7.737	9.306	16.16	22.87
360	93.75	171.9	122	173.3	16.7	34.40	37.75	52.50	8.422	9.885	17.2	24.52

Table 2: Comparison between the power values of the laser beam coming out of the laser diodes, coming out of the fan-out before the splicing of the machined fibre and after the splicing, for the inscribed waveguide-based fan-out type.

4.4 Microchanels fabrication: Power,speed, number of repetitions and depth combinations results

Scan speed (mm/s)	Power ± 0.01 (W)	Repetitions of scans (N)	Machined depth ± 0.005 (mm)
60	4.60	5	0.040
60	9.20	5	0.080
60	18.40	5	0.092
60	23.00	5	0.013
80	4.60	5	0.043
80	9.20	5	0.107
80	18.40	5	0.083
80	23.00	5	0.155

100	4.60	5	0.027
100	9.20	5	0.094
100	18.40	5	0.077
100	23.00	5	0.090
120	4.60	5	0.051
120	9.20	5	0.056
120	18.40	5	0.081
120	23.00	5	0.079
110	4.60	5	0.090
110	9.20	5	0.095
110	18.40	5	0.100
110	23.00	5	0.119
110	4.60	10	0.021
110	9.20	10	0.077
110	18.40	10	0.151
110	23.00	10	0.144
110	4.60	15	0.126
110	9.20	15	0.195
110	18.40	15	0.256
110	23.00	15	0.291
110	4.60	20	0.133
110	9.20	40	0.200
110	18.40	40	0.275
110	23.00	40	0.319
150	13.80	30	0.286
150	9.20	25	0.201
150	13.80	30	0.374

4.5 Two opposed fibres initial experiments

Before the development of the machined MCF trapping system, some preliminary trapping was conducted to repeat work from the literature using non-machined single

core optical fibres. Two opposing fibres were used to create a dual, counter-propagating beam trap. This type of trapdemands precision alignment between two single core fibres.Fig. 4. 1 shows optical trapping of a single yeast cell (a) and two yeast cells (b) using two opposed single-core fibres with optical powers P_1=71 mW for the one fibre and P_2=77 mW for the second fibre.
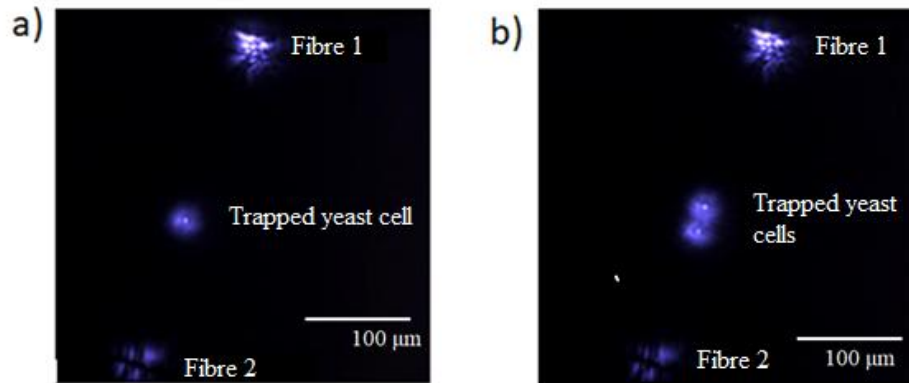

Fig. 4. 1:Dual beam fibre optical trapping of a)a single yeast cell and b) two yeast cells, using two oppposed single-core optical fibres, of output optical powers equal toP_1=71.0 mW±0.1mW and P_2=77.0 mW±0.1mWfor fibre 1 and fibre 2, respectively. The light areas are laser light scattered from the fibre ends and the trapped cells.

For this purpose, a long micro-channel of a width equal to the fibre polymer jacket diameter (360 μm ± 1 μm) that would traverse the whole length of the microscope slide was fabricated to hold the fibre stably in place and thus eliminate its fragility. In the middle of the channel, a squared well with increased depth of 124 μm was needed in order to be filled with the sample liquid. Furthermore, two circular-shaped areas along the micro-channel have been machined to act as glue reservoirs that hold the fibres aligned and in place (Fig. 4. 2), and seal the fibre to prevent fluid leakage along the fibre channels.
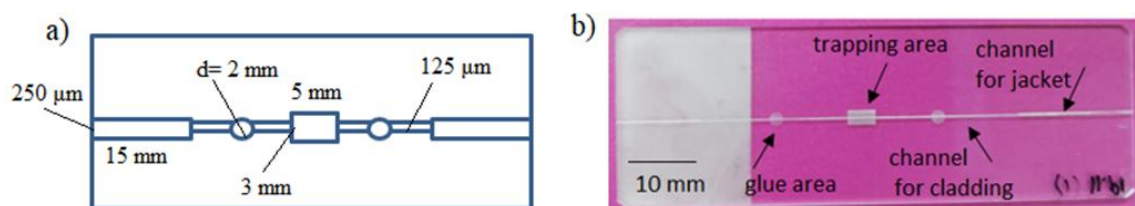
Fig. 4. 2: a) Design of microchannels and trapping area (squared-shaped reservoir) on the surface of a microscope slide. The pattern consisted of a long microchannel to hold the two fibres in place, two circular areas for glue to fix the fibres in place and a deeper squared area as a trapping area, where the cell sample is placed. b) Fabricated slide according to the designed dimensions in a).

The optical fibre used here was singe-core (SM800-5.6-125, Thorlabs). This fibre had a cladding diameter of 125 μm and a jacket of 245 μm outer diameter, as denoted from the product specification sheet. The channel and reservoir design for the dual beam fibre

trap is shown in Fig. 4.2 and the fabricated slides is shown in Fig. 4.2 b. The dimensions and the respective depth of the design are presented below (Table 4.4).

Area	Width (mm)	Length (mm)	Depth (mm)
Trapping area	3	5	0.124
Fibre microchannel	0.125	45	0.107
Jacket area	0.300	15	0.124
Glue area	Diameter=1.6		0.063

Table 4. 1: Dimensions of the fabricated patterns on the surface of the microscope slide (all dimensions are given in millimeters).This slide was used for the two opposed fibres optical trapping experiments.

5.1 Matlab code for cell position tracking

```
%run in loop 1st group
clear all;
c=cell(1,4);
for i=1:1:18
    c{i}=imread(sprintf('tiffs cropped  (%d).tif',i));
    I{i}= rgb2gray(c{i});
T{i}=imcomplement(I{i})
C=[1:1:23]
R=[1:1:23]
P{i}=impixel(T{i},C,R)
max(P{i})
min(P{i})
Ithr{i}=(max(P{i})+min(P{i}))/2
highvalues{i}=T{i}>208;
lowvalues{i}=T{i}<208;
A{i}=highvalues{i}+lowvalues{i}
labeledImage = bwlabel((A{i}));
measurements = regionprops(labeledImage,A{i},'Centroid');
centreOfMass1{i} = measurements.Centroid;
end
%run in loop 2nd group
c1=cell(1,4);
for i=1:1:27
    c1{i}=imread(sprintf('tiffs cropped1 (%d).tif',i));
    I1{i}= rgb2gray(c1{i});
T1{i}=imcomplement(I1{i})
C=[1:1:23]
R=[1:1:23]
P1{i}=impixel(T1{i},C,R)
max(P1{i})
min(P1{i})
I1thr{i}=(max(P1{i})+min(P1{i}))/2
highvalues1{i}=T1{i}>173;
lowvalues1{i}=T1{i}<173;
A1{i}=highvalues1{i}+lowvalues1{i}
labeledImage1 = bwlabel((A1{i}));
measurements1 = regionprops(labeledImage1,A1{i},'Centroid');
centreOfMass2{i} = measurements1.Centroid;
end

%show raw image with marker
for i=1:1:18
```

```matlab
B{i} = centreOfMass1{i};
y{i}= B{i}(:,2);
x{i}=B{i}(:,1)
h=figure
imshow(c{i})
hold on; % Prevent image from being blown away.
plot(x{i}, y{i},'x');
saveas(h,sprintf('FIG%d.tif',i));
end


%show raw image with marker(part2)
for i=1:1:10
B1{i} = centreOfMass2{i};
y1{i}= B1{i}(:,2);
x1{i}=B1{i}(:,1)
h1=figure
imshow(c1{i})
hold on; % Prevent image from being blown away.
plot(x1{i}, y1{i},'x');
saveas(h1,sprintf('FIGG%d.tif',i));
end


%plot particle trajectories in x
table=cell2mat(centreOfMass1(:))
table1=cell2mat(centreOfMass2(:))
table2=[table;table1]
table3=0.29*table2 %transform pixel into microns
table3(:,1)=table3(:,1)-3.5079
table3(:,2)=table3(:,2)-3.4965
b=[0.1:0.1:4.5]
plot(b,table3(:,1),'o')



%plot particle trajectories in y
plot(b,table3(:,2),'o')

%plot centres of mass and centre of the centres
M = min(table3,[],1);
m = max(table3,[],1);
cent = (M + m) / 2;
plot(table3(:,1),table3(:,2),'o')
hold on
plot(cent(:,1),cent(:,2),'*');
hold off



%plot position with lines
line_color=['b''g''y''c''m''r'];
ca=cell(1,length(line_color));
for k=1:length(line_color)
    plot(table3(:,1),table3(:,2),'color',line_color(k));
hold on
B=scatter(table3(:,1),table3(:,2), 20, 'b', 'filled')
B=scatter(table3(:,1),table3(:,2), 'r', 'filled')
end

n=18
colors=hsv(n)
h=plot(table3(:,1),table3(:,2),'-k');
hold on
B=scatter(table3(:,1),table3(:,2), 20, 'b', 'filled')
B=scatter(table3(:,1),table3(:,2), 'r', 'filled')
```

```matlab
hold off
set(h,{'color'},num2cell(jet(45),45))
R = 3 ;
nBinsX = 2 ;
nBinsY = 2 ;
xg      = linspace( R, R+1, nBinsX+1 ) ;
yg      = linspace( R, R+1, nBinsY+1 ) ;
nCells = nBinsX * nBinsY ;
figure(1) ;  clf ;  hold on ;
set( gcf, 'Color', 'w', 'Units', 'Normalized', ...
'Position', [0.1,0.1,0.6,0.6] ) ;
% - Plot grid.
plot( [xg;xg], repmat( [R;R+1], 1, numel( xg )), 'Color', 0.8*[1,1,1]
) ;
plot( repmat( [R;R+1], 1, numel( yg )), [yg;yg], 'Color', 0.8*[1,1,1]
) ;

labels = arrayfun( @(k)sprintf( '%d', k ), 1:nCells, 'UniformOutput',
false ) ;
[X,Y]  = meshgrid( (xg(1:end-1)+xg(2:end))/2, (yg(1:end-
1)+yg(2:end))/2 ) ;
text( X(:), Y(:), labels, 'Color', 'b', 'FontSize', 14 ) ;
y1=get(gca,'ylim')
plot( table3(:,1),table3(:,2), 'rx', 'LineWidth', 2, 'MarkerSize', 8 )
;
hold on;
plot([3.5079 3.5079],y1)


%count how many points are away from cent by a specific distance (x-
axis)

N=50
V=zeros(N,1) + 3.5079
I = [0:0.005:0.245]
J = [0.005:0.005:0.250]
C=table3(table3(:,1)>3.5079)
D=table3(table3(:,1)<3.5079)
for k=1:numel(I)
    i = I(k);
    j = J(k);
   distances1 = pdist2(C, V);
   distances2 = pdist2(D, V);
closePoints1 = [distances1<j & distances1> i];
closePoints2 = [distances2<j & distances2> i];
N2(k) = nnz(closePoints1(:,1)) % Use i and j
N3(k) = nnz(closePoints2(:,1)) % Use i and j
end

%plot the distribution of the x-points, by creating a plot between the
%numbers of points and x-axis coordinates
N3=flip(N3)
N=[N3,N2];
Y=[-0.245:0.005:0.250]
scatter(Y,N);
xlim([-0.300 0.300])
ylim([0 8])

%plot the distribution of the y-points, by creating a plot between the
%numbers of points and y-axis coordinates
R = 3 ;
nBinsX = 2 ;
```

```matlab
nBinsY = 2 ;
xg      = linspace( R, R+1, nBinsX+1 ) ;
yg      = linspace( R, R+1, nBinsY+1 ) ;
nCells = nBinsX * nBinsY ;
figure(1) ;   clf ;   hold on ;
set( gcf, 'Color', 'w', 'Units', 'Normalized', ...
'Position', [0.1,0.1,0.6,0.6] ) ;
% - Plot grid.
plot( [xg;xg], repmat( [R;R+1], 1, numel( xg )), 'Color', 0.8*[1,1,1]
) ;
plot( repmat( [R;R+1], 1, numel( yg )), [yg;yg], 'Color', 0.8*[1,1,1]
) ;

labels = arrayfun( @(k)sprintf( '%d', k ), 1:nCells, 'UniformOutput',
false ) ;
[X,Y]  = meshgrid( (xg(1:end-1)+xg(2:end))/2, (yg(1:end-
1)+yg(2:end))/2 ) ;
text( X(:), Y(:), labels, 'Color', 'b', 'FontSize', 14 ) ;
x1=get(gca,'xlim')
plot( table3(:,1),table3(:,2), 'rx', 'LineWidth', 2, 'MarkerSize', 8 )
;
hold on;
plot(x1,[3.4965 3.4965])
u1=table3(:,1)
h = histfit(u1)
xlim([-0.25 0.25])
ylim([0 22])
u2=table3(:,2)
h = histfit(u2)
xlim([-0.25 0.25])
ylim([0 22])
N2=50
V2=zeros(N2,1) + 3.4965
I = [0:0.005:0.245]
J = [0.005:0.005:0.250]
C2=table3(table3(:,2)>3.4965)
D2=table3(table3(:,2)<3.4965)
for k=1:numel(I)
    i = I(k);
    j = J(k);
   distances1 = pdist2(C2, V2);
   distances2 = pdist2(D2, V2);
closePoints1 = [distances1<j & distances1> i];
closePoints2 = [distances2<j & distances2> i];
N4(k) = nnz(closePoints1(:,2)) % Use i and j
N5(k) = nnz(closePoints2(:,2)) % Use i and j
end

%plot the distribution of the x-points, by creating a plot between the
%numbers of points and x-axis coordinates
N5=flip(N5)
N6=[N4,N5];
Y=[-0.245:0.005:0.250]
scatter(Y,N6);
xlim([-0.300 0.300])
ylim([0 7])
```

6.1 Raman Power measurements

Power percentage (%)	Power (±0.1 mW)-20×objective lens

100	92
50	38.3
10	11
5	4.8
1	2
0.5	0.9
0.1	0.2
0.05	0.1
0.0001	0.0052
0.00005	0.0038
0.00001	0.0017

6.2 PCA analysis- Matlab code

```
clear all;
[~,scores,pcvars]=princomp(PCAepiesesgreen3300');
x=scores(:,1);
y=scores(:,2);
group1=celltype';
gscatter(x,y,group1);
```